Characterization of Electrohydrodynamic (EHD) heat transfer enhancement mechanisms in melting of organic Phase Change Material (PCM)

Characterization of Electrohydrodynamic (EHD) heat transfer enhancement mechanisms in melting of organic Phase Change Material (PCM)

By
David Nakhla, M.A.Sc., B.Sc.

A Thesis
Submitted to the School of Graduate Studies
in Partial Fulfillment of the Requirements
for the Degree of
Doctor of Philosophy

McMaster University

DOCTOR OF PHILOSOPHY (2018)
(Department of Mechanical Engineering)

McMaster University
Hamilton, Ontario, Canada

TITLE:	Characterization of Electrohydrodynamic (EHD) heat transfer enhancement mechanisms in melting of organic Phase Change Material (PCM)
AUTHOR:	David Nakhla, M.A.Sc (McMaster University)
SUPERVISOR:	Dr. James S. Cotton, Professor Department of Mechanical Engineering
NUMBER OF PAGES:	299, xxvii

"To the memory of my grandparent "

“

Abstract

The effect of using high voltage DC and AC on the heat transfer process during the melting of a Phase Change Material (PCM) in a rectangular enclosure was studied experimentally and numerically. The experiments were conducted for two configurations: (a) a horizontal rectangular enclosure in which the initial melting process is governed by heat conduction, (b) a vertical rectangular enclosure in which the initial melting process is governed by heat convection.

The level of heat transfer enhancement was quantified by using a novel experimental facility for the horizontal configuration. The experimental methodology was verified first against non-EHD melting cases and then was further expanded to include the EHD effects. The experiments showed that EHD forces can be used to enhance a conduction dominated melting up to a maximum of 8.6-fold locally and that the level of enhancement is directly related to the magnitude of the applied voltage. It was found that the main mechanism of enhancement in these cases can be attributed to the electrophoretic forces and that the role of the dielectrophoretic forces is minimal under the applied voltages.

In the vertical configuration, the effect of the magnitude of the applied voltage, the applied voltage wave-form, the gravitational Rayleigh number, Stefan number and the aspect ratio of the enclosure on the heat transfer enhancement were investigated experimentally. A novel shadowgraph experimental measurement system was developed and verified against the analytical correlations of natural convection in rectangular

enclosures and the non-EHD melting performance was verified against the bench mark experiments of Ho (1984). The shadowgraph system was used to measure the local heat transfer coefficient across the heat source wall (the heat exchanger surface). The local heat transfer measurements along with the melting temporal profiles were used to explain and visualize the coupling between the Electrohydrodynamics (EHD) forces and the gravitational forces.

It was found that the EHD forces could still enhance the melting process even for an initially convection dominated melting process. The mechanism of enhancement was found to be a bifurcation of the initial convection cell into multiple electro-convective cells between the rows of the electrodes. The shadowgraph system was used to assess the interaction between the electrical and the gravitational forces through the visualization of these cells and quantifying their size. The EHD heat transfer enhancement factor was found to increase by the increase of the applied voltage, reaching a 1.7 fold enhancement at the lower gravitational Rayleigh number tested and 1.45 fold for the highest gravitational Rayleigh and Stefan number. The effect of the polarity of the applied voltage was tested for the different cases and it was found that there was no significant difference between the positive and the negative polarities when the magnitude of the applied voltage was below 4 kV. At higher voltages- 6kV- the negative polarities showed better level of enhancement when compared to the positive applied voltage. It was again found that the main mechanism of enhancement is attributed to charge injection from the high voltage electrodes.

A scaling analysis was conducted based on the previous conclusions and the dominant mechanism of enhancement to describe the problem in non-dimensional form. An electrical

Rayleigh number was introduced and its magnitude was correlated to the magnitude of the injected current. The melt volume fraction was then represented against the non-dimensional parameter $(n+1)\frac{H}{W}\,Fo.Ste.Ra_{E/c}^{0.25}$ and the melt fraction temporal profiles for the different voltages collapsed well against this parameter.

Finally, a numerical analysis was conducted on the role of the dielectrophoretic forces during the melting of Octadecane and when they would become of significant importance. The results of the numerical model supported the experimental findings and suggested that a minimum of 15 kV is needed in order to realize the effect of the dielectrophoretic forces. The numerical model was used to understand the interaction between the gravitational and the dielectrophoretic forces at different ranges of both gravitational Rayleigh number and electrical Rayleigh number. The model was complemented with scaling analysis to determine the governing scales of the problem and the dielectrophoretic Rayleigh number was deduced from the study.

Acknowledgements

First and foremost, I would like to express my sincere gratitude to my supervisor Dr.Cotton for his continuous support, motivation and guidance throughout the past seven years. It has been an invaluable experience because of your mentoring, openness to new ideas and caring on the personal level.

I would like also to extend my appreciation to my supervisory committee Dr. Ching and Dr, Lightstone, your guidance and comments were extremely important in realizing this work.

I would also like to thank the mechanical engineering technicians; Ron, Joe, Mark, Jim, Michael and Dan for their help throughout this project.

I would like to thank all the happy members of the TMRL Lab, your friendship and the distraction you provided out of the research and your comments during our four hours meeting every week were exquisite.

I would like to thank my Parents and brothers, whom they sacrificed a lot during this past years for me to fulfil my dreams. I will always be in debt for your unconditional love and the support that you provided with all your heart during my hardships.

Last but not least, I deeply thank my wife who has happily endured with me the last years and for always showing her appreciation and never complaining. Without you, these years would have never passed this easily. Finally, to our little bundle of joy “Nathaniel”, you have made me truly realize what Dostoevsky once said that “The soul is healed by

being with children". Since, your birth and you have brightened our world with joy and happiness, but most of the time with loads of diapers.

Nomenclature

A	*Area* $[m^2]$
B	*Magnetic flux [T]*
c	*Heat Capacitance [J/kg.K]*
d	*Diameter [m]*
$\bar{E}$	*Electric Field Strength [V/m]*
$\bar{f}$	*Body Force* $[N/m^3]$
g	*Gravitational acceleration* $[m/s^2]$
h	*Heat transfer coefficient* $[W/m^2K]$
H	*Height [m]*
I	*Electric current [A]*
$\bar{J}$	*Current density* $[A/m^2]$
k	*Thermal conductivity [W/mK]*
K	*Ion mobility* $[m^2/Vs]$
L	*Length [m]*
m	*Mass [kg]*
n	*Refractive index*
s	*Melt thickness [m]*
t	*Time [s]*
T	*Temperature [K]*

Subscripts

b	*Body*
c	*Cold*
e	*Electric/ Electrodes*
f	*Fluid/Final*
h	*hot*
i	*Initial*
L	*Liquid*
q	*Charge*
r	*Relative/ Reference*
S	*solid*
Sc	*Screen*
v	*Vertical*

Greek Symbols

α	*Thermal diffusivity* $[m^2/s]$
β	*Volumetric expansion coefficient [1/K]*
δ	*Thermal boundary layer thickness [m]*
μ	*Dynamic viscosity [Pa.s]*
ν	*Kinematic viscosity* $[m^2/s]$

u	*Velocity [m/s]*	$\boldsymbol{\sigma}$	*Electrical conductivity [S]*
Q	*Thermal Power [W]*	$\boldsymbol{\tau}$	*Timescale [s]*
$\boldsymbol{Ste}$	*Stefan number*	$\boldsymbol{\lambda}$	*Wavelength [m]*
Fo	*Fourier number*	$\boldsymbol{\rho}$	*Density [kg/m^3]*
$\Delta \boldsymbol{H_f}$	*Latent Heat of Fusion [J/kg]*		
Nu	*Nusselt number*		
VF	*Volume fraction*		

Table of Contents

List of Figures

Chapter 1 Introduction

1.1 Background

The primary energy consumption in the residential sector in Canada is attributed to meeting thermal demands. According to Natural Resources of Canada (NRCan) in 2015, space and water heating demands contributed to 67.8 % and 19.7 % respectively of the total energy consumption with the remaining towards electrical and cooling loads. This is also the case for the commercial sector where the combined space and water heating loads presented 55 % of the total energy consumption.

Upon examining the size of the energy storage project installation for the last three decades in the United States and Canada, one can perceive the increased global awareness towards the installation of thermal energy storage systems compared to the other types of storage [Figure 1.1]. The Department of Energy (DOE) database demonstrates that since 2004, the size of the thermal energy storage projects increased almost exponentially up to the recent years. The other two types of storage shown in the figure are electro-chemical (electrical batteries: Lead/acid or Lithium ion batteries) and electro-mechanical (compressed air or flywheels). The electro-chemical storage type is also experiencing an

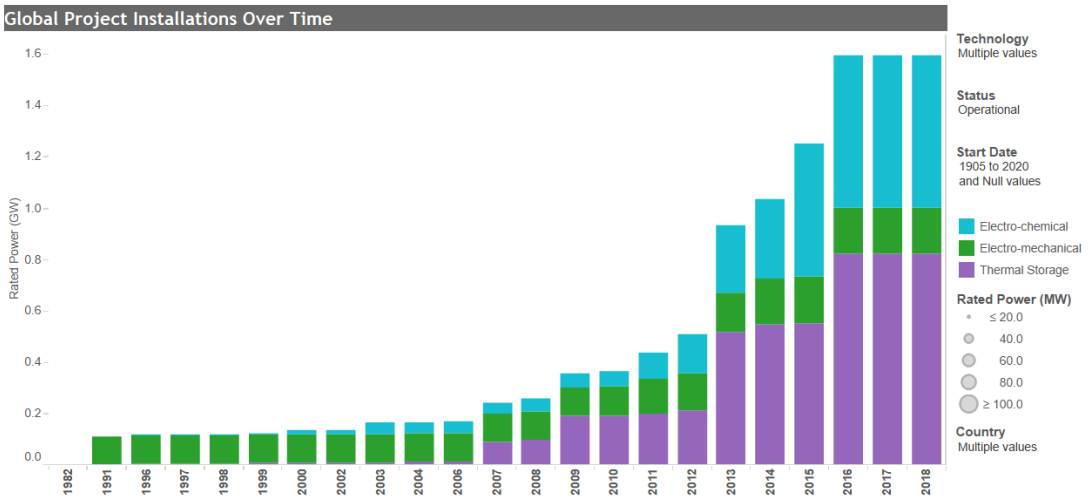

Figure 1.1 Energy storage project installations over time for Canada and United States. [Source: DOE Global energy storage database DOE website]

exponential increase in capital projects due to the advancements in PV solar panels and the fast pacing reorientation towards electric vehicles.

Overall, the use of an energy storage system is becoming an attractive solution towards more sustainable, energy efficient communities and a promising solution for reducing the Greenhouse Gas (GHG) emissions. In a study by Arce et al. (2011)[1], they estimated a 6% annual potential reduction of CO_2 emissions in the European Union (EU-27) from implementing thermal energy storage systems (TES) in buildings and industrial sectors. The use of a TES system becomes viable in many different scenarios, the most common of which are: serving as a buffer zone to meet the mismatch between the supply and the consumer demand, peak shifting and peak shaving.

The work of this dissertation is focused on thermal storage systems. These kinds of storages are often integrated thermal systems subjected to prolonged times of mismatch

between the thermal supply and the consumer thermal demand. These mismatched conditions are, for example, highly pronounced in solar thermal systems, combined heat and power plants (CHP) and waste heat recovery systems. In such applications, thermal storage acts as a buffer and provides an efficient solution for the energy mismatch problem.

1.2 Thermal Energy Storage (TES)

In TES there are three main methods that are used to store the thermal energy. These methods can be classified to:

a) Sensible heat thermal storage (SHTS)

b) Latent heat thermal storage (LHTS)

c) Thermo-Chemical storage

These three systems are inherently different in their mechanism of storage, thermal storage density, range of temperature application and their performance when integrated with a thermal system.

A. <u>Sensible heat thermal storage (SHTS)</u>

In SHTS the heat is stored in the form of sensible energy where the temperature of the storage medium increases while capturing the heat and decreased during the energy discharge process. The amount of the heat energy stored can be calculated as

$$Q_{sensible} = m \int_{T_i}^{T_f} c \, dT \qquad (1.1)$$

The amount of heat stored is proportional to the mass of the storing media, specific heat capacity (c) and the temperature increase of the medium $(T_f - T_i)$.

The most common materials used as the storage media in SHTS are rock beds and water. In residential applications, water is a favorable option to using rocks for domestic heating. Water sensible storage systems offer several advantages, of them are the logistic advantage of being used as the storage medium and serve as the working fluid in the thermal system. Water is readily available, cheap and abundant and they are chemically stable and the system does not face any degradation issues. Further, water systems do not face significant volumetric variations during operation as long as the working temperatures are below that of the boiling. However, the main disadvantage of the sensible systems in general is that the thermal storage density for these systems are lower than that of the other two systems (LHTS and electro-chemical storage). This disadvantage is more pronounced if the system is working under small temperature variations.

B. Latent heat thermal storage (LHTS)

The second type of thermal storage systems is the latent heat type. In this storage system, the thermal energy is stored in the form of latent heat of fusion in a Phase Change Material (PCM). During the phase transformation process either melting or solidification during energy storage and recovery respectively, the amount of energy stored could be highly significant while the temperature change of the system is small.

The amount of the energy stored during melting of the PCM can be calculated as

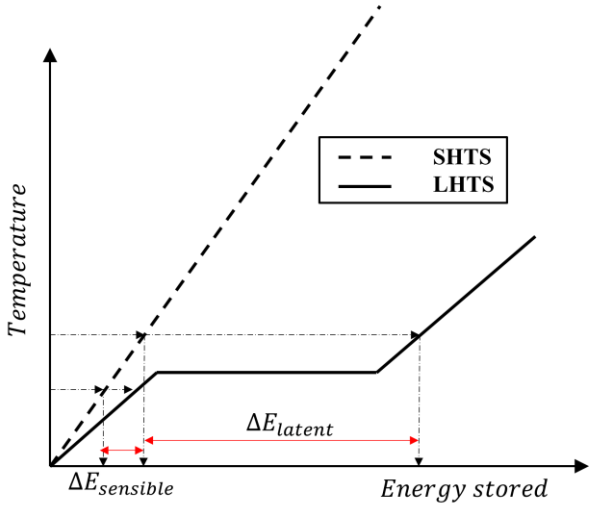

Figure 1.2 Sensible vs Latent heat thermal storage capacity vs temperature

$$Q_{latent} = m\left(\int_{T_i}^{T_m} c_S \, dT + \Delta H_f + \int_{T_m}^{T_f} c_L \, dT\right) \tag{1.2}$$

Where c_S and c_L are the specific heat capacities of the solid and the liquid PCM respectively and T_m is the melting temperature of the PCM and ΔH_f is its latent heat of fusion. Figure 1.2 shows the energy storage capacity for a LHTS vs SHTS, the figure highlights the significant advantage of using a PCM compared to sensible system when operating under small temperature variations. Table 1.1 highlights the typical thermal storage densities for the different types of storage. For example, the difference between the storage density between water and a typical paraffin PCM both undergoing a temperature difference of 20°C, the LHTS offers almost 2.5 times the capability of thermal storage of that for water. Another advantage for the PCMs is their feasibility for being integrated passively in the building structure, they can be placed inside gypsum plasterboards,

incorporated under the floor or above the ceiling to limit the temperature fluctuations in the building and therefore reducing the energy required for heating or cooling [2], [3].

Although LHTS seems to be an outperformer for SHTS, they have several drawbacks that needs to be addressed and limit their feasibility of integration into thermal systems. These main drawbacks are:

a) Most PCMs that can be integrated for space and heating applications ($T_m < 90℃$) are characterized by a very low thermal conductivity ($k \approx 0.1 \rightarrow 0.6\ W/m.K$) [4]–[6]which slows the heat transfer process during charging and discharging.
b) Some PCMs are expensive, others are chemically unstable and degrades over time. [The different types of PCMs and their limitations will be discussed later in detail in section 2.1].
c) PCM's specific heat capacities are relatively lower (approximately 2 times lower) than that of water which limits their benefit on working above or lower their melting point.

C. <u>Thermo-Chemical storage</u>

The last type of thermal storages is the thermo-chemical heat storage type. In these systems the storage medium is typically a chemical solution that undergoes an exothermic/endothermic chemical reaction.

$$A \underset{Exothermic}{\overset{Endothermic}{\rightleftharpoons}} C + D \qquad (1.3)$$

Table 1.1Typical thermal storage densities for the different types of storages[5], [8]

Type of Storage system	Storage density (kJ/kg)	Temperature
Sensible storage		
Granite	17	ΔT=20 °C
Water	84	ΔT=20 °C
Latent heat storage		
Water	330	Melting temperature 0 °C
Water	2450	Boiling temperature 100 °C
Paraffins	200	Melting temperatures 5-130 °C
Thermochemical heat storage		
$NH_3+\Delta H \rightleftarrows 1/2N_2+3/2H_2$	3940	Ammonia/Reaction temperature 400→ 500 ℃
$Mg+H_2 \rightleftarrows MgH_2$	2808	Temperature range 350-450 °C
$2Mg+fe+3H_2 \rightleftarrows Mg_2FeH_6$	1980	Temperature range 450-550 °C

Typically, the thermal storage density for these types of storages exceed both the sensible and the latent heat storage systems [Table 1.1]. However, they are best suited for high temperature applications as in concentrated solar power plants and some of these reaction need to be stored under pressurized systems [7].

1.3 Motivation

The focus of this dissertation is on LHTS and specifically systems that use Organic PCMs. Organic PCMs are typically characterized by being cheap, non-corrosive,

chemically stable and therefore is always considered an attractive candidate in these systems. However, as mentioned before their major drawback is the very low thermal conductivity ($0.1 \rightarrow 0.6\ W/mK$), thus in turn limits the heat transfer rates and restricts the system storage capacity for a given charging period.

In order to overcome this problem several heat transfer enhancement techniques have been investigated to decrease the overall thermal resistance of the PCM in the thermal storage system. These heat transfer enhancement techniques are mainly passive techniques and can be generally summarized as follows: using extended surfaces, thermal conductivity enhancements by using high thermally conductive materials in the PCM, and microencapsulating the PCM [These enhancement techniques will be discussed later in detail in the second chapter of the dissertation]. The outcome of using these techniques can result in a significant augmentation in the heat transfer rates, however it takes away from the thermal storage density because of the volume of the foreign material introduced. It was found that in spite of increasing the volume of the foreign material in the PCM matrix, which increases the overall heat transfer in melting and solidification, that these techniques also impact damping of natural convection currents that are favorable in the melting stage. This has an overall influence of equalizing the melting and the solidification time as the volume of the added material increases due to the transformation of the melting process from convection to conduction dominated as that of the solidification [9] which may pose engineering design constraints.

Another heat transfer enhancement technique that can be used along with gravitational forces to enhance the heat transfer process is Electrohydrodynamics (EHD). EHD is an

active heat transfer enhancement technique that is characterized by small power consumption, low volume occupation and the absence of any moving parts. The EHD method of enhancement works by imposing an additional body forces in the dielectric fluid thus enhancing mixing, acting on the thermal boundary layer and sometimes acts on the interface of multiphase systems [EHD will be addressed in more detail in Chapter 3]. This enhancement method can take relatively less space compared to the other passive techniques which rely on adding foreign material in the PCM, while on the same time imposing forces that could intensify gravitational forces or analogously create pseudo-gravity like effects in micro-gravity environments[10], [11].

The current research is motivated by our recent findings [Nakhla et al. (2015) [12]], that using high electric fields during melting of paraffin wax can enhance the heat transfer rates and shorten the melting time. The PCM (paraffin wax) was enclosed in a rectangular enclosure made from acrylic to allow for optical visualization inside the cell and the melting of the PCM was carried by an electric heater connected to a DC power supply to provide a constant heat flux boundary condition. The electric heater in this configuration was mounted on a copper sheet on the top of the enclosure to establish a conduction dominated melting scenario and naturally promote a thermally stratified PCM, thus intentionally suppressing any natural convection cells [Figure 1.3]. The high voltage was applied through a series of cylindrical electrodes embedded into the PCM and placed in a staggered arrangement.

The experiments were conducted for three different magnitudes of heat flux and the heater's surface temperature and PCM's melt thickness were measured for EHD and non-

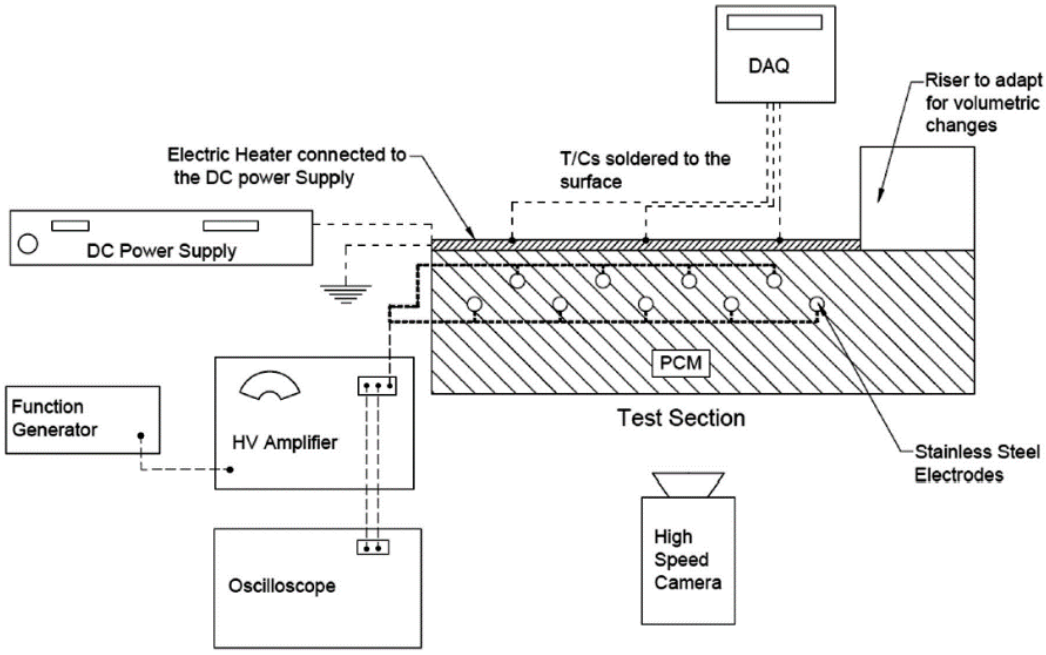

Figure 1.3 Schematic for the previous experimental facility. [Source: Nakhla et al. (2015)[12]*]*

EHD assisted melting cases and the results were compared against each other. It was found that the heater's surface temperature for the EHD assisted melting cases was always lower than that for the non EHD cases indicating an augmentation in the heat transfer rates to the solid/liquid interface because of the induced EHD body forces in the PCM.

It was shown that by applying a negative 8 kV DC voltage through the electrodes, that melting times can be reduced by up to 40 % when compared to a 0-kV case (non-EHD) [Figure 1.4]. The instantaneous EHD heat enhancement factor was also evaluated and was defined as the ratio between the melt front velocities for an EHD-assisted melting to a non-EHD assisted melting case. Although the overall melting time was reduced by 40 %, it was found that the EHD enhancement factor was not constant along the whole melting process

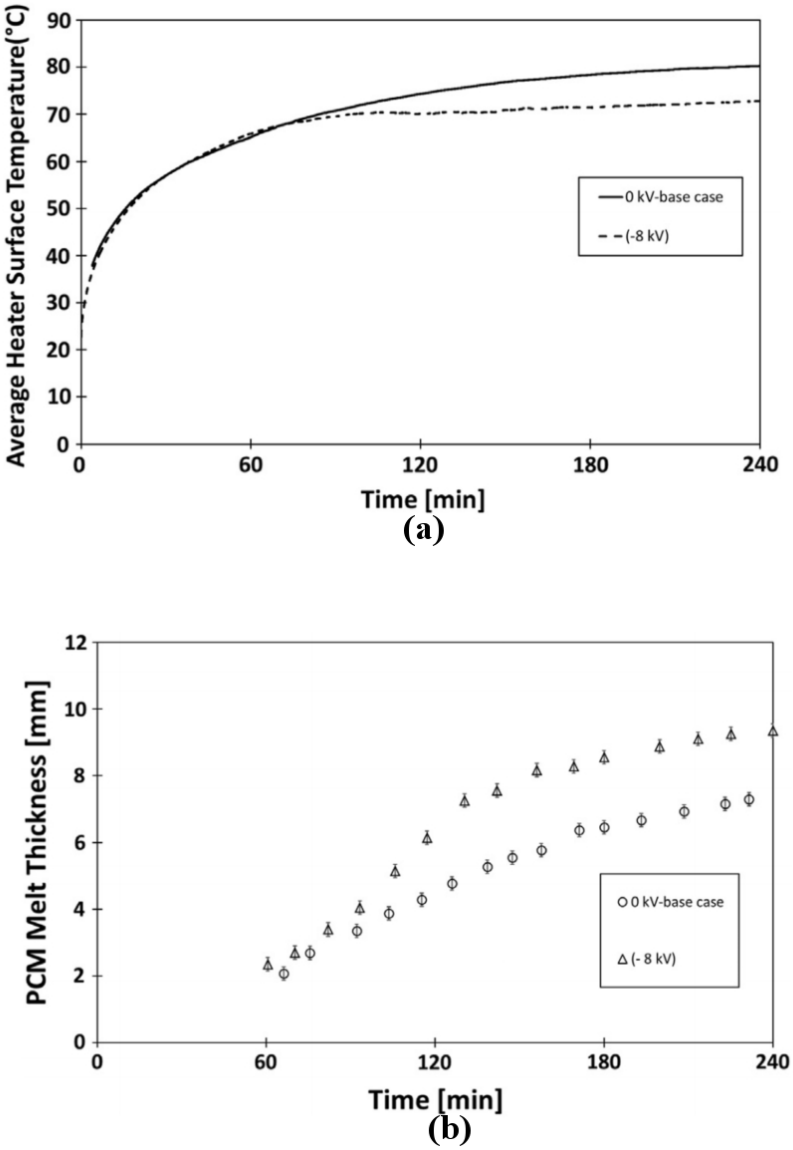

Figure 1.4 (a) Heater's surface temperature temporal profile, (b) Melt thickness temporal profile [Source: Nakhla et al. [12], [13]*]*

but at certain instants, it can reach high values up to 6 folds [13]. The reason for the varying EHD enhancement factor along the melting process was attributed to the non-uniformity of the electric field distribution used in the experiments.

The study showed that EHD forces acted on both the bulk of the molten wax and on the solid/liquid interface. The EHD forces induced electro-convective cells inside the liquid wax and acted on the solid/liquid interface pulling the solid dendrites from the solid/liquid interface. The study identified the phenomenon as “Solid Extraction” and found it similar to the well-known EHD “Liquid Extraction” phenomena in liquid/vapor multi-phase systems. A high speed imaging visualization was used in the study and discovered that the solid dendrites within the mushy zone were extracted from the mushy zone towards the liquid bulk by EHD. This phenomenon was believed to contribute to the overall EHD heat transfer enhancement mechanisms in the latent heat thermal storage system tested.

This study was the first in the field and served as a proof of concept on the applicability of using EHD as an enhancement technique in melting of PCMs. The study did not examine the role of the different EHD body forces towards the overall heat transfer enhancement and were mainly conducted on conduction dominated melting experiments only.

1.4 Research Objectives

The scope of this research will address the following points:

1) Investigate the melting performance of Octadecane under gravitational and Electrical body forces in an initially conduction dominated melting under different voltages, wave forms and temperature boundary conditions.
2) Design, build, instrument and verify an experimental facility capable of accurately quantifying the average EHD heat transfer augmentation factor.

3) Examine the coupling between the gravitational and EHD body forces during melting of Octadecane in an initially convection dominated regime under different Rayleigh numbers, voltages, waveforms and temperature boundary conditions.
4) Develop and utilize a non-intrusive heat and flow visualization technique to envisage the interaction between EHD and gravitational forces.
5) Evaluate the contributive role of the different EHD body forces towards the overall heat transfer augmentation.
6) Express the experimental results in non-dimensional terms upon understanding the dominant enhancement mechanism.
7) Develop numerical models to quantify and understand the contribution of the EHD body forces.
8) Introduce a novel EHD electrical arrangement that can be used in moving boundary problems.

1.5 Dissertation layout

The work of this research is organized in the dissertation in eight chapters. These chapters are:

Chapter One: Provides a background and an introduction to thermal storage systems in general and the latent type in specific. The chapter also presents the motivation of the current research and state the research objectives.

Chapter Two: Serves as a literature review for the different types of PCMs found in literature. The chapter covers and explains the fundamentals of the melting process of PCMs in conduction and convection dominated heat transfer processes and highlights the difference between a melting and a solidification problem. The chapter then exposes the reader to various heat transfer enhancement techniques that has been studied extensively in literature for melting and solidification of PCMs.

Chapter Three: Presents the basic equations and the fundamentals of Electrohydrodynamics. The chapter then highlights the applicability of using EHD as a heat transfer enhancement technique for both single and multi-phase systems.

Chapter Four: Describes the two experimental facilities used in this work: the conduction dominated melting experimental facility and the convection dominated one. The chapter details the complementary optical setup used for shadowgraph imaging system developed. The chapter also explains the data reduction procedures used for the two experimental facilities.

Chapter Five: Presents the experimental results of melting under EHD and gravitational forces for an initially conduction dominated melting regime. A verification for the experimental methodology is also discussed.

Chapter Six: Discusses the experimental results of melting under EHD and gravitational forces for an initially convection dominated melting regime. The chapter discusses the results for non-EHD assisted melting to set the base cases for comparison and then discuss the results conducted with EHD. The findings were explained in non-

dimensional parameters at the end of the chapter and the transformation criterion from gravitational to mixed electrical and gravitational regime is highlighted.

Chapter Seven: Presents the numerical model developed for the dielectrophoretic forces and the verification of the model. The numerical results highlighted the difference between an electrically and gravitationally dominated regime. The results were complemented with a scaling analysis for verification. The numerical results along with the scaling analysis supported the experimental observations and conclusions drawn in chapter six.

Chapter Eight: Presents the summary and the conclusions for the current project and provides recommendations for future work.

Chapter 2 Literature Review: Latent Heat Thermal Storage Systems

This chapter outlines the state of the art in studies related to the field of thermal storage systems and specifically for latent heat systems and enhancement. The chapter first identifies the most common PCM types used in residential heating applications with the focus on the pros and cons for each. The physics of the heat transfer problem for moving boundaries and the difference between the melting and solidification is discussed. Finally, the chapter outlines the main enhancement techniques that are used in conjunction with the PCMs and their mechanism of enhancement and the accompanying advantages and disadvantages for each of these mechanisms.

2.1 Phase change materials

In solid-liquid latent heat storage systems, the PCMs can be usually classified to two main types [6]:

a) Organic PCMs

b) Inorganic PCMs

For each of these two types, they can be further classified into compounds or eutectic mixtures. The eutectic mixture PCMs are characterized by possessing a defined sharp melting point and the most common ones studied in literature are binary mixtures of fatty

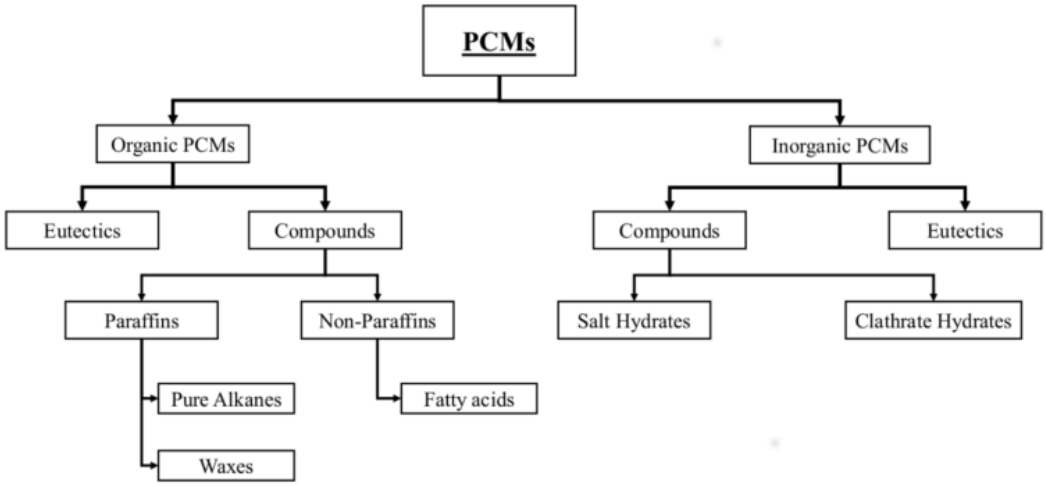

Figure 2.1 Classification of PCMs types

acids [capric, lauric, palmitic and stearic acids] [14]. The use of binary mixtures to produce eutectic PCMs is a desirable and attractive candidate for commercial PCMs because it mainly uses mixture of fatty acids-which are readily available- and tailor it to produce a PCM with a defined melting point. This is attractive as it allows for a wider range of PCM selections that can cover wider temperature ranges and applications.

However, the use of binary mixtures to produce a thermally reliable and stable eutectic PCMs has not been investigated or tested compared to the other type of PCM compounds until recently and more studies are needed in this topic [8]. Further attention will not be given to eutectic mixtures in this work, however the applicability of using them as a candidate PCM for the current research is valid as they are treated as mixture of Organics.

2.1.1 Organic PCMs

Figure 2.1 shows the most common classification for the PCM types according to Abhat [6]. Organic PCMs are the most common and commercial PCMs available and studied. They are mainly divided into two main categories: Paraffins and non-Paraffins.

Paraffins are further subdivided into:

a) Pure Paraffins: These are mainly alkanes (C_nH_{2n+2}). Octadecane ($C_{18}H_{38}$). which is the PCM used in this work is considered one of them. Even chained paraffins are called (n-paraffins) and the odd chained ones are called iso-paraffins. The melting point of the pure paraffin PCM increases as the length of the carbon chain increases. Since they are pure materials, they possess a well-defined melting point.

b) Paraffin waxes: The paraffin waxes are the commercial type of paraffins and are usually called wax. They are cheaper than pure paraffins as they are considered as technical grade. Paraffin waxes are composed of mixture of pure paraffins with a weight percentage between 75-100 % [6]. Since they are mixture of different carbon chains, the PCM often possess a wider melting temperature range compared to pure paraffins.

Paraffin organic PCMs are the most common type to be used in thermal storage systems as they offer many advantages compared to other types. These advantages can be summarized in the following points:

a) They are commercially and readily available with a variety of paraffins that cover wide temperature range.
b) They are cheaper than the other types of PCMs.
c) They are dielectric materials-as all organic PCMs-, which make them a good candidate for using EHD as an enhancement technique which is the core of this research work.
d) Solidification occurs without supercooling.
e) They are compatible with most of the enclosure materials.

Paraffin type Organics, however have several serious disadvantages that had prevented wide spread adoption. These disadvantages are mainly:

a) For any given paraffin PCM, the melting temperature is rather defined as a melting range and not a sharp defined melting point.
b) The volumetric expansion and contraction associated with the phase change process for liquid to solid and vice versa is higher than the other types of PCMs which impose design limitations on the enclosure.
c) They tend to have a lower thermal conductivity compared to inorganic PCMs $[k = 0.1 \rightarrow 0.6\ W/mK]$.
d) The latent heat of fusion for Organic PCMs is relatively lower compared to the inorganics.

The other type for the Organic PCMs is the non-paraffin type which is usually referred to as fatty acids. The chemical composition for the fatty acids held the general form of $[CH_3(CH_2)_{2n}COOH]$. Fatty acids constitute the main advantages as that for the paraffins

with better thermal cycling without degradation, however they are almost two times more expensive compared to the technical grade paraffin waxes.

2.1.2 Inorganic PCMs

The second main type of PCMs is the inorganic materials and they are mainly classified to salt hydrates and clathrate hydrates. From these two types the salt hydrates are the more common ones for being used in hot thermal storage systems, the later is often used for cold storages- air conditioning applications- and or focus here will be drawn on the salt hydrates only.

The main advantages for the salt hydrates are:

a) They offer higher latent heat of fusion compared to the Organic PCMs, therefore a thermal storage system with inorganic PCM will be smaller in size than the one running with organic PCMs
b) Their thermal conductivity is higher than that of Organic ones, hence the need of enhancement technique is not as essential as it is the case for Organics
c) The melting temperature range window is narrower for a given salt hydrate compared to commercial grade paraffin waxes

However, the main disadvantage for the salt hydrates are:

a) They are highly corrosive materials if being used around any metallic enclosures
b) Phase segregation is one of their biggest problems. The Phase segregation problem occurs at the melting process in which the salt hydrate decomposes into salt or lower hydrate and water. The salt or the lower hydrate usually settles at

the bottom of the container due to the higher density and therefore inhibiting further homogenous solidification [4].

c) They may experience excessive supercooling due to their inherently poor nucleating property; hence a nucleating reagent is usually needed[15].

2.1.3 Summary

The summary of the advantages and the disadvantages for the different types of PCMs given in the previous two sections, shows that the selection process for a PCM in a thermal storage system is not trivial. Each PCM type is unique and serve better functionality than others in only certain points and the engineer should evaluate and weight the different design factors before a selection is made.

An extensive review with a list of the different PCMs and their thermo-physical properties can be found in review papers like (Zalba et al., 2003) [5] and (Sharma et al., 2009)[16].

As mentioned earlier, the focus of this work is Organic PCMs from which Octadecane was selected as the working PCM for this dissertation. Octadecane was selected as the PCM is this study because of its well known properties in the literature of phase change materials. It also has a relatively low melting point (28 ºC) which is favorable for minimizing heat losses to the surroundings. Octadecane is also an organic dielectric material, with properties similar to those of paraffins which are widely used as common PCMs for low temperature range applications. The main drawback is the lower thermal conductivity ranger of these materials- since they are good dielectric materials, they are good thermal insulator as well-

the need for a heat transfer enhancement technique is essential and this will be covered in the third section of this chapter.

2.2 Moving boundary problem

This section will explain the governing physics and the heat transfer mechanisms in melting and solidification [moving boundary problem]. The section will explain the basics and the difference between a conduction dominated melting and convection dominated melting. The difference between the melting and the solidification problem will be highlighted and dominating thermal resistances are identified.

2.2.1 Conduction dominated melting

In conduction dominated melting, the heat transfer from the heat source to the solid/liquid interface occurs through conduction only. The problem is usually classified into two main types:

1) One region problem: the one region problem means that the initial solid is at the melting temperature exactly during the melting process or the liquid phase is at the melting temperature during the start of the solidification process
2) Two regions problem: for this case the solid or the liquid phases are at an initial temperature lower or higher than the melting point for the melting and the solidification processes respectively.

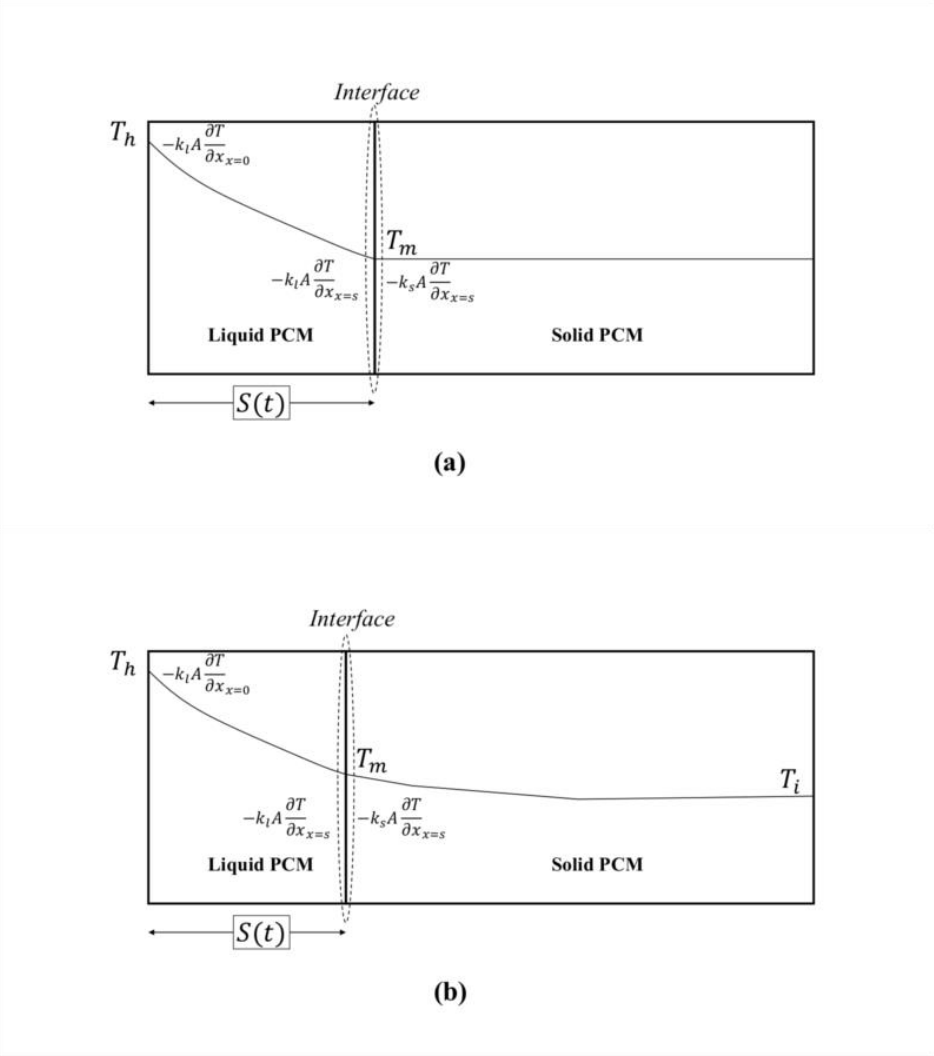

Figure 2.2 Schematic for Stefan and Neumann moving boundary problem

For these two problems, exact solutions can be found under certain assumptions. The solution for the one region problem is referred to by the Stefan solution [17] and the solution for the two-region problem is usually called Neumann solution.

Figure 2.2 is a schematic description for the one and the two-region problem with the temperature boundary conditions labelled for a melting case. The exact solution for these two problems is used to determine the location of the interface as a function of time $S(t)$

and thus the amount of melt fraction for a conduction dominated melting. The general assumptions used in both the Stefan and Neumann exact solutions are:

1) The heat transfer problem is 1D problem.
2) The heat source wall temperature (T_h) is constant and is not affected by the amount of heat transfer.
3) The melting temperature of the PCM is sharp and defined as (T_m) and no mushy zone could exist.
4) There is no volume change accompanying the phase transformation process.
5) The solid phase is at an initial temperature equal to the melting point in case of Stefan problem and at an initial temperature T_i which is lower than the melting point for Neumann solution.
6) The solution is derived for an infinite slab.

Since the governing heat transfer mechanism in this case is conduction only, the energy balance on the solid/liquid interface yields

$$-k_l A \frac{\partial T}{\partial x}_{x=s} + k_s A \frac{\partial T}{\partial x}_{x=s} = \rho A \Delta H_f \frac{ds}{dt} \tag{2.1}$$

Equation (2.1) shows that the rate of melting is governed by the difference between the liquid heat flux and the solid heat flux. At early stages of melting, the conductance thermal resistance in the liquid PCM is small and therefore higher heat flux in the liquid side is achieved and the melting rate is relatively high. As melting progresses and the solid/liquid interface moves away from the heat source, the conductance thermal resistance in the liquid

PCM increases and accordingly the melting rate decreases. The solid heat flux is dependent on the initial temperature of the solid phase, the lower the initial solid temperature means higher degree of subcooling and subsequently higher solid heat flux is needed to first heat up the solid phase to reach the melting temperature before melting starts. This fact implies that the melting rate for a Stefan problem (no subcooling) is always higher than that of Neumann problem (subcooled solid) with the same temperature boundary conditions.

The exact solution for the Stefan problem is

$$S = 2\lambda\sqrt{\alpha t} \tag{2.2}$$

Where (λ) is a constant for the problem that depends on Stefan number(Ste). The Stefan number is a dimensionless number defined as the ratio between the sensible heat to the latent heat of the PCM.

$$Ste = \frac{C_p(T_h - T_m)}{\Delta H_f} \tag{2.3}$$

The constant (λ) is calculated from the transcendental equation as

$$\lambda e^{\lambda^2} erf(\lambda) = \frac{Ste}{\sqrt{\pi}} \tag{2.4}$$

The general form for the Neumann solution takes the same form as that for Stefan as formulated in equation (2.2), while the transcendental equation for the constant λ is different and involves more factors than just the Stefan number. The degree of subcooling and the ration between the liquid and the solid thermal conductivity are all also rooted in

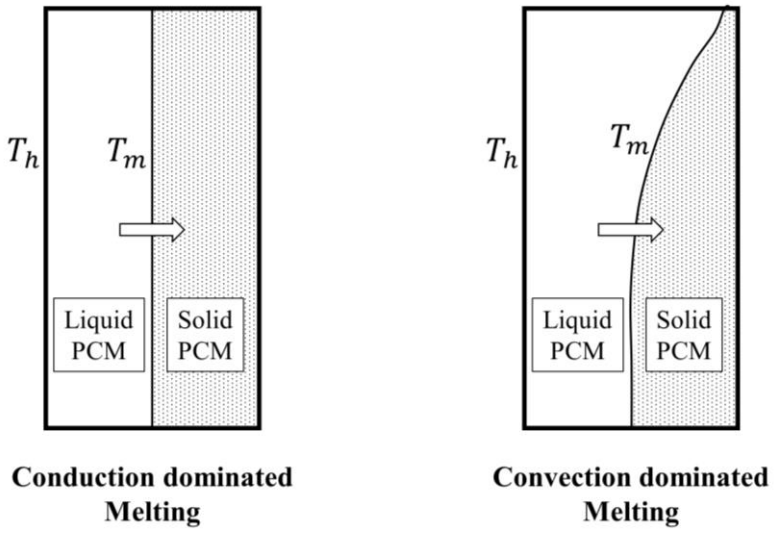

Figure 2.3 A schematic for conduction vs convection dominated melting

the Neumann's transcendental equation. A summary for the governing equations from solving the temperature distribution in the liquid and the solid phase and the melting rate for the Neumann's solution can be found in Faghri & Zhang [18].

2.2.2 Convection dominated melting

The second type of melting is in which the melting is mainly governed by convection heat transfer. In this case, the solid/liquid interface no longer travels parallel to the heat source wall but rather exhibits a curvature away from the heat source [Refer to Figure 2.3]. The convection dominated melting problem has been studied for the last three decades specially for Organic PCMs- high Prandtl number fluid- where convection heat transfer becomes of greater effectiveness than heat conduction

Among the early experimental work conducted on melting of Organic PCMs in rectangular enclosures was that of Ho and Viskanta [19][20]. Ho studied the melting of n-Octadecane in vertical enclosures for both rectangular and cylindrical geometries under constant temperature boundary condition. The experimental results emphasized the importance of natural convection in augmenting the heat transfer process during the melting process as the rate of melting is significantly greater when compared to conduction dominated process.

The melting experiments for rectangular enclosure were conducted under three different values of Stefan and Rayleigh numbers and with a fixed aspect ratio. The experimental facility used a shadowgraph heat transfer measurement technique to measure the wall heat transfer coefficients. The shadowgraph and the heat transfer coefficient measurement showed that the heat transfer was governed by conduction during the early stages of melting followed by a change to convection heat transfer that continued through the whole melting process. The results gave insight on the non- dimensional parameters that can be used to describe the melting with natural convection process and a correlation between the melt volume and the dimensionless parameter ($Ste.Fo.Ra^{0.25}$) was suggested. However, these experimental results were not tested against different aspect ratios and the melt fraction results were reported for the first hour of melting only, during which the melt interface in the upper region of the enclosure reached the adiabatic wall on the other side.

Other experimental studies can be found in literature that expanded the understanding of the convection melting problem, from these studies is the one of Bareiess and Beer [21][22]. Bariess and Beer studied the melting for different organic PCMs in vertical

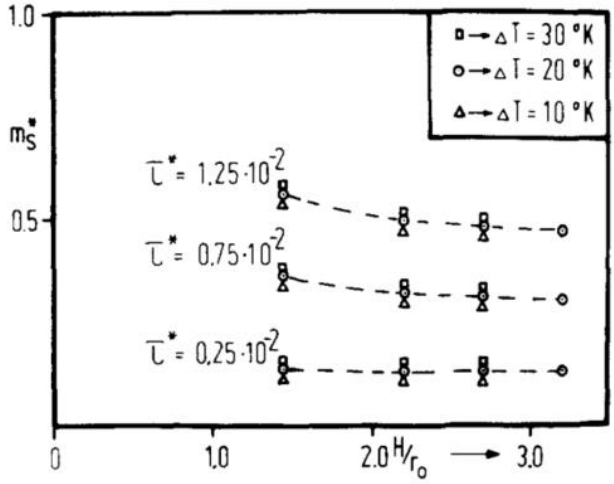

Figure 2.4 The corresponding melt fraction for different aspect ratios at different times [21]

cylindrical enclosures. The tested PCMs were: n-Octadecane, n-hexadecane, p-xylene and cyclohexane. Their studies were conducted for different values of Stefan and Rayleigh numbers under different aspect ratios for the enclosure (ratio between the height of the cylinder to the radius). The studies showed that the transition from conduction melting to convection melting is delayed by increasing the aspect ratio of the enclosure. Figure 2.4 shows the melt mass fraction for several vertical enclosures with different aspect ratios but the same Rayleigh number and at different dimensionless time. The study highlighted that enclosing the material in a few smaller cells is better than enclosing it in one big cell.

Benard et al. [23]studied the melting of n-Octadecane under higher Rayleigh number compared to the previous studies mentioned above. The tested Rayleigh number was in the range of ($Ra = 10^9$) which is an order of magnitude higher than the previous studies. Benard showed that the flow in the cavity was still laminar even under this high Rayleigh

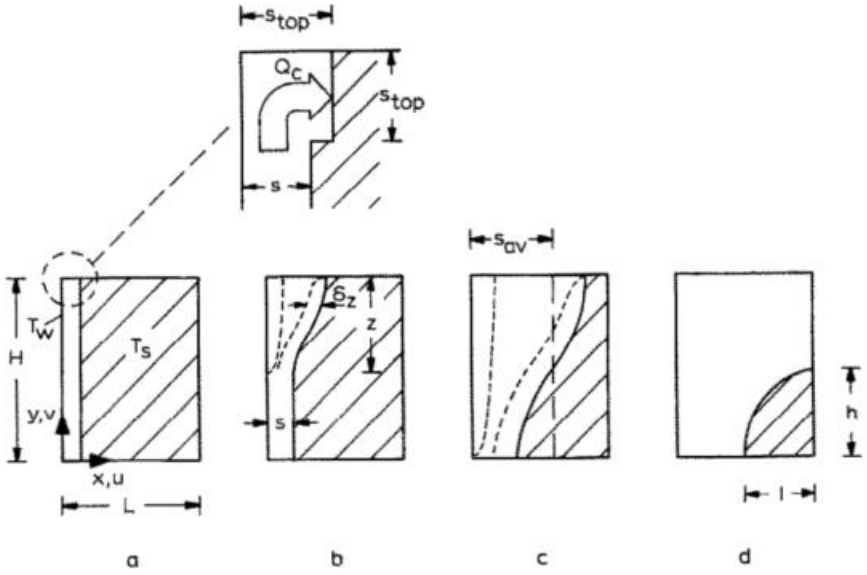

Figure 2.5 The four basic regimes during melting [24]

number. Benard showed also that the standard Nusselt number formulations for natural convection in rectangular still holds even with the irregular shape of the interface from the convection melting process. The study further showed that the local Nusselt number at a given height in the enclosure remains constant during the melting process once the initial conduction stage ends and the two thermal boundary layers- the hot at the heat source side and the cold at the solid liquid interface- fully develop along the span of the wall and the interface [Refer to Figure 2.5c].

The basic regimes of the melting process and the time scales involved in the process from changing between conduction to fully convection dominated melting are explained in great details in the work of Jany & Bejan [24]. Figure 2.5 shows the four basic regimes identified by the authors. These regimes are:

1) The fully conduction regime

2) Mixed conduction and convection regime. In this regime the cold boundary layer starts at the top of the melt interface and grows downwards until it hits the uprising hot boundary layer. Therefore, the upper region of the enclosure is governed by heat convection and the lower region is by conduction heat transfer
3) The fully convection regime. In this regime the two boundary layers separate and the heat transfer is totally governed by convection
4) The knee regime. This regime commences when the melt interface at the upper region touches the opposite adiabatic wall

The important time scales identified in the work of Jany and Bejan were: the start of the fully convection regime and that of the knee regime. The onset of the fully convection regime is determined by

$$\theta_{convection} \sim Ra^{-0.5} \tag{2.5}$$

Where (θ) is the dimensionless time, defined as

$$\theta = Fo.Ste = \frac{\alpha t}{H^2}.Ste \tag{2.6}$$

The onset of the knee regime occurs at

$$\theta_{knee} \sim \frac{L}{H} Ra^{-0.25} \tag{2.7}$$

Only when $(\theta_{knee} > \theta_{convection})$ does the full convection regime takes place, which implies that

$$Ra^{0.25} > \frac{H}{L} \tag{2.8}$$

2.2.3 Solidification problem

The solidification problem is fundamentally the same as that of the melting problem for pure conduction cases. The Stefan and the Neumann solutions work for both melting and solidification problems without any discrepancy. The main difference between the melting and the solidification problems are in the role of the convection heat transfer for both cases. As explained in the previous section, that convection enhance the melting rate and augment the heat transfer compared to a pure conduction case. In order to understand the effect of the convection heat transfer on the solidification, one can start by examining energy balance equation at the solid/liquid interface [equation 2.1] and modifying it to include the convection heat transfer

$$hA(T_L - T_m) - k_s A \frac{\partial T}{\partial x}_{x=s} = \rho A \Delta H_f \frac{ds}{dt} \tag{2.9}$$

Equation (2.9) shows that the convection heat transfer acts opposite to the conduction heat transfer through the solidified melt thickness and is dependent on the degree of superheating of the liquid phase. In a solidification case for an initially non-superheated liquid phase, the convection heat transfer does not exist and the solidification process is solely governed by heat conduction through the liquid phase.

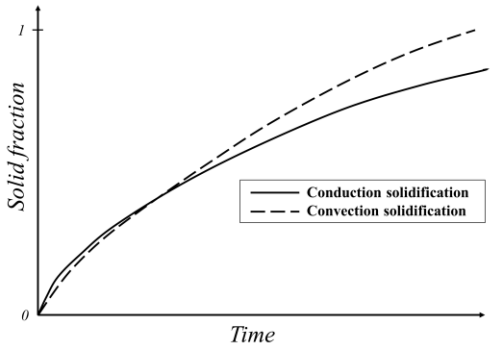

Figure 2.6 Typical solidification temporal progress for pure conduction case vs convection

The role of the convection in solidification becomes important only at high degrees of superheating. This is rare for a typical latent heat thermal storage system as operating over high temperature ranges limit the benefits of PCM storage due to the low specific heat of liquid PCMs [25], [26]. Figure 2.6 shows a typical graph representing the temporal solidification progress for a pure conduction solidification case vs one including the natural convection effects for a high degree of superheating. As shown in the figure, the convection case solidifies slower compared to the conduction case at the early stages of melting and then convection begins to solidify faster and shows a modest improvement on the overall solidification. During the early stages of solidification, the natural convection is dominant as the liquid phase is still superheated and this leads to slower solidification at the beginning, as sensible heat is extracted from the liquid phase. After this stage, the degree of superheating decrease quickly compared to a conduction case and the rate of solidification increases.

In conclusion, convection heat transfer during solidification allows for the extraction of the stored sensible heat in the liquid phase early during the first stages of solidification, while the conduction heat resistance of the solid is still relatively small. While for pure conduction phase, the sensible heat stored is extracted through the whole solidification process and that is the reason for the slower solidification rates at high degrees of superheating.

2.3 Heat transfer enhancement techniques

The use of an enhancement technique is a requirement when dealing with Organic PCMs due to their low thermal conductivity. The difference between these techniques vary in many aspects, among which is whither a passive or an active enhancement technique is used. An active heat transfer enhancement technique comprises an additional power requirement to the system, however it provides an opportunity to control the system operation. A passive enhancement does not involve any additional power requirement to the system, however it lacks the controllability of an active technique. The sizing criterion of the enhancement technique are often bounded with the maximum heat transfer rates that can be achieved with using the enhancement technique and the penalty of larger and heavier enclosures and subsequently sacrificing the thermal storage capacity as well as cost. This section will represent a literature survey on the passive and the active enhancement techniques that have been studied for heat transfer augmentation of melting and solidification of PCMs.

2.3.1 Passive enhancement techniques

The passive type of heat transfer enhancement techniques is the one that is most commonly used in conjunction with the LHTS. These techniques can be mainly divided into 5 main categories as reported by Kenisarin & Mahkamov [27], Jegadheeswaran et al. [28], Agyenim et al. [29] and Dhaidan and Khodadadi [30]:

i) Using extended surfaces
ii) Thermal conductivity enhancement
iii) Employing multiple PCMs method
iv) Micro-encapsulation of PCM
v) Using Nano particles

The difference between these techniques and their impact on enhancing the melting and solidification rates will be explained briefly in this section. The first, second and the fifth type of these techniques will be the only types explained here in this chapter as they are the closest in theory to the work of this dissertation while for the other techniques the reader can be referred to the review papers mentioned for extensive review. The first of these techniques is the usage of extended surfaces which are commonly referred by using highly thermal conductive fins attached to the heat source and embedded into the PCM structure and they are in fact the most common method used in literature.

2.3.1.1 Extended surfaces [fins]

The use of fins has been studied for different types of PCMs and under different configurations including heating from the top, bottom or from the side using different types enclosures and fin designs.

Fins are used to increase the heat transfer surface area and minimize the thermal conductance, therefore decreasing the thermal resistances in the system and potentially augmenting the heat transfer process. The effect of adding fins inside the PCM is basically enhancing the heat conduction process, therefore their advantage on decreasing the solidification time is always greater than reducing that of the melting time as the first is conduction governed process while the latter involves heat transfer by convection.

Lacroix and Benmmadda [31] studied numerically the melting of a PCM from a finned vertical wall. The study investigated the effect of the number of fins, their length and the degree of superheating and subsequently the Rayleigh number in a fixed height cavity. Figure 2.7 shows the schematic of the numerical domain used in the simulations with the geometric parameters on the left side. On the right side, the temporal melt fraction for the highest Rayleigh number simulated is shown for both short and long fin cases.

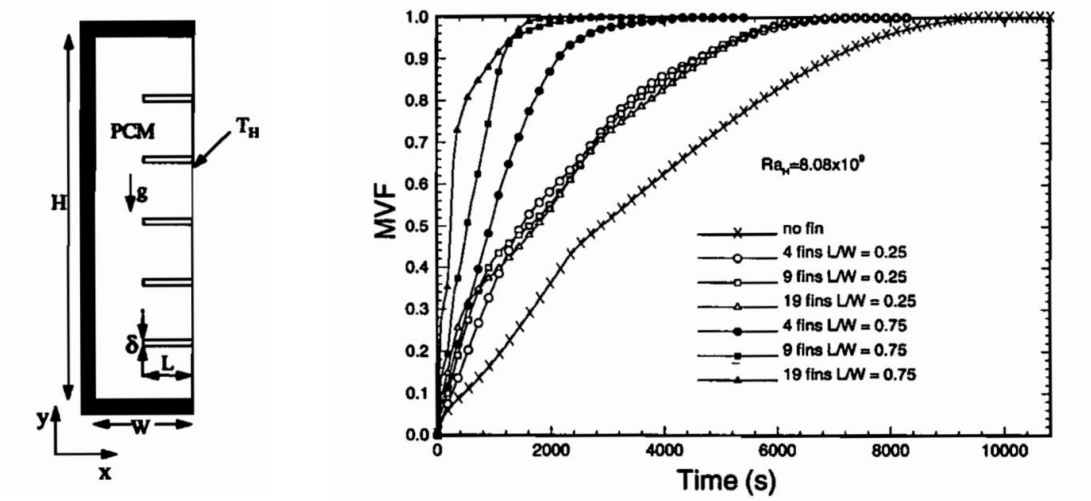

Figure 2.7 Fin configuration and the temporal volume fraction with and without fins[Source Lacroix and Benmmadda [31]*]*

A summary of the enhancement factor for all the cases simulated in their study is presented in Table 2.1. The study concluded that using fewer number of longer fins is better than using larger number of shorter fins in terms of enhancing the heat transfer rates during the melting process. The study also showed that the advantage of using fins decreases by increasing the degree of superheating and the reason for that was attributed to the hampering of natural convection currents caused by the presence of fins. The hampering effect was more pronounced in the shorter fins cases. This can be seen as a decline in the melting rates for the 19 fins case compared to the 9 fins after passing the 40 % melt fraction mark [Refer to Figure 2.7]. Increasing the number of fins gradually transforms the heat transfer mode to pure conduction and damps any convection currents. In solidification case, the study showed that increasing the number of fins significantly enhance the solidification rates as the heat transfer process is mainly governed by heat conduction.

Table 2.1 Reduction in melting time by using fins vs Rayleigh number [Lacroix and Benmmadda (1997)]

Ra	No fins	L=0.01 m			L=0.03m		
		4 fins	9 fins	19 fins	4 fins	9 fins	19 fins
1.6×10^9	1	1.63	1.75	2	2.28	3.33	5.42
4.85×10^9	1	1.19	1.24	1.3	1.83	2.81	3.46
8.08×10^9	1	1.32	1.33	1.37	2.13	3.37	3.76

Stritih [32] experimentally studied the melting and solidification of paraffins encapsulated in a vertically heated rectangular enclosure with vertical oriented fins. The orientation of the fins in this study does not interrupt the natural convection flow in the same manner as the one mentioned earlier in Lacroix and Benmmadda study. Figure 2.8 shows the fin configuration used in their work along with the fin effectiveness in both melting and solidification cases. The vertical fins proved to be more effective during the solidification compared to melting, because solidification process is purely conduction governed process. In fact, the fin effectiveness reported during the early stages of melting was shown to be less than 1 and this was attributed to the damping of the natural convection currents. In the solidification process, the fin effectiveness reached a maximum value of 3 and showed a 40% reduction in the solidification time compared to a non-finned geometry.

The difference in performance of the fins in between the melting and the solidification process was also pointed out in the work of Darzi et al. [33]. The numerical study was conducted for understanding the melting and solidification of n-Eicosane in a cylindrical annulus enhanced by the addition of nano-particles and the use of different number of fins.

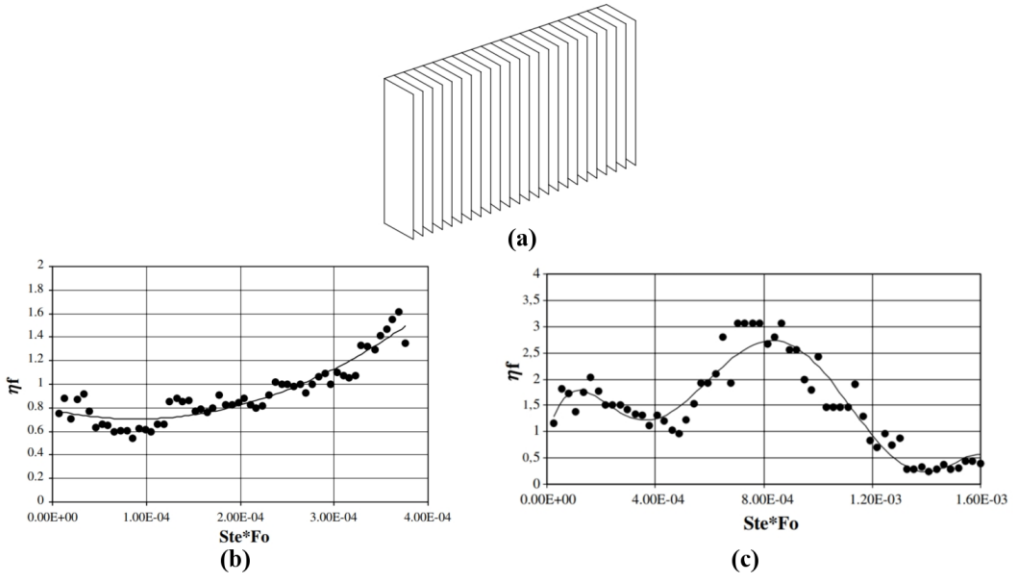

Figure 2.8 (a) Fin configuration, (b) Fin effectiveness during melting, (c) Fin effectiveness during solidification. [Source Stritih [32]*]*

The study showed that by increasing the number of fins above 10 did show minimal reduction in the melting, while for solidification case, the solidification time was proportionally reduced by increasing the number of fins.

Kamkari and Shokouhmand [34] experimentally studied the melting and solidification of Lauric acid in vertical rectangular enclosures with horizontal partial fins [a similar configuration to the one of Lacroix's numerical study]. The study compared the melting and solidification performance under three different degrees of superheating for 1 and 3 fins against a non-finned geometry. The study showed the significance of natural convection effect for the smaller number of fins and how does it affect the shape of the melt front. Figure 2.9 shows the typical shape of the melt front profiles and the transformation from convection to conduction dominated melting by increasing the number of fins. The

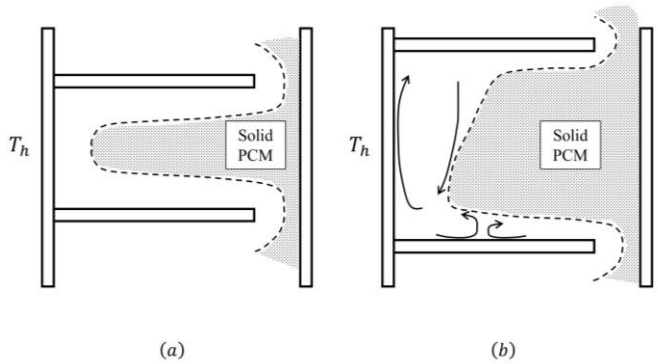

Figure 2.9 Effect of decreasing the fins spacing/increasing the number of fins on the heat transfer characteristic

study showed that the effectiveness of the fins and the reduction in the melting time was the highest at the lower degrees of superheating [wall temperature] [Refer to Figure 2.10]. These results are in line with the earlier findings of Lacroix et al. (1998), however neither of the two authors tried to rule out the effect of Rayleigh number from the degree of superheating.

Further experimental and numerical studies were conducted for the study of the performance of electronic cooling by using finned structures and PCMs. However, these studies were mainly focused on showing the impact of adding PCMs to the finned structures in limiting the temperature fluctuations on the electronic cooling side and not on the exact heat transfer governing parameters on the melting and solidification process. An example of these studies can be found in the work of Wang and Yang [35], Fan et al. [36] and Pakrouh et al. [37].

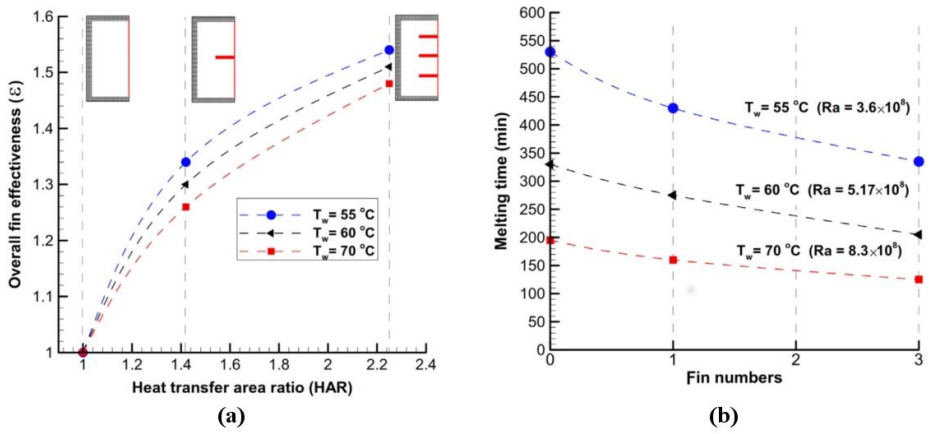

Figure 2.10(a)Fin effectiveness vs number of fins (b) Reduction in melting time vs number of fins at different degrees of superheat [Source: Kamkari et al. (2014)]

Several other works on the effect of using fins in different types of enclosures can be found in literature and summarized in detail in review papers mentioned earlier. In spite of the efforts conducted in studying the different fin parameters as: fin height, number of fins, length of fins, etc., there was not a systematic parametric study ever done to correlate the geometric parameters with the melting and solidification parameters. The closest is the work of Kamkari and Shoukouhmand [34] that included the representation of the results in terms of the dimensionless parameter $[Ste^{*2}Fo.Ra^{0.25}(1+N)^{0.5}]$, where N is the number of fins. Although the experimental results collapsed well against the dimensionless correlation, the experiments were conducted for 1 and 3 fins only which is insufficient to generalize the formulation and the rationale behind the new dimensionless parameter was not explained.

2.3.1.2 Thermal conductivity enhancements

The other type of passive enhancement techniques is adding high thermal conductive materials in the PCM. These thermal conductive materials can take the structure of metal foams additives, lesser rings, graphite flakes, aluminum or copper powders and many other different shapes. By introducing a higher thermal conductive material structure into the PCM it produces an effect of increasing the overall effective thermal conductivity of the system. Therefore, the higher the relative volume of the embedded structure to the PCM, the higher is the overall enhancement in shortening the melting and the solidification times.

Velraj et al. [38] studied the solidification of paraffin wax- Rubitherm 60 (RT 60)- in an annulus geometry for three different enhancement techniques. These techniques were using fins, adding hollow cylindrical steel structures called lesser rings and bubble agitation [Refer to Figure 2.11a]. Using the lesser rings, the solidification time was shortened significantly by 9 times compared to a case of pure paraffin only. However, this was achieved at 20 % volume fraction and the overall thermal storage density of the system was decreased compared to using 4 radial fins [Refer to Figure 2.11b]. The study also showed that using bubble agitation method is only beneficial in enhancing the heat transfer rates during the melting process and is not effective method for solidification.

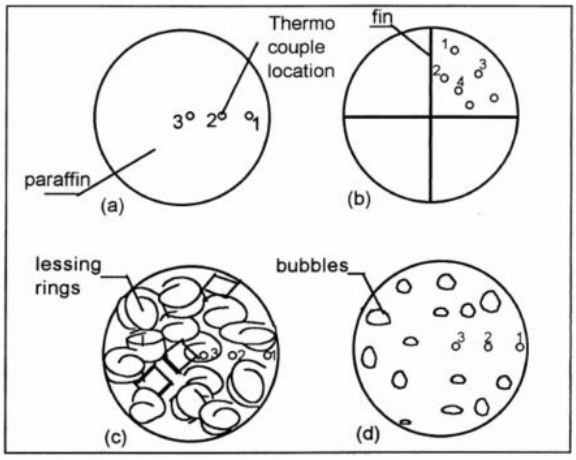

(a)

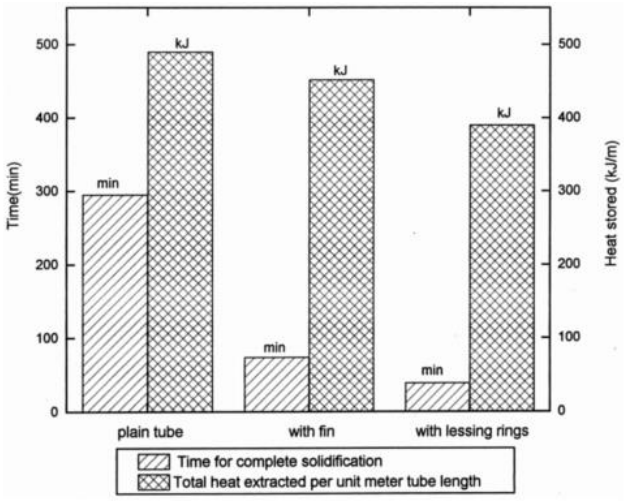

(b)

Figure 2.11(a) Enhancement techniques used in the study (b) heat recovered during solidification [Source: Velraj et al. (1999) [38]*]*

Mesalhy et al. (2005) studied numerically the melting and solidification of a PCM impregnated into a porous matrix. The study identified the effect of the matrix porosity and the thermal conductivity of the metal used on the enhancement of melting and solidification. The range of the volumetric porosities reported in the study was 0.85, 0.9

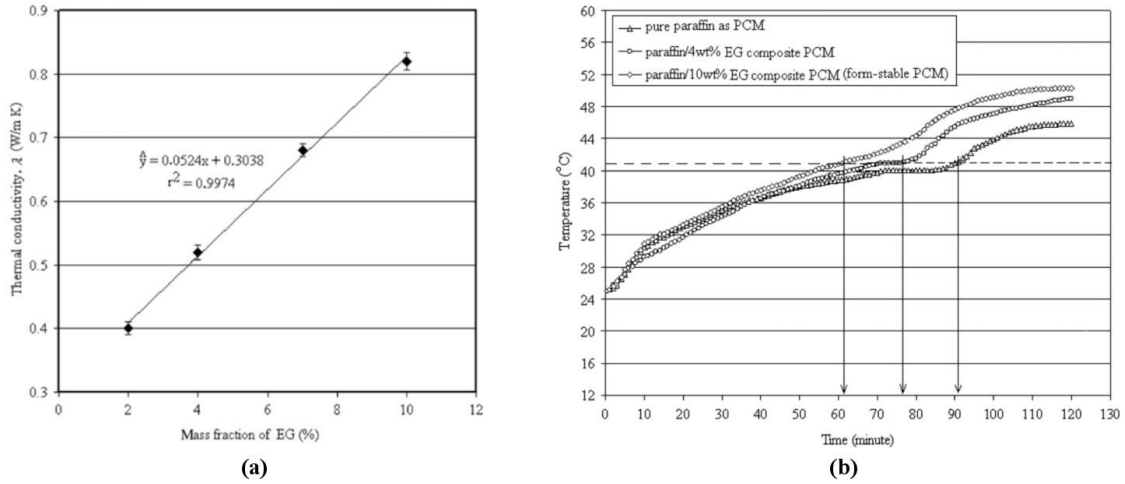

Figure 2.12 (a) Thermal conductivity enhancement vs mass fraction, (b) Melting performance vs mass fraction [Source: Sari & Karaipekli [40]*]*

and 0.95 and that of the ratio between the metal thermal conductivity to that of the PCMs were 50, 100 and 200. The study concluded that using high porosity matrices of higher thermal conductivity metals is more advantageous than using less porous materials with lower thermal conductivity because lower porosity matrices damp the natural convection. The study was conducted for one case only and the effect of Stefan and Rayleigh numbers were not reported.

Mettawee and Assassa [39] studied experimentally the effect of adding aluminum metal powder dispersed in paraffin wax on the melting and the solidification rate. The powder constituted 0.5% of the mass fraction of the enclosure and the particle size was of 80 μm. The study showed that at this mass fraction, the melting time can be reduced by 60 % compared to pure paraffin. The study did not report the behavior and the stability of the dispersion under consecutive melting and solidification cycles.

Sari and Karaipekli [40] studied experimentally the effect of using PCM absorbed in Expanded Graphite (EG) on the overall thermal conductivity of the system. The study investigated the effect of increasing the mass percentage on the overall thermal conductivity and found that by using EG with a mass fraction up to 10 %, the thermal conductivity of paraffin can be increased from 0.22 to 0.82 $W/m.K$ which is almost 4 times [Refer to Figure 2.12a]. Figure 2.12b shows that at the highest mass fraction tested, the melting time can be reduced by 1.46 times. The results reported in the study were shown for only one experimental case and the effect of the different boundary conditions on the level of enhancement was not reported.

2.3.1.3 Using Nano-particles

The use of nano-particles as an additive heat transfer enhancement technique for PCMs is a relatively new field of study compared to the other techniques and there is currently a discrepancy in literature between the numerical and the experimental findings in understanding and evaluating their enhancement effect [41].

The effect of dispersing nano-particles in a PCM on the thermal conductivity and electric resistivity of the dispersion was studied by Kim & Drzal [42]. In this study, the authors examined the effect of stirring exfoliated graphite nanoplatelets (XGnP) in liquid paraffins from 1% to 7% mass loading content. The authors confirmed that the nanoplatelets were dispersed uniformly in the paraffin through examining the solid samples with scanning electron microscopy (SEM). Figure 2.13a shows the effect of the loading content of xGnP on the electrical resistivity where the material was found to be transformed from being

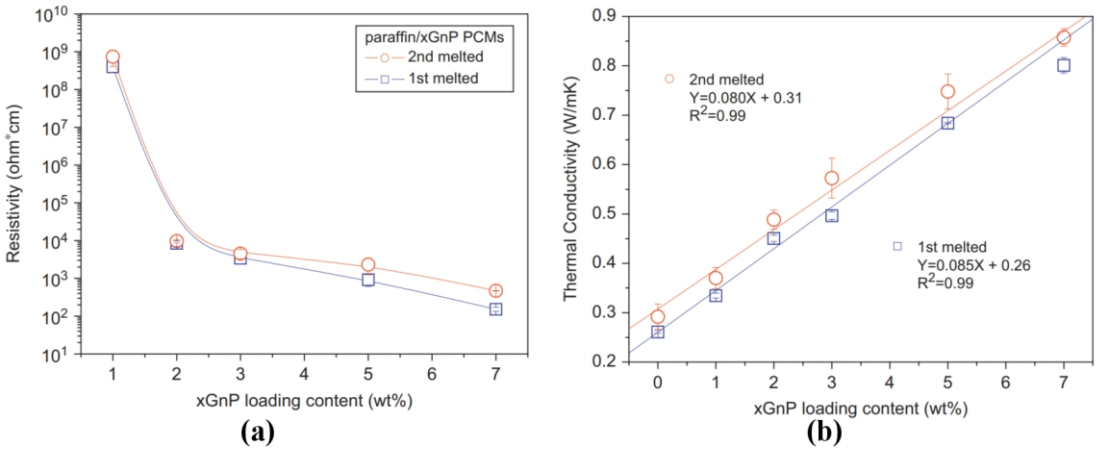

Figure 2.13 (a) effect of xGnP loading content on electrical resistivity, (b) effect of xGnP loading content on the thermal conductivity. [Source: Kim & Drzal (2009)]

electrically insulative to electrically conductive at around 2 % wt loading. The thermal conductivity plot- Figure 2.13b- showed a linear increase by increasing the loading content reaching almost 4-fold increase at 7 % loading content. The results were shown for two samples and a repeatability between both was reported. The study did not include any experimental trials on melting or solidification cycles.

Zeng et al. [43] studied experimentally the melting performance of 1-dodecanol PCM with 1% and 2 % wt. loading dispersion of carbon nano-tubes. The PCM was placed in a vertical cylinder heated from below to promote natural convection effects and the melting performance with the nano-tubes was compared against pure PCM. The experiment showed that the nano-particles drastically increase the dynamic viscosity of the mixture. Figure 2.14a shows the experimental measurements of the dispersion's viscosity for the different loading content against the predicted values from analytical correlations. The measurements clearly identify the discrepancy between the predicted values and the

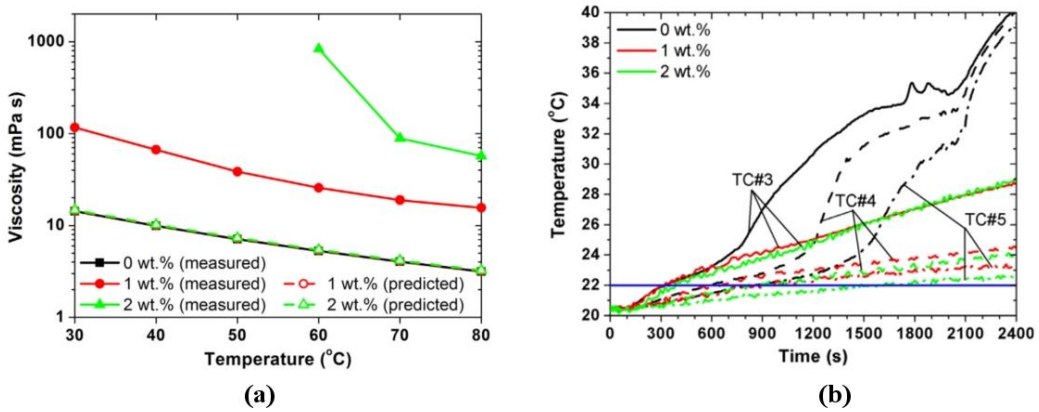

Figure 2.14(a) carbon nano-tubes loading content effect on the viscosity, (b) the temporal temperature measurements against different loading contents. [Source: Zeng et al. (2013)]

experimental measurements. The increased viscosity significantly impeded the Rayleigh number and the natural convection effects were completely dampened in the mixture. Figure 2.14b shows the temperature measurements for the different loadings against a pure PCM case, the temperature temporal profiles shows that the process was conduction dominated by adding the nano-tubes and that the overall melting performance was degraded when using the nano additives.

Ho & Gao [44] studied the melting of n-Octadecane in a vertical rectangular enclosure heated from the side. The nano-particles used in this study were aluminum oxides (Al_2O_3) and the study compared the melting performance of a pure PCM to 5 and 10 % weight loading content of nano-particles. The experimental results were reported for different range of Rayleigh numbers from 1.7E6 to 5.6E7. The results showed that the melting performance was significantly degraded when using the nano-partcles and a decrease in the Nusselt number by up to 60 % was observed at 10 % loading when compared to a pure

PCM. The study concluded that the thermal conductivity enhancement by the nano-particles was significantly overweighed by the increased viscosity and the damping of natural convection.

Similar experimental findings were reported by Fan et al. [45] by studying the melting performance in a spherical containing 1-dodecanol as the PCM and enhanced with graphite nano-sheets. The study showed that the thermal conductivity of the dispersion increased by 1.5 times at 1% wt loading of the nano-sheets while the viscocity was increased by 60 folds. As a result, the melting time was reported to be shortened by 10 % at the lowest Stefan number tested and at 0.5 % wt loading, while for all other cases- (higher loading or higher degree of superheating)- the melting time was increased.

2.3.2 Active enhancement techniques

The use of an active heat transfer enhancement technique in a LHTS is less common than that of passive techniques and the amount of work that has been done in this area is limited. The use of an active enhancement technique is desirable when a control on the level of enhancement is required. The control on the level of enhancement would usually give another piece of control on the temperatures of the integrated systems to the PCM-heat exchanger loop. Active heat transfer enhancement techniques could be also advantageous in cases where the mass and the size of the PCM containment is of crucial impact on the system, for example in space applications. Active techniques could occupy less space and mass compared to passive techniques.

Their applicability is limited to their power consumption and the relative magnitude to the original thermal input into the system. Therefore, the figure of merit when studying active enhancement techniques is the power consumption and the corresponding level of heat transfer enhancement.

As mentioned earlier, the studies conducted on the application of active enhancement techniques to melting or solidification of PCMs are scarce in literature. To the best of our knowledge, these studies are limited to:

a) The use of ultrasonic vibrations

b) The use of Electrohydrodynamics (EHD)

The use of ultrasonic vibrations will be explained in this chapter, while the previous work on using EHD will be discussed in detail in the next chapter about Electrohydrodynamics.

2.3.2.1 Ultrasonic vibrations

Oh et al. [46] studied the melting of paraffin wax in a rectangular enclosure subjected to a constant heat flux with and without ultrasonic vibrations. The melting enclosure was placed in a water bath and the ultrasonic vibrators were placed in conjunction with the water bath. The ultrasonic vibrators were placed to the water bath and not directly onto the solid paraffin to prevent them from overheating [Refer to Figure 2.15a]. The heater surface temperature was recorded through the duration of the experiment, a particle image velocimetry (PIV) system was used to examine the velocity profiles under the effect of

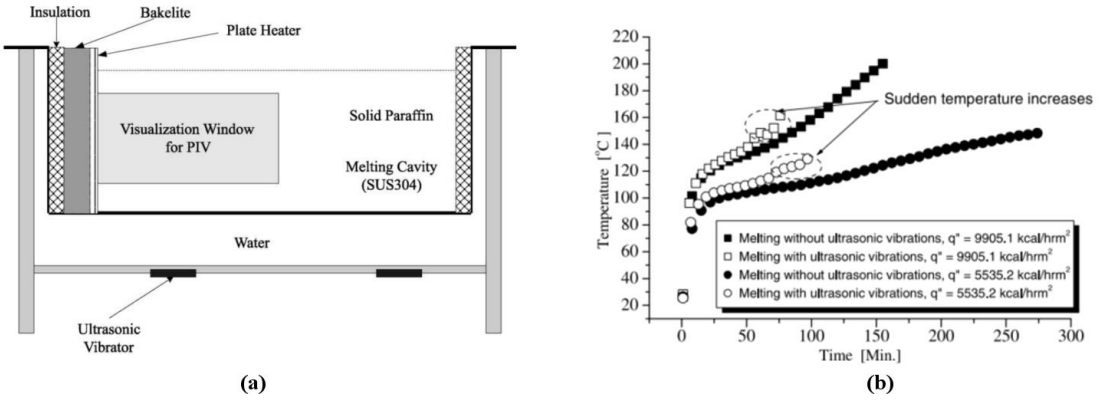

Figure 2.15 (a) Schematic for the test rig, (b) Temporal heater temperature with and without ultrasonic vibrations. [Source: Oh et al. (2002)]

ultrasonic activity and a thermal infrared camera was used to examine the temperature distribution.

The experimental results showed that the melting time can be reduced by 2.5 times for the lower heat flux case when using the ultrasonic vibrations. The enhancement was attributed to three mechanisms:

a) Acoustic streaming: the PIV measurements showed that the ultrasonic vibrations caused local increase in the amplitude of the velocity vectors near the ultrasonic vibrators reached up to 3 folds increase in velocity.
b) Cavitation: the use of ultrasonic vibrations caused cavitation in the liquid phase which augmented the acoustic streaming effect. The presence of the bubbles caused a sudden increase in the heater temperature towards the end of the melting due to the accumulation on the surface of the heater [Refer to Figure 2.15b]

Heat flux (kcal/h m^2)	Melting time (min)	Heater (Wh)	Ultrasonic vibration generator (Wh)	Total consumed electricity (Wh)
9905.1	161	448.1	–	448.1[a]
	76	211.5	–	445.9[b]
5535.2	275	444.6	–	444.6[a]
	94	152.0	–	441.8[b]

[a] Melting with a heater.
[b] Melting with a heater and ultrasonic vibrations.

Figure 2.16 Total thermal and electric energy consumption. [Source: Oh et al. (2002)]

c) Thermally oscillating flow: the combined effect of acoustic streaming and cavitation caused a thermally oscillating fluid motion

The total energy consumption- thermal and electric- was calculated for all cases and the results are shown in Figure 2.16. The energy consumption shows that the ultrasonic vibrators consumed 289 electric Wh for the lower heat flux case compared to 152 thermal Wh from the heaters and 234 electric Wh for the higher heat flux case compared to 211 thermal Wh. The level of the energy consumption is very high compared to the thermal input and the study concluded that the electric consumption can be lowered if the ultrasonic vibrators were directly connected to the PCM. However, no further studies were conducted to confirm or expand the findings of this study.

Chapter 3 Literature Review: Electrohydrodynamics (EHD)

This chapter includes the basics and the fundamentals of the science of Electrohydrodynamics (EHD) and the applicability in the heat transfer enhancement studies. The chapter highlights the previous work of EHD as an enhancement technique for single and multi-phase systems.

3.1 Definition and Governing Equations

EHD is the study of the interaction between dielectric fluids and the high intensity electric fields. The applied electric fields impose an additional body forces in the bulk of the dielectric fluid.

The additional body forces from the application of an electric field, were first formulated by Chu (1959) [47] as

$$\bar{f}_{eB} = \rho_q \bar{E} + J_x \bar{B} - \frac{1}{2} E^2 \nabla \varepsilon - \frac{1}{2} H^2 \nabla \mu + \nabla \left[\frac{1}{2} \rho E^2 \left(\frac{\partial \varepsilon}{\partial \rho} \right)_T + \frac{1}{2} \rho H^2 \left(\frac{\partial \mu}{\partial \rho} \right)_T \right] \quad (3.1)$$

Equation (3.1) provides the effect of both Electrohydrodynamic and Magnetohydrodynamic forces. The force terms in the right-hand side of the equation from

left to right are: Electrophoretic forces (Coulomb forces), electromagnetic forces acting on charged particles in motion, dielectrophoretic force due to spatial gradients in electric permittivity, magnetic forces arising due to spatial gradients in dielectric permeability, the electrostriction and magnetostriction forces.

In case of dielectric materials, the magnitude of the electric current produced from the application of electric field usually does not exceed milliamps range owing to their low electrical conductivity that falls in between 10^{-10} to 10^{-19} S/m. Therefore, the induced magnetic field from the current and the moving charges can be neglected and the electric body forces for dielectrics can be reformulated as

$$\bar{f}_{eB} = \rho_q \vec{E} - \frac{1}{2} E^2 \nabla \varepsilon + \frac{1}{2} \nabla \left[E^2 \left(\frac{\partial \varepsilon}{\partial \rho} \right)_T \right] \tag{3.2}$$

The applied electric field and current will constitute an additional energy source term into the energy transport equation. This term is equal to the joule heating effect and can be calculated as

$$q'''_{eB} = \sigma_e E^2 \tag{3.3}$$

The higher the electrical conductivity and the electric field, the higher will be the joule heating effect into the energy transport. Therefore, the EHD heat generation term must be always evaluated and examined in comparison to the thermal input of the system.

The electric field and charge distributions in the dielectric fluid are governed by the basic Maxwell's equation for electrostatics. The Maxwell's equations for electrostatics constitute two main equations: Gauss's law and the charge conservation equation.

Gauss's law

$$\nabla.\vec{D} = \rho_q \tag{3.4}$$

Where the electric displacement field $(\vec{D})$ is defined as

$$\vec{D} = \varepsilon_0 \varepsilon_r \vec{E} \tag{3.5}$$

and (ε_0) is the vacuum permittivity constant and (ε_r) is the relative permittivity of the dielectric fluid.

Charge conservation equation

$$\nabla.\vec{J} + \frac{\partial \rho_q}{\partial t} = 0 \tag{3.6}$$

The electric current density $(\vec{J})$ can be decomposed into three main components for the dielectric fluid by

$$\vec{j} = \rho_q \vec{u} + \rho_q K_q \vec{E} - D\nabla\rho_q \tag{3.7}$$

The first component on the right-hand side of equations (3.7) is the convective current arising from the motion of the dielectric fluid. The second component is the charge mobility term which represents the ionic drift from the electrodes and is directly proportional to the

magnitude of the electric field and the third component is charge diffusion and it is usually neglected when compared to the other two components. The diffusion component only becomes important at the micro or nano level in which the charge gradients become significantly high [48].

3.1.1 EHD Body forces

The three EHD body forces as formulated in equation (3.2) are:

a) Electrophoretic/ Coulomb forces $\left(\rho_q \vec{E}\right)$

b) Dielectrophoretic forces $\left(-\frac{1}{2}E^2\nabla\varepsilon\right)$

c) Electrostrictive forces $\left(\frac{1}{2}\nabla\left[E^2\left(\frac{\partial\varepsilon}{\partial\rho}\right)_T\right]\right)$

3.1.1.1 Coulomb forces

The Coulomb force acts on the free charges present in the dielectric fluid. The vector of action of the force is aligned with the electric field lines, causing the charged media to migrate either towards or away from the electrode depending on the nature of the charges [Refer to Figure 3.1a]. These free charges present in the dielectric fluid can be created by either of three different mechanism. These mechanisms are:

1) Charge induction
2) Charge conduction
3) Charge injection

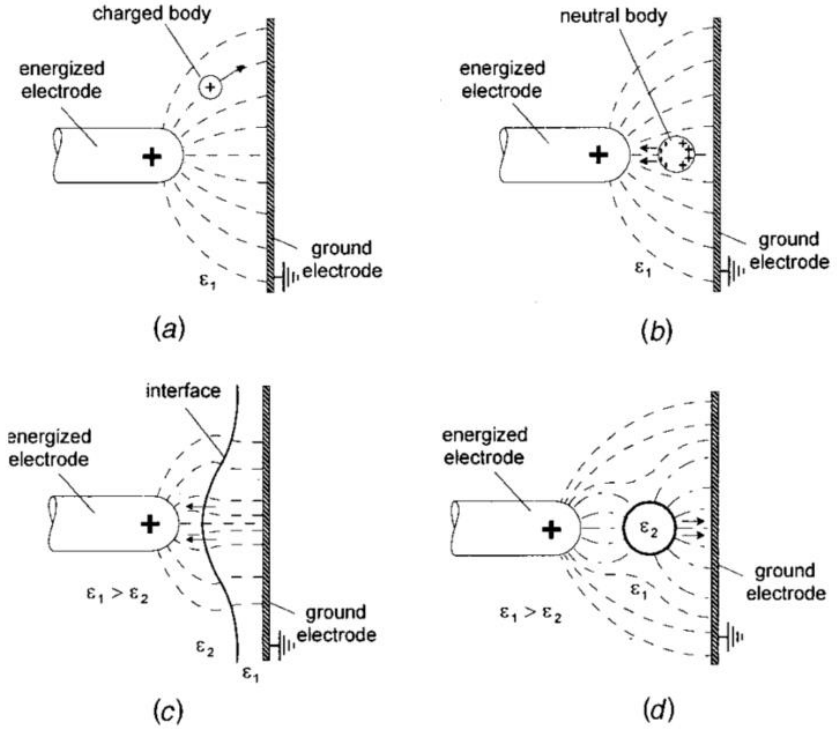

Figure 3.1 Schematic for the different EHD body forces in action. (a) Coulomb forces acting on free charges, (b) dielectrophoretic forces acting on dielectric fluid, (c) polarization forces acting on interface between two fluids (d) dielectrophoresis acting on droplets [Source: Bryan & Yagoobi [49]*]*

The first of these mechanisms is important for slightly conducting fluids ($\sigma \sim 10^{-5} \rightarrow 10^{-15}\ S/m$) [50]. The induction mechanism of charge creation is triggered by spatial gradients in electrical conductivity. The electrical conductivity gradients can exist because of temperature gradients or for multi-phase flows across the interface. Melcher & Firebaugh [51] showed that by imposing a temperature gradient on a slightly conducting liquid and subjecting it to a travelling electric field wave that is perpendicular to the temperature gradients, enough charge can be created in the bulk of the fluid and a pumping action was noticed. Further experiments and analysis proved that a charge can be generated on the

interface between two different fluid which can then be used for mixing [52] or pumping of the two phase system [50].

The second of these mechanisms is charge generation by conduction. The understanding of the conduction mechanism is well described by Atten & Yagoobi [53]. Conduction charge creation takes place in mildly polar liquids ($\sigma < 10^{-7} S/m$) under electric fields magnitude that is lower than charge injection threshold. Under such electrical fields, a process of dissociation and recombination of neutral electrolytic species (A^+B^-) occurs in the dielectric fluid. The dissociated ions are attracted towards the electrodes of the opposite polarities and form a layer that is called a heterocharge layer. The charged layer within the vicinity of the electrodes causes fluid motion toward the electrode.

$$A^+B^- \underset{Recombination}{\overset{Dissociation}{\rightleftharpoons}} A^+ + B^- \tag{3.8}$$

As the electrical conductivity of the fluid increases, the rate of the dissociation increases and the length of the heterocharge layer decreases, which puts a threshold on the lower bound of the electrical conductivity. The threshold value was identified theoretically [53] by the conductivity parameter (C_0)- which is defined as the conduction current divided by the injection current-, where ($C_0 \gg 1$) for conduction to occur. The conductivity parameter is function of the fluid electrical properties and the electric field as

$$C_0 = {\sigma d^2}/{2K_q \varepsilon V} \tag{3.9}$$

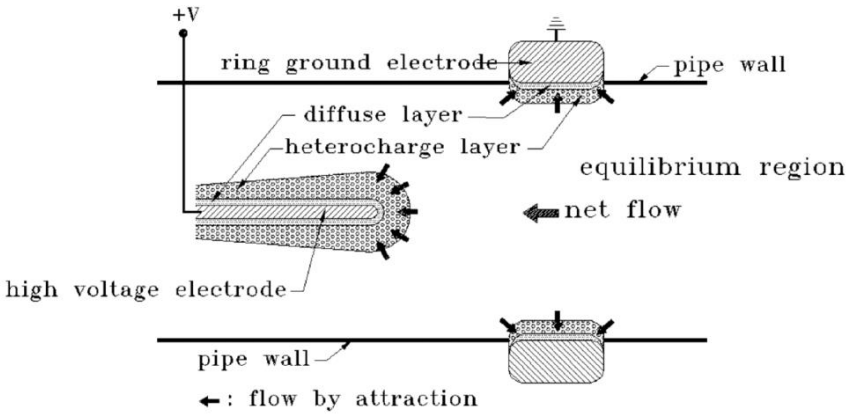

Figure 3.2 Net flow produced by charge creation from conduction mechanism through the application of non-uniform electric field. [Source: Jeong & Yagoobi [54]*]*

In which (d) is the electrodes spacing and (K_q) is the ionic mobility and (ε) is the electrical permittivity of the dielectric.

This mechanism of charge creation was used to pump dielectric fluids of slightly polar properties. By designing a system of electrodes with one relatively smaller in radius than the other (higher electric field), a net flow can be produced from the blunt electrodes towards the smaller radii electrode [54] [Refer to Figure 3.2]. As the applied voltage increases, the charge creation mechanism switches from conduction to injection and the direction of the flow is reversed (from the sharper electrodes towards the blunt). Recent reviews on the basics of conduction pumping and the advances in theoretical and experimental work can be found in the following papers [55], [56].

The last mechanism of charge generation in a dielectric fluid is direct charge injection. In case of highly insulating fluids, the dissociation process occurs around the electrode/liquid interface rather than in the bulk of the dielectric fluid [57]. The electrode's

surface ions are then accelerated by the high electric fields from the electrode towards the ground electrode and dragging the fluid along with it. The injected ions usually induce a jet or plume like structures from the emitting electrode towards the ground electrode, causing a fluid pumping effect and enhancement in heat transfer. This mechanism of charge creation will be explained in further detail in heat transfer enhancement section.

3.1.1.2 Polarization forces

The second and the third terms in the EHD body forces are collectively called polarization forces. The term polarization refers to their association with the bound charges in the media rather than the free charges that is associated with the Coulomb forces.

The dielectrophoretic forces arise with spatial gradients in electric permittivity of the fluid. These spatial gradients are either induced by temperature gradients in the dielectric fluid or highly pronounced in multi-phase flows where a sudden jump in permittivity exists at the interface between the two fluids.

The third term is the Electrostrictive force which is a gradient force caused by changes in dielectric constant with density and its effect on heat transfer is often neglected for incompressible single phase systems [48],[58]. In single phase systems, the additional body forces can induce secondary motions in the bulk of the fluid which enhance mixing and can cause disruptions in the boundary layer at the heat transfer surface. For most of the isothermal single phase systems under DC voltages, the EHD forces can be simplified to only Coulomb force, while for non-isothermal single phase systems both the Coulomb and

the dielectrophoretic force can play an important role in producing convective instabilities in the bulk of the dielectric.

Turnbull & Melcher [59] investigated theoretically and experimentally the effect of the dielectrophoretic forces in producing a semi-Rayleigh Taylor instability in corning oil. The theoretical model was verified experimentally by imposing an AC electric field with high frequency alternating potential which would not provide enough time for the charges to relax. The high frequency AC electric field is equivalent to a DC electric field with rms value of that for the AC. It was found that the dielectrophoretic force caused by thermal gradients could enhance the Nusselt number up to 3 times.

In multiphase systems the polarization forces can be important, as the term $\nabla\varepsilon$ becomes significantly large at the interface between the two media (surface of discontinuity). In this case the Dielectrophoretic force induces an interfacial normal stress where it acts on the fluid of higher permittivity causing it to migrate towards regions of higher electric field. This was observed in liquid/vapor multiphase systems, where the liquid dielectric (higher permittivity fluid) was extracted towards regions of higher electric fields in a phenomenon known as liquid extraction [60]. EHD technique was studied extensively and proved to act as heat transfer enhancement technique for both dielectric single phase and multiphase systems. For example; the studies on EHD effect on convective evaporation demonstrated heat transfer enhancement by two folds as reported by Yabe et al. [61], Norris et al. [62], Cotton et al. [63] and can increase heat transfer by as much as seven to ten folds as reported by McGranaghan and Robinson [64] and Salehi et al. [65]. An analogous phenomenon to the liquid extraction was also observed in solid/liquid multiphase systems in which the

solid's phase electrical permittivity is higher than that of the liquid and upon the application of high voltage, an extraction of the dendrites from the solid/liquid interface towards the liquid phase was observed [12].

3.2 EHD as a heat transfer enhancement technique

The introduction of the additional EHD body forces in the bulk of the dielectric fluid flows, set EHD as a candidate in heat transfer enhancement techniques. These body forces were used in single and multi-phase flow systems and were proven to cause electro-convective flow, multi-phase redistribution and overall decreasing the thermal resistance of the system.

EHD can be used with high effectiveness in micro-gravity applications in which the additional forces were used to generate a pseudo electrical gravitational effect that is analogous to gravity. The absence of any mechanical moving parts and the low power consumption of EHD makes it a favorable heat transfer enhancement technique in space applications.

In this section, the most recent advances in using EHD as an active heat transfer enhancement technique will be discussed for single phase systems and multi-phase systems including liquid/vapor and solid/liquid systems.

3.2.1 EHD in single phase systems

EHD was used to enhance the heat transfer process in single phase systems for both gaseous and liquidous phases. In gaseous systems, the EHD enhancement was often caused

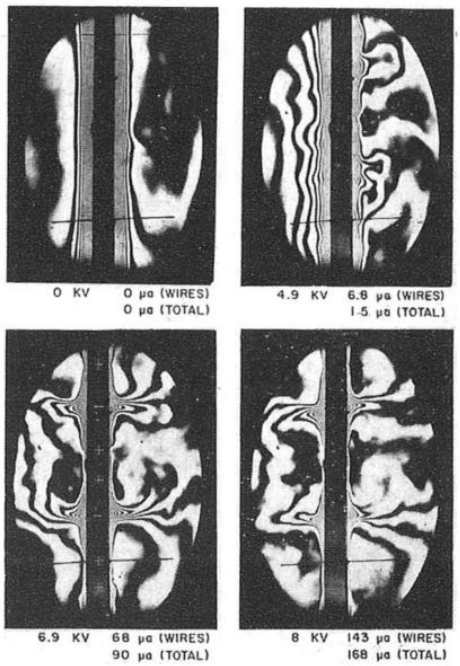

Figure 3.3 Interferograms for the thermal boundary layer disruption from corona discharge at different applied voltages. [Source: Franke (1969)]

by corona discharge. Franke [66] studied natural convection enhancement from a heated vertical plate by applying corona discharge through 0.05mm (0.002 in) diameter wires. The study showed that the convective heat transfer can be augmented by two folds by using EHD and that the level of enhancement increased by increasing the electric field intensity. The thermal boundary layer was visualized using Mach-Zehnder interferometer and counter-rotating vortices were noticed with the maximum thinning of the thermal boundary layer occurring opposite to the high voltage electrodes. [Refer to Figure 3.3]

Fernández & Poulter [67] investigated the effect of using EHD in enhancing the performance of an oil heater. The high voltage electrode was placed in the center of the tube and the oil was heated from the outer surface which was grounded. By applying high

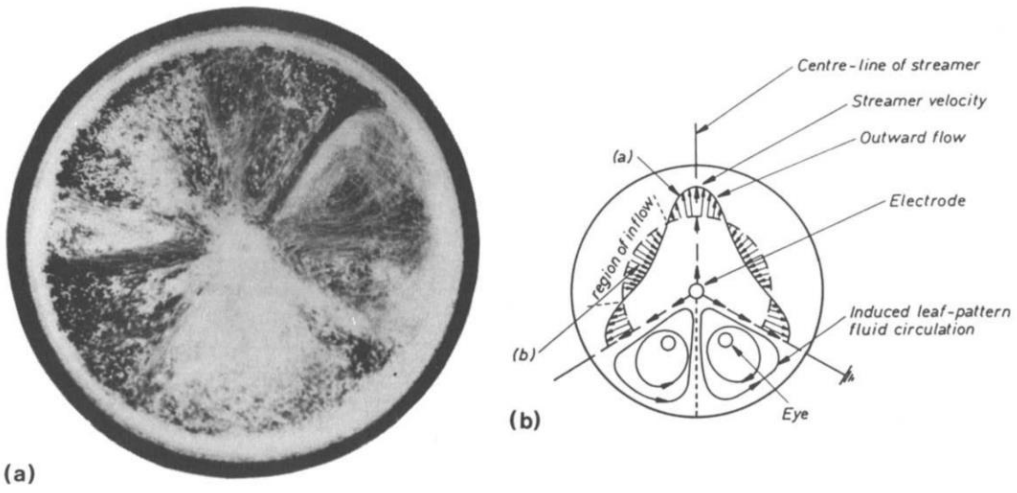

Figure 3.4 (a) Streak flow visualization, (b) Schematic representation for the velocity distributions in the observed leaf pattern flow induced by EHD. [Source: Fernández & Poulter (1987)]

voltage through the electrode, a radial motion of the oil was observed forming leaf pattern shape [Figure 3.4]. This radial motion enhanced the heat transfer process by 20 folds while increasing the pressure drop through the section by 3 times. The study showed that the level of enhancement was lower at the beginning of the cross section and increased along the span of the tube as the temperature increases and the oil viscosity decreased. The main enhancement mechanism was attributed to the electrophoretic forces and the mechanism of charge generation was suggested to be through charge injection. The level of heat transfer enhancement was directly correlated to the injecting current and the study showed that the level of charge injection was higher for negative polarities.

Fujino et al. [68] investigated the effect of applying DC electric field on laminar forced convective flow of fluorocarbon in a parallel plate heat exchanger configuration. The applied heat transfer boundary conditions were constant heat flux applied to the high

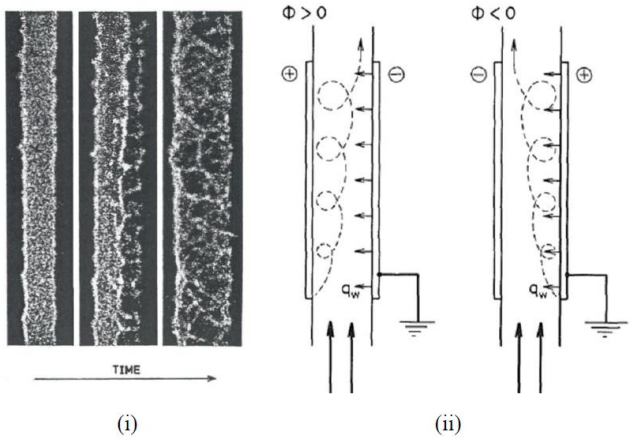

Figure 3.5 (i) Shadowgraph images showing the direction of propagation of longitudinal rolls from electro-convection, (ii) Schematic representation for the development of the longitudinal rolls. [Source: Fujino et al. (1989)]

voltage side plate. The effect of heat flux magnitude and voltage polarity on heat transfer enhancement were studied. The experiments showed that the level of heat transfer augmentation was independent on the magnitude of the applied heat flux and thus the temperature gradients in the fluid. A heat transfer enhancement of up to 4-folds was noticed at the highest applied voltage, and longitudinal rolls were observed originating from the positive electrode and propagating towards the negative side [Figure 3.5]. The study showed that the level of enhancement was higher for negative polarities which is in agreement with Fernandez et al. (1987), and the mechanism of charge generation is by injection from both electrodes or from one side.

Kasayapanand [69] studied experimentally and numerically the effect of applying DC electric fields through a series of wire electrodes on the natural convection of air in a rectangular enclosure heated from the side. The author investigated the impact of changing the number of electrodes and their arrangement on the heat transfer enhancement and the

study was conducted for different Rayleigh numbers. It was found that the EHD forces enhanced the overall heat transfer from the vertical wall by disrupting the thermal boundary layer. The heat transfer enhancement factor increased with the increase of the applied voltage and decreased with the increase of the gravitational Rayleigh number. The number of electrodes was varied in the study from 1 to 33 electrodes and it was found that the maximum enhancement was achieved in around 5 to 9 electrodes. As the number of electrodes increased above 9, the vortices started to recombine and form rather big convection cells causing the level of enhancement to decrease. The numerical model considered the electrophoretic forces only; however, it demonstrated good agreement with the experimental results within 10 % maximum deviation in the level of enhancement. As the experiments were conducted for air as the dielectric fluid, the effect of the dielectrophoretic forces was expected to be minimal. This work was the first of many other numerical work conducted for natural convection enhancement in gases [70]–[72].

The effect of the dielectrophoretic forces on enhancing natural convection in vertical annuli was recently studied by Futterer et al. [73]. The study relied on using high frequency alternating (AC) electric field to suppress the effect of the Coulomb forces in the bulk of the fluid. The heating was established with electric cartridges connected to the inner cylinder and the cooling was performed on the outer cylinder and the electric field was applied between the two cylinders. The results were presented against the electrical Rayleigh number which is a non-dimensional parameter analogous to the traditional gravitational Rayleigh Number.

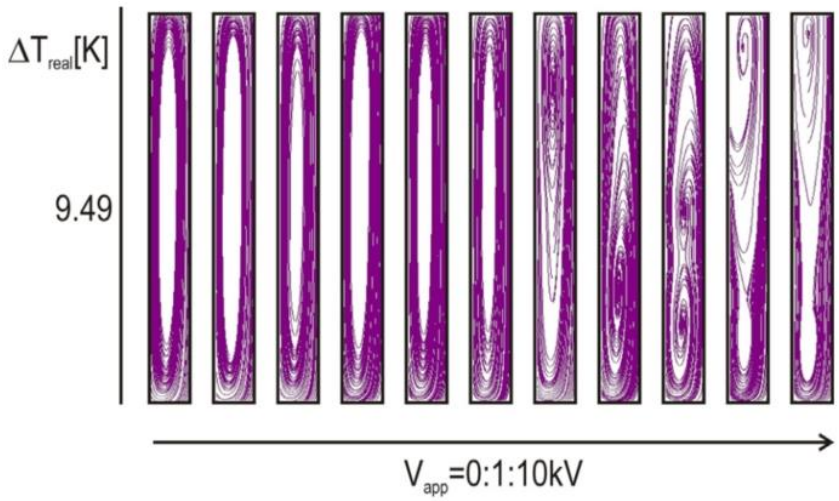

Figure 3.6 Development of the flow patterns with the increase of the applied voltage. [Source: Futterer et al. (2016)]

The study showed that at lower electric Rayleigh numbers, the heat transfer was damped and the heat transfer enhancement increased by increasing the electric Rayleigh number. The augmented heat transfer noticed at the higher electric Rayleigh numbers was attributed to the transition to multi-cellular pattern. This experimental study was one of the first in the field and the authors recommended that further studies are needed to understand the superposition of natural and electrical convection.

3.2.2 EHD in multi-phase systems

The EHD effect on the heat transfer enhancement of liquid/vapor multi-phase systems has been studied extensively in literature. On the contrary, very limited research has been conducted on the application of EHD in solid/liquid multi-phase systems. In fact, up to the best of the author's knowledge, only two references can be found on the effect of EHD on solid/liquid systems and one of those is the motivation for the current research.

In this section, a summary of the previous work in application of EHD in liquid/vapor systems will be presented along with the research in solid/liquid systems. The reader can refer to the following review papers for a more extensive exposure on the application of EHD in thermal systems [74], [75].

3.2.2.1 EHD in boiling and condensation

The effect of EHD forces on the boiling and condensation has been studied extensively and specially for the boiling phenomenon. An example of these previous studies can be found in the work of Yabe et al. [61], Singh et al. [76], Salehi et al. [65] , Cotton et al. [63][77] and Nangle-Smith & Cotton [78]. It was found that the heat transfer augmentation was directly related to the magnitude of the applied voltage and that the power consumption from using EHD forces is negligible compared to the thermal load.

In general, it was found that the EHD forces induce mixing and a redistribution of the flow in the liquid/vapor systems. This induced mixing often has an adverse effect on the pressure drop of the system and the pressure drop was found to increase by increasing the applied voltage.

The mechanism of action of the EHD forces in these systems were found to be relying on the liquid extraction phenomenon. The liquid extraction causes a redistribution in the flow, sometimes increasing the wetter surface area and thus enhancing the overall heat transfer process and it could be as well used in drying and hence degrading the overall heat transfer [62]. The studies conducted on convective evaporation showed that the heat transfer can be increased by two folds [61]–[63] and sometimes up to ten folds [65]. Cotton

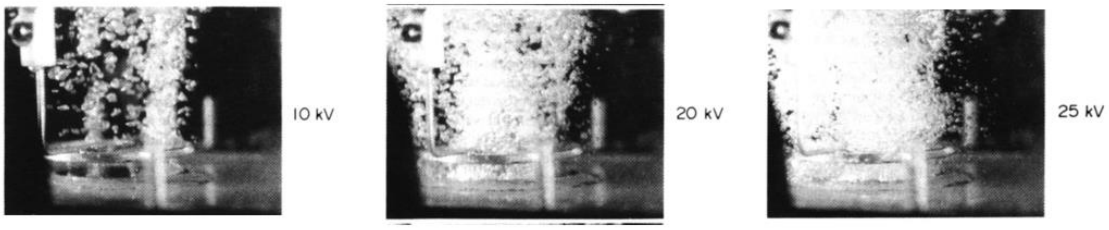

Figure 3.7 Boiling of R-11 under EHD forces. [Source: Ogata & Yabe [80]*]*

et al. [77] showed that the level of heat transfer enhancement decreases by increasing the mass flux of the refrigerant and the EHD forces becomes significant when the dimensionless Masuda number is in the same order of magnitude of the square of the Reynolds number ($Md \sim Re^2$). The authors developed a two-phase flow pattern map under the EHD forces and validated it against the experimental results. Nangle Smith et al. [79] investigated the effect of polarity for in tube convective boiling and concluded that negative DC voltages showed better enhancement compared to positive. It was found that for both polarities, the dielectrophoretic forces acts on the refrigerant and causing extraction of the refrigerant towards the center electrodes. The difference between both polarities was noticed after the refrigerant reached the center electrode. In the negative polarity case, the extracted refrigerant acquired negative charge from the electrodes which caused uniform repelled liquid columns around the electrode. This new regime offered larger wetted heat transfer area compared to the positive polarity and better heat transfer augmentation.

In nucleate boiling, the EHD forces interact with the bubbles forming on the heat transfer surface as well by breaking up the large bubbles and decreasing the bubble detachment diameter and therefore increasing the number of bubbles [80], [81] [Figure 3.7].

The early studies by Velkoff & Miller [82] showed the impact of using high electrostatic fields on the condensation process. They studied the condensation of R-113 refrigerant on a vertical plate under EHD forces. The authors examined the condensation behavior under different electrical configurations: single wire electrode parallel to the vertical plate and wired mesh electrodes parallel to the vertical plate. It was found that the heat transfer was augmented by 1.5 folds for the single wire and up to 3 folds for the wired mesh case. The EHD forces acted on the condensate causing a destabilization on the interface and caused further pumping of the condensate that lead to thinning and therefore reduced the thermal resistance.

Several experimental studies followed Velkoff & Miller's to understand the impact of the different EHD parameters on the condensation process. Yabe et al. [83] studied the condensation over vertically oriented cooled tubes under EHD forces. The study used a helical electrode wrapped around the vertical tube and connected to the high voltage source while grounding the tube. The heat transfer was enhanced by 2.8 folds and the mechanism of enhancement was by liquid extraction and subsequently de-wetting the heat transfer surface. The study showed that the EHD forces can remove more than 94 % of the condensate from the cooled surface.

Cheung et al. [84] studied the condensation under EHD forces for both horizontal and vertical smooth tubes. The maximum heat transfer enhancement recorded in this study was 7.2 folds and the corresponding electric power consumption did not exceed 0.06 % of the thermal load. Again, in this study the heat transfer augmentation mechanism was attributed to liquid extraction and the subsequent thinning of the condensate film. The study

emphasized that EHD forces can diminish the difference in condensation heat transfer coefficients between vertical and horizontal tubes showing that an EHD-assisted condensation is insensitive to the orientation.

Gidwani et al. [85] studied in-tube condensation for smooth and corrugated surface tubes. It was found that heat transfer enhancement factor can reach up to 18.8 folds for in tube condensation of R-404a in smooth pipes, however the corresponding pressure drop penalty was 11.8 times increase. It was found that the EHD heat transfer enhancement increased with the decrease of the mass flux, average vapor quality and with the increase of the saturation temperature.

Sadek et al. [86] investigated the convective condensation of R-134 in an annular channel flow with 45 % inlet quality. The study showed that the EHD forces were able to extract enough liquid from an initially stratified flow regime and redistribute the flow to produce an annular flow regime. The subsequent heat transfer enhancement from the flow redistribution was found to be 3 folds accompanied with 3 times increase in the pressure drop. Further studies by the same author [87] noticed the difference between transient EHD flow patterns and that of the steady state. The formation of twisted liquid cones at the instant of applying high voltage were observed, which diminished as the system gets to steady state.

3.2.2.2 EHD in melting and solidification

The studies conducted on using EHD to improve the melting and the solidification processes are very few in literature. These studies mainly focused on the implementation

of external body forces to reduce the natural convection currents during the solidification process of semiconductor crystals[88]. This convection damping is desired during the solidification of single crystals to ensure minimum contamination that could be produced from the small particles in the crucible wall and being carried by the natural convection currents[88], [89]. In fact, these studies were numerical studies only and since these studies were conducted on solidification of metals, they involved the study of Magneto-hydrodynamics effects [88], [89] which are considerably different than EHD.

The first experimental work in this field was conducted by Dellorusso [90] was unsuccessful. Dellorusso investigated the effect of EHD forces on the overall heat transfer during melting of a paraffin wax of melting temperature 55 ℃. The PCM was stored inside a double wall fin array configuration made of aluminum [Refer to Figure 3.8] and an applied voltage of 15 kV (DC and AC) on the PCM side was used during EHD testing. It was concluded that EHD forces had a negative effect on the solidification process and a minimal enhancement on the melting process. The adverse effect on the solidification was attributed to the fact that conduction is the main mechanism of heat transfer during solidification, while EHD forces may have caused disturbance in the liquid PCM which hindered crystal growth and it was hypothesized that EHD may have limited the number of nucleation sites.

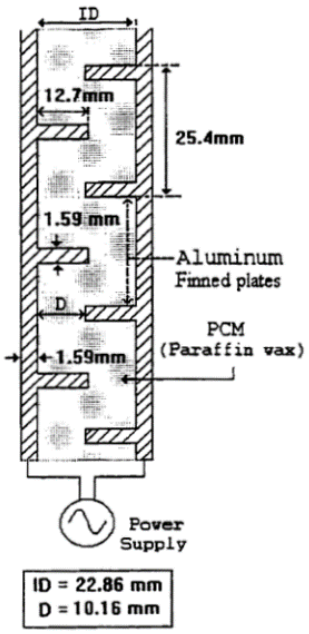

Figure 3.8 The finned wall latent heat thermal storage module used in experiments. [Source: Dellorusso [90]*]*

The results showed that EHD did not change the melting performance opposite to what was expected of enhancing the melting process. The author concluded that the non-significant effect of EHD during melting can be attributed to the cell design. It was suggested that the cell design did not promote melting by convection until the late stages of melting which was not sufficient for EHD to enhance the overall progress. The author also added that using such complex design was not a good choice, as a better electrode configuration and a simpler geometry can be more effective design as it would enhance the natural convection within the molten PCM.

Thompson and Cotton [91] studied the solidification of Octadecane under EHD forces in a rectangular enclosure cooled from the bottom. The cell configuration was designed to ensure uni-directional solidification by conduction only and to promote thermal

stratification in the cell. The study was conducted for different degrees of initial superheating of the liquid phase and under negative 8 kV DC voltage. The study that EHD forces enhanced the solidification process and reduced the solidification time by a maximum of 10 % and that the degree of enhancement was highest at the highest degree of superheating. This was attributed to the electroconvection effect by EHD forces which enhance the dissipation of the sensible content during the solidification process. These findings highlight the fact that EHD forces that could cause electroconvection in the liquid phase would have a limited enhancement effect on the solidification process as the thermal resistance of the solidified layer will always be the dominating thermal resistance in the system.

As mentioned in the introduction section, that the scope of this dissertation is motivated by the earlier findings of Nakhla et al. [12] - the Author of this dissertation - that showed a significant enhancement of melting of paraffin wax using EHD. The PCM (paraffin wax) was enclosed in a rectangular enclosure heated from the top with an electric heater to provide a constant heat flux. The configuration intentionally promoted thermal stratification and therefore the EHD enhancement was compared against a conduction dominated melting. It was found that by applying (-8) kV DC through the electrodes during melting that the melting time can be reduced by up to 40 % when compared to a 0-kV base case. By using high speed imaging visualization, a phenomenon analogous to the liquid extraction phenomenon was discovered and named “Solid Extraction”, where the solid dendrites or the equiaxed grains within the mushy zone were extracted from the mushy

zone towards the liquid bulk. The solid extraction phenomenon was observed for certain range of melt thickness of and at certain areas along the interface

The current study will examine the melting behavior of an organic PCM under both gravitational and EHD forces. The study will focus on understanding and quantifying the possible mechanisms of enhancement during the melting process under EHD forces. The instantaneous level of enhancement will be calculated during the different stages of melting and the flow regimes will be interpreted by the aid of shadowgraph measurement. The understanding of the mechanisms will allow to represent the problem in non-dimensional parameters and estimate the criterion of transforming from a gravitational dominated melting to mixed electrical and gravitational regime.

Chapter 4 Experimental Methodology

This chapter explains the details of the experimental methodology used in this research, the experimental facilities, the measured parameters and the associated data reduction.

Two main experimental facilities were constructed to understand the effect of EHD forces on two different methods of melting: a heat conduction governed melting and a natural convection governed melting.

4.1 Conduction dominated melting experimental facility

This facility was used for melting experiments that are governed by heat conduction under a near isothermal heat transfer surface boundary condition. This condition is true for thermal systems configurations in which the melt front displacement vector is in the same direction of the gravitational field, or in micro-gravity conditions. The experimental facility was designed to satisfy the conditions of the first case by encapsulating the PCM between two heat exchangers. The top heat exchanger is the hot source while the bottom one is the cold sink. This configuration naturally promoted a thermally stratified liquid PCM phase under normal gravity conditions. Any fluid perturbation was naturally damped by the opposing gravitational and viscous forces.

The novel design of this experimental facility allowed for accurate quantification to the heat transfer augmentation caused by the EHD forces. In fact, the experimental

methodology used in this facility is not limited for quantification of the EHD effect, but also can be used for assessing the performance of other heat transfer enhancement techniques in phase change materials as will be explained in the data reduction section.

The methodology relies on studying the melting process of the PCM which is a dynamic process in nature, rather under quasi-steady environment. The quasi-steady environment allows for accurate quantification for the heat flux through the liquid and the solid PCM with and without EHD, thus allowing for accurate evaluation of the augmented heat transfer through different melt thicknesses. This theory was achieved by using a simultaneous controllable heating and cooling at the same time. The PCM was encapsulated between two heat exchangers, the top heat exchanger had water running at a temperature (T_h) which is higher than the melting temperature (T_m) of the PCM, while the bottom heat exchanger has water running at a temperature (T_c) which is lower than of the PCM melting point. The simultaneous heating and cooling from both sides allowed for reaching a steady state and controlling the location of the solid/liquid interface.

4.1.1 Facility Overview

Figure 4.1 shows a schematic for the steady state experimental facility. This experimental facility was built with the aid of 4M06 capstone project [92] and by Benoit Lacroix [93] (an internship student from INSA). The experimental rig consists of a polycarbonate test section, in which the phase change material is contained. The container had internal dimensions of 40 mm in height, 50 mm in depth and 156 mm long. The walls of the container are made of 0.5-inch polycarbonate. Two heat exchangers were fastened

to the top and bottom of the test section. These heat exchangers provided the heat source and sink for the experiments. The heat exchangers were designed to use water as the working fluid, the water passed through internal channels which were machined into the aluminum heat exchangers. A flat surface on the heat exchanger was used to heat and cool the phase change material.

The two heat exchangers were connected to two controlled thermal baths with a reported temperature stability of $\pm 0.01\,℃$, thus maintaining constant temperature boundary condition for each heat exchanger. The hot heat exchanger was connected to- Neslab RTE-10- thermal bath and the cold heat exchanger is connected to- Neslab RTE-7- thermal bath. The mass flow rates through both the hot and the cold heat exchanger were high enough to ensure a maximum temperature drop or rise of $0.3\,℃$ between the inlet and the outlet of the heat exchangers. Each heat exchanger had eight thermocouple slots, uniformly located along its body, to assess the condition of temperature uniformity across the heat exchanger. The thermocouples used were type-T thermocouples and were calibrated against DP251 precision RTD with reported accuracy of $\pm\ 0.027\,℃$. The thermocouples were connected to a 16 channels data acquisition card (NI-DAQ 9213), which in turn was connected to LABVIEW program for real time monitoring and logging of temperature data.

The solid/liquid interface shape and location was captured by using a time-lapse camera (Nikon D5200), that was placed perpendicular to the long side of the test section.

The electric field was generated using a high voltage DC power supply [Glassman PS/EL30R01.5] with maximum output voltage of $30\,kV$. The high voltage DC power

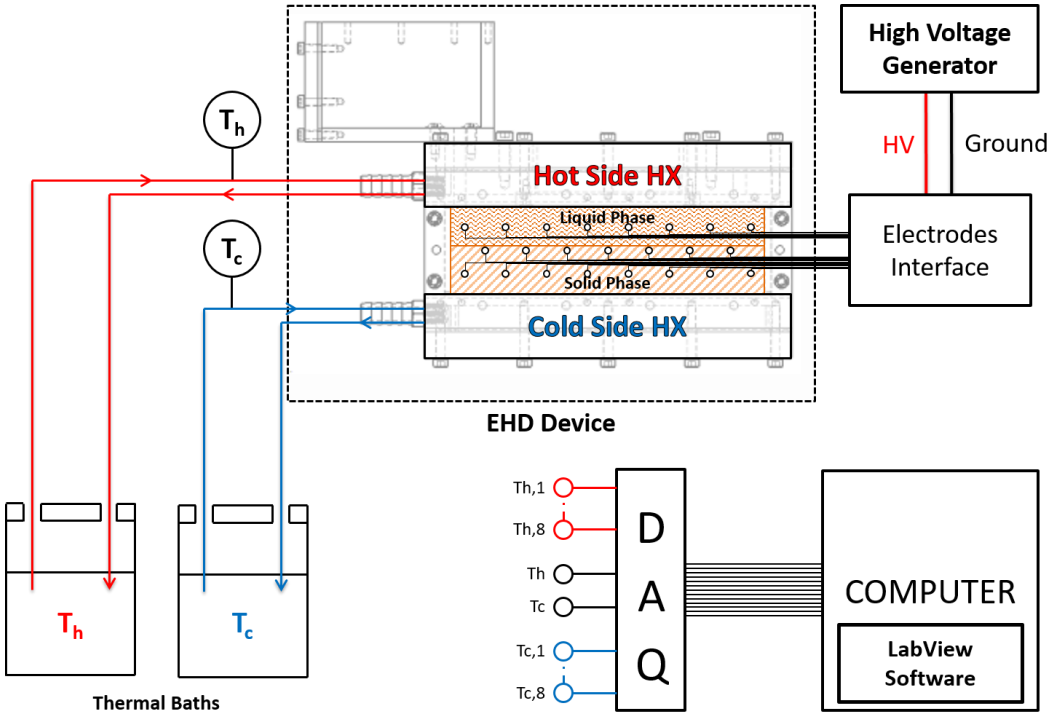

Figure 4.1 Conduction dominated melting experimental facility

supply was connected to a group of cylindrical electrodes that are embedded into the PCM. Figure 4.2 shows a section from the test cell with the electrodes arrangement in the PCM.

The cylindrical electrodes were 3.2 mm (1/8-inch) in diameter and made of Brass. The electrodes were placed in a three rows staggered configuration, with the horizontal spacing between each row was 20 mm and the vertical spacing was 10 mm. The vertical spacing between the heat exchangers and the closest row of electrodes was 10 mm. The two heat exchangers and the middle row of electrodes were electrically grounded through the ground connection of the high voltage DC supply, while the first and the third row of electrodes were connected to the high voltage side.

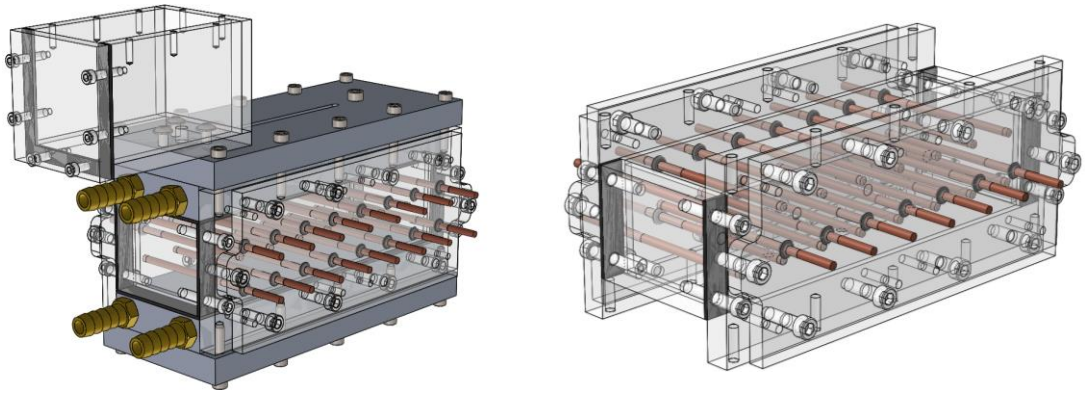

Figure 4.2 PCM Chamber assembly (Left) PCM chamber side panels with embedded electrodes from sides (Right)

4.1.2 The PCM chamber

The PCM chamber was made from polycarbonate because of its transparency, ease of machinability and high softening temperature ($> 144℃$). The higher temperature resistance was desired in this test facility for future testing of PCMs with higher melting temperatures. Nylon screws and Viton® gaskets were used for the sealing between the chamber walls and the two heat exchangers. Viton was specifically used for its chemical compatibility with paraffin oils and alkanes. The electrodes were sealed by using Viton O-rings. The O-rings were placed around the electrodes and pressed into place by using external acrylic plate clamped into the chamber's side walls [Figure 4.2].

A riser was clamped on top of the hot heat exchanger to accommodate for the volumetric expansion/contraction accompanied by the PCM melting and solidification. The use of a riser was essential for reducing the entrapment of any air bubbles inside the PCM during

the solidification and for avoiding excessively high pressures that may be arise from the expansion during melting.

The PCM chamber was covered from all sides with wool glass insulation of 4-inch thickness and by a 1 inch thickness wool glass from the top and the bottom of the heat exchangers. The side insulation was taken out during the times of capturing the solid/liquid interface shape and was then put back after the measurements were taken.

4.1.3 Phase Change Material

The PCM used in this research was 99% pure Octadecane $C_{18}H_{38}$, purchased from Sigma-Aldrich and Alfa-Aesar scientific materials. Octadecane was used because of its relatively low melting point ($T_m = 28$ ℃), thus minimizing the heat losses to the ambient under lab conditions. In fact, the Octadecane material offers several advantages

that was desired in the scope of this work. These advantages are: accurate characterization of its thermo-physical properties in literature [19], [94] for both solid and liquid phase, Octadecane is a transparent material in liquid state and opaque in solid-state which are desirable properties for visualization. Lastly, Octadecane is an organic material with electrical properties that are suitable for EHD application, owing to the extremely high electrical resistivity ($> 10^{15}\ \Omega m$)[95] and the low dielectric constant (≈ 2.1).

The thermo-physical and electrical properties of Octadecane are presented in Appendix A.

4.1.4 Experimental Procedures

The following experimental procedures were followed during the initial process of filling the PCM chamber with Octadecane or any other PCM

a) The PCM was first melted in a furnace outside the experimental facility.
b) The top and the bottom heat exchangers were connected to the two thermal baths and the temperatures were set to 10 degrees higher than that of the Octadecane melting point.
c) The liquid Octadecane was then poured into the PCM chamber through the riser slowly to minimize air bubbles entrapment in the liquid PCM. The PCM chamber was filled completely and half of the riser. During the filling process, the whole assembly was tilted with an angle to allow the escapement of any entrapped bubbles through the riser.
d) After the PCM chamber filling process, the thermal bath connected to the cold heat exchanger was set to the desired temperature of the next experiments, while the one connected to the hot heat exchanger was set to a temperature slightly higher than Octadecane's melting point.
e) After the previous step, the PCM started to solidify, starting from the bottom heat exchanger and moving up toward the top heat exchanger. The solidification process was left running for 24 hours.

f) After the 24 hours, the hot heat exchanger was then set to the same temperature of that of the cold heat exchanger and the rest of the PCM was left to completely solidify.

The previous steps were used for the initialization of the experimental facility and were not required to be done for every experiment. The following experimental procedure was then followed for each experiment afterwards.

a) After ensuring that the PCM was completely solidified from the last step, the thermal bath temperatures were set to the desired temperatures of testing.
b) The solid/liquid interface location was captured every 20 minutes as it moved from the hot heat exchanger towards the cold side.
c) Step (b) was repeated until the solid/liquid interface movement stopped for at least 2 hours with a maximum of $\pm$ 0.2 mm deviation. This condition ensured that a steady state had been reached.
d) The reported melt thickness at step (c) was the steady state melt thickness at 0 kV.
e) The electrodes terminals were then connected to the high voltage DC supply, and the voltage was adjusted to the desired test value.
f) The applied voltage induced electrical body forces inside the test cell, which decreased the thermal resistance at the molten PCM side and the solid/liquid interface started moving again away from the hot heat exchanger.
g) Steps (b) and (c) were repeated until a new steady state was achieved which signifies the heat transfer enhancement induced by EHD.

h) The reported melt thickness in step (g) was the new steady state melt thickness at the tested voltage

4.1.5 Data Reduction

In this section the data reduction methodology used for the conduction dominated melting experimental facility is explained in details. The facility used a novel method in estimating the heat transfer enhancement caused by the added heat enhancement technique, which is EHD in this case. However, as mentioned before the method can be used for other enhancement techniques as long as the heat flux through the solid phase is not disturbed by the added heat enhancement technique.

Figure 4.3 shows a schematic section from the test cell along with the simplified thermal circuit for non-EHD and EHD cases. Before applying EHD, the system is at an initial steady and the solid/liquid interface is stationary at a thickness of (S_0). At this point, the heat flow from the hot heat exchanger through the liquid PCM $(Q_{L,0})$ is equal to the heat flow through the solid PCM $(Q_{s,0})$ to the cold heat exchanger.

For the non EHD steady state, the heat flux through the liquid PCM is calculated as:

$$Q_{L,0} = \frac{T_h - T_m}{R_{L,0}A} = k_L \frac{T_h - T_m}{S_0} \tag{4.1}$$

and the heat flux through the solid PCM is calculated as:

$$Q_{s,0} = \frac{T_m - T_c}{R_{s,0}A} = k_s \frac{T_m - T_c}{H - S_0} \tag{4.2}$$

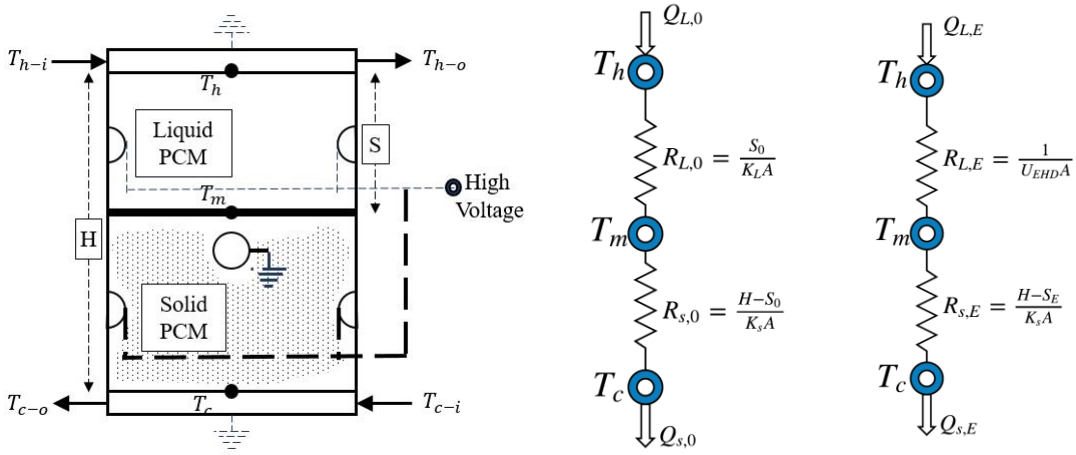

(a) (b) (c)

Figure 4.3 (a)Schematic section of the test cell, (b) Thermal circuit at 0 kV (before applying EHD), (c) Thermal circuit after applying EHD

From equation (4.1) and equation (4.2), the initial steady state thickness (S_0) can be evaluated as:

$$S_0 = H\left(1 + \frac{k_S(T_m - T_c)}{k_L(T_h - T_m)}\right)^{-1} \tag{4.3}$$

Once EHD is applied, the heat transfer through the liquid PCM is no longer governed by pure conduction only, but rather a mixed conduction/convection heat transfer takes place due to the induced EHD body forces. In this case, the thermal resistance of the liquid PCM $(R_{L,E})$ decreases and the solid/liquid interface moves towards the cold side until the system reaches a new steady state at a melt thickness (S_E).

At the new steady state (S_E), the steady state heat flux can not be estimated from the liquid side due to the unknown thermal resistance in the liquid side. However, it can be calculated from the solid side as the heat transfer through the solid PCM is by conduction only.

$$Q_{L,E} = Q_{s,E} = \frac{T_m - T_c}{R_{s,E}A} = k_s \frac{T_m - T_c}{H - S_E} \tag{4.4}$$

The results for this experimental facility were also analyzed in terms of dimensionless numbers. For the heat transfer results, the dimensionless Nusselt number was used to report the heat transfer enhancement. This in fact is very adequate for this facility, as the Nusselt number in definition is the ratio between the heat transfer by convection to the heat transfer by conduction. The average electrical Nusselt number is equal to the ratio between the conduction thermal resistance through the liquid PCM to the EHD thermal resistance.

$$Nu_E = \frac{Q_E}{Q_0} = \frac{R_{L,E-conduction}}{R_{L,E-EHD}} \tag{4.5}$$

The conduction thermal resistance through the liquid PCM at the new steady state (S_E)

$$R_{L,E-conduction} = \frac{S_E}{k_L A} \tag{4.6}$$

The EHD thermal resistance can be calculated through the energy balance at the interface

$$R_{L,E-EHD} = R_{s,E}\frac{T_h - T_m}{T_m - T_c} = \frac{(H - S_E)(T_h - T_m)}{k_S A(T_m - T_c)} \quad (4.7)$$

The average electrical Nusselt number formula is then equal to

$$Nu_E = \frac{k_s S_E(T_m - T_c)}{k_L(H - S_E)(T_h - T_m)} \quad (4.8)$$

The above correlation can be presented in terms of the Stefan number of super heating and sub cooling for the liquid and the solid PCM respectively

$$Nu_E = \frac{\alpha_s \rho_s S_E Ste_s}{\alpha_L \rho_L (H - S_E) Ste_L} \quad (4.9)$$

From equation (4.8), the average electrical Nusselt number depends on the ratio between the liquid melt thickness to that of the solid thickness and the degree of superheating in the liquid PCM to that of the subcooling of the solid PCM.

The electrical Nusselt number will correspond to 1 when $S_E = S_0$, thus indicating no enhancement is caused by the EHD forces and that the heat transfer mode is by conduction only.

4.2 Convection dominated melting experimental facility

4.2.1 Facility overview

The second experimental facility was designed and built to study the melting of the PCMs in a vertical configuration. This kind of melting starts as a conduction dominated

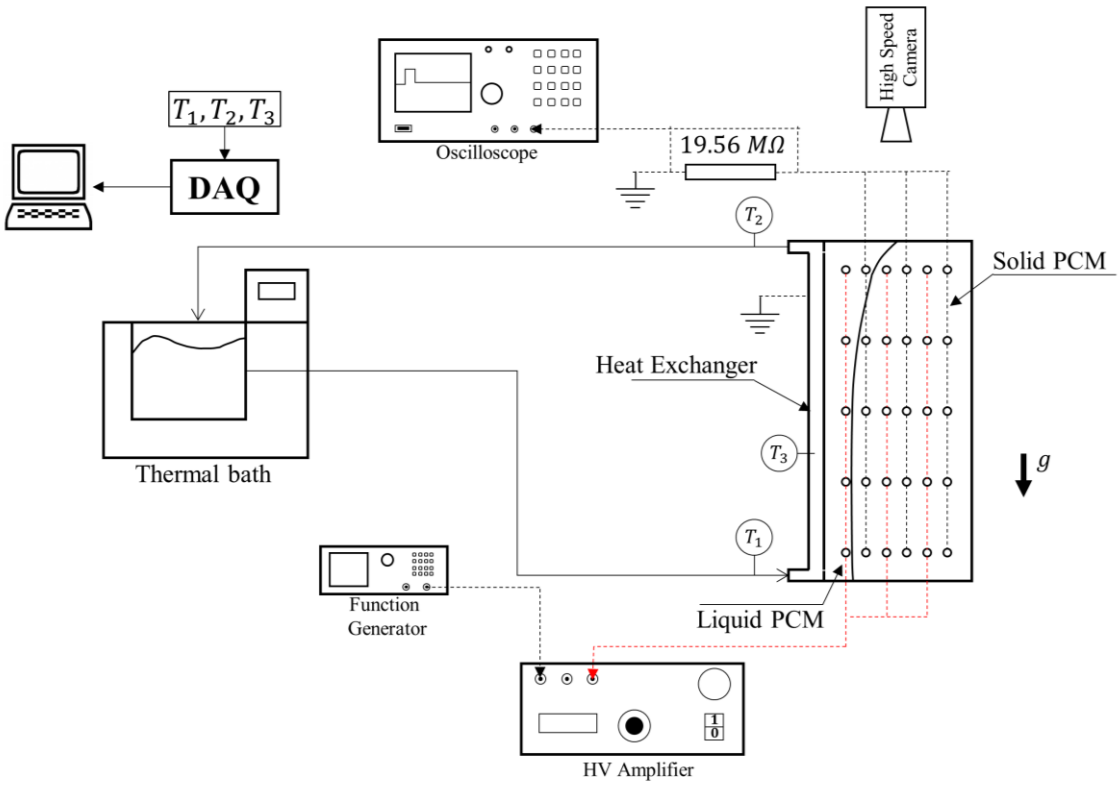

Figure 4.4 Convection dominated melting experimental facility

melting but as the melt front moves away from the heat exchanger, the buoyancy force starts to overcome the viscous resistance of the fluids and natural convection cell starts to appear within the vicinity of the liquid PCM. This experimental rig allowed for the study of the melting of PCM from an isothermal vertical wall under both gravitational and electrical forces.

Figure 4.4 shows the layout for the convection dominated melting experimental facility. The PCM was encapsulated between 0.5-inch thickness acrylic and an aluminum heat exchanger. The dimensions of the heat exchanger were 390 mm in height 100 mm in width. The heat exchanger was connected to RTE-10 NESLAB thermal controlled bath to adjust the setting temperature. The heat exchanger had three T-type thermocouples that were connected to the DAQ. The three thermocouples were inserted at the inlet, outlet and the body of the heat exchanger. The thermocouples were calibrated against DP251 precision RTD with reported accuracy of ± 0.05 ℃ and were connected to the 16 channels NI9215 data acquisition card.

An external cold junction made from an ice bath was used to minimize the DAQ uncertainties accompanied with the embedded cold junction compensation in the DAQ. The reported final accuracy of the thermocouples was 0.3 ℃. The mass flow rate of the working fluid from the thermal bath to the heat exchanger was kept high enough to maintain a maximum temperature drop between the inlet and the outlet of the heat exchanger of 0.3 ℃.

The inner dimensions of the test cell of the PCM were 120 mm in height, 50.5 mm in width and 100 mm in depth. The acrylic side walls were fastened to the heat exchanger with stainless steel screws. Viton gaskets were used in between the acrylic side walls and the aluminum body of the heat exchanger for sealing. Viton was chosen for its chemical compatibility with oils and paraffin despite of its expensive price. Other gaskets were tried before Viton as: natural rubber and silicon but were found to be non-compatible with Octadecane and changed the characteristics of the PCM. The design of the cell facilitated

the changing of the acrylic side panels with different ones of different lengths and different electrodes configuration for future testing.

The sides and the bottom of the PCM test cell were all insulated with 3-inch thickness glass wool insulation to minimize the heat losses to the surroundings. The top side of the PCM was not enclosed by acrylic walls, but rather a 20-mm air gap was left to allow for the expansion of the PCM as it melts. The air gap was closed on top by 5-inch glass wool insulation. The heat exchanger and the PCM assembly were then clamped to a solid Aluminum fixture stand mounted on top of a high precision optical table. The optical table dimensions were 44 x 32 inch and also used for the optical mounts.

The test facility was complemented with a novel shadowgraph heat transfer measurement method to measure the temperature gradient along the heat exchanger surface. The details of the shadowgraph setup is explained in section 4.2.3 in detail.

The electric field was produced by 30 cylindrical electrodes made of Brass. The electrodes were 3.2 mm (1/8-inch) in diameter and 109 mm in length. Half of the brass electrodes were connected to TREK 20/20C high voltage amplifier and the rest were grounded and connected to the ground terminal for the high voltage amplifier along with the heat exchanger body which was also grounded. The high voltage amplifier input signal was acquired from Tektronix AFG 3021B function generator. The electric current through the grounded electrodes was calculated by measuring the voltage across a 19.56 $M\Omega$ resistance connected between the electrodes and the ground side. The maximum voltage drop across the resistance was found to be 25 V which is less than 1.25 % of the minimum input voltage to the high voltage electrodes. The two terminals of the resistance were

connected to a BNC cable and the other side was connected to the Agilent DSO-X-2014A oscilloscope for real time monitoring and logging of the data.

A high-speed camera Photron SA4 was used for capturing both the melt front location and the shadowgraph images. The high-speed imaging was essential for the shadowgraph images in case of the EHD and was used for ion mobility measurement experiments. The three devices: function generator, high speed camera and the oscilloscope were all synchronized through the function generator trigger.

4.2.2 Test Cell

The test cell which encapsulated the PCM was created from acrylic side panels that can be mounted to the aluminum heat exchanger. The side panels design allowed for the flexibility to change the cell height, electrodes geometry and configuration if needed. The current design can accommodate up to a cell height of 350 mm, which may be needed for testing at high gravitational Rayleigh number ($\sim 10^9$). The maximum tested gravitational Rayleigh number in the course of this work was (1.8×10^8) at a cell height of 100 mm.

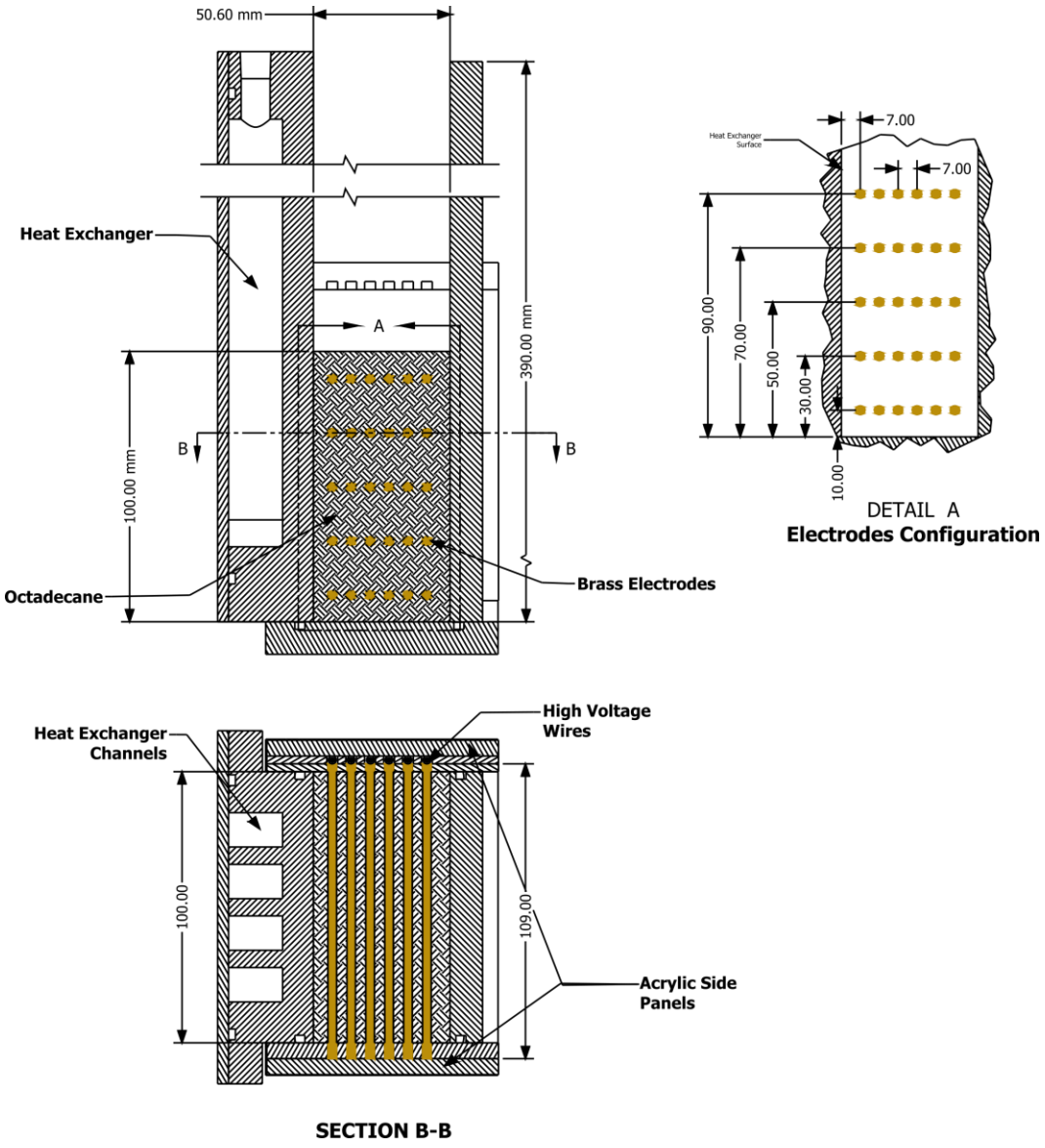

Figure 4.5 Test cell section and electrodes configuration

The Brass electrodes were maintained within the acrylic enclosures without any protrusion outside the cell. This was desired to minimize the heat losses from the test cell through the electrodes to the surrounding. The thirty Brass electrodes were arranged in a rectangular array of 5 rows by 6 columns. The vertical spacing between the rows was 20

mm and the horizontal spacing between the columns was 7 mm. The array was positioned away from the bottom acrylic panel by 10 mm and from the surface of the heat exchanger by 7 mm. Figure 4.5 shows a section in the test cell and the details of the electrodes configuration. The electrical wiring was all kept inside the acrylic side panels and then up through the sides to the connectors.

4.2.3 Optical test setup

This section illustrates the details for the optical setup of the novel shadowgraph technique used in this work for measuring local temperature gradients and thus local heat transfer coefficients along the surface of the heat exchanger. Shadowgraph, like other optical heat transfer measurement method as Schlieren and Interferometry, relies on sensing the disturbance in a refractive index for transparent media. These perturbations in the refractive index could be caused by the slightest changes in the density of the fluid which could be induced by for example: thermal gradients, turbulence (mixing), change in concentration and shock waves.

In such cases, the rays of light no longer travel in straight line when faced with spatial gradients in index of refraction, but rather refracts away from lower index of refraction to higher one regions. In case of thermal gradients, this will translate to refracting away from higher temperatures towards colder regions.

The basics and the physics behind these techniques are well established in literature [96], [97]. These techniques offer unique advantages over other measurement techniques, in being non-intrusive and highly sensitive methods to small temperature variations. The non-

intrusiveness advantage was distinctly desired in this work to minimize electric field interference by measurement probes.

Shadowgraphy was used before in studying the melting process of organic PCMs [98], [99], however the methodology and the setup used in the current research is different than the existing ones in literature.

A common shadowgraph setup will consist of a point source for light and a collimating lens that project a parallel beam of light into the test section. As the light travels parallel, yet touching the heat source surface it bends away and the refracted light is projected on a screen. The projected shadow image is then used as a representation for the temperature gradient on the surface of heat source.

The new shadowgraph system used in this research is different than the one described above. The new system used a collimated sheet of laser with a defined thickness instead of a beam of light. The collimated projected sheet deflects away from the heat source surface and also distorted. Both of the sheet local maximum deflection and distortion were used for better temperature gradient estimation than the existing method used in literature. The shadowgraph system data reduction will be presented in more details in the data reduction section. The derivation of the new shadowgraph correlation and comparison to the methods used in literature are discussed in detail in Appendix B.

Figure 4.6 shows the shadowgraph optical setup used in the experiments. The top section represents a front view for the assembly and the bottom one is a top view. The optical setup consisted of: a collimated red laser module of Class 3R from ThorLabs [CPS635], a Plano-

Concave (PCV) cylindrical lens, a Plano-Convex (PCX) condenser lens, a screen and a high-speed camera.

A collimated laser beam of 1 mm in diameter is projected to the PCV lens and a divergent laser sheet is formed. The divergent sheet passes through the PCX lens and a collimated laser sheet is then produced and pass through the test section parallel, yet touching the surface of the heat exchanger. The refracted sheet exits the test section and is projected on a screen where the sheet's maximum displacement and distortion are recorded using the high-speed camera. The distance between the two lenses (PCX and the PCV) were adjusted according to their focal lengths. The focal length of the PCV lens is -6.4 mm and that of the PCX lens is 250 mm and its diameter is 125 mm which is equal to the length of the collimated sheet at the entrance of the test section.

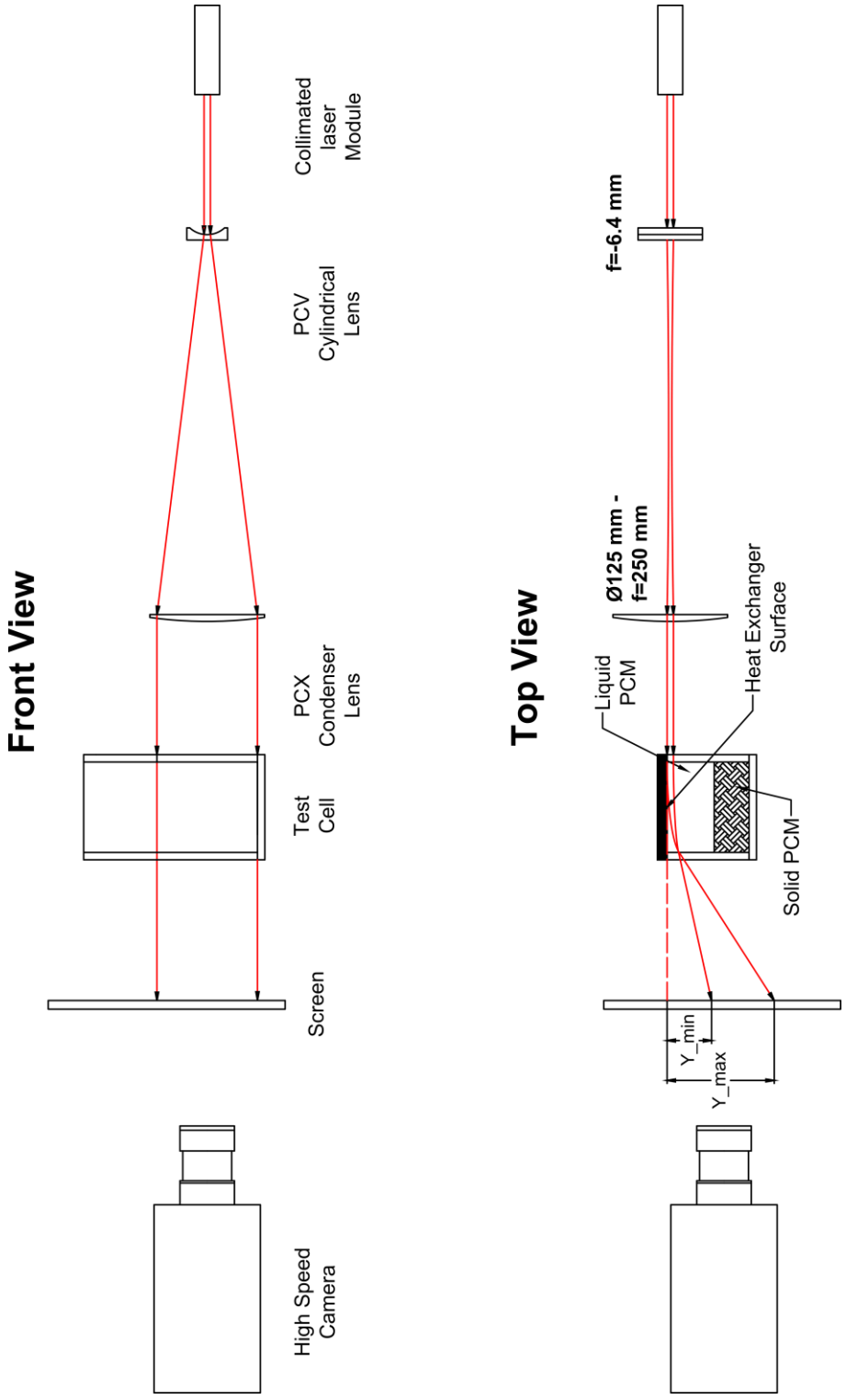

Figure 4.6 Shadowgraph optical setup

4.2.4 Experimental procedures:

The experimental procedures for this test section were different from those described for the steady state rig [conduction dominated melting experimental facility]. The fact that this facility was designed for unidirectional melting or solidification made the preparation for the experiments more time demanding than the previous experimental facility. The following steps were taken before running each experiment.

a) Molten Octadecane was poured slowly into the test section up to the desired height of the next experiment for the first time in operating the experimental rig. Otherwise, the level was only adjusted by syphoning the excess molten Octadecane from the previous experiment till the level is adjusted for the next experiment
b) The thermal bath temperature was adjusted at 18 ℃ and the test cell is left to solidify over the night for at least 18 hours
c) The top surface of the solidified Octadecane formed a convex shape due to the volumetric contraction accompanying the uni-directional solidification
d) Molten Octadecane was then poured gradually to fill in the cavity formed by the contraction, thus restoring the rectangular shape of the test section
e) The previous step lasted for 6 hours until the newly poured molten Octadecane was solidified as the rest of the sample
f) The thermal bath temperature was then adjusted to 27 ℃ which corresponds to 1 degree of initial subcooling for the Octadecane

g) The thermal bath was left running at this temperature for at least 18 hours before the next experiment took place to ensure uniform temperature distribution in the whole PCM. After this step the cell was ready for the next experiment

h) The thermal bath temperature was then adjusted to the desired temperature boundary condition for the experiment

i) Every 20 minutes the HV supply was turned off twice. The first time is to remove the insulation and turned on again right away to allow for solid/liquid interface, shadowgraph visualization and the second time is for putting back the insulation after capturing the images. The turn off time of the HV supply for both cases were less than a minute.

j) The electric current through the grounded electrodes was measured along with the previous step through the oscilloscope

4.2.5 Experimentally measured parameters and Data Reduction

The following section deals with the experimental measured parameters and the data reduction associated with melt fraction calculation, local and average heat transfer coefficients.

The main experimental measured parameters were:

1) Solid/ Liquid interface temporal shapes
2) Laser sheet maximum and minimum displacement [Sheet distortion]
3) Heat exchanger inlet, outlet and body temperature

4) Electric current through the grounded electrodes

5) The input electrical voltage

4.2.5.1 Melt fraction

The recorded shape of the solid/liquid interface was used to estimate the molten fraction at each instant of time. The images were converted from gray scale images to binary images to identify the difference between the liquid and the solid phases using the image processing software Digimizer™. The images were correctly scaled according to the dimensions of the test cell and the solid/liquid interface coordinates were then acquired. The statistical error in estimating the location of the solid liquid interface was found to be less than ± 0.1 mm based on the image resolution.

The melt mass fraction can be evaluated by integrating over the area of the solid Octadecane as

$$MF = 1 - \frac{\int_0^H \left(W - x_{s/L}\right) dy}{W \times H} \tag{4.10}$$

The value of the integral in equation (4.10) was calculated by trapezoidal integration from the coordinates as

$$\int_0^H \left(W - x_{s/L}\right) dy = \sum_{1}^{i=end} 0.5 \left(2W - x_{i_{s/L}} - x_{i+1_{s/L}}\right) \left(y_{i+1_{s/L}} - y_{i_{s/L}}\right) \tag{4.11}$$

4.2.5.2 Local heat transfer coefficients

The measurement from the shadowgraph technique was used to estimate the local temperature gradient along the heat exchanger surface. The exact derivation of the shadowgraph method used in this work is explained in details in Appendix B. The images of the shadowgraph were processed using MATLAB ™ by binarizing the image first then extracting the sheet maximum displacement and minimum displacement.

As the beam of light passes parallel to the heat exchanger, it bends away towards the colder region as it moves inside the test cell. If the temperature profile within the vicinity of the beam path is linear, the rays in the collimated laser sheet will always experience the same temperature gradient and the collimated sheet will not get distorted (i.e. the laser sheet thickness before and after the test section is the same). However, if the sheet is distorted at the exit of the test section, this is due to the non-linear temperature within the sheet trajectory. In case of assuming a quadratic temperature profile in the sheet trajectory path, the beam distortion (δ) is only dependent on the second order coefficient (a_0)(the slope of the first order derivative) and the sheet thickness (Δ). The beam distortion is defined as the difference between the maximum and the minimum deflection.

$$\delta = Y_{max} - Y_{min} \tag{4.12}$$

The local temperature gradient at the wall is a function of the sheet maximum displacement at each point and the corresponding sheet distortion. [Refer to Appendix B].

$$\frac{dT}{dx} = -\frac{2a_0 Y_{max}}{\left[\frac{\delta}{\Delta} + 1\right]} \tag{4.13}$$

The local heat transfer coefficient at each point is calculated by energy balance between convection and conduction at the surface of the heat exchanger and using the hot wall temperature and the melting point of Octadecane as the temperature difference

$$h = \frac{2ka_0 Y_{max}}{\left[\frac{\delta}{\Delta} + 1\right](T_w - T_m)} \tag{4.14}$$

The non-dimensional Nusselt number in this case was estimated based on the cell height. However taking into account an average thickness of the liquid fraction is more of an appropriate length scale but due to the transient nature of the problem, the fixed cell height is usually preferable to be used as established also in literature [24].

$$Nu = \frac{2Ha_0 Y_{max}}{\left[\frac{\delta}{\Delta} + 1\right](T_w - T_m)} \tag{4.15}$$

Chapter 5 Conduction dominated melting under EHD forces

This chapter investigated the melting of Octadecane in the conduction dominated melting experimental facility (Horizontal configuration. The effect of high voltage DC and AC waveforms on the melting will be examined in this chapter.

The chapter is presented in the same form as the recently published paper *"D. Nakhla, E. Thompson, B. Lacroix, and J. S. Cotton, "Measurement of heat transfer enhancement in melting of n-Octadecane under gravitational and electrohydrodynamics (EHD) forces," J. Electrostatics, vol. 92, pp. 31–37, Apr. 2018 ".10.1016/j.elstat.2018.01.004*

The introduction and the descriptive part of the experimental facility in the mentioned paper are not presented here in this chapter to avoid any repeatability for the sake of the reader. The experimental facility was explained in detail in the previous chapter.

5.1 Verification of the experimental facility

Before starting the EHD tests, the accuracy of the experimental rig was verified by conducting energy balance on the solid/liquid interface. Four experiments were conducted for different temperature combinations between the hot and the cold heat exchanger and the results of these experiments were used for verifying the experimental methodology.

At steady state and assuming no heat losses, the heat passing through the liquid phase is equal to that passing through the solid phase. Without EHD forces, the only heat transfer mechanism is conduction in both the liquid and the solid phase, because of the orientation of the test cell which promotes a thermally stratified liquid phase. The energy balance can be formulated in this case as

$$k_L \frac{T_h - T_m}{S_0} = k_s \frac{T_m - T_c}{H - S_0} \tag{5.1}$$

Where $(S_0)$is the solid/liquid interface location at 0 kV steady state measured from the top heat exchanger, (k_L) is Octadecane's liquid thermal conductivity which is equal to $0.152\ W/mK$, (k_s) is the solid thermal conductivity and is equal to $0.358\ W/mK$ [19] and (H) is the spacing between the two heat exchangers and is equal to 40 mm. Therefore,

$$S_0 = H\left(1 + \frac{k_s(T_m - T_c)}{k_L(T_h - T_m)}\right)^{-1} \tag{5.2}$$

From equation (5.2), it is evident that the location of the solid/liquid interface at steady state is only dependent on the thermal conductivity ratio of the solid and the liquid PCM (k_s/k_L) and ratio between the temperature difference between the hot side and the melting point to that of the difference between the cold side and melting point.

Figure 5.1 shows the results for the experimental melt thickness of the tested validation cases against the temperature dimensionless group. Four test cases were conducted that covered a range of different melt thicknesses from 7 mm up to 23 mm. Figure 5.1 shows that the experimental steady state melt thickness agreed well with the analytical correlations

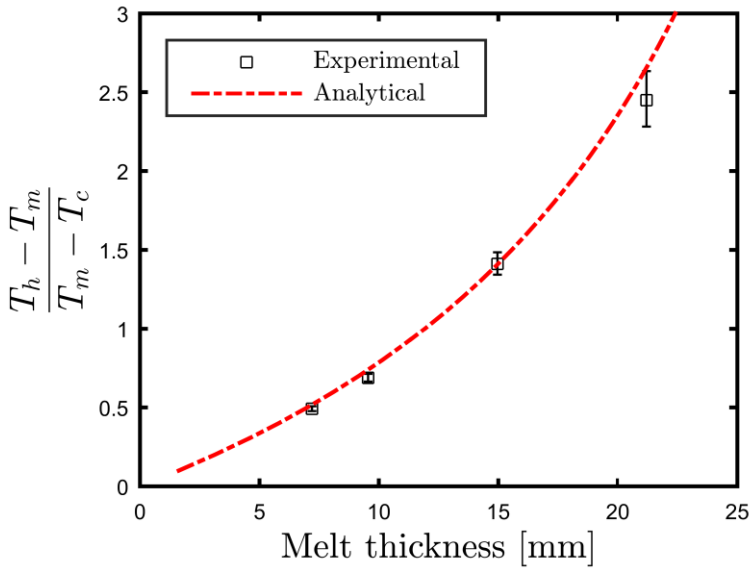

Figure 5.1 Experimental rig verification through energy balance

within the experimental uncertainty, thus verifying the adequacy of the assumptions and the methodology used in quantification of the heat fluxes in both liquid and solid phases. The higher experimental uncertainty around the 20-mm range of melt thickness is mainly attributed to the higher percentage error in the cold side temperature difference as the melt thickness increases.

Table 5.1 Test Matrix

T_h [°C]	T_c [°C]	V [kV]	Waveform	Case
40	3.6	0	N/A	1
35	18	0,8 and 10	DC [-]	2
40	10.8	0,4,6,8 and 10	DC [-]	3
40	10.7	10	Square	4
40	19.5	0,4,6,8 and 10	DC [-]	5

Table 5.1 shows the test matrix for the conducted tests. Each combination of temperature boundary conditions and wave-forms was given a case number to facilitate referencing from here after.

5.2 Experimental Results

5.2.1 DC Experiments

The first test cases were conducted to understand the effect of negative DC voltages. The tests were conducted also at different hot side temperatures to understand the effect of the heat flux on the EHD enhancement and the nature of charge creation inside the Octadecane PCM.

Before EHD testing, every test case was conducted in the following manner:

a) The Octadecane was completely molten first and poured slowly into the test chamber and then the temperatures for both the heat exchangers were set at higher temperatures than the melting point to allow for the escapement of entrapped air bubbles.
b) The cold heat exchanger was then set to the desired operating temperature and the hot heat exchanger was adjusted to 29 ℃ [1 ℃above the melting point]. This allowed for a uni-directional solidification to start from the bottom heat exchanger and progress upwards to the hot heat exchanger.

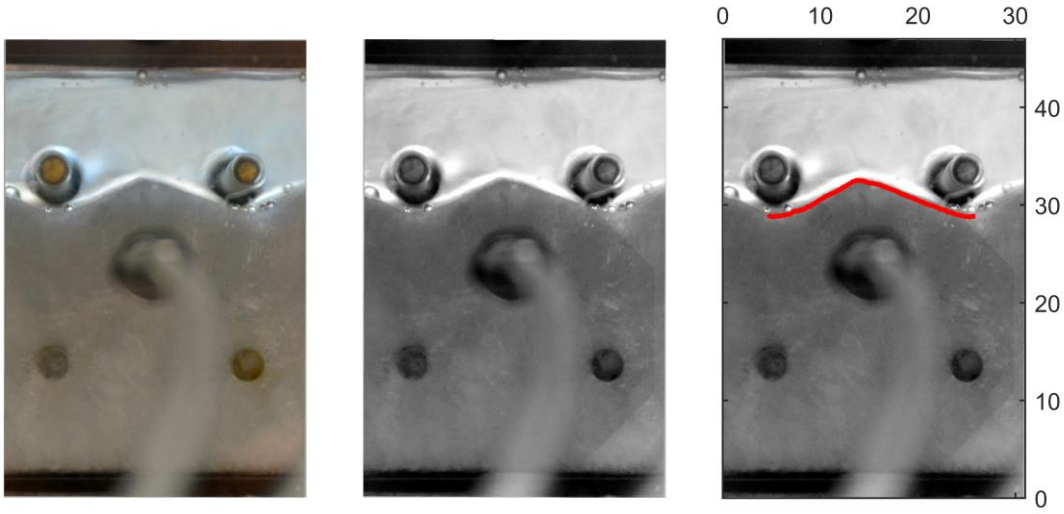

Figure 5.2 Interface digitization procedures

c) The hot heat exchanger was then set to the desired temperature for testing and the melting front progress is captured with a time lapse camera until the solid-liquid interface reaches the steady state position.

d) Steady state position is estimated when the melt front stays stationary for a period of at least 1 hour.

e) After that the high voltage amplifier is turned on to the desired voltage for testing and the melt front starts to progress again until a new steady state is achieved.

The experiments were conducted by starting from 0 kV and then gradually increasing the voltage to the desired values and capturing the steady state correspondent to each voltage.

Figure 5.2 shows an example for the interface digitization procedures taken from Case 3, at 4 kV and after 46 minutes. The Octadecane's interface is clearly visible owing to the

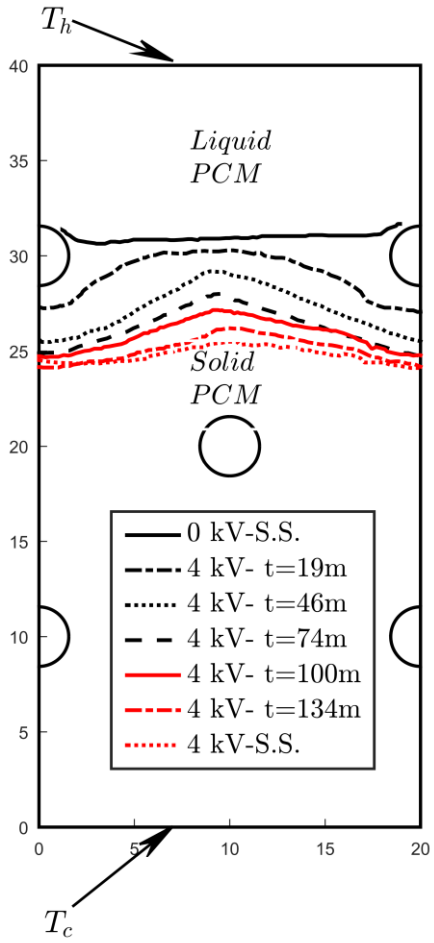

Figure 5.3 Case 3 solid/liquid interface location progress

different opacity of the liquid and the solid phase. The images were first converted from RGB to grayscale images and then Digimizer image analysis software was used to capture the solid/liquid interface.

Figure 5.3 shows the melt front progress with time for Case 3, starting from a 0 kV steady state (S.S.), then applying 4-kV until a new steady state is achieved. At the start of the experiment at 0 kV, the solid/liquid interface is seen parallel to the two heat exchangers

indicating an initially pure conduction heat transfer mode without EHD due to the thermal stratification.

As the 4 kV is applied, the solid/liquid interface starts to progress downwards, however the interface contour changes from being parallel to the heat exchanger to a wavy interface. The flow visualization showed a disturbance in the liquid Octadecane indicating the presence of strong electro-convection cells in the bulk of the molten Octadecane. Observation of the flow during the transition to the new steady state also revealed that for the first 45 minutes, the interface moved faster around the electrodes than the surrounding regions. This could mean the possibility of an ion injection behavior from the high voltage electrodes. In such case, the high voltage electrodes produce free ions in the dielectric liquid around the electrode of the same polarity, which in turn induces a jet-like structure initiated from the electrodes and moving towards the grounded electrode, thus impinging on the solid/liquid interface. This act of jet impingement will lead to the highest heat transfer enhancement in the regions around the electrodes where the velocity of the jets is the highest [67].

As time progresses the interface flattens until it reaches the new steady state for the EHD case. In this new steady state case, the solid/liquid interface moved towards the cold heat exchanger by almost 7 mm from the 0-kV initial steady state, and happened within the course of 3 hours.

Figure 5.4 shows the melt thickness variation with the different applied voltages for four cases. It is found that as the electric potential increases, the melt thickness increases for all cases except for Case 4. In Case 2 and Case 3 the melt thickness increased by almost 10

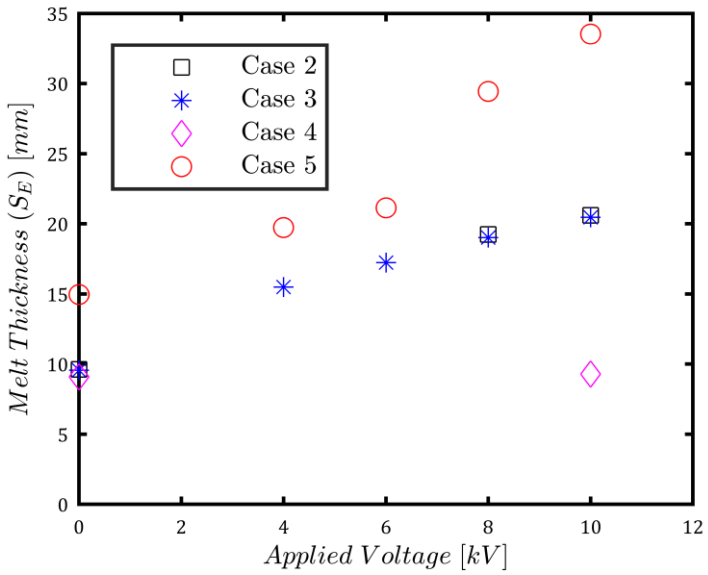

Figure 5.4 Steady state melt thickness vs. applied voltage

mm by increasing the voltage from 0 kV to 10 kV and for Case 5, the melt thickness was increased by 17 mm.

Although Case 2 and Case 3 have the same initial steady state at 0 kV, they have different temperature boundary conditions and inherently different fluxes. It is found that the melting thicknesses for both Case 2 and Case 3 are nearly identical for each applied voltage tested despite their different temperature gradients.

This result is an indication that the role of the dielectrophoretic forces in the liquid Octadecane could be minimal compared to the other EHD forces at such temperature gradients, since the dielectrophoretic forces in the liquid would depend mainly on the temperature gradients $\left(-\frac{1}{2}E^2\frac{d\varepsilon}{dT}\nabla T\right)$ as long as the electric field between the different

cases was kept the same Thus, in turn it is either the Coulomb forces or interfacial forces that play the major role in the enhancement mechanism.

The average Nusselt number at the hot heat exchanger can be calculated from the energy balance. Nusselt number is a dimensionless quantity which is defined as the ratio between the conduction thermal resistance in the liquid phase (S_E/k_l) to the convection thermal resistance induced by the EHD forces $(1/h)$. The ratio between these two thermal resistances will be equivalent to the ratio between the heat transfer by convection to that by conduction through the liquid phase, if the absolute temperature difference $(T_h - T_m)$ is considered as the driving temperature for both the conduction and the convection.

In this case, the augmented heat transfer [convection] (Q_{EHD}) from EHD can be calculated from an energy balance at the interface for the EHD steady state case (S_E)

$$Q_{EHD} = k_s \frac{T_m - T_c}{H - S_E} \tag{5.3}$$

And the conduction heat transfer is the theoretical heat conduction through the liquid phase at the EHD steady state

$$Q_{cond} = k_l \frac{T_h - T_m}{S_E} \tag{5.4}$$

And the Electric Nusselt number can be derived from equation (5.3) and equation (5.4) as

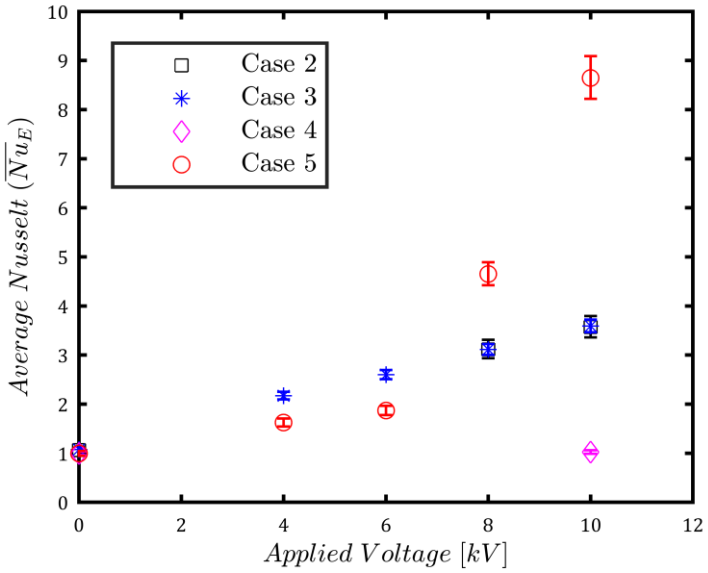

Figure 5.5 Average Nusselt number at the hot heat exchanger vs. applied voltage

$$\overline{Nu_E} = \frac{k_s(T_m - T_c)\, S_E}{k_l(T_h - T_m)(H - S_E)} \tag{5.5}$$

Figure 5.5 shows the average Nusselt number at the hot heat exchanger surface for the three cases. For Case 2 and Case 3 the average electrical Nusselt number was the same at different applied voltages, with the highest value at the 10 kV and is equal to 3.5. The Nusselt number increased almost linearly with the voltage for these two cases. By looking at Case 5, one sees that the Nusselt number first increases with a lower slope than that of Case 2 and Case 3 and then the slope rapidly increases once it crosses the 6-kV potential. The Nusselt number in Case 5 reaches a maximum of 8.6 ± 0.4 which is a substantial heat transfer augmentation.

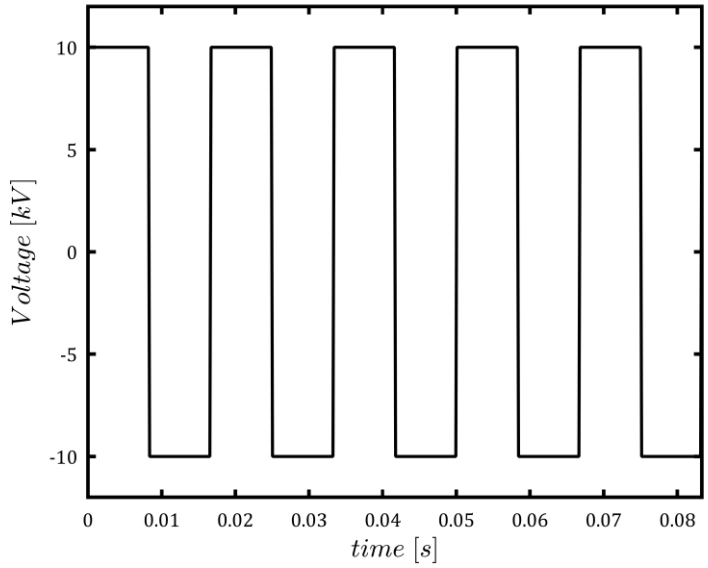

Figure 5.6 The applied square wave in Case 4

5.2.2 AC Experiments

To identify the contribution of the dielectrophoretic forces, whether in the bulk of the molten PCM or at the solid/liquid interface, Case 4 experiment was conducted where a symmetric square wave of 10 kV with an average of 0 kV was applied under the same temperature boundary conditions as that of Case 3[Refer to Figure 5.6]. A symmetric square waveform will maintain the RMS value for the voltage at the same level as that for the DC [100] without altering the maximum voltage applied. By applying a square wave form with a frequency that is higher than the charge relaxation time, this will not allow the formation of charges in the bulk of Octadecane. The cycle duration for the square wave was chosen to be orders of magnitude smaller than the charge relaxation time (τ_e) and the viscous time scale (τ_v) for Octadecane [101].

A square wave with frequency of 60 Hz was found to be adequate in such case.

$$\tau_e = \frac{\varepsilon}{\sigma} \sim 1000\ s \tag{5.6}$$

$$\tau_v = \frac{d^2}{\vartheta} \sim 10s \tag{5.7}$$

Investigating the results for Case 4 in Figure 5.4 and Figure 5.5, it is evident that there was almost no effect for applying the 10 kV square wave on enhancing the heat transfer process. The melt thickness only increased by 0.25 mm [close to the bounds of the experimental uncertainty] compared to the 11-mm increase for Case 3 under 10 kV DC.

5.3 Discussion

The results for the DC and the AC experiments give insight about the EHD enhancement mechanisms in the melting of Octadecane. The AC experiments [Case 4 -square wave form] showed almost no heat transfer enhancement compared to the DC experiments carried under the same voltage and the temperature boundary conditions. The AC results mean that the contribution of the dielectrophoretic forces toward the overall heat enhancement is negligible. This conclusion is valid for either the dielectrophoretic forces acting in the bulk of the molten Octadecane due to temperature spatial gradients or at the interface between the solid and the liquid phases due to the difference in the electric permittivity between the two phases. These AC results indicate that the Coulomb forces are responsible for the main mechanism of heat transfer enhancement under the tested voltages. This observation (under the application of AC field) in combination with the earlier

findings by Nakhla et al [12] where the solid extraction phenomenon was first identified, were used to better understand the possible mechanisms of extraction. These possible mechanisms are:

(i) Solid extraction occurs due to the accumulation of free charges at the interface. The Coulomb forces then act on the charged dendrites at the interface and remove them from the mushy zone.

(ii) Solid extraction could be due to dielectrophoretic forces acting at the interface due to the difference in the solid and liquid dielectric constants, but without the presence of EHD induced convection by Coulomb forces, limited enhancement could be achieved.

(iii) Solid extraction may not take place in Octadecane as it is considered a pure material and the existence of dendrites and mushy zone is almost absent.

In all these cases, the importance of the Coulomb force and its impact on the augmentation of the heat transfer seems to be the main driving mechanism. Further experiments with different PCMs will be needed to confirm these findings and it is the subject of future work.

In order to understand the nature of the charge carriers creation and whether they depend upon the heat flux and the spatial temperature gradients or not, Case 2 and Case 3 were conducted. Case 2 and Case 3 have the same initial steady state value (S_0) at 0 kV, however the temperature gradient for Case 3 is higher than that for Case 2. From Figure 5.4, it was found that the melt thickness relation against the electric field magnitude was almost the same for these two cases. This is an indication that the free charges created in the bulk of

the Octadecane is independent of the temperature field [68] and that an ionic injection mechanism or conduction are the two most likely mechanisms of charge creation.

To further investigate which mechanism, an estimation for the electric field distribution was acquired by solving numerically Gauss's equation assuming no free charge density in the liquid or the solid Octadecane using ANSYS Fluent solver.

$$\nabla.\left(\varepsilon\vec{E}\right) = 0 \tag{5.8}$$

$$\vec{E} = -\nabla V \tag{5.9}$$

The numerical model solved for one of the repetitive sections of the electrode arrangements. The boundary conditions were set at 1 V for the upper and lower rows of electrodes and ground conditions for the upper and lower heat exchangers and for the middle row of the electrodes. The sides of the numerical domain were set to symmetry boundary conditions. The dielectric constant for the liquid Octadecane was set to 2.06 and that for the solid Octadecane to 2.15 [102].

The contours plot is shown in Figure 5.7. The figure shows the electric field distribution for a unit potential difference applied at the electrodes. The maximum electric field regions are always near the upper and the lower electrodes. A recent study by Daaboul et al [103] studied the transition between the conduction to injection mechanism and found that the transition occurred at an electric field magnitude around 3×10^5[V/m]. Although this value would depend on the material properties, the order of magnitude in field strength is expected to be similar. In the current study, the maximum electric field around the

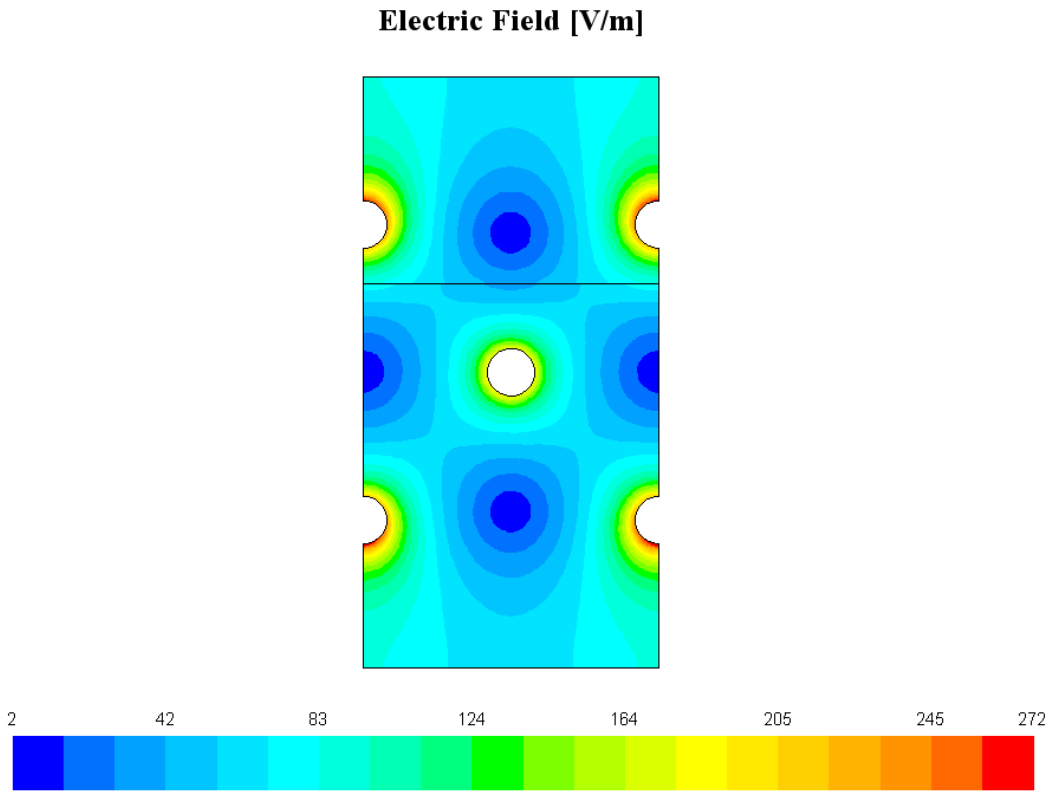

Figure 5.7 Electric field distribution (V/m) for a unit potential difference across the electrodes [S=14 mm]

electrodes at 4 kV [the lowest tested voltage] corresponds to an electric field magnitude ~10^6 [V/m] which indicates that the charge creation mechanism in this case is likely due to injection from the electrodes. In fact, a weak injection regime is the one that often occurs in non-polar dielectrics [104], however it is the least examined and understood in literature. The results require further investigation with flow visualization inside the cell to confirm the nature of Coulomb forces and estimate the velocity field around the electrodes and this is a subject for another ongoing work [The next chapter in the dissertation].

In Case 5, the hot side temperature was kept the same as that for Case 3, however the initial steady state condition at 0-kV is different with the interface location is closer to the cold heat exchanger. It was found that the Nusselt number at the hot surface is lower for Case 5 than that for Case 3 until 6-kV, this could be attributed to the thicker melt thickness at steady state (S_E) [21 mm] in Case 5 compared to that of Case 3 [17 mm] which means higher opposing gravitational forces.

Although the test cell configuration was designed to suppress natural convection effects, it is apparent that EHD forces de-stratify the system. The larger the melt thickness, the higher the stabilizing gravitational Rayleigh number $Ra \sim S^3$. After 6 kV, there is a sudden jump in the Nusselt number for Case 5. By examining the steady state melt thickness at the 6 kV point [Figure 5.4] where $S_E = 21$ mm, it is found that the solid-liquid interface starts to cross the center of the second row of electrodes (y=20 mm) [grounded]. Since, the electric field magnitude is highest around the electrodes [Figure 5.7], as the interface passes the second row of electrodes, it reveals higher electric field regions in the liquid Octadecane [Figure 5.7] which intensifies the EHD induced electro-convection cells. This revealed row of electrodes in the liquid Octadecane from this point and after, also opens a second path for the moving charge carriers in the liquid phase beyond the top grounded hot heat exchanger. The higher electric fields and the second ground path possibly augment the electro-convection cells and enhance the average Nusselt number at the wall.

5.4 Conclusion

An experimental facility was built to understand and quantify the EHD heat transfer enhancement for melting of Octadecane in a steady state environment. The EHD forces were examined under different temperature gradients and for negative DC voltages and AC square wave forms to understand and quantify the contribution of the different EHD heat transfer enhancement mechanism.

It was found that the dielectrophoretic forces contribution in the heat transfer enhancement can be neglected and that it is mainly the Coulomb forces that play the major role in the heat transfer augmentation in the investigated cases.

It was concluded that the mechanism of charge creation is independent on the temperature gradients, thus it is more likely to be a charge injection mechanism rather than a conduction mechanism.

In this examined configuration, the EHD forces worked against gravitational forces. The coupling between these two forces was manifested as a lower EHD enhancement for cells of larger thickness at the same electric potential. As the number of the revealed electrodes in the liquid region increased, the EHD Nusselt number increased significantly.

These experimental findings are crucial to the understanding of a new emerging science of using EHD as an active enhancement technique and it shows the capability of using it as a tool to control the level of heat transfer augmentation in latent heat thermal storage systems.

The electrode configuration studied here was rather simple to better elucidate the physics of EHD induced flow. Further investigation with more practical geometries, such as vertically oriented cells for example, are the next steps to understand the coupling between the gravitational and the EHD forces.

Chapter 6 Convection dominated melting under EHD forces

This chapter discuss the results of the experimental findings of melting under EHD forces for vertical configurations where the melting is initially dominated by gravitational forces.

First the melting under gravitational forces was examined without additional EHD forces and the results of these experiments were compared against previous findings in literature and underlines the understanding of the mechanisms of heat transfer under such melting problems.

Second, the melting performance was examined under EHD forces where the effect of the different parameters was studied. These parameters were: the magnitude of the applied voltage, the effect of the polarity of the applied voltage, the waveform and finally the gravitational Rayleigh number and the temperature difference.

6.1 Melting in vertical enclosures without EHD forces

6.1.1 Volume fraction experimental results

The vertical orientation experimental facility outlined in section 4.2.1 is used for these experiments. Two sets of experiments were first conducted one with the cylindrical

electrodes in place and embedded inside the Octadecane and the other one is without the presence of the 30 Brass electrodes in the PCM. These experiments project the sole effect of the presence of the electrodes on the melting performance and how it may hamper the natural convection current and/or emphasize the heat conduction effect.

The experiments conducted without applying high voltage through the electrodes are summarized in Table 6.1. Four experiments were conducted for two different Rayleigh numbers and two different Stefan numbers to understand the effect of each on the melting behavior of the PCM. The degree of subcooling in all of these experiments was fixed to 1 degree of subcooling in the initial solid phase below the melting point. It is known from previous work how is the degree of subcooling affect the melting rate, where as the degree of subcooling increases, the melting rate decreases for the same Rayleigh and Stefan number. The decline in the melting rate is caused by the fact that not all of the heat flux from the heat exchanger is effectively used in the melting of the PCM but rather a conduction heat flux from the solid/liquid interface is existent that is responsible for preheating the solid phase to the melting temperature. As this effect of subcooling is already known in literature -often referred to by Neumann solution for two region problems- it was not investigated in the current EHD experiments. Furthermore, it is not expected to have a different impact in the current investigation, specially for a material as Octadecane where the solid/liquid interface has a sharp defined melting point and the existence of a mushy zone may not be there.

The first two tests presented in Table 6.1 were carried to solely quantify the effect of the presence of brass electrodes in the PCM on the melting performance before starting any

Table 6.1 Test Matrix for non-EHD melting experiments for convection facility

Cell Height (H) [mm]	Wall Temperature (T_h)[℃]	Initial Temperature (T_i)[℃]	Stefan number (Ste)	Subcooling number (Sc)	Rayleigh number (Ra)	Electrodes/ no Electrodes
100	38	27	0.089	0.009	1.8E8	No
100	38	27	0.0089	0.009	1.8E8	Yes
100	33	27	0.0445	0.009	9E7	Yes
87.3	42.9	27	0.13	0.009	1.8E8	Yes

EHD tests. The brass electrodes held a small percentage of the volume of the PCM enclosure and they occupied exactly 4.7 % of the volume of the test cell. At such percentage, there effect on the melting performance was expected to be insignificant.

Figure 6.1 shows the timewise progress of the liquid volume fraction with and without electrodes for the first two cases presented in Table 6.1. The difference in the liquid volume fraction between the two cases is minimal with a maximum deviation of 0.03 which is less than 4 % variation. The volume fraction progress for the electrode case was slightly higher than that without electrodes. In theory, the electrodes may enhance the heat conduction phase at the beginning of the melting process, however it will have a hampering effect once the natural convection phase starts as they impose an additional viscous resistance to the flow. As shown in Figure 6.1 both effects were minimal. One way to better understand and compare between the two cases, is to look at the exact volumes for the molten Octadecane between the two cases, as this will give a better quantification to the amount of heat stored

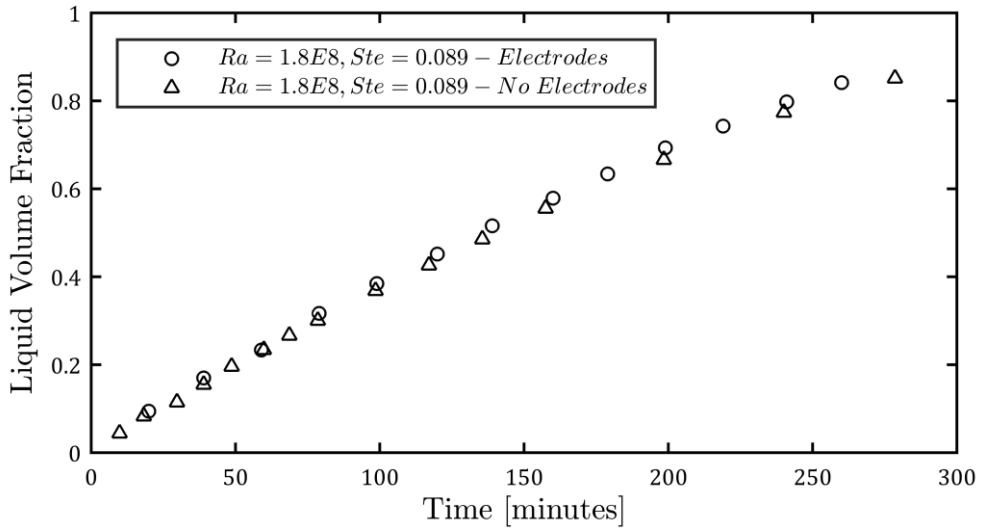

Figure 6.1 Liquid volume fraction temporal progress with and without electrodes for Ra=1.8E8, Ste=0.089 and V=0 kV.

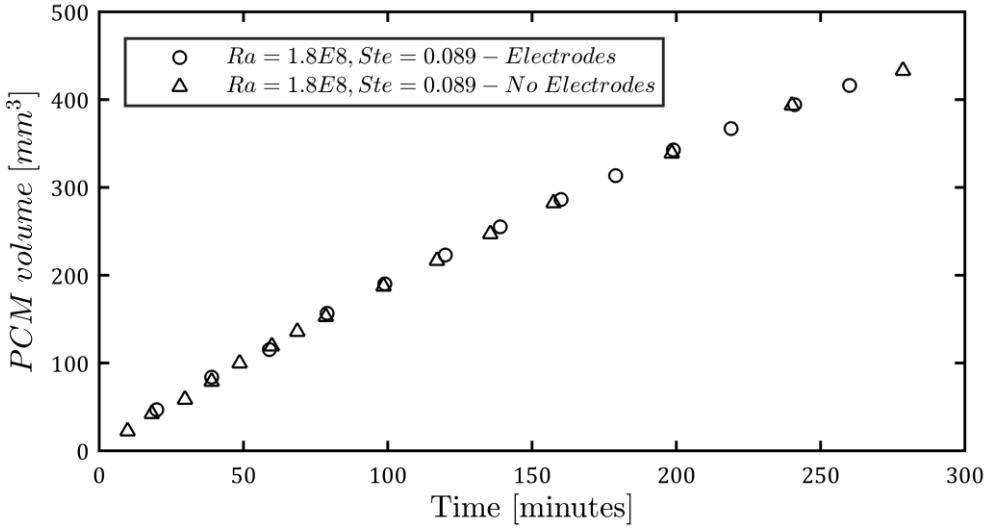

Figure 6.2 Molten PCM volume temporal progress with and without electrodes for Ra=1.8E8, Ste=0.089 and V=0 kV.

in the cell. Figure 6.2 shows the volume of the molten Octadecane for the two cases and it is clear that at the beginning of the melting up to 20 minutes from the start of the

experiments, the amount of the molten Octadecane was higher for the electrodes case due to the enhanced conduction by the brass electrodes. After 20 minutes, the timewise progress of the molten PCM volume was the same for the two cases, which indicates the slight decrease in the natural convection due to the presence of the electrodes.

Figure 6.3 and Figure 6.4 show the temporal profiles of the melt front for these two cases. From these two figures, it is clear that for the first twenty minutes the solid/liquid interface travels parallel to the heat exchanger wall indicating a predominant heat conduction regime except for the upper portion of the cell. The higher conductivity of the brass forms a less thermal resistance pass to the conductive heat permitting a higher heat transfer towards the electrodes and thus more melt compared to the surrounding region.

As time progresses, the role of the conduction heat transfer starts to diminish and the effect of density variation due to temperature gradients in the liquid octadecane starts to induce a buoyancy driven flow. The direction of rotation of this induced natural convection flow is in the clockwise direction starting from the bottom of the left wall and moves along the heat exchanger wall and then flows downwards convecting the heat along the solid liquid interface. The topmost position of the solid/ liquid interface will experience the highest temperature gradient as a cold boundary layer will start to grow on the melt front side. This will cause higher melt front velocities at the top of the cell and the tilting of the melt front away from the heat exchanger surface as seen from the figures. Figure 6.4 shows the same behavior even with the presence of the electrodes, where the melt front shape is still tilted away from the heat exchanger surface, indicating convection predominated heat transfer mode during the later stages of melting. The scoops around the electrodes are still

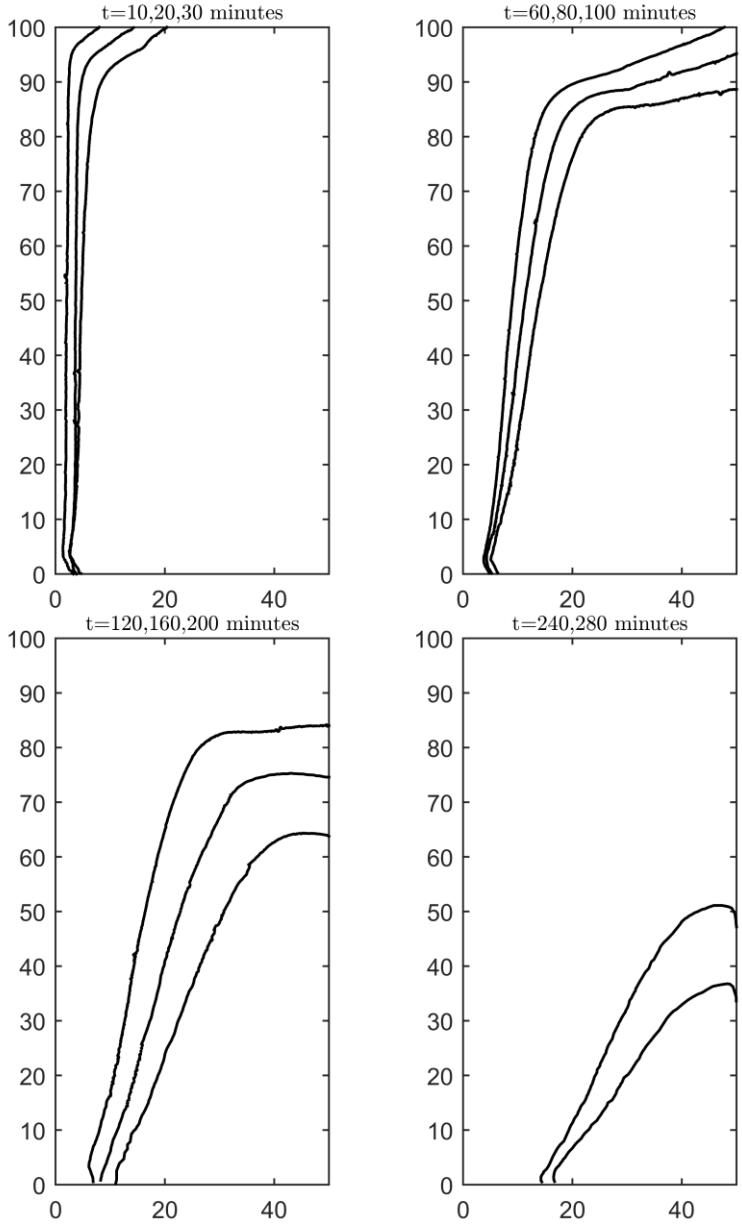

Figure 6.3 Profiles of melt front progress with time for Ra=1.8 E8, Ste=0.089

obvious but their existence is limited only to within the close vicinity of the electrodes and not along the whole span of the solid/liquid interface.

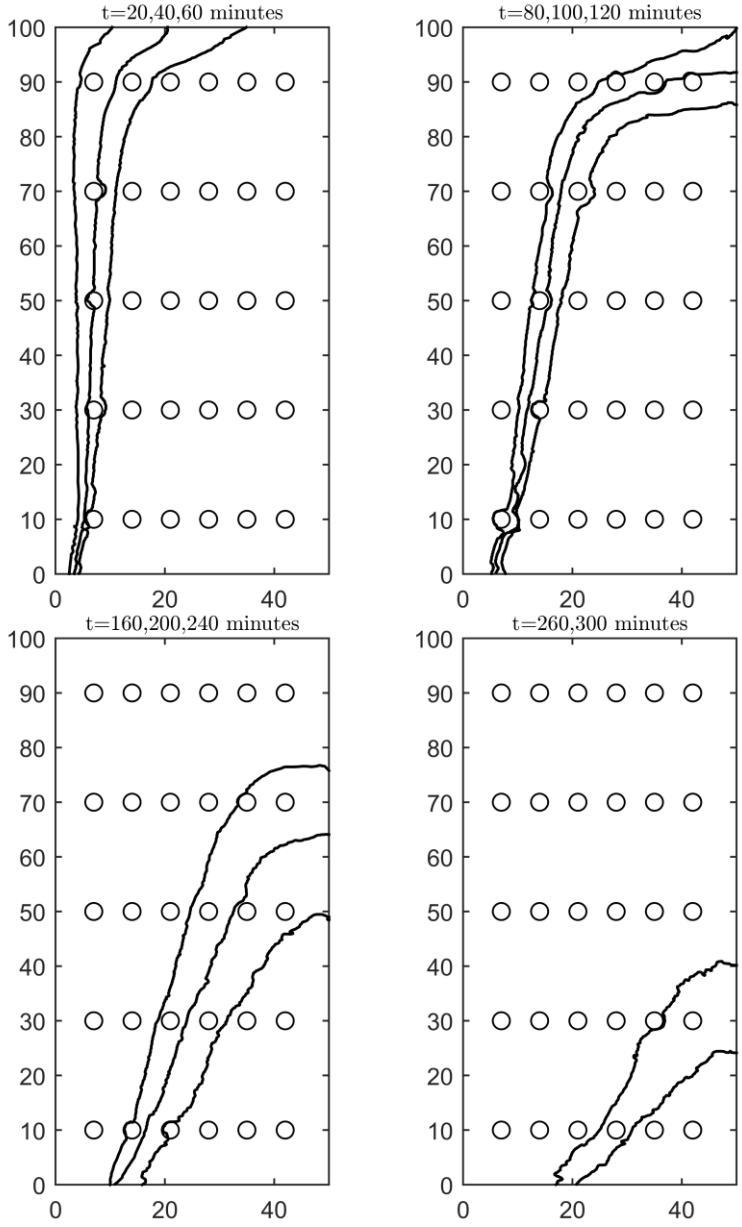

Figure 6.4 Profiles of melt front progress with time for the electrode case for Ra=1.8E8, Ste=0.089 and V=0 kV

Figure 6.5 shows the comparison between the current experimental results against the early experiments of Ho's [98] under the same conditions for a Ste=0.089 and cell height

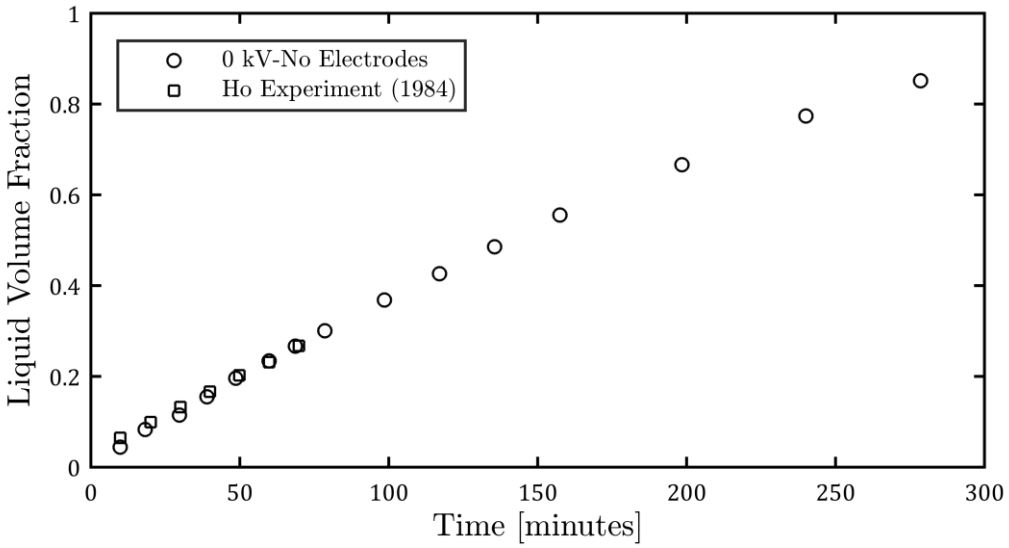

Figure 6.5 Liquid volume fraction temporal variation vs Ho's Experiment (1984) for Ste=0.089 and H=100 mm

of 100 mm and an initial 1 degree of subcooling. Ho's experiment was conducted for a short period of time- only 70 minutes- compared to the current experiment, during that period of time the melt front at the top of cell would just have reached the opposite wall to the heat exchanger. The temporal progress of liquid volume fraction between the two experiments is in a very good agreement with a deviation less than 1 % at the end of the 70 minutes period for Ho's experiment. The agreement between the two experiments provides a validation for the current experimental methodology and the experimental facility used for the EHD experiments as well.

Two additional cases were conducted for non EHD experiments to understand the effect of the Stefan number and the Rayleigh number on the melt front progress and get a better understanding for the governing dimensionless parameters. It is worth noting that the amount of experimental work in studying the melting of phase change materials under

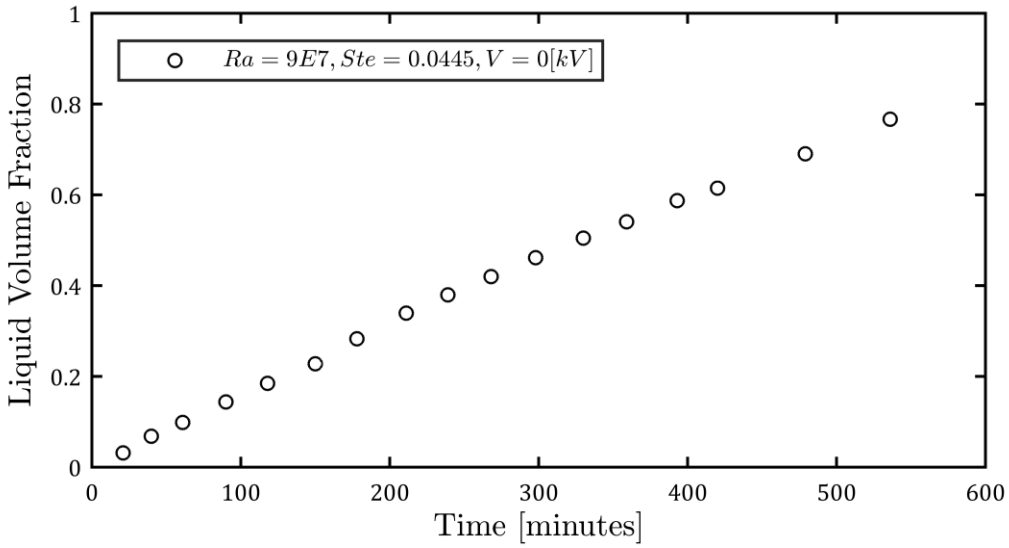

Figure 6.6 Liquid volume fraction temporal progress with and without electrodes for Ra=9E7, Ste=0.0445 and V=0 kV.

different boundary condition and aspect ratio is very limited in literature when compared to the amount of the numerical work that has recently been conducted in this field [105].

The next experimental case studied, was a case in which the left wall temperature was reduced to a temperature difference of 5 degrees between it and that of the melting temperature of the Octadecane. The cell height was kept at 100 mm as the first two cases and the corresponding Stefan and Rayleigh numbers for this case were St = 0.0445 and Ra=9E7 respectively.

Figure 6.6 shows the temporal liquid volume fraction with time for this case and it shows a similar behavior to the first two cases were the melt front velocity-depicted from the slope of the curve- is high at the beginning of the melting where conduction predominates the heat transfer. After that the slope is almost constant which indicates a constant natural

convection dominated melting and after that a decreasingly melt front velocity as the interface reaches the opposite wall and the height of the cold boundary layer decreases leading to a lower heat flux extracted from the hot side. In this case, the experiment almost took 10 hours for the molten Octadecane volume fraction to reach around 80 % compared to 5 hours for the previous two experiments.

Figure 6.7 shows the melt front profiles timewise progress for this case. The melt profiles indicate a conduction dominated heat transfer mode up to 60 minutes from the start of the experiment where the solid/liquid interface is travelling parallel to the left wall. After the 60 minutes mark, the interface starts tilting away from the left wall indicating the onset of a convection heat transfer mode along the span of the interface. After 4.5 hours, the top of the interface reaches the other side of the enclosure and the height of the solid Octadecane starts to decrease. From this point, the natural convection effect decreases due to the smaller heights of the cold boundary layer. This phenomenon of switching from conduction to convection will be explained in more details in the next section of heat transfer coefficients measurement.

The last experimental case without EHD forces conducted was for a Rayleigh number of 1.8E8 similar to the first two cases tested but this time at reduced height and a higher Stefan number [0.13] so that the aspect ratio of the enclosure is lower than the last three cases.

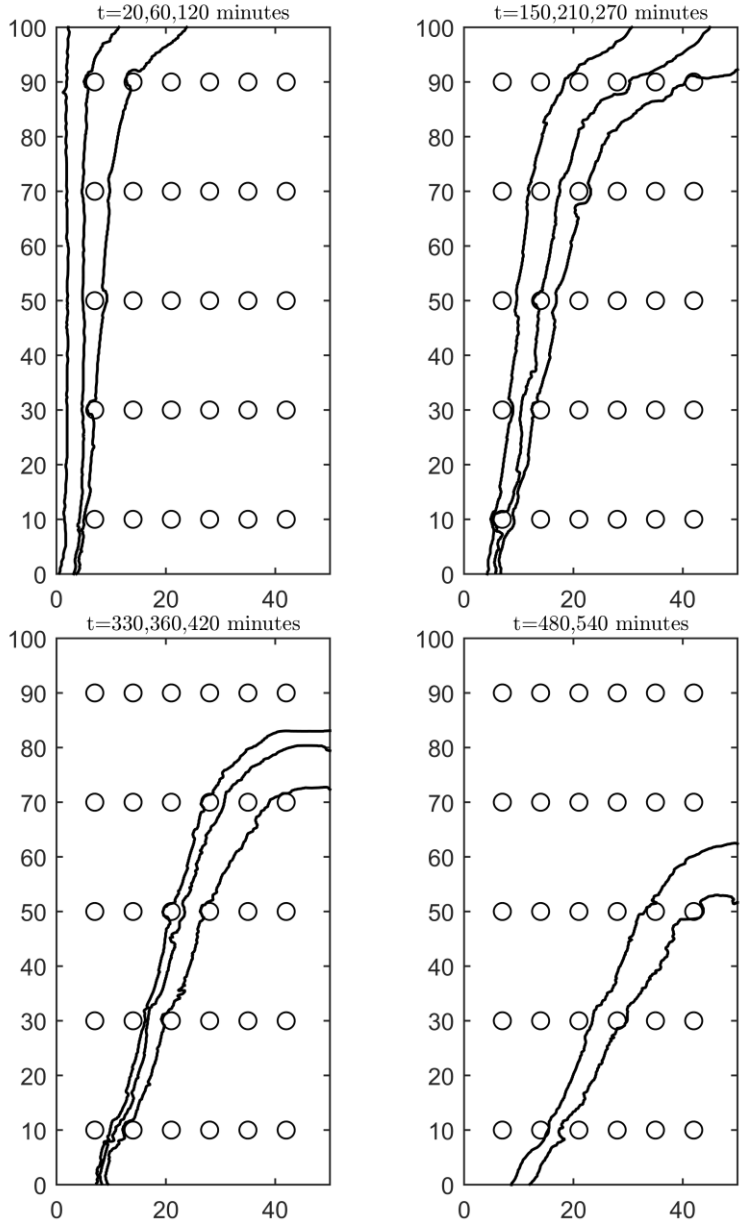

Figure 6.7 Profiles of melt front progress with time for the electrode case for Ra=9E7, Ste=0.0445 and V=0 kV

Figure 6.8 shows the temporal liquid volume fraction progress for the high Stefan number case. This time the melt fraction reached almost 90 % by 3 hours compared to 5 hours for the same Rayleigh number for the first two cases.

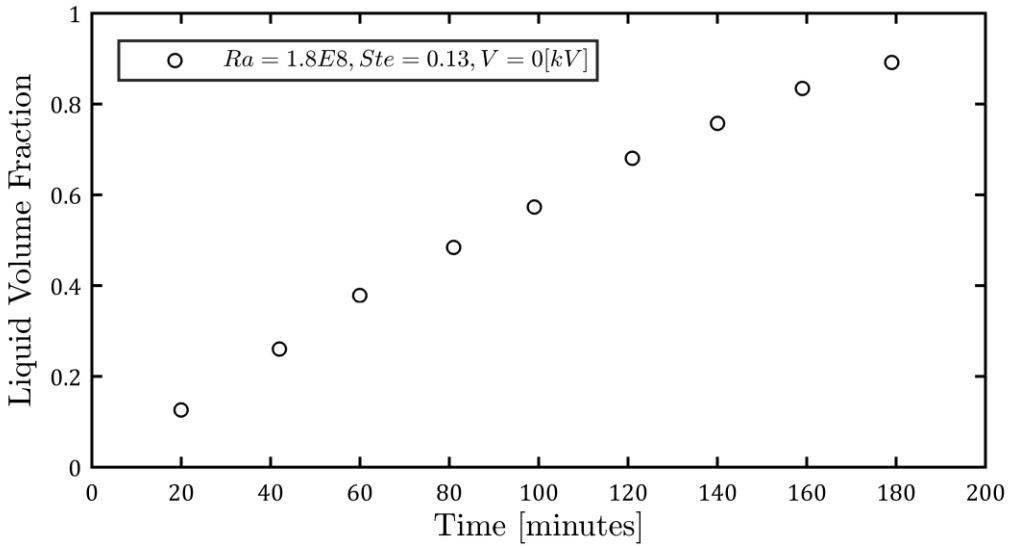

Figure 6.8 Liquid volume fraction temporal progress with and without electrodes for Ra=1.8E8, Ste=0.13 and V=0 kV.

Figure 6.9 presents the melt front profiles for the last tested non-EHD case. In this case, it is clear from the interface profiles that conduction stage ended much earlier than all other cases where at 20 minutes mark the interface is already tilted away from the heat exchanger wall. The interface reached the other wall between 40 to 60 minutes. In this experiment only 4 rows of electrodes are within the PCM compared to 5 in all other cases as the cell height was shorter than the other cases and the top row of electrodes were in the air cavity (not shown here in the figures).

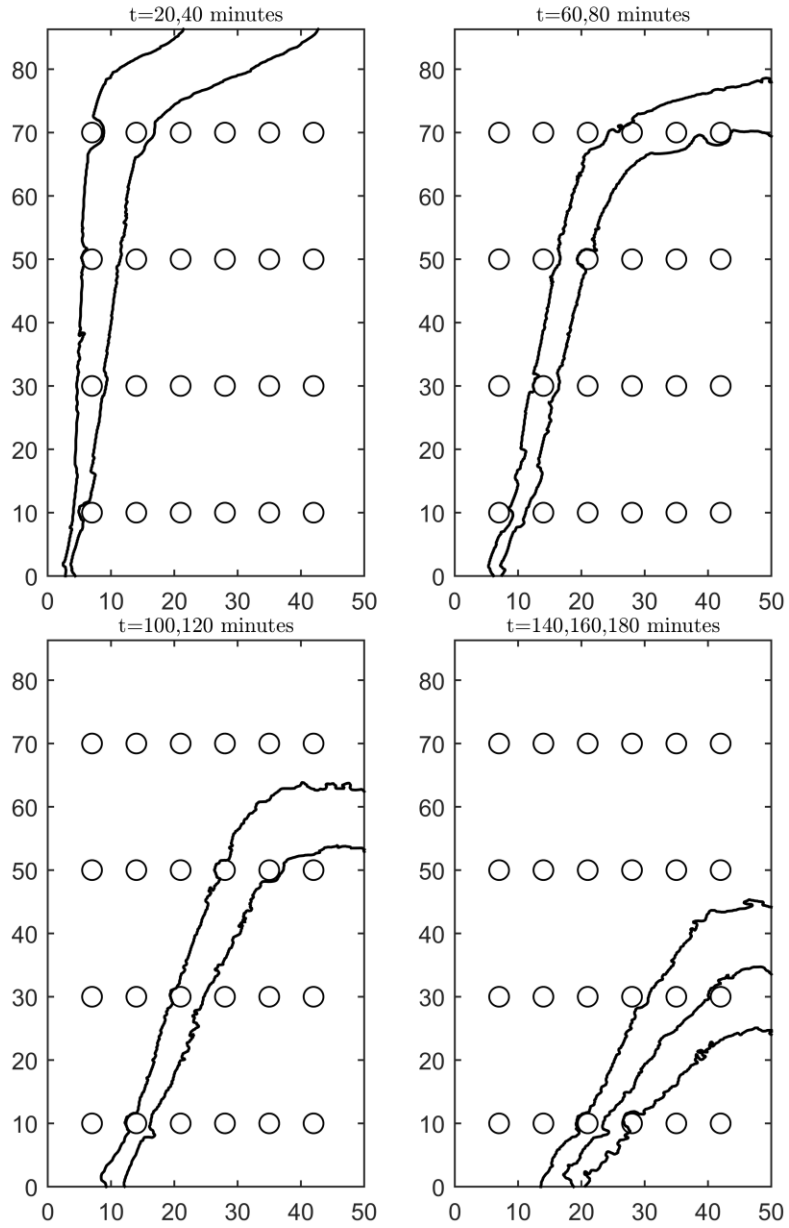

Figure 6.9 Profiles of melt front progress with time for the electrode case for Ra=1.8E8, Ste=0.13 and V=0 kV

6.1.2 Heat transfer coefficient measurements

This section demonstrates and explain the measurements from the Shadowgraph setup to measure the local temperature gradients along the height of the heat exchanger wall. The measurements taken in this section from local temperature gradients were used to calculate the local and the average heat transfer coefficient along the heat exchanger wall and to illustrate the transition from conduction to convection predominated heat transfer mode in melting of Octadecane. In all the Shadowgraph measurements, a small section of the measurement was not clear and taken out from the data which corresponds to two pieces of acrylic welded together. This area was not clearly visible as it was within the vicinity of the two welded pieces, the unclear section occupied 17-mm starting from the bottom section of the heat exchanger wall. The average heat transfer coefficient at the heat exchanger wall was calculated by integrating the heat transfer coefficient distribution along the wall and dividing it over the wetted length of the heat exchanger. The heat transfer coefficient distribution along the unclear section was evaluated using linear extrapolation of the slope of the neighboring points to this section. Linear extrapolation in this region will yield a lower average heat transfer coefficient than the actual heat transfer coefficient as the real distribution in this region is logarithmic The impact of the linear simplification in this region on the average coefficient was assessed against numerical simulations and was found to underestimate the average heat transfer coefficient by a max of 8 % under the examined test conditions and a maximum of 12 % if the unclear section was excluded from the average heat transfer coefficient evaluation. The unclear section was excluded from the

analysis when comparing the results between EHD and non EHD cases for the sake of consistency.

Figure 6.10 shows the heat transfer coefficient measurement along the wall of the heat exchanger using the Shadowgraph measurement for the third case in Table 6.1 where the Rayleigh number is equal to 9E7 and Stefan number is equal to 0.0445. The figure clearly shows that conduction is the predominant mode of heat transfer up to the first 43 minutes of the melting process. This is manifested in the high heat transfer coefficient along the whole length of the heat exchanger surface. It is interesting to see peaks in the heat transfer coefficient distribution at 30,50,70 and 90 mm mark along the span of the heat exchanger wall. These 4 locations at the heat exchanger wall are directly opposite to the centre of the opposite electrodes. In fact the enhancement at these locations further proves a dominant heat conduction transfer mode at this stage where the brass electrodes enhances the heat conduction within their vicinity.

After the 43 minutes mark at around 1 hour, a mixed conduction and convection heat transfer mode appears. The conduction effect is still evident from the heat transfer coefficient peaks opposite to the electrodes and the convection heat transfer is evident from the general distribution of the local heat transfer coefficients along the span of the heat exchanger wall. Higher heat transfer coefficients towards the bottom end of the heat exchanger and lower towards the top, indicates a convection heat transfer mode in which the hot thermal boundary layer starts from the bottom and grows along the span of the heat exchanger wall.

The mixed conduction and convection heat transfer mode continues up to almost 150 minutes. As time progresses, one can notice that the effect of the electrodes on the conduction began to diminish and troughs are starting to form at the 30,50,70 and 90 mm marks opposite to the electrodes which are caused by the cold downward plume adjacent to the interface interfering with the uprising plume at the heat exchanger surface.

After 150 minutes, the heat transfer mode is mainly by convection and there is almost no interference caused by the electrodes by that time. After 280 minutes, the top of the interface reaches the opposite wall to the heat exchanger and the height of solid Octadecane starts to decrease. As this occurs, the local heat transfer coefficients at the top region of the heat exchanger starts to flatten indicating no further growth of the hot boundary layer at this position and the flattened portion with the lower heat transfer coefficient grows with time along with the diminishing height of the solid Octadecane. The point at which the interface reaches the opposite wall is often called the start of the knee as per the earlier work in literature by Jany et al (1988) [24].

Figure 6.11 shows three shadowgraph images for the above case at different times. The first picture is taken at 43 minutes mark and it clearly shows larger deflection in the light sheet opposite to the electrodes location. The deflection of the light appears to be more or less equal along the whole length except for the electrodes position and the thickness of the light sheet is rather constant along the whole length and is less than the other two images which further proves a conduction dominated heat transfer mode. The second image highlights the taking over of the convection mode and the third image highlights the shortening of the thermal boundary layer as the height of the solid Octadecane decreases.

The values for the local heat transfer coefficients were used to calculate the overall average Nusselt number along the heat exchanger surface and the results are presented in Figure 6.12. The graph clearly identifies the main key transitional points: the end of conduction phase, stable natural convection mode and the knee point from which the heat transfer rate starts to decrease. These values are verified against the analytical correlation for natural convection in rectangular enclosures. In case of tall enclosures $\left(\frac{L}{H}Ra_H^{0.25} \geq 5\right)$ in which both the hot and the cold boundary layers are fully developed and do not interact with each other. The steady state heat flux is dependent only on the height of the enclosure and is not dependent on the width [106]. In this case the overall heat transfer rate can be calculated as follows

$$q' = 0.364k\Delta TRa_H^{0.25} \tag{6.1}$$

and accordingly, the average Nusselt number correlation using the enclosure height as the characteristic length is equal to

$$\overline{Nu}_H = 0.364\ Ra_H^{0.25} \tag{6.2}$$

For the discussed cased, the analytical correlation yields an average Nusselt number equals to 35.5 and the experimental results yields an average Nusselt number of 33.5 at this region which is less than the analytical correlation prediction by 5.5 %.

Figure 6.13 and Figure 6.14 shows the average Nusselt number temporal variation for the other two cases where Ra=1.8E8, Ste=0.089 and Ste=0.13 respectively. At this Rayleigh number, the analytically Nusselt correlation yields a maximum average Nusselt

number of 42.1 [before the knee]. Figure 6.13 shows that the average Nusselt number before the knee point was equal to 41 which is in good agreement with the theoretical number. While for the higher Stefan number case [Ste=0.13, H=87.3 mm], the experimental average Nusselt number before the knee point was Nu=38 which is lower than the correlated value by 10 %.

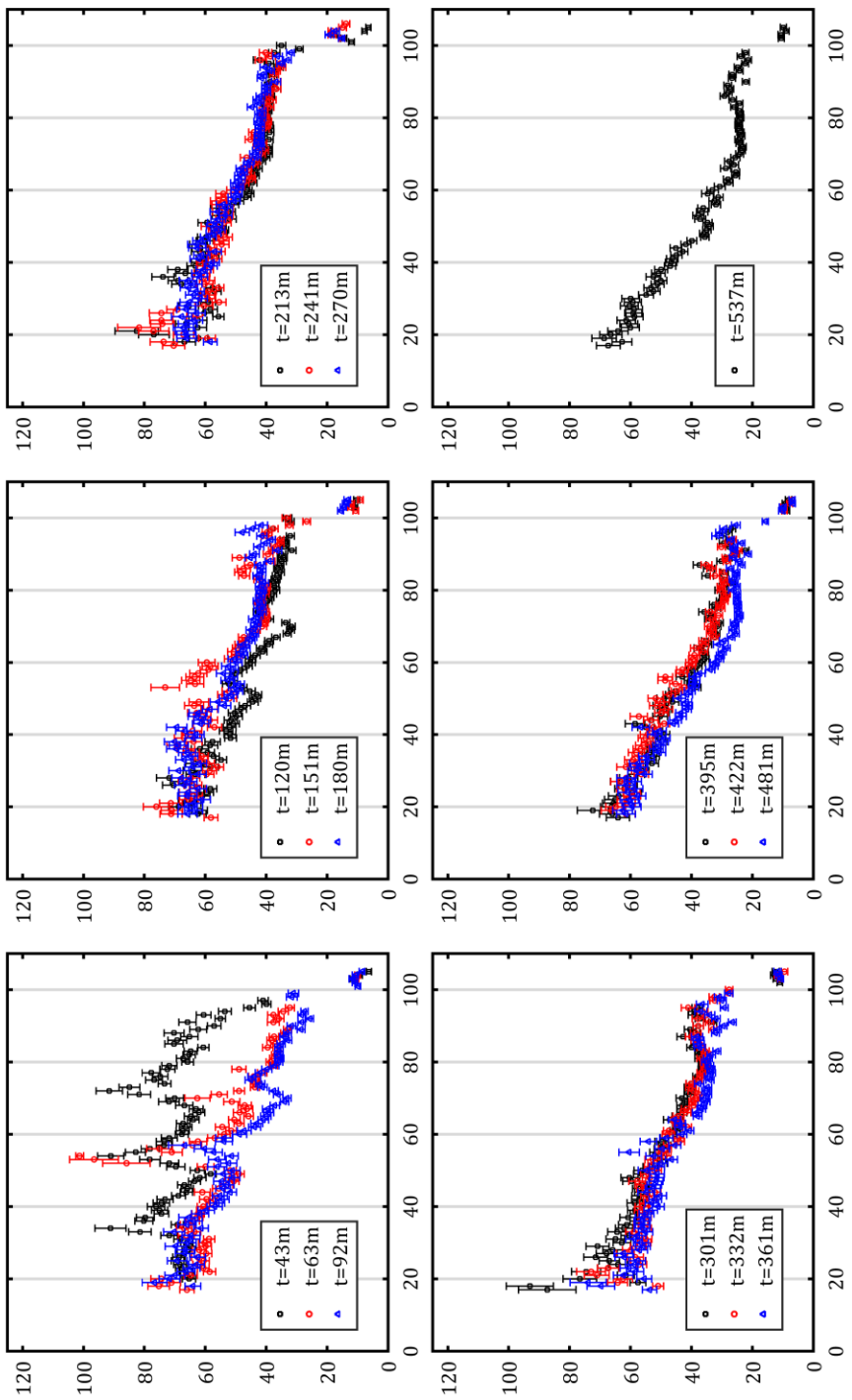

Figure 6.10 Heat transfer coefficient measurement along the left wall for Ra=9E7, Ste=0.0445 and V=0 [kV]

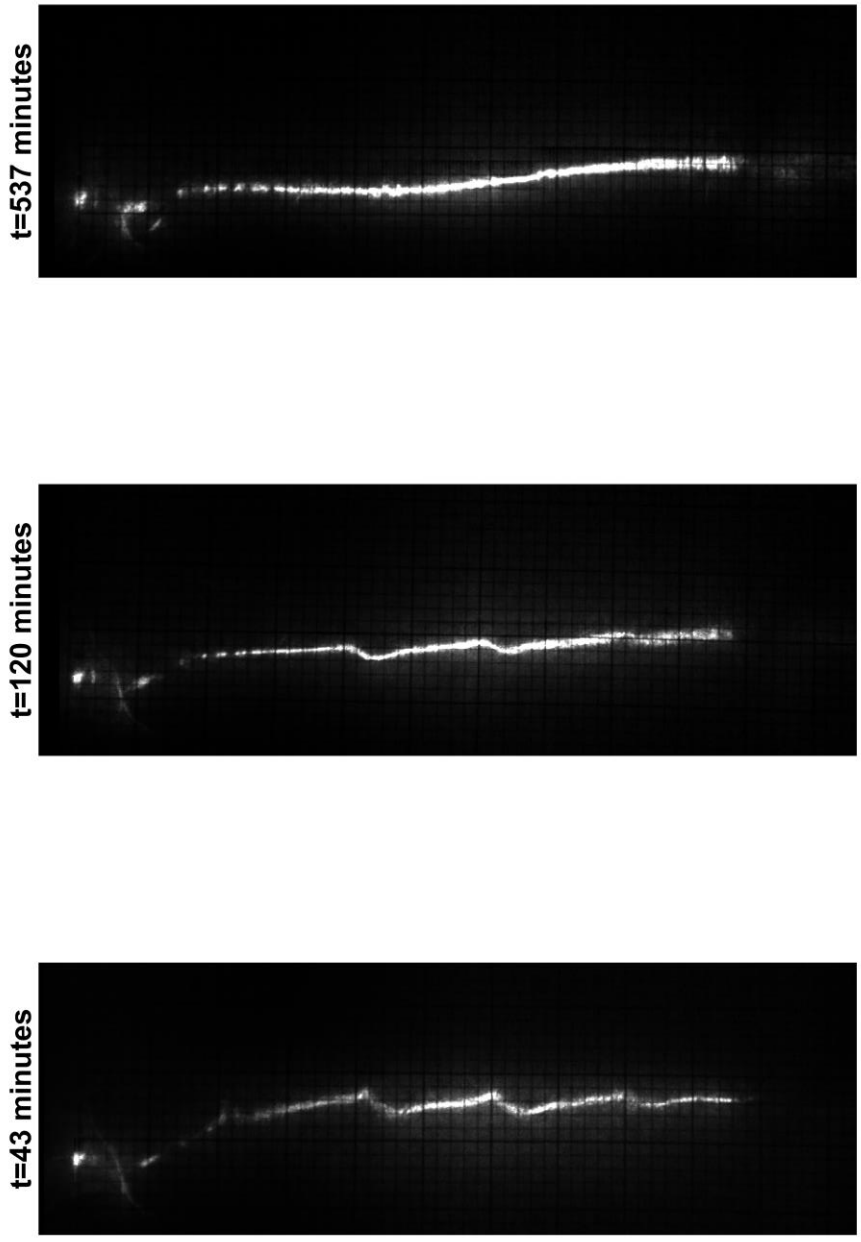

Figure 6.11 Shadowgraph images at different times for Ra=9E7, Ste=0.0445 and V=0 [kV]

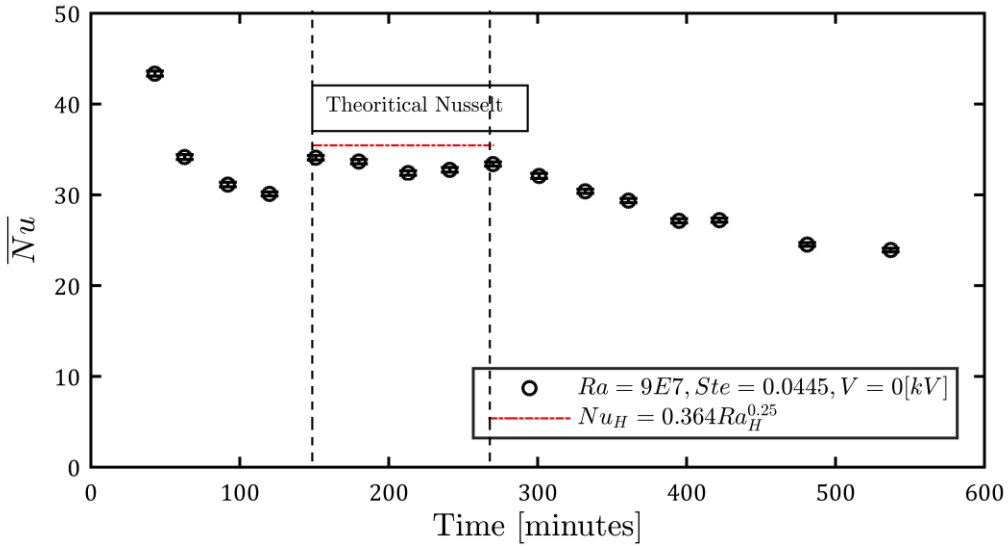

Figure 6.12 The average Nusselt number at the heat exchanger wall for Ra=9E7, Ste=0.0445 and V=0 [kV]

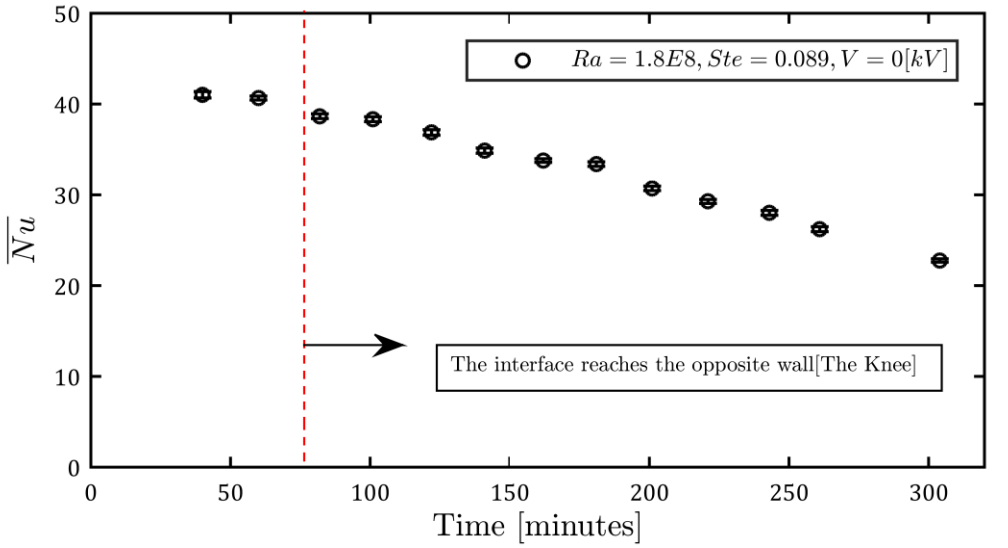

Figure 6.13 The average Nusselt number at the heat exchanger wall for Ra=1.8E8, Ste=0.089 and V=0 [kV]

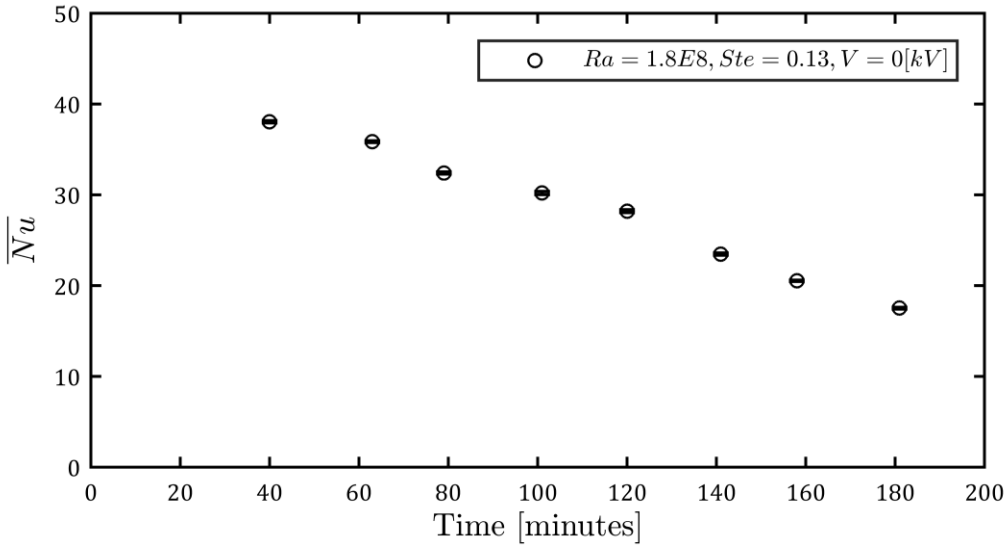

Figure 6.14The average Nusselt number at the heat exchanger wall for Ra=1.8E8, Ste=0.13 and V=0 [kV]

6.1.3 Summary for the non EHD results

The results for the non EHD experiments will serve as a base case for comparison to the EHD experiments outlined in the next section. The results showed good agreement with both previous experimental work and theoretical work and the shadowgraph method assisted in explaining the predominant heat transfer mode during different melting stages and showed good quantitative agreement as well with the theoretical work of natural convection in rectangular enclosures. The experimental results confirmed that the effect of the electrodes does not cause any significant impact on the overall melting progress.

One way to look at the total results and understand the melting process is by using non-dimensional parameters to describe the problem. The dimensionless parameters are

explained in detail in the work of Jany and Bejan [24] and the same theory was used here to look at the results with slight modification.

Assuming a quasi-steady solution at all times for conduction and convection. At conduction, the steady state heat flux is equal to

$$Q_{cond} = Hk_L \frac{\Delta T}{S_{av}} \tag{6.3}$$

Where S_{av} is the average melt thickness and is calculated as $(VF \times W)$ the product of the melt volume fraction by the width of the enclosure. This conduction heat rate is equal to the rate of melting

$$Q_{melt} = \rho V_0 \Delta H_f \frac{d(VF)}{dt} \tag{6.4}$$

From equation (6.3) and (6.4), the temporal volume fraction function can be calculated as

$$VF_{cond} \sim \frac{H}{W}\sqrt{2\,Fo.Ste} \tag{6.5}$$

At the convection stage before the knee, the convection heat flux is given by equation (6.1) and by equating it with equation (6.4) yields the following

$$VF_{conv} \sim \frac{H}{W}\,Fo.Ste.Ra_H^{0.25} \tag{6.5}$$

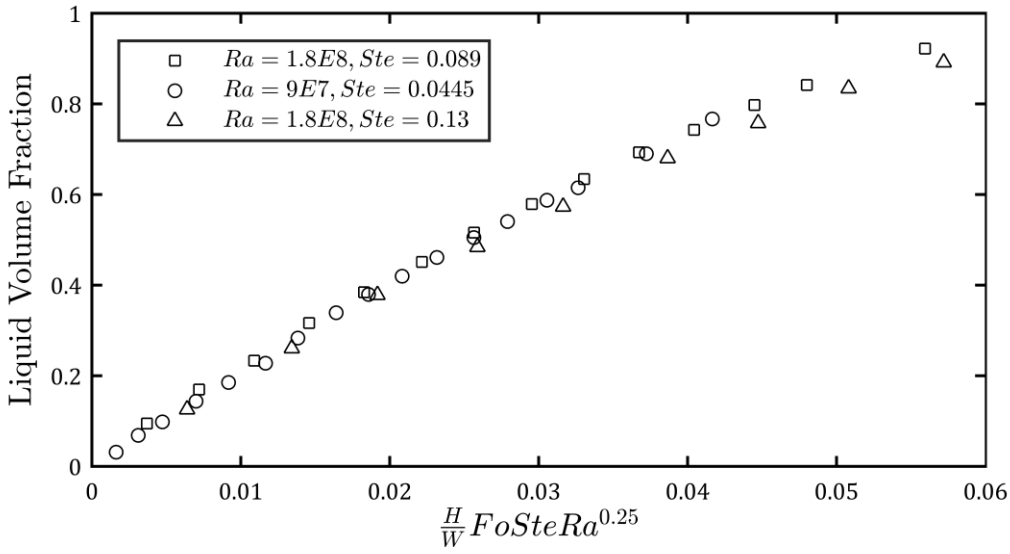

Figure 6.15 The temporal volume fraction variation for the non EHD experiment against the dimensionless parameters

The above equations show that the volume fraction is mainly function of three dimensionless parameters, which are the dimensionless time $(Fo.Ste)$, the aspect ratio of the enclosure $\left(\frac{H}{W}\right)$ and the Rayleigh number.

Figure 6.15 shows the volume fraction temporal variation against the dimensionless parameter $\left(\frac{H}{W}Fo.Ste.Ra^{0.25}\right)$. The results collapse well specifically at the convection region and the maximum deviation is noticed for the high Stefan number case at the knee region.

6.2 Melting in vertical enclosures with EHD forces

This section details and explain the findings for applying EHD at melting for vertical enclosures. The experiments outlined in this section are conducted under the same temperature boundary condition as those outlined in Table 6.1 but under an applied high voltage to investigate the effect of EHD forces on the heat transfer during the melting of Octadecane. The experiments were conducted to investigate and explain different criterion when looking at EHD forces under convection dominated melting. The results highlight the transition from gravitationally dominated melting to mixed electrical and gravitational melting regime. The experiments conducted here were used to understand the main EHD enhancement mechanism for melting of Octadecane. This section also investigates the effect of the magnitude of the applied voltage, the applied voltage polarity and temperature difference on the level of heat transfer enhancement. The results of the experiments were also used to understand the EHD convective flow regimes, the effect of the applied waveform on the transients of the EHD flow and the correlation between the enhancement and the electric current measured.

6.2.1 Effect of the magnitude of the DC applied voltage

6.2.1.1 Ra=9E7, Ste= 0.0445

The first set of tests were conducted for the Rayleigh number case of 9E7 and Ste=0.0445 [temperature difference of 5 ℃] under two different applied voltage [+3 kV] and [+6 kV]. The melt volume fraction, the melt front profiles, shadowgraph images and

the current measurements were all recorded during the experiments. In all of the experiments outlined in this section and forward, the electrical wiring for the electrodes followed what was shown in Figure 4.4 in the experimental facility chapter. The first, third and fifth columns of electrodes were connected to the high voltage supply and the second, fourth and sixth columns of electrodes were grounded and the electric current was measured from their side.

Figure 6.16 shows the temporal progress of the melt front with the applied voltage of positive 3 kV. The melt front profiles are very different from those without EHD forces acting within the PCM. At the beginning of the melting stage- up to 40 minutes from start of melting- the melt front travelled much faster than that without EHD. The melt front progress was faster specially around the high voltage electrodes and the interface was symmetrical around the electrodes during these early stages. This symmetry up to 40 minutes indicate that the melting is initially electrically dominated at this stage. As time progresses, the interface starts to tilt away from the heat exchanger surface at the uppermost part similar to the non EHD experiments with natural convection which dictates the presence of gravitational forces. However, the effect of the electrical forces is still present as seen between each successive two rows of electrodes and as indentation around the electrodes at all times.

In order to get a better understanding on the relation between the electrical and the gravitational forces in play and what is the mechanism of electro-convective flow the shadowgraph images were used to better understand the coupling between the two dominant forces. Figure 6.17 shows three shadowgraph images at the applied voltage of

positive 3 kV at three different times [41, 182 and 303 minutes]. The shadowgraph contours in these images are quite different from those without EHD forces [Refer to Figure 6.11]. The shadowgraph contours show a rather symmetrical distribution at the early times [41 minutes] and this symmetricity starts to gradually approach a semi-natural convection distribution towards the end. Figure 6.18 details the measurement of the local heat transfer coefficient along the heat exchanger wall through out the melting process. It is evident from this measurements that the heat transfer coefficients peaks are always almost coincident to the locations opposite to the electrodes [30,50,70 and 90 mm from the bottom of the wall]. Upon examining the local heat transfer coefficients, it is clear that at early stages of melting- up to almost 100 minutes- the local heat transfer coefficient distribution is almost symmetric between each two successive rows of electrodes with the highest peak values at the earlier stages [41 minutes]. This kind of symmetrical distribution in the local heat transfer coefficient with peaks facing the electrodes suggests the presence of two opposing electro-convection cells between each two rows of electrodes. These cells are initiated from the high voltage electrodes and impinging to the surface of the heat exchanger. Upon examining the magnitude of the heat transfer coefficient peaks at [41 minutes], it was found that the magnitude of the heat transfer coefficient peaks corresponding to 10, 30 and 50 mm are higher than the top two peaks corresponding to 70 and 90 mm. This observation still suggests the presence of gravitational forces effect in which the average flow at the heat exchanger side is moving up.

As time progresses- after 100 minutes- the magnitude of the peaks starts to decrease towards the top of the heat exchanger wall which indicates further intensification of the

relative magnitude of the natural convection flow. These observations suggest the presence of a mixed electrical-gravitational flow and the presence of an enveloping primary convection cell due to gravitational forces enclosing multiple electric-convection cells due to the electrical forces.

The mechanism of flow hypothesis can be further confirmed by examining the heat transfer coefficient distribution after 160 minutes, not only do the magnitude of the peaks decreases as you move up along the heat exchanger surface, but also the symmetricity of the secondary convection cells starts to be altered. This can be noticed first at the secondary cells located at the top of the heat exchanger, where the upper convection cell is stretched towards the top and the lower convection cell is rather decreased in size. This kind of behavior is highly manifested towards the later stages in melting and can be seen in all secondary convection cells. The presence of these electro-convection cells that are originating from the high voltage electrodes along with the presence of the natural convection flow can explain the shape of the interface during the melting in terms of the higher melt front velocity around the electrodes at all times [EHD effect] and the higher melt front velocity at the upper part [Gravity effect].

Under the same temperature boundary conditions, another case was tested which is positive 6 kV of applied voltage. The electrical wiring was the same as the first case and the results are presented in terms of melt front profiles and shadowgraph images. Figure 6.19 shows the melt front profiles temporal variation for the [+6 kV] and Figure 6.20 represent the local heat transfer coefficient variation for the same case. The positive 6 kV

applied voltage showed substantial increase in the melt volume compared to the positive 3 kV and the non EHD experiments as well under the same temperature boundary condition.

The progress of the melt front away from the heat exchanger was rather more uniform under the 6 kV case than that of the 3 kV. This can be realised from the distance covered by the melt front at the uppermost part compared to the distance covered by the lower end near the bottom heat exchanger wall. It can be deduced that the percentage covered by the bottom part compared to the upper part for the 6 kV is almost double that for the 3 kV which indicates better enhancement overall and less of an effect of gravitational forces compared to EHD forces under the 6 kV case.

The shadowgraph images in Figure 6.20 further confirms these observations. The local heat transfer coefficient distributions in this figure still suggests the presence of two opposing electro-convective cells between each two successive rows of electrodes with the mechanism of jet impinging directly opposite to the location of the electrodes.

6.2.1.2 Ra=1.8E8, Ste=0.089

The EHD experiments were conducted this time on a higher Rayleigh and Stefan number than of the previous case. The EHD enhancement was measured at three different applied voltages. These applied voltages are +2, +4 and +6 kV and the results were compared against the non EHD experiments.

Figure 6.21 shows the melt front profiles temporal progress with positive 2 kV applied through the high voltage electrodes. The general trend of the melt front profiles looks very similar to that at 0 kV (without EHD forces) except for the regions around the electrodes

where a slight improvement can be seen. However, the improved front velocity around the electrodes at 2 kV is not as noticeable compared to the 3 kV applied voltage in the previous case. In order to better understand the interaction between EHD and gravitational forces under this applied voltage, one can examine carefully the shadowgraph results presented in Figure 6.22.

The local heat transfer coefficient distribution under 2 kV [Figure 6.22] indicates a gravitationally dominated flow with onset of electrical effect opposite to the electrodes. The local heat transfer coefficients trend is following a typical distribution for natural convection flow with the highest heat transfer coefficients at the bottom and lowest at the top. This kind of distribution shows that the primary flow regime is composed of one big cell that encloses the liquid melt volume. There is slight local enhancement in the heat transfer coefficient opposite to the electrode and this effect could be contributed to the electrical forces causing thinning of the thermal boundary layer imposed by the additional EHD pressure forces induced by the opposing injecting electrodes.

Figure 6.23 and Figure 6.24 present the timewise variation in the melt front profiles and the local distribution of heat transfer coefficient respectively under positive 4 kV applied voltage. The progress of the melt volume fraction was faster than the positive 2 kV case and the shape of the interface suggests higher electrical forces effect. The heat transfer coefficient distribution supports the observation where the local peaks opposite to the electrodes are higher in this case than the 2 kV case.

Finally, Figure 6.25 shows the melt front profiles under 6 kV applied voltage through the high voltage electrodes. The shape of the melt front profiles in this case indicate a higher

dominance of electrical forces over the gravitational ones when compared to the previous case of 4 kV applied voltage.

Figure 6.26 overlays the melt front profiles for the three different applied voltage mentioned in this section at different instances of time. The figure highlights the level of enhancement reached by increasing the applied voltage and the corresponding transfer from gravitational to mixed electrical and gravitational dominated melting. Take for instance the time corresponding to 120 minutes, by carefully examining the melt front profiles, one can identify the dominance of gravitational forces for (+2 kV) case from the tilted interface at the top of the cell. A mixed regime and a sense of magnitude of each of the electrical and gravitational forces can be observed for (+4 and +6 kV cases), the symmetricity between the successive rows of electrodes is more pronounced in the 6 kV case.

6.2.1.3 Ra=1.8E8, Ste=0.13

In this case, the Rayleigh number was kept the same as the previous case, however, the temperature difference between the heat exchanger and the melting point of Octadecane was raised to 15 ℃ instead of 10 and in order to keep the Rayleigh number the same, the cell height was reduced.

Figure 6.27, Figure 6.28 and Figure 6.29 show the melt front profiles at different times during the melting process for +2, +4 and +6 kV applied voltage respectively. The same behavior from switching between gravitational to a mixed gravitational and electrical mode are noticed through the melt front profiles for the different applied voltages. The main difference between these results and the ones for the previous case- [Ra=1.8E8 and

Ste=0.089]- is that the effect of the EHD forces caused an improvement in the melting progress even for low voltages as for positive 2 kV which was not clear in the previous case[Refer to Figure 6.33 and Figure 6.45]. These results will be further explained in detail along with the current measurement in section 6.2.5.

6.2.2 Effect of the polarity

In order to better understand and expand the knowledge of the impact of EHD forces on the melting of PCMs, the same experiments as outlined in the previous section were conducted under the same applied voltages but at different polarity in an effort to elucidate and understand the mechanism of action of the EHD forces.

6.2.2.1 Ra=9E7, Ste=0.0445

For these temperature and Rayleigh conditions, another EHD experiment was conducted for negative applied voltage at the same magnitude of the maximum voltage tested for the positive polarity to highlight the difference between both polarities at maximum voltage. The results outlined in this section are for negative 6 kV applied voltage.

Figure 6.30 shows the temporal melt volume fraction progress for the two different polarity cases applied vs the reference experiment (No EHD forces, V=0 kV). The amount of the molten fraction under a given time was significantly enhanced for the EHD cases under both negative and positive polarity. It was found that the amount of molten fraction was almost the same for both the positive and the negative polarities at the early stages of melting up to almost 2.5 hours. After 2.5 hours, the case with negative applied voltage (-6

kV) showed more enhanced melting progress over the positive polarities and the effect seems to be more exaggerated with time.

In order to understand the physics behind this difference, the temporal melt front profiles were examined for both cases. Figure 6.31 draws the difference between the positive [red color] and negative [blue color] polarities on the temporal melt front profiles under the applied voltage 6 kV. The overall shape of the melt front profiles is the same for both the positive and negative polarities which indicate that the electro-convection flow regimes are not different when the polarity is switched. In fact, by examining the shadowgraph results in Figure 6.32 for the negative polarity and comparing it to that for the positive polarity [Refer to Figure 6.20] one can notice the same general distribution for the local heat transfer coefficients. The main distinctive difference between the two cases is that the negative polarity case shows higher local heat transfer coefficient opposite to the lower electrodes when compared to the positive polarity case. The higher local heat transfer coefficient for the negative polarity indicate that the effect of the electrical forces is higher for the negative case than that for the positive.

In the light of the shadowgraph results and by examining the melt front profiles, the difference in the EHD effect for the negative and positive cases can be understood. The results can be explained in the light of the following hypothesis. This hypothesis is:

a) During the melting of the Octadecane, the electrical and the gravitational forces are interacting together and defining the velocity of the melt front and the shape of the profile

b) The ratio between these two forces are the one which define how the interface would progress.

c) In case of higher gravitational forces to electrical forces, the interface will be move faster at the top of the enclosure and slower at the bottom owing to the thickness of the cold boundary layer

d) In case of higher electrical forces to gravitational forces, the interface will move faster around the electrodes and almost the same everywhere else. This leads to a more uniform interface progress and delay in reaching the knee stage

e) If both forces are in the same order of magnitude, a mixed combination between both will appear where a tilt in the overall shape of the interface would still be observed due to the effect of the gravitational forces and a more uniform progress in the bottom due to the effect of the EHD forces.

At early stages of melting, the melt front moves faster at the bottom of the enclosure for the negative case compared to the positive case, while the upper portion of the enclosure the opposite happens where the melt front velocity is higher for the positive case. This in fact suggests that the magnitude of the EHD forces are higher for the negative case than that for the positive and consequently the ratio between the EHD to gravitational forces are higher for the negative case. In both of the positive and the negative cases, it is evident that the melting occurs in the mixed regime and both of them showed almost the same melt fraction. This is true until the melt front touches the opposite adiabatic wall. After this point [≈ 260 minutes], the magnitude of the gravitational forces starts to diminish and the ratio between EHD forces to gravitational forces starts to increase- higher for the negative case-

and be of higher importance and that is the reason for the higher melt front velocities and overall melt fraction for the negative case compared to the positive case.

6.2.2.2 Ra=1.8E8, Ste=0.089

The polarity effect was tested at the higher Rayleigh number 1.8E8 and higher Ste 0.089. This time the experiments were conducted at three different applied voltages [-2, -4 and -6 kV] to understand the effect of the applied voltage polarity even at relatively lower voltages.

The results of the experiment and the effect of the polarity temporally on the amount of melt fraction are presented in Figure 6.33. The figure shows that the temporal melt progress was almost the same regardless of the polarity of the applied voltage. The effect of the polarity at the higher voltage end seems to be in favor of the negative polarity but with relatively lower enhancement than that for the previous case at lower Rayleigh number. At the lowest applied voltage [2 kV], the melt volume fraction was in fact almost the same as that for without EHD forces. This shows that the relative magnitude of the EHD forces to gravitational forces is very small at 2kV. In fact, the negative polarity cased showed slight retardation in the melt front progress compared to non-EHD case while that for the positive showed slight enhancement. The possible reason for that should be further investigated, as such magnitude of applied voltage seems to lie within the bound of transitional regime from fully gravitational dominated melting to a mixed electrical and gravitational one. The shape of the melt front profiles for the highest voltages [+6 and -6 kV] in Figure 6.34 appears to

support the same observations at the lower Rayleigh number case, where the negative applied voltage provides higher melt front velocities around the electrodes.

6.2.3 Effect of the waveform

The main objective of this section is to use different waveform shapes to understand the main mechanisms of enhancement in the melting under EHD forces and not to present a full investigation on the effect of the different waveforms parameter on the melting process. The later can be a separate study on its own and would require a bigger test matrix than what will be presented here. In this section two wave-forms only will be examined: the pulse wave form with 50 % duty cycle and a square wave form with 50 % duty cycle.

By examining the EHD body forces equation

$$\overrightarrow{f_e} = \rho_q \vec{E} - \frac{1}{2} E^2 \nabla \varepsilon + \frac{1}{2} \nabla \left(\rho E^2 \left(\frac{\partial \varepsilon}{\partial \rho} \right)_T \right) \tag{6.6}$$

One can supress the effect of the Coulomb forces in the bulk of the dielectric liquid by applying an alternating electric that is symmetric about a 0-electric potential, such that in this case the $\bar{E} = 0$. However, the applied alternating electric field's frequency has to be high enough to surpass the shortest electrical time scales. The important electrical time scales involved this problem are the charge relaxation time [107] [time required for the charges to be neutralized by opposite charge carriers] and the ionic transit time [time taken by the ions to drift from the injector to the grounded side]. If the applied electrical field's frequency is order of magnitude higher that the shortest of these two scales, it will not give

enough time for the charges to rise in the bulk of the dielectric fluid and the contribution of the dielectrophoretic forces can then be investigated.

In fact, the space charge relaxation time for Octadecane is not the limiting time scale in this scale as Octadecane's electrical conductivity is extremely low ($\sim 10^{-16}$) [101] which yields a charge relaxation time equal to

$$\tau_{sc} \sim \frac{\varepsilon}{\sigma} \sim 10^{3} \tag{6.7}$$

The ionic transit time scale is equal to

$$\tau_{kq} = \frac{l^2}{K_q V} \tag{6.8}$$

In order to estimate the ionic transit time scale, the ionic mobility of Octadecane has to be known first. The ionic mobility is related to the viscosity of the material according to Walden's rule $\left(K_q = {constant}/{\mu}\right)$ and Adamczewski et al (1975)[108] calculated the ionic mobility for saturated hydrocarbons [alkanes] from viscosity [P] as

$$K_q = \frac{1.5 \times 10^{-11}}{\mu^{1.5}} \quad [m^2 V^{-1} s^{-1}] \tag{6.9}$$

From the above correlation, the ionic mobility for the positive charge carriers at 30 ℃ is equal to $[2 \times 10^{-9} m^2 V^{-1} s^{-1}]$. By using the horizontal spacing between the electrodes as the characteristic length (l) in equation (6.8) and the maximum applied voltage in the experiments (6 kV), the ionic transit time scale was found to be equal to $\sim 4\ s$. Any applied

alternating symmetric wave form whose period is shorter at least by an order of magnitude than the ionic transit time scale will suppress the effect of the Coulomb forces in the bulk of Octadecane. In the current configuration, the calculated frequency of such waveform was found to be at least 2.5 Hz under 6 kV and 1.25 Hz under 3 kV.

6.2.3.1 Square waveform

First, square waveforms were applied through the high voltage electrodes at different frequencies to understand the main mechanism of EHD enhancement. In these experiments, the shadowgraph measurements were used to understand the flow regimes and the difference between DC test and the alternating fields tests.

Table 6.2 shows the test matrix for the applied EHD tests with square waveform under condition of Ra=9E7 and Ste=0.0445. Three frequencies were tested with the lowest of 0.5 Hz and the highest of 20 Hz with a voltage amplitude of 3 kV. Figure 6.35 shows the waveform shape for 3 kV amplitude and for an applied frequency of 0.5 Hz.

Table 6.2 Test matrix for applied square waveforms tests

Waveform	Amplitude [kV]	Frequency [Hz]
Square	3	0.5
Square	3	1.75
Square	3	20

Figure 6.36 shows the shadowgraph images transient response for applying 3 kV wave form with a frequency of 0.5 Hz. The shadowgraph images show that the flow is still responding to the alternating electric field applied. The local peaks behavior in the heat

transfer coefficient still can be noticed opposite to the electrodes and the behavior seems to be alternating along the span of the heat exchanger wall. The overall heat transfer coefficient distribution still affected by the EHD forces and the distribution is not similar to a natural convection flow which still indicates the dominance of EHD forces even at this frequency.

Figure 6.37 shows the shadowgraph measurement transient response for an applied square wave of 3 kV amplitude and of frequency of 1.75 Hz. The figure indicates that the mean flow suggests a non- disturbed natural convection regime with the flow is locally responding to the EHD forces mainly towards the top of the enclosure opposite to the electrodes. These observations mean that at such frequency the effect of the Coulomb force is almost diminished which is in agreement with the calculated transit ionic scale, but most importantly these results indicate that the dielectrophoretic forces magnitude is minimal at these applied voltages.

In order to further confirm and evaluate the role of the dielectrophoretic forces at the applied voltage, the frequency of the square wave form applied was increased to 20 Hz. The transient shadowgraph images in Figure 6.38 corresponds to an initial case of -3 kV DC voltage [t=0 ms] suddenly subjected to a square wave of 3 kV amplitude and a frequency of 20 Hz. It can be seen from the shadowgraph images that once the high frequency wave form was applied, the flow completely switched from electrical flow to natural convection regime. These results are aligned with the previous conclusions drawn in chapter 5, that the main mechanism of enhancement in the current study is due to

Coulomb force and that the effect of dielectrophoretic forces towards the overall enhancement is minimal in the case of melting of Octadecane.

6.2.3.2 Pulse waveform

In this section, a pulse wave form was examined and compared to a DC voltage with the same average electric field intensity as that for the pulse. By applying a pulse wave form with a duty cycle of 50 %, one can expect two possible scenarios. If the dielectrophoretic forces role is minimal under the applied voltage, a pulse wave form with shorter period than that of the ionic transit time scale will induce a mean electro-convective flow that is equal to that of a DC applied voltage with a magnitude equal to half that of the amplitude of the pulse wave form.

A pulse wave form of an amplitude of +6 kV and 50 % duty cycle and a frequency of 2 Hz [Refer to Figure 6.39] was applied for Ra=9E7 and Ste=0.0445 case and the results were compared against that of +3 kV DC applied voltage. Figure 6.40 shows the shadowgraph measurement transient response for the applied pulse wave form and it is obvious that the mean flow is not disturbed by the alternating electric field, but only locally opposite to the electrodes where the effect of the alternating electric field can be noticed. Three positions along the heat exchanger wall were chosen to examine the temporal heat transfer coefficient response for the applied wave form. The transient (h) response for these three positions is presented in Figure 6.41. The figure shows that for both [Y=50 and 69 mm] which are positions corresponding to peak local heat transfer coefficients and are opposite to the electrodes, a periodic behavior is noticed which corresponds to the frequency of the applied

waveform. While at [Y=63 mm] where the local (h) is minimum is barely affected by the applied waveform.

The temporal average (h) distribution for the pulse wave form case was calculated and plotted against the local distribution for +3 kV DC case which provides the same average electric field. The results are presented in Figure 6.42, and it was found that the local (h) distribution for both cases exactly match. These results further confirm that the main mechanism of enhancement is due to Coulomb forces in the bulk of the molten Octadecane.

6.2.4 Solid Extraction

Finally, the Solid extraction phenomenon was investigated for the current configuration and under DC (-6 kV) which produce an electric field similar in magnitude to that reported by Nakhla et al [12] where the solid extraction was first reported for paraffin wax in the mushy zone.

Tracing the solid extraction phenomenon is very challenging experimentally, because it is a phenomenon that occurs on a micro-scale level particle attached to a moving boundary [solid/liquid interface] with velocities in millimeter per second range, thus making it practically impossible to visualize the whole process along the span of the interface.

In the current experimental facility, a microscopic lens [7X-Magnification] was connected to the high-speed camera and focused on one location at a time through the duration of the experiment. Two locations were carefully captured which thought to be correspondent to the strongest extraction phenomenon if it occurs. The locations were in

the middle section between the second and the third column of electrodes and between the third and the fourth columns.

The microscopic high-speed imaging did not show significant solid extraction. The images rather showed very small particles [either dust particles or dissolved air bubbles] in the order of $\approx 35\ \mu m$ in diameter. These particles were found to be flowing with the flow and not extracted from the interface and they were present even for non EHD experiments.

Figure 6.43 showed the interface visualization as a response for applying negative 6 kV DC applied voltage case at Ra=1.8E8 and Ste=0.089, the time difference between the images is 240 milliseconds. The location of the interface in these pictures is highlighted in red for the last frame in the figure. In these visualizations, the closest to the solid extraction can be noticed starting from the fourth frame where a small particle [marked in red] is seen extracted originally from the interface and migrated towards the high voltage electrode. Another particle starts to appear from the fifth frame in the figure, however it looks much bigger than the first particle and fuzzier for being out of focus and the same behavior is noticed as the first particle.

These observations still cannot provide complete evidence that this is an occurring solid extraction phenomenon because of two reasons:

a) First, the size of the particles marked in the figure did not change during their migration towards the electrodes, which would have occurred if they were Octadecane solid particles.

b) Second, the expected influence from these particles migration [if they are in fact Octadecane] on the heat transfer enhancement is minimal owing to their small fraction of the interface span.

As a conclusion, the solid extraction phenomenon is not one of the main enhancement mechanisms noticed in this work of melting of Octadecane under EHD forces. This conclusion was supported by experimental interface visualizations and the alternating electric field experiments which showed no melting enhancement.

Solid extraction was first reported on paraffin wax [12] where a thick mushy zone could exist, however this is not the case for Octadecane as it is a pure material which lacks the existence of a mushy zone but rather a well defined solid/liquid interface. Further study will be needed to estimate the effect of the solid extraction and the dependency of the material composition on the level of EHD enhancement.

6.2.5 Summary and Analysis

This chapter provided the first experimental work of melting of a phase change material under electrical and gravitational forces in vertical enclosures. The results of these experiments showed how the EHD and gravitational forces interact during the melting process and the augmentation of the heat transfer.

The main EHD mechanism of enhancement was found to be Coulomb [electrophoretic component] forces. The mechanism of the Coulomb force was found to be injection from the high voltage electrode. As the magnitude of the electrical forces increase by increasing the voltage, the flow starts to move from being an initially gravitationally dominated [one

convection cell encompassing the boundaries of the molten liquid] into a mixed electrical and gravitational regime. In the mixed electric and gravitational regime, a bifurcation for the original convection cell starts to occur, where two opposing electrical convection cells bifurcate between each two consecutive rows of high voltage electrodes. At lower voltages, the size of the two opposing electro-convection cells is different because of the gravitational forces. As the voltage increases, the two electro-convection cells become as similar in size and the overall enhancement effect is highly augmented. This bifurcation mechanism and the creation of the multiple cells is the main reason for the heat transfer enhancement during the melting process.

The level of EHD enhancement was different against the different Rayleigh numbers tested and depended on the magnitude of the applied voltage and on the polarity of the applied voltage towards the higher end of the voltages tested. The temporal liquid volume fraction progress is presented collectively for all the tested voltages in Figure 6.44, Figure 6.33 and Figure 6.45.

The level of EHD enhancement was quantified as the ratio between time required to melt 50% of the PCM volume with EHD forces compared to that without EHD forces. The EHD enhancement factor vs the applied voltage for the different Rayleigh number cases tested is shown in Figure 6.46. From the figure, it is observed that the Enhancement factor is proportional to the magnitude of the applied voltage with the maximum enhancement factor achieved for the lowest Rayleigh number [9E7] case at -6 kV and is equal to 1.7 times enhancement. At the higher Rayleigh number [1.8E8], the level of enhancement was

lower and was equal to 1.6 times at -6 kV and at the highest Stefan Rayleigh number cases the maximum enhancement achieved was equal to 1.45 times.

In order to better understand the results for the collective experiments of EHD, the results were examined in a light of scaling analysis procedure in an effort to describe the problem in non-dimensional parameters. In the following scaling analysis, only the electrophoretic forces from the EHD body forces will be considered in the momentum conservation equation as it was found from the experiments that the main mechanism of enhancement is caused by the electrophoretic forces.

6.2.5.1 Scaling Analysis

Upon following the same concepts of scaling analysis by Bejan [106] for natural convection in enclosure and that of Golak et al [109] for heating in cylindrical enclosure under gravitational and EHD forces, an order of magnitude analysis was conducted for the main governing equation to define the problem in non-dimensional parameter.

Assuming an electrically dominated flow, the electrophoretic forces will form two opposing electro-convective cells between each two consecutive rows of electrodes. The vertical spacing between the rows of electrodes is referred by (S_v) and the width of the thermal boundary layer is (δ_T) [Refer to Figure 6.47].

The viscous forces are scaled according to

$$Viscous \sim \upsilon \frac{V}{\delta_T^3} \tag{6.10}$$

The electrical Coulomb forces are scaled as

$$Electrical \sim \frac{\rho_q E}{\rho \delta_T} \tag{6.11}$$

and the inertia of the dielectric fluid is scaled by Prandtl number to

$$Inertia \sim \frac{1}{Pr} \tag{6.12}$$

For organic PCMs, the Prandtl number falls in the range of ~ 50 and the inertial terms can be neglected, knowing that the flow is governed by the balance between the electrical and the viscous forces.

$$1 \sim \frac{\rho_q E \delta_T^2}{\mu V} \tag{6.13}$$

Before electric-convection starts [stationary fluid/ without gravitational forces]- at time (t=0), heat starts to conduct and penetrate from the hot surface towards the cold surface and initially, the conduction thermal boundary layer is related to time by

$$\delta_T \sim (\alpha t)^{0.5} \tag{6.14}$$

As time increase, the convection starts and the energy equation becomes a balance between the convection and the conduction through the thermal boundary layer, where

$$V \frac{\Delta T}{S_v} \sim \alpha \frac{\Delta T}{\delta_T^2} \tag{6.15}$$

Using equations (6.13-15), the thermal boundary layer thickness can be expressed as a function of

$$\delta_T \sim \left(\frac{\mu S_v \alpha}{\rho_q E}\right)^{0.25} \sim S_v Ra_{E/c}^{-0.25} \tag{6.16}$$

The thickness of the thermal boundary layer is directly proportional to the vertical spacing length between the electrodes. The longer the distance between the rows of electrodes, the thicker the boundary layer grows.

The second term in the thermal boundary layer equation is the conductive Electrical Rayleigh number $\left(Ra_{E/c}\right)$. The term conductive is given to separate this term from the electrical Rayleigh number used in chapter 7 that is used to relate the dielectrophoretic forces to the viscous forces. The electrical conductive Rayleigh number is dimensionless parameter the defines the electrical to viscous body forces $[Gr_{E/c}]$ multiplied by the Prandtl number of the fluid. The electrical Rayleigh number is calculated as

$$Ra_{E/c} = Gr_{E/c} \times Pr = \frac{\rho_q E S_v^3}{\alpha \mu} \tag{6.17}$$

If there are (n) number of electrode's rows in the configuration, the amount of heat convected from the hot side to the solid liquid interface would be equal to

$$Q_E \sim 2(n+1) S_v k \frac{\Delta T}{\delta_T} \sim 2(n+1) k \Delta T Ra_{E/c}^{0.25} \tag{6.18}$$

In order to estimate the conductive electrical Rayleigh number, one has to quantify the charge density (q). From the charge transport equation, the electric current density is given by

$$j = \rho_q(u + K_q E) - D\nabla\rho_q \tag{6.19}$$

Where D is the charge diffusion coefficient. The charge diffusion contribution towards the overall current is usually neglected under injection mechanism. In this case the electric current density is defined by the convective charge component$(\rho_q u)$ and the ion drift one$(\rho_q KE)$. In case of weak injections both components are in the same order of magnitude and the charge can be scaled to

$$\rho_q \sim \frac{J}{K_q E} \sim \frac{I}{AK_q E} \tag{6.20}$$

In this equation, (I) is the electric current measured at the electrodes and (A) is the surface area of the electrodes. Accordingly, the conductive Electrical Rayleigh number can be redefined as [58]

$$Ra_{E/c} = \frac{IS_v^3}{K_q A\alpha\mu} \tag{6.21}$$

The conductive electrical Grashoff number [sometimes referred as EHD number [77]] is then equal to

$$Gr_{E/c} = \frac{IS_v^3}{\rho K_q A v^2} \tag{6.22}$$

By using the formulation of heat transfer and the progress of volume fraction as described in equation (6.4), the volume fraction temporal progress can then be related to the electrical Rayleigh number in the same manner

$$VF_{EHD} \sim 2(n+1)\frac{H}{W}\, Fo.Ste.Ra_{E/c}^{0.25} \tag{6.23}$$

Validity of the scaling analysis

The scaling analysis for the role of the electrophoretic forces is only valid upon the fulfillment of the following list of assumptions. These assumptions are:

a) High Prandtl number PCMs $(Pr \gg 1)$. This assumption is generally valid for organic PCMs in which the thermal conductivity is very low $(k < 0.6\, W/mK)$

b) The relative magnitude of the dielectrophoretic forces in the bulk of the liquid PCM due to temperature gradients is much smaller than that from the electrophoretic forces from the injected charges. This assumption is only valid when

$$\frac{\rho_q E}{E^2 \frac{d\varepsilon}{dT}\frac{dT}{dx}} \sim \frac{I}{AK_q E^2 \frac{d\varepsilon}{dT}\frac{dT}{dx}} \sim o^2 \tag{6.24}$$

c) No Solid Extraction is observed. This condition might be fulfilled for pure paraffins only in which the melting occurs at a defined melting point rather than a melting range which further implies the absence of a mushy zone

6.2.5.2 Results in non-dimensional parameters

Using the knowledge of the correct dimensionless parameters that can be used to describe the problem and the correct length scales, one can investigate the results in the term of these dimensionless parameters and to understand the possible governing forces during the melting process.

In order to quantify the conductive electrical Rayleigh number and get an estimate for the charge density in the liquid Octadecane, the electrical current was measured through the grounded 15 electrodes for the following two cases under the different applied voltages:

a) Ra=9E7, Ste=0.0445

b) Ra=1.8E8, Ste=0.089

In the highest Stefan number case [Ra=1.8E8, Ste=0.13], the electrical current measurement was not accurate- as the upper row of electrodes was exposed to air- and therefore the current measurement cannot be used to estimate the charge density in Octadecane and therefore was not considered in the analysis. However, this is not expected to alter the behavior of the EHD forces in the Octadecane as the injected charges in the octadecane would depend only on the electrode/octadecane characteristics.

Figure 6.48 and Figure 6.49 shows the temporal current measurement in nano-amperes for the above-mentioned cases under the different applied voltages. The current transient profile appears the same for all the cases where the electric current decreases with time and then it increases back again and reaches an almost steady state value. This current behavior could be due to the fact the grounded electrodes are progressively being subjected to a

change in exposure from an initial solid phase to a liquid phase afterwards. The solid electrical conductivity and mobility are order of magnitude higher than that for the liquid phase [110] and this could be the reason for the initial decrease in the current by the beginning of the melting process. As the melting progress further, the current increases as number of injecting electrodes exposed in the liquid phase starts to increase. This hypothesis must be tested and confirmed with further tests and individual current measurements through each electrode instead of the current configuration where all the grounded electrodes are wired together and the current is being measured collectively.

The electric current was substantially higher for the negative polarity compared to the positive polarity at higher voltages ($> 2kV$) which could explain the better EHD enhancement for negative polarities at these higher voltages. The current was also higher with the higher temperature gradients which could be attributed to the higher electrical mobility $\left(K_q = \frac{constant}{\mu^{1.5}}\right)$ at the higher temperatures.

With an accurate measure of the electrical current, the value of the current that can be used in the electrical Rayleigh correlations has to be indicative to the charge density in the liquid phase. As seen from the temporal current measurements, the value of the current was not constant along the melting experiment due to the change of the number of wetted injecting electrodes as melting progresses. Therefore, the current values corresponding to the latest stages of melting- when all injecting electrodes are wetted- were used in the calculation for the conductive electrical Rayleigh number and not the instantaneous values.

Figure 6.50 shows the ratio between the calculated conductive electrical Rayleigh number and the gravitational Rayleigh at the different applied voltages and polarities. Upon examining the ratios calculated based on the conductive electrical Rayleigh number, the results support evidence to the correct scaling of the problem for two reasons:

a) The ratio between the electrical and the gravitational Rayleigh number at lower voltages (+2 and -2 kV) did not exceed 1.25 times. At these low voltages, there was not heat transfer enhancement observed and the melt fraction was almost equal to that without EHD and the 50% enhancement factor was close to 1 for both cases. [Refer to Figure 6.33and Figure 6.46]

b) Higher enhancement factors were measured for the lower Rayleigh number case and for the negative polarities at the higher voltages and this was confirmed in the figure through the higher ratios between electrical to gravitational Rayleigh number at [Ra=9E7] cases and for the negative polarities specifically.

The volume fraction temporal progress was then plotted for all cases against the dimensionless time ($Fo \times Ste$) multiplied by the electrical or gravitational Rayleigh number raised to the fourth power. The results for the lower gravitational Rayleigh case are shown in Figure 6.51 and for the higher gravitational case in Figure 6.52. The figures clearly show the success of using the dimensionless parameters in describing the physics of the problem where all the different voltages collapsed in a fairly well defined band that encapsulates all the data.

The most distinguished feature in these two graphs is that the volume fraction for the EHD experiments at the very beginning is always higher than that for the gravitational one

at the same dimensionless parameter $(Fo.Ste.Ra_E^{0.25})$. The reason behind this early enhancement- take for example +3 kV- is the earlier onset of the multiple electrical convection cells compared to the onset of natural convection for a gravitationally dominated case. This is clearly manifested in the shadowgraph measurements for the average Nusselt number at the wall when plotted against the melt volume fraction. Figure 6.53 shows the average Nusselt number for Ra=9E7 against the melt volume fraction at the different applied voltage, upon examining the Nusselt number enhancement for +3 kV case, one can see the highest enhancement compared to 0 kV up to 20 % of volume fraction which then decreases and saturates along the same level of that of 0 kV as time progress.

In order for the electrical or natural convection to start along the whole path of the hot heat exchanger wall, the thickness of the liquid zone must be greater than the width of the velocity boundary layer. Before the electrical/natural convection onset the thickness of the liquid zone $(S_{cond})$is governed by conduction heat transfer according to

$$S_{cond} \sim H(2Fo.Ste)^{0.5} \tag{6.25}$$

At the time of the onset of convection, the velocity boundary layer thickness (δ_v) can be correlated to the thermal boundary layer as [106]

$$\delta_v \sim Pr^{0.5}\delta_T \tag{6.26}$$

In case of natural convection, the onset time of convection $(\theta_{c/g})$is calculated as [24]

$$\theta_{c/g} \sim Pr\ Ra_g^{-0.5} \tag{6.27}$$

In case of electrical convection, the onset time of convection will be calculated $(\theta_{e/g})$as

$$\theta_{e/g} \sim \left(\frac{S_v}{H}\right)^2 PrRa_E^{-0.5} \tag{6.28}$$

These correlations show that the onset of electrical convection is shorter than that of natural convection onset by $\left(\frac{S_v}{H}\right)^2$ times. This fact highlights the important role that EHD forces can play for tall enclosures where the onset of natural convection is delayed and the electrical body forces can curtail it by earlier electrical onset.

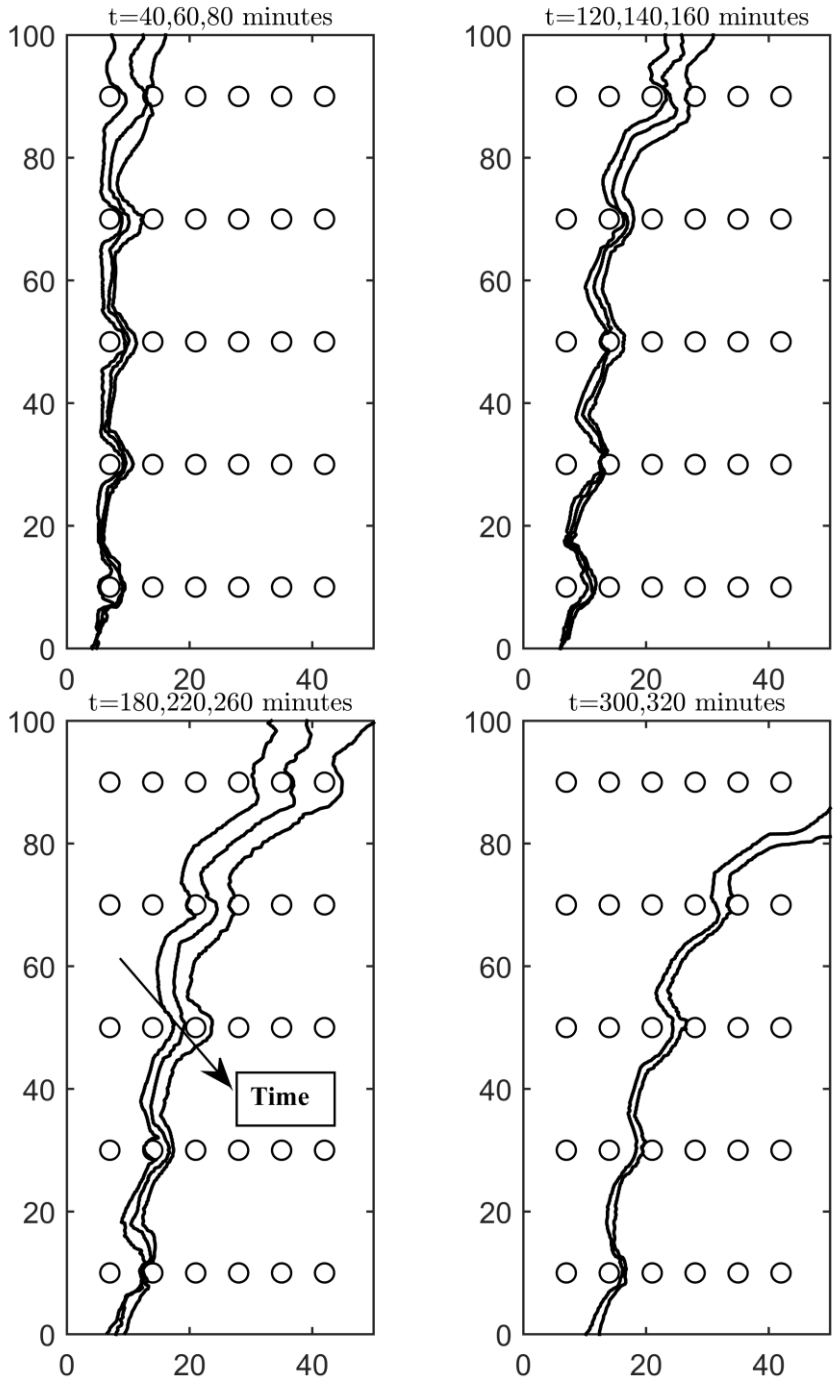

Figure 6.16 Melt front profiles timewise variation for Ra=9E7, Ste=0.0445 and V=+3 [kV]

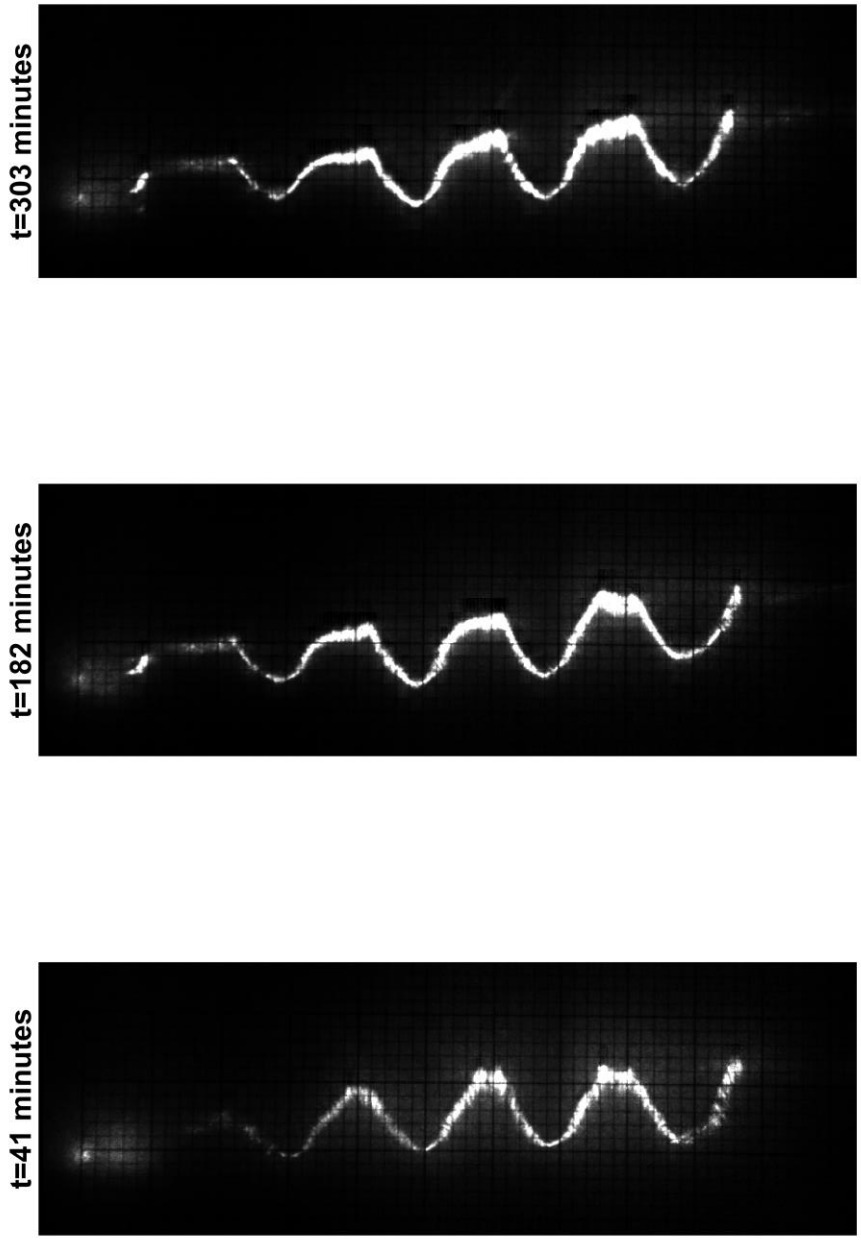

Figure 6.17 Shadowgraph images at different times for Ra=9E7, Ste=0.0445 and V=+3[kV]

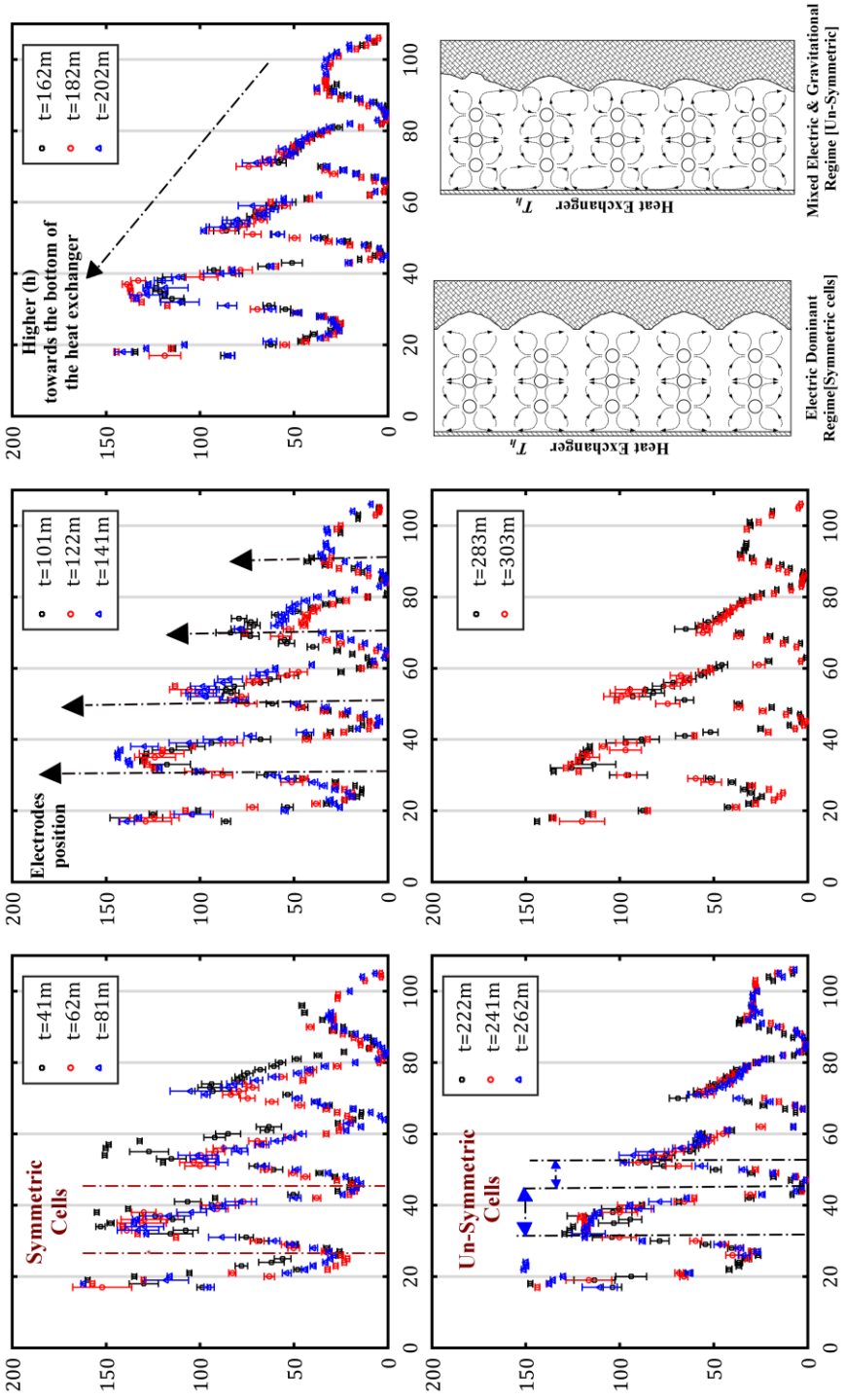

Figure 6.18 Heat transfer coefficient measurement along the left wall for Ra=9E7, Ste=0.0445 and V=+3 [kV]

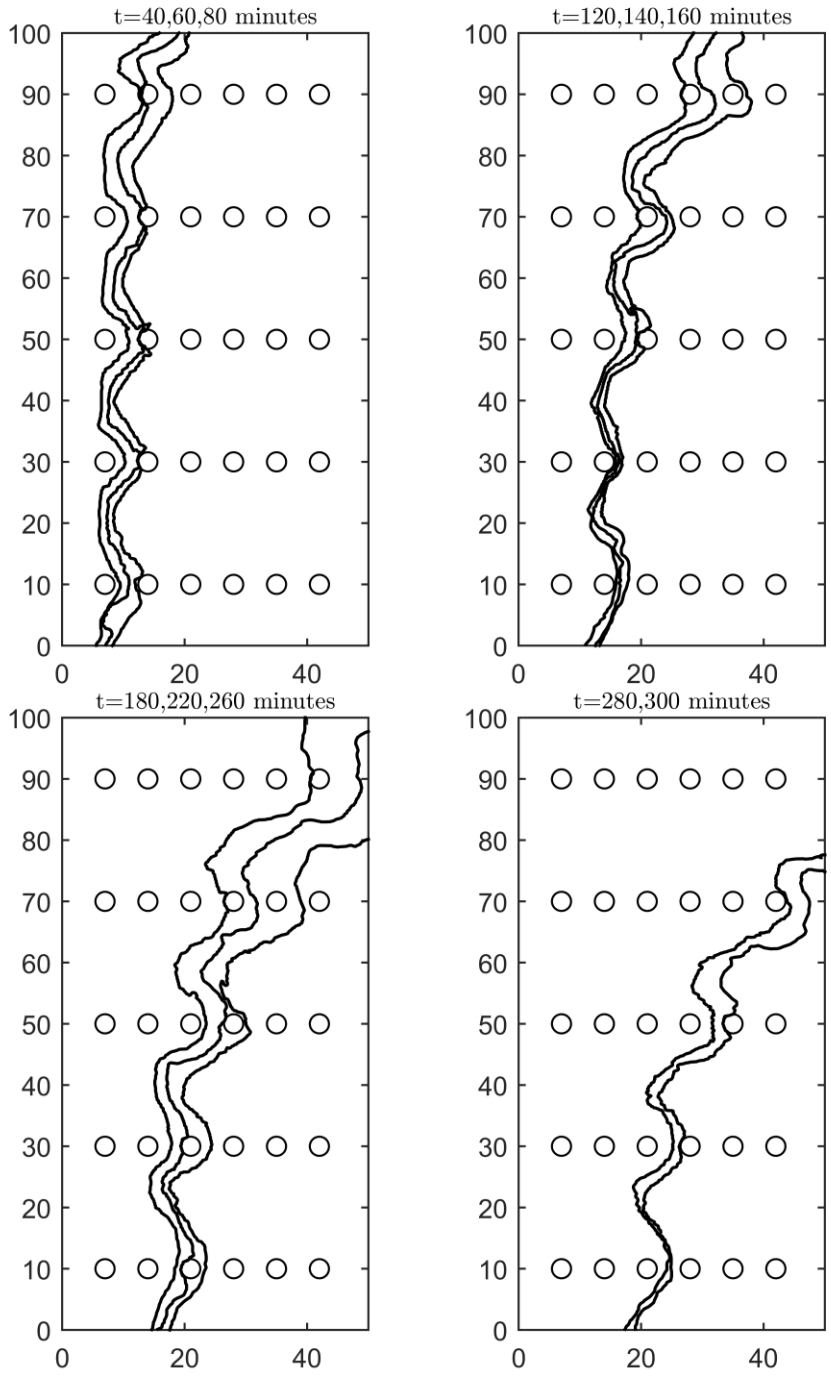

Figure 6.19 Melt front profiles timewise variation for Ra=9E7, Ste=0.0445 and V=+6 [kV]

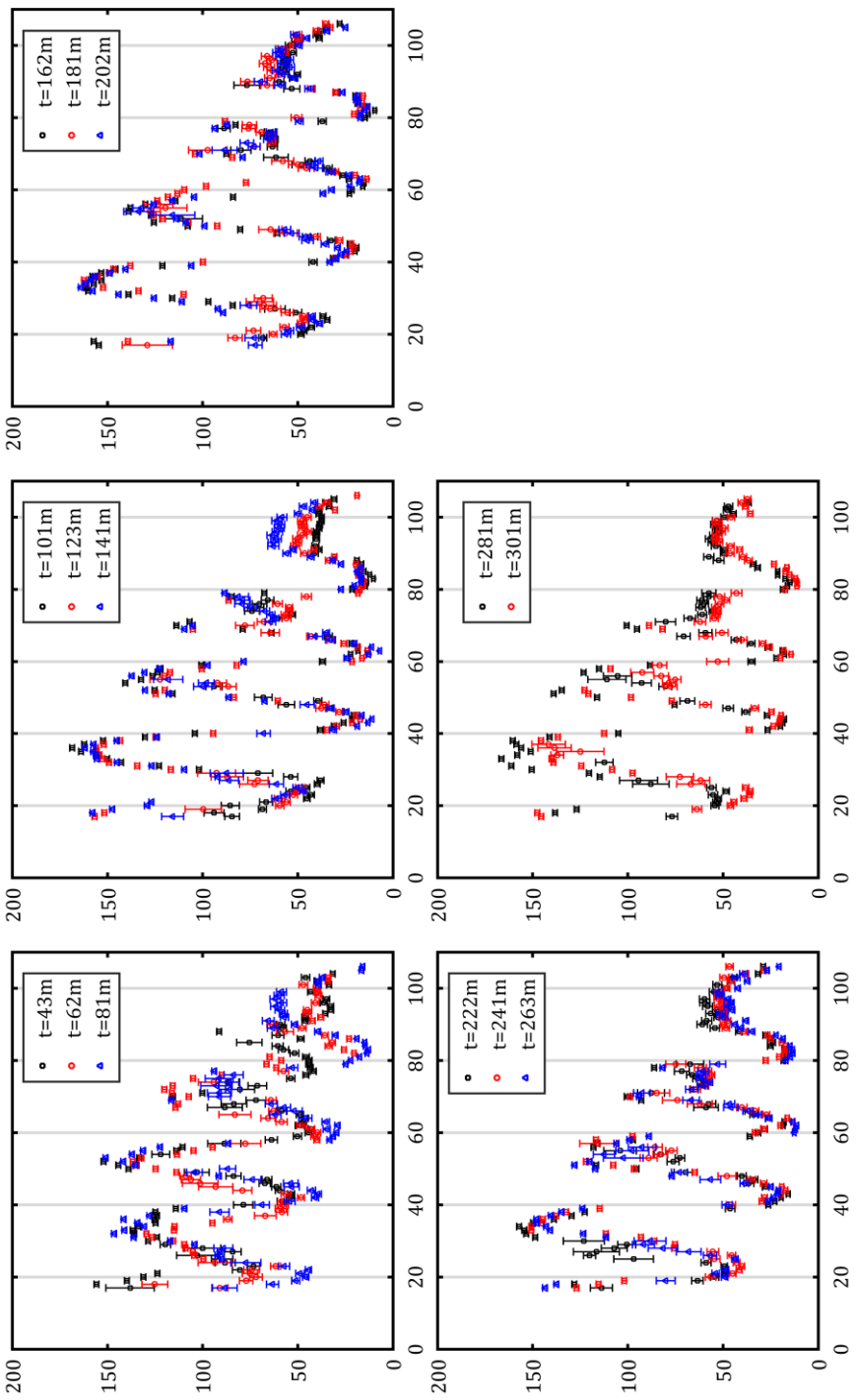

Figure 6.20 Heat transfer coefficient measurement along the left wall for Ra=9E7, Ste=0.0445 and V=+6 [kV]

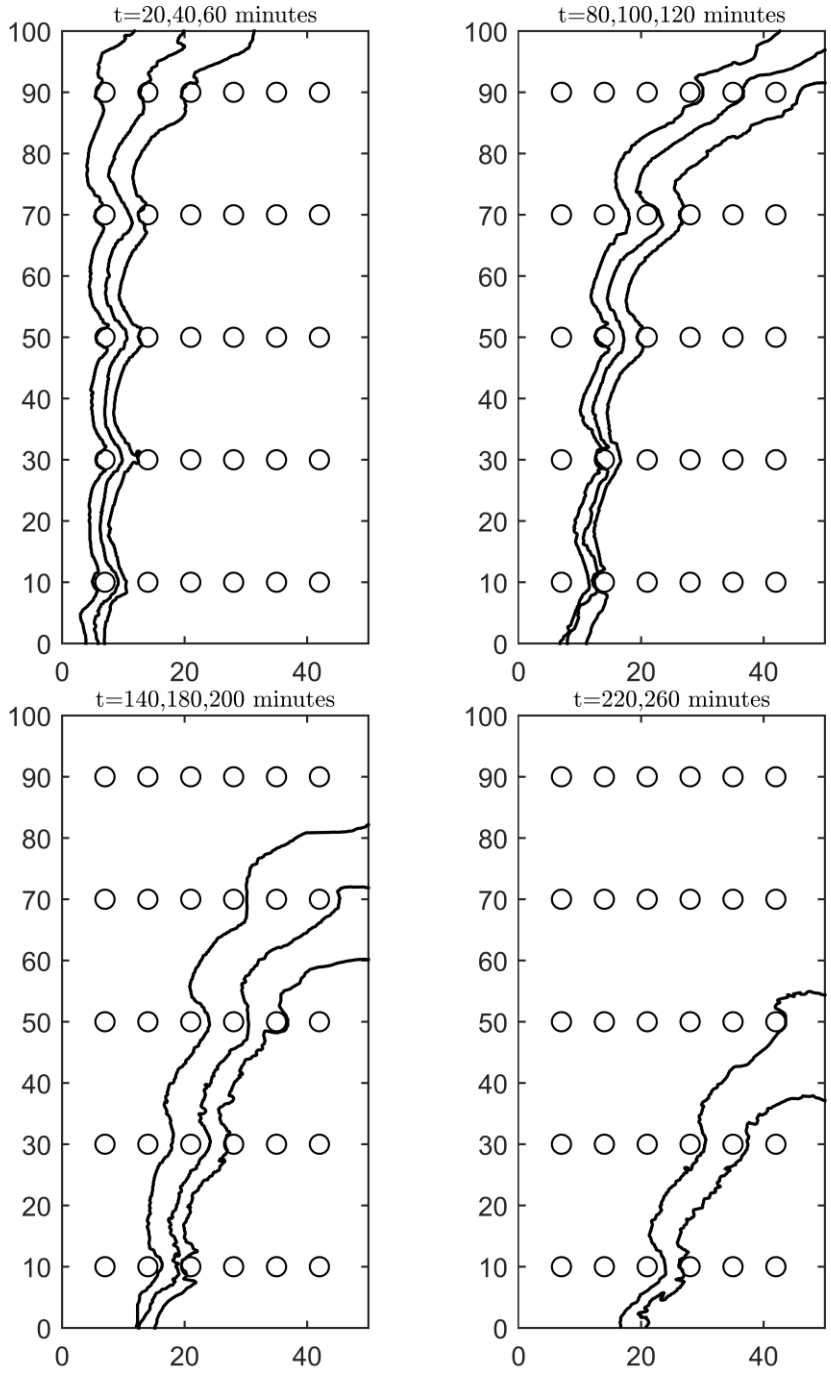

Figure 6.21 Melt front profiles timewise variation for Ra=1.8E8, Ste=0.089 and V=+2 [kV]

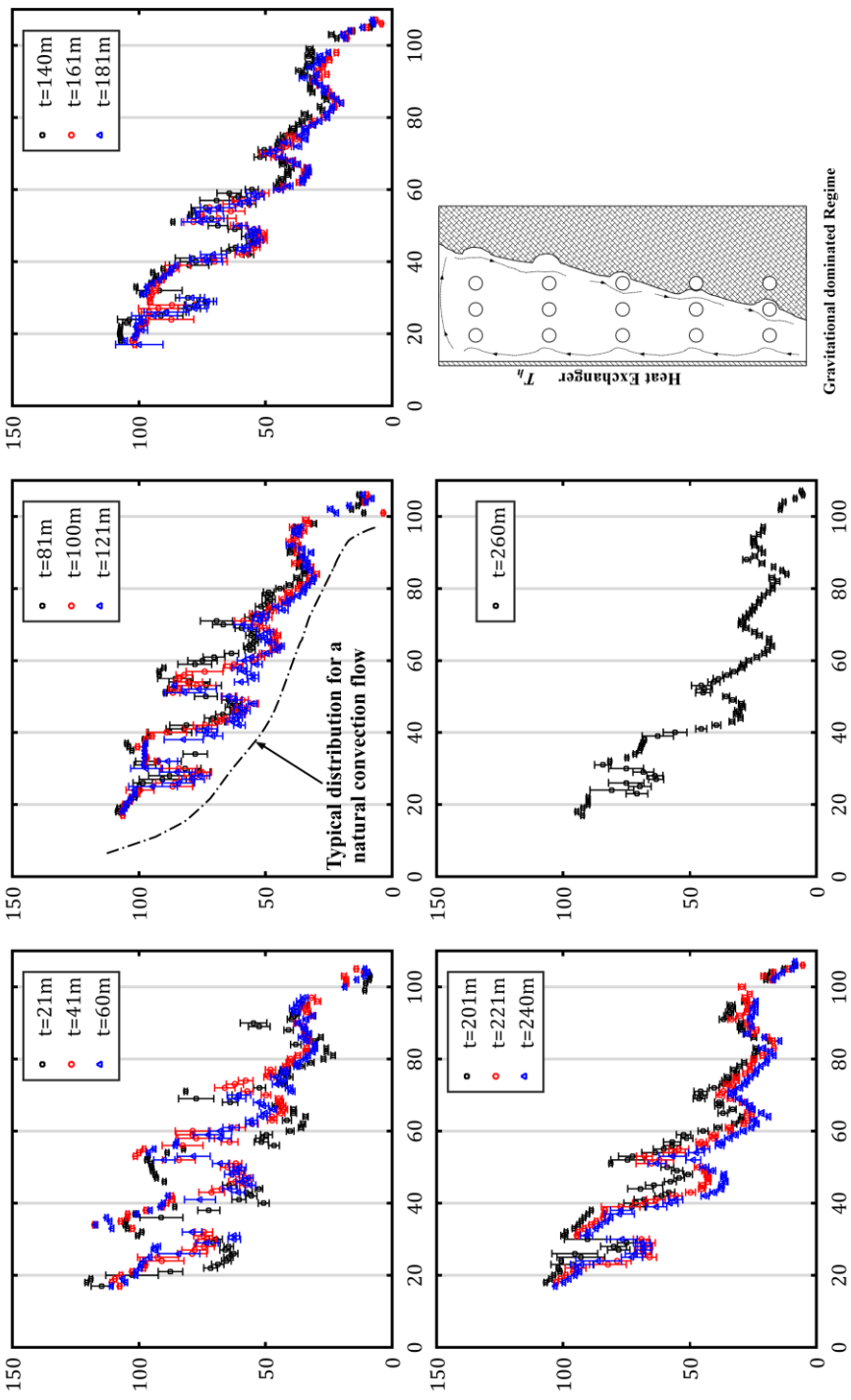

Figure 6.22 Heat transfer coefficient measurement along the left wall for Ra=1.8E8, Ste=0.089 and V=+2 [kV]

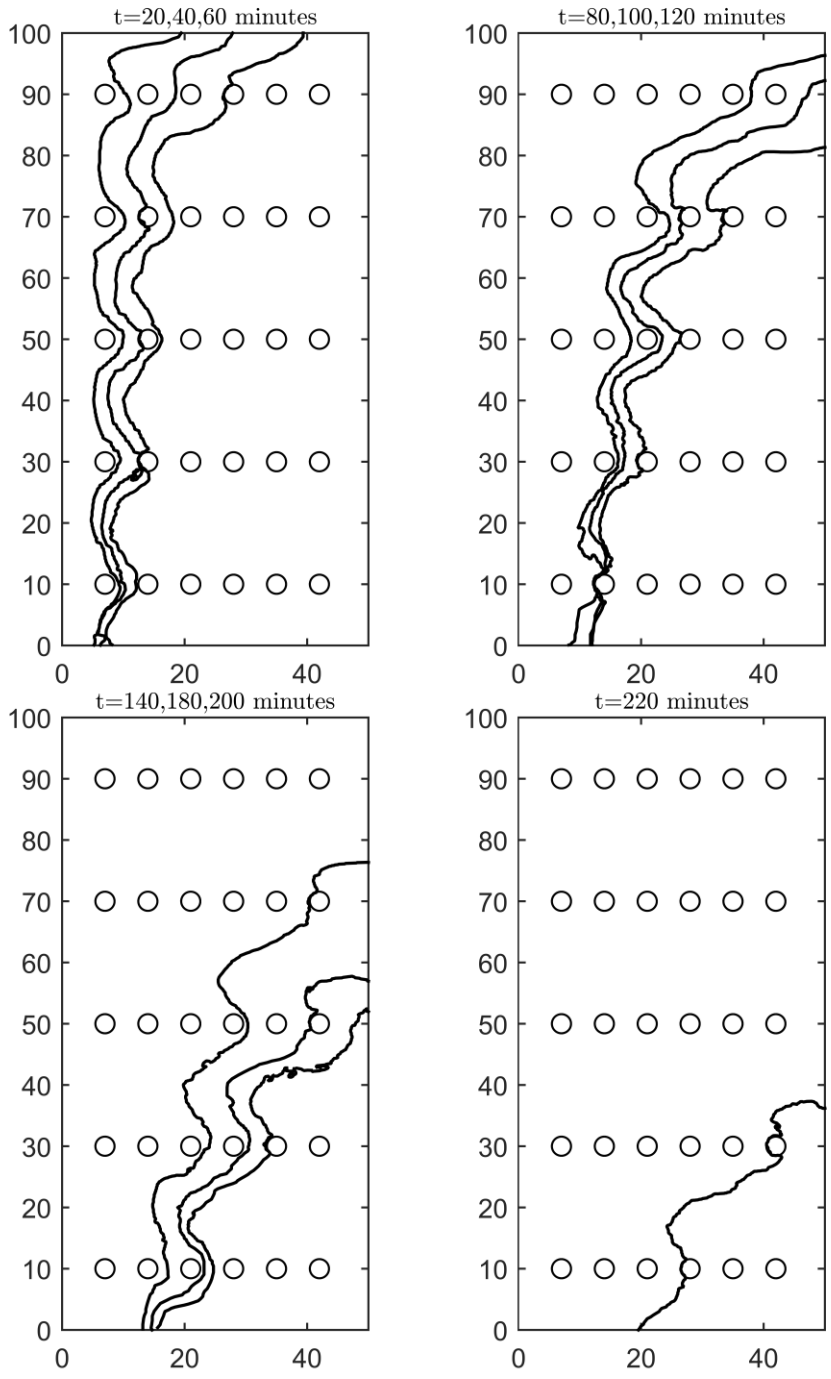

Figure 6.23 Melt front profiles timewise variation for Ra=1.8E8, Ste=0.089 and V=+4 [kV]

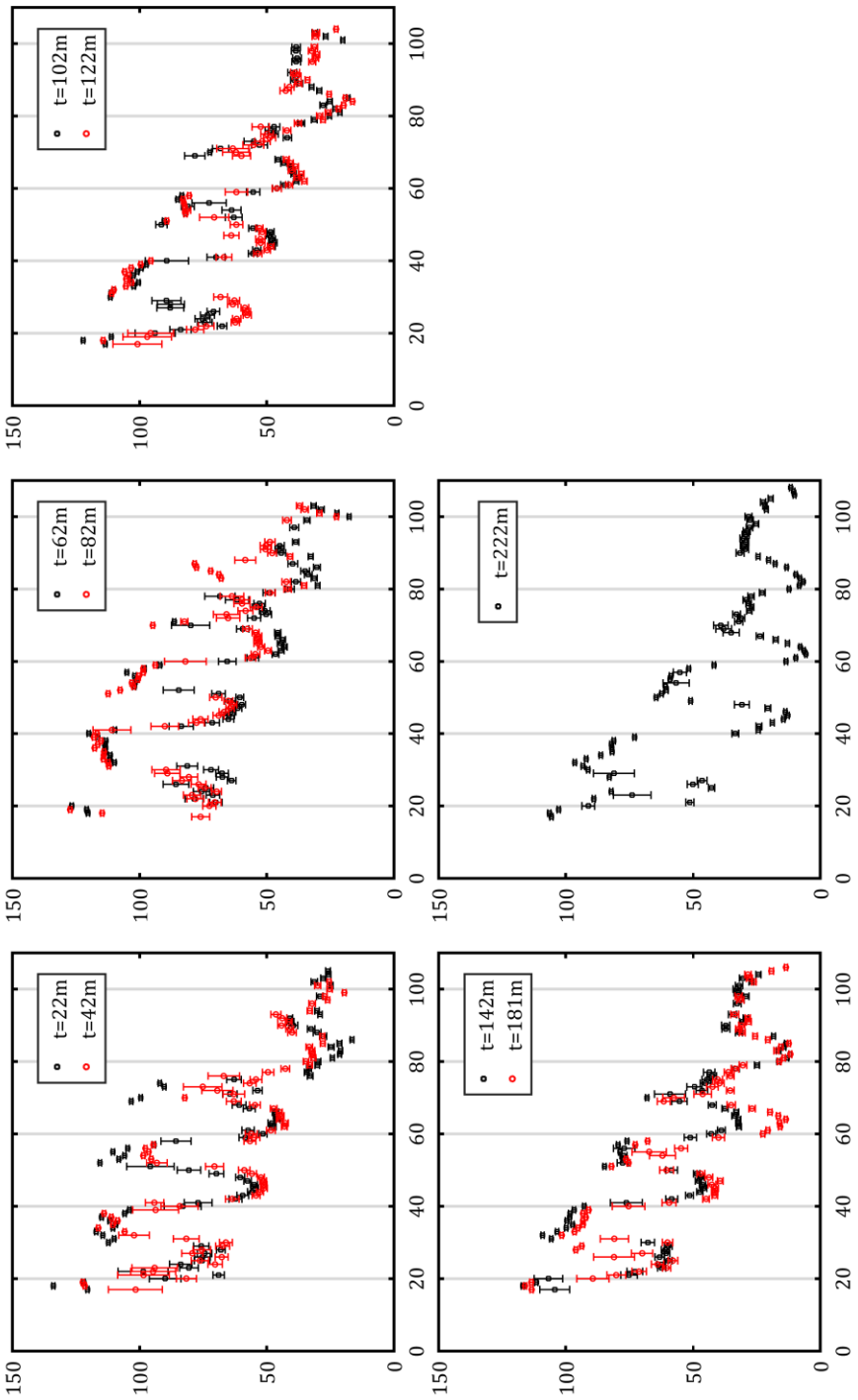

Figure 6.24 Heat transfer coefficient measurement along the left wall for Ra=1.8E8, Ste=0.089 and V=+4 [kV]

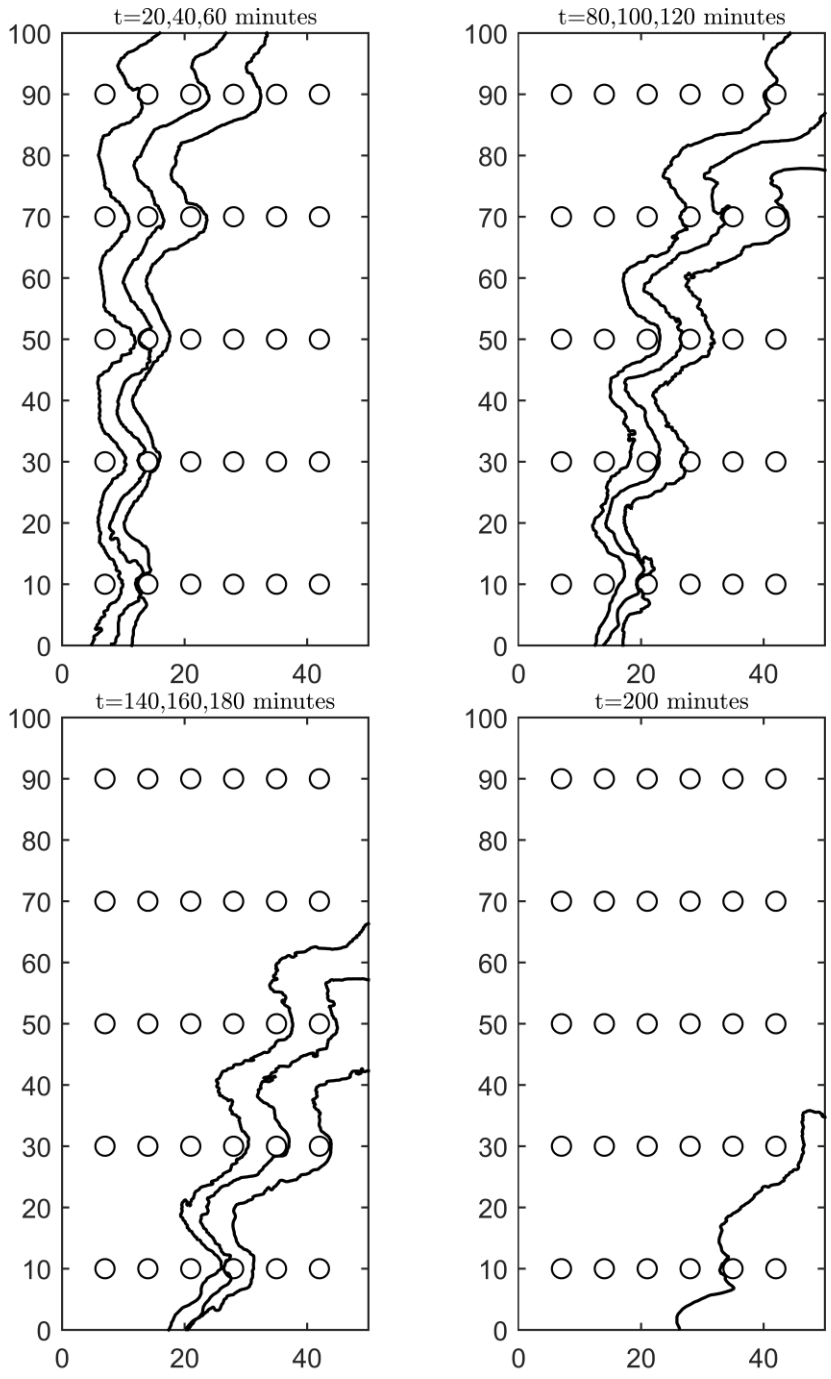

Figure 6.25 Melt front profiles timewise variation for Ra=1.8E8, Ste=0.089 and V=+6 [kV]

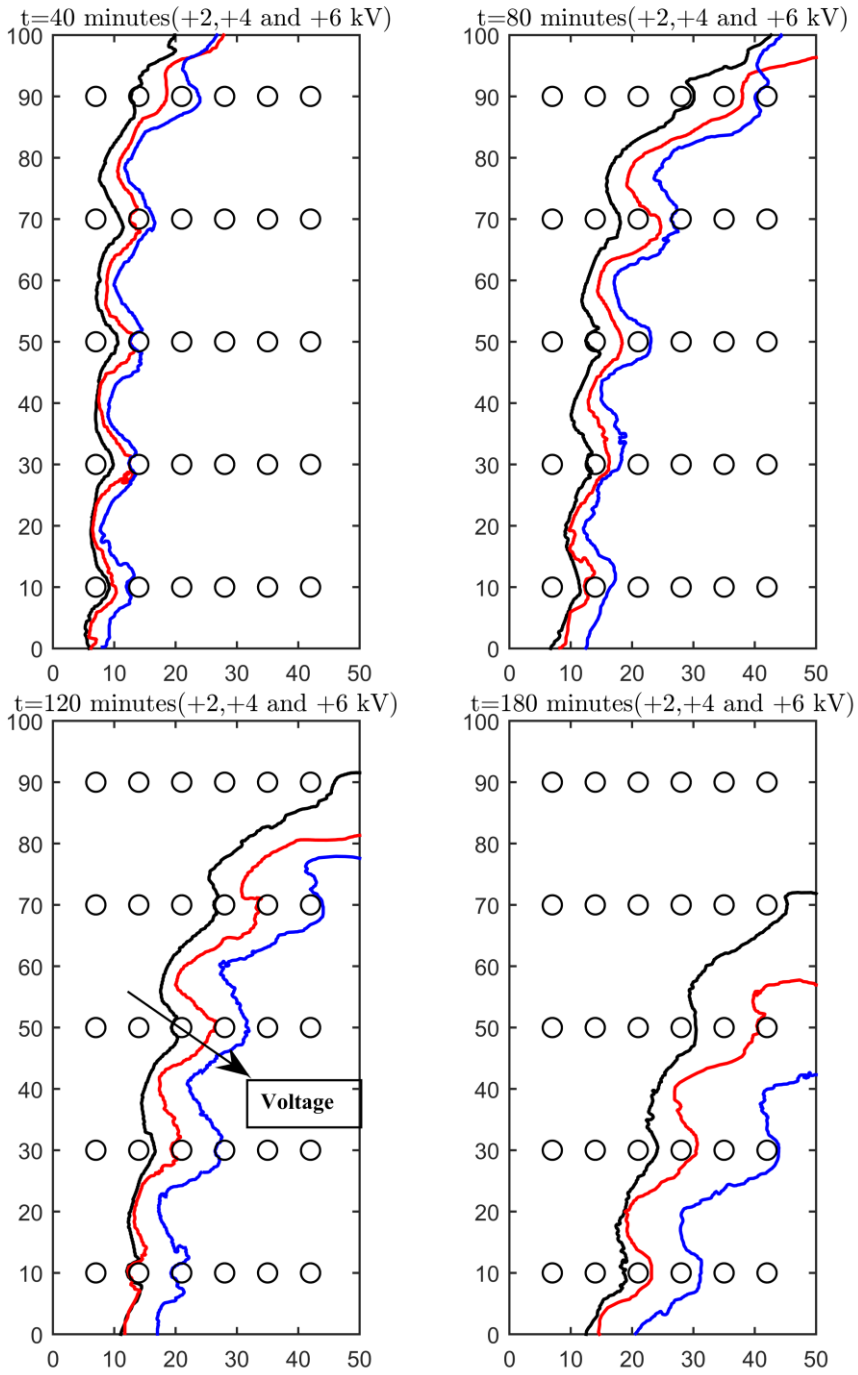

Figure 6.26 Melt front profiles comparison at different applied voltage [+2, +4 and +6 kV] for Ra=1.8E8 and Ste=0.089

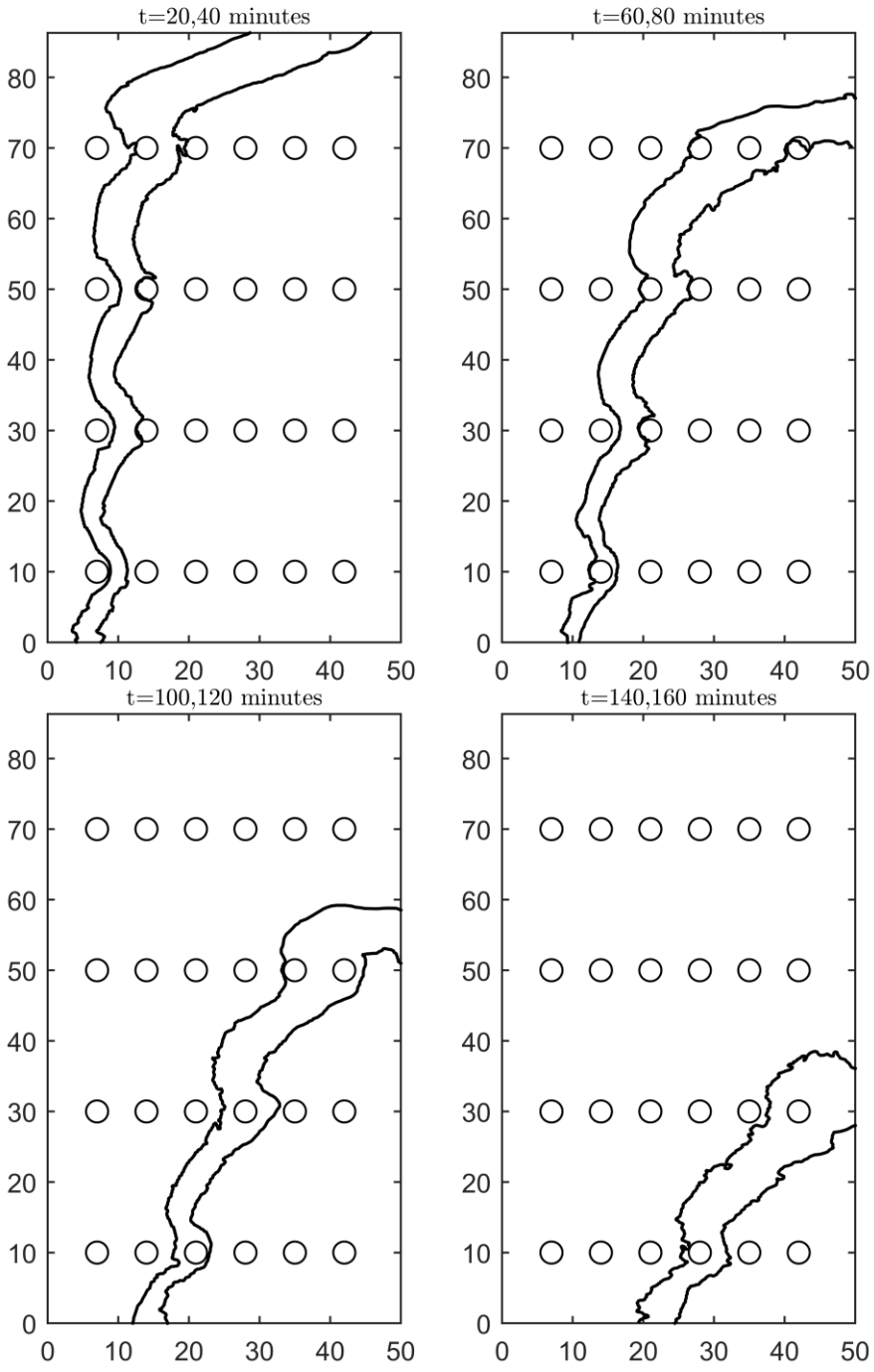

Figure 6.27 Melt front profiles timewise variation for Ra=1.8E8, Ste=0.13 and V=+2 [kV]

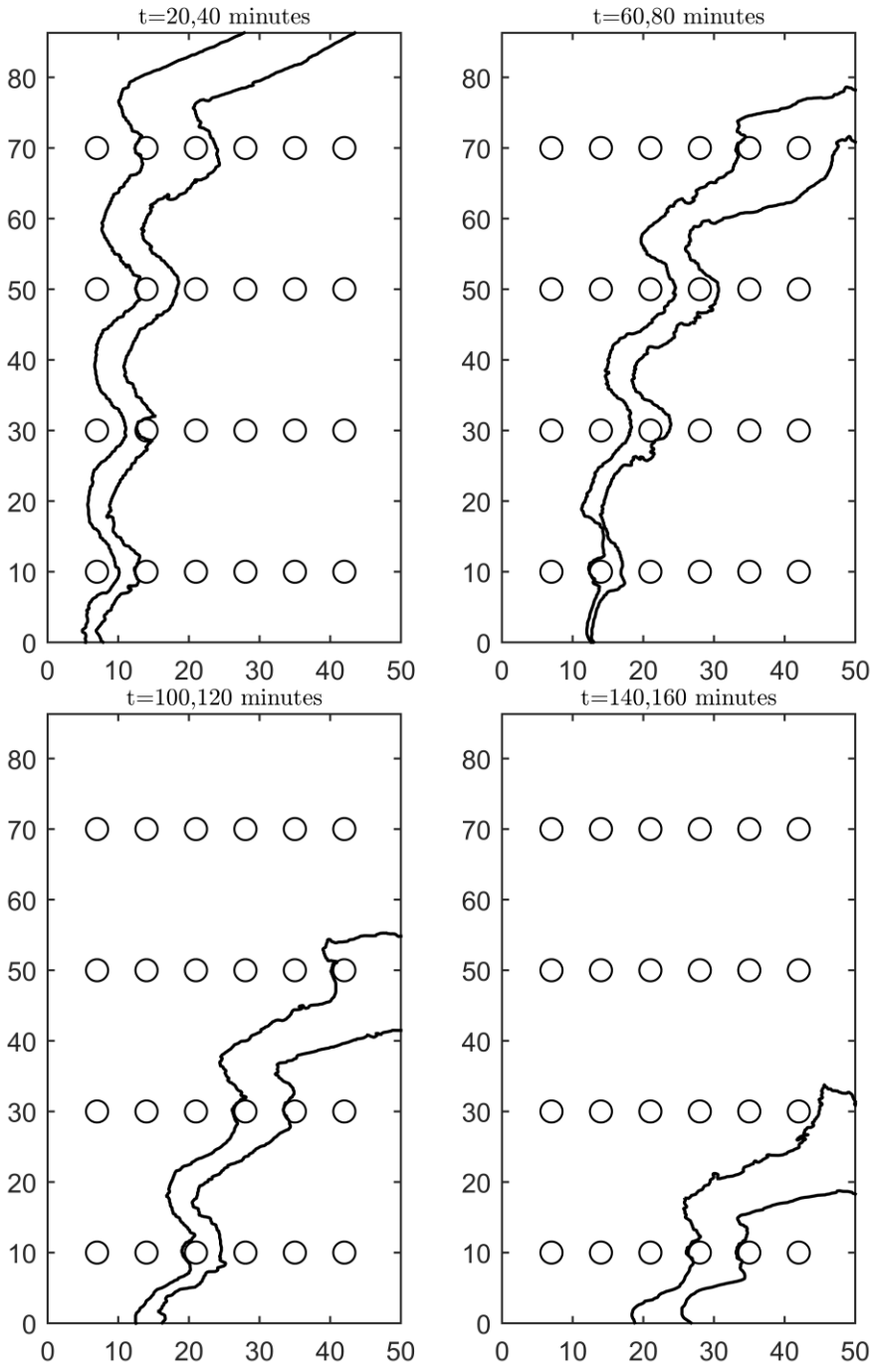

Figure 6.28 Melt front profiles timewise variation for Ra=1.8E8, Ste=0.13 and V=+4 [kV]

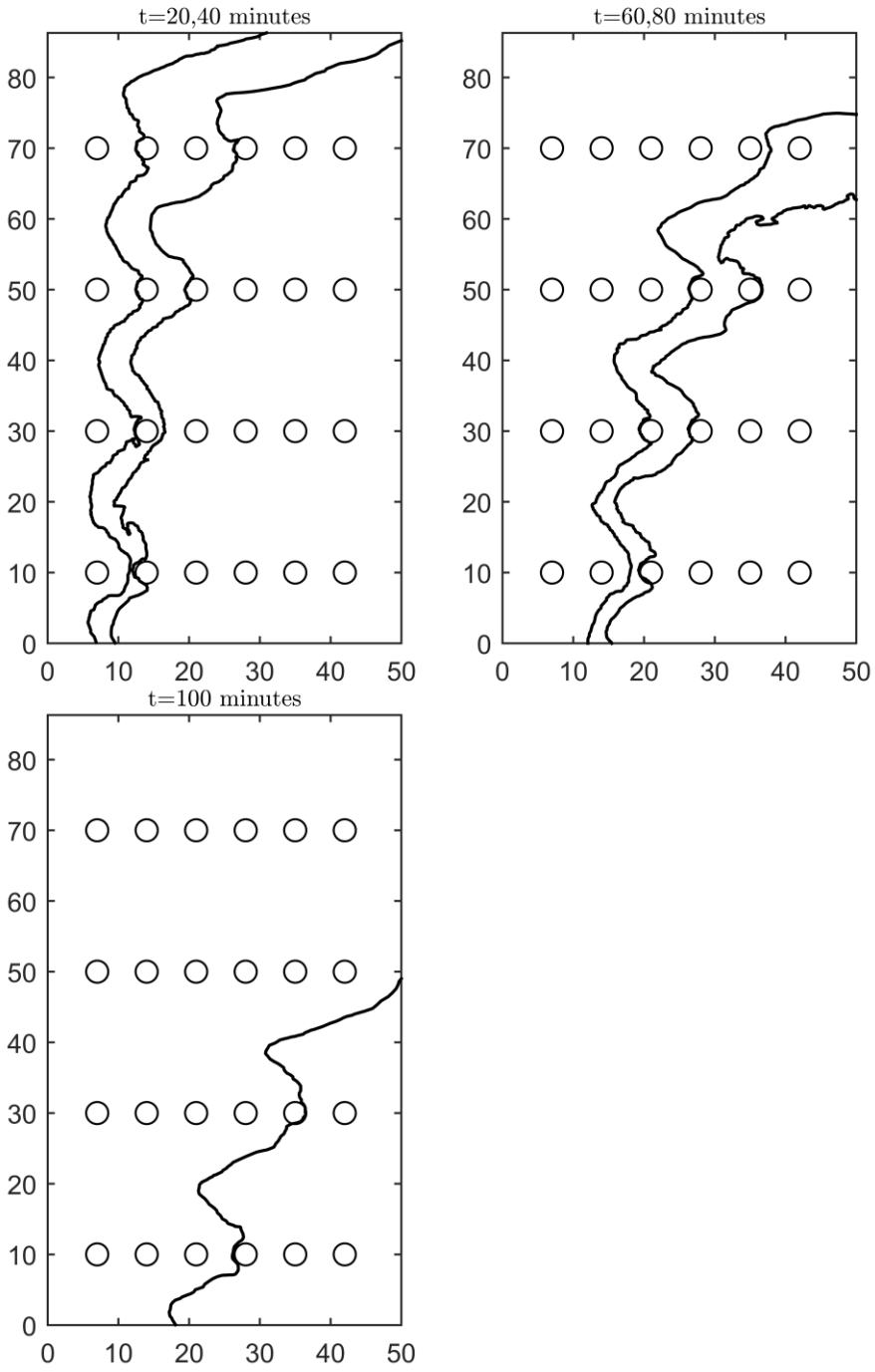

Figure 6.29 Melt front profiles timewise variation for Ra=1.8E8, Ste=0.13 and V=+6 [kV]

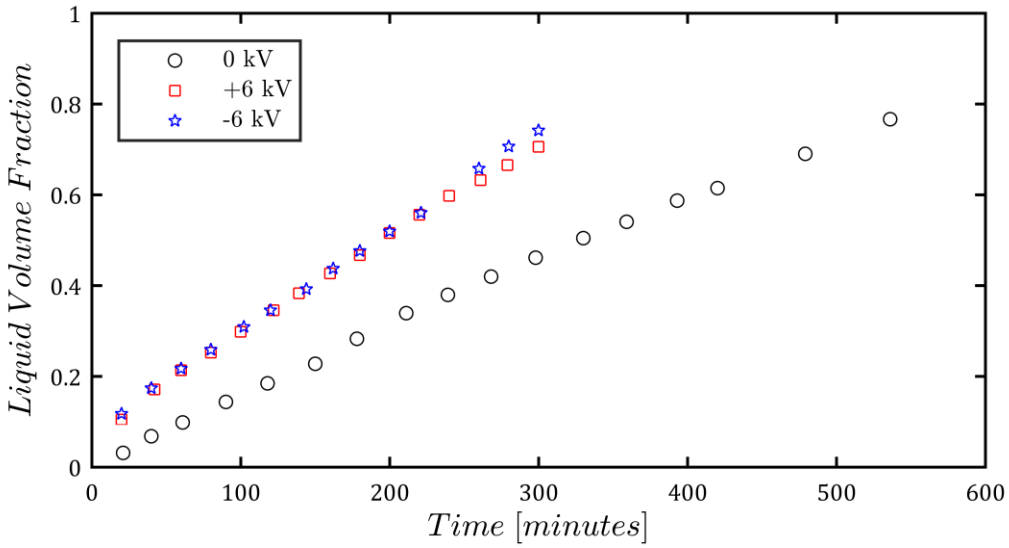

Figure 6.30 Liquid volume fraction temporal progress for Ra=9E7, Ste=0.0445. The effect of voltage polarity [+6, -6 kV vs 0 kV]

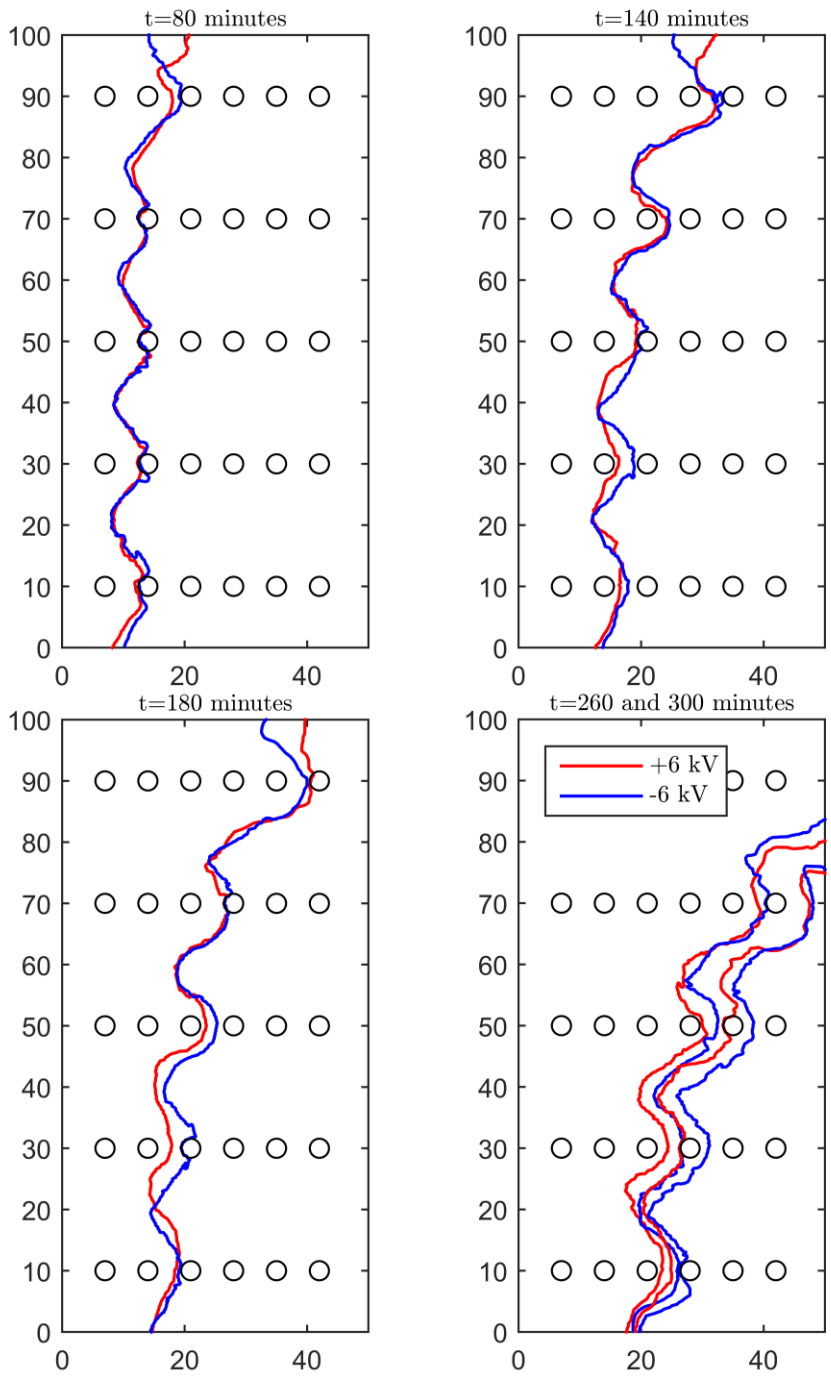

Figure 6.31 Comparison of temporal melt front profiles upon changing the polarity of the applied voltage [+6 vs -6 kV] for Ra=9E7 and Ste=0.0445

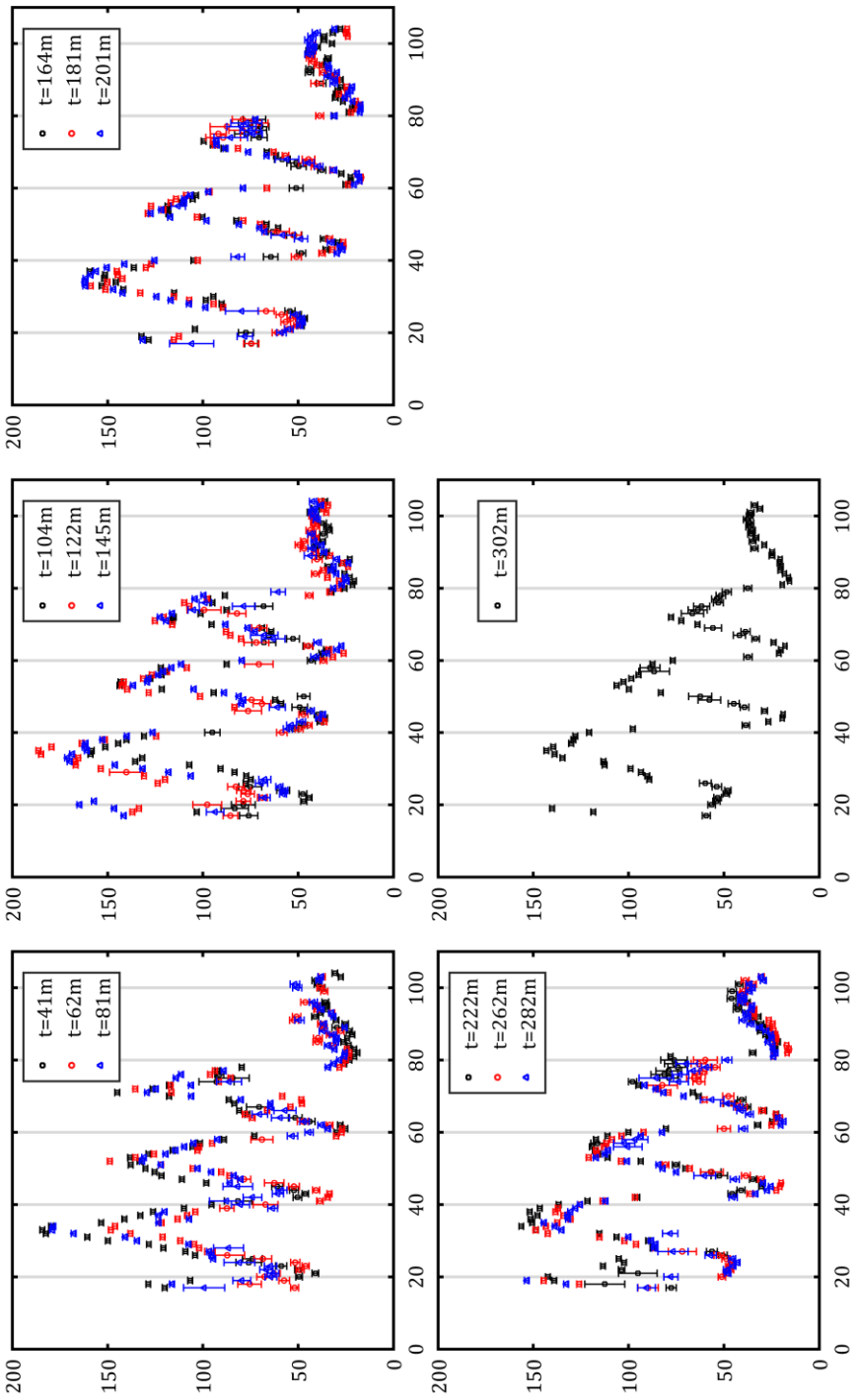

Figure 6.32 Heat transfer coefficient measurement along the left wall for Ra=9E7, Ste=0.0445 and V=-6 [kV]

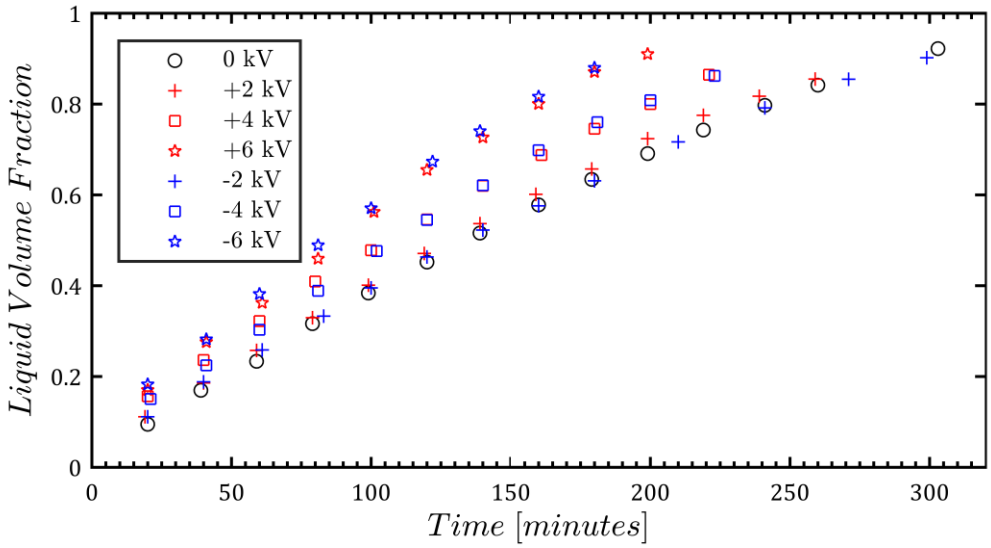

Figure 6.33 The effect of voltage polarity on liquid volume fraction temporal progress for Ra=1.8E8, Ste=0.089

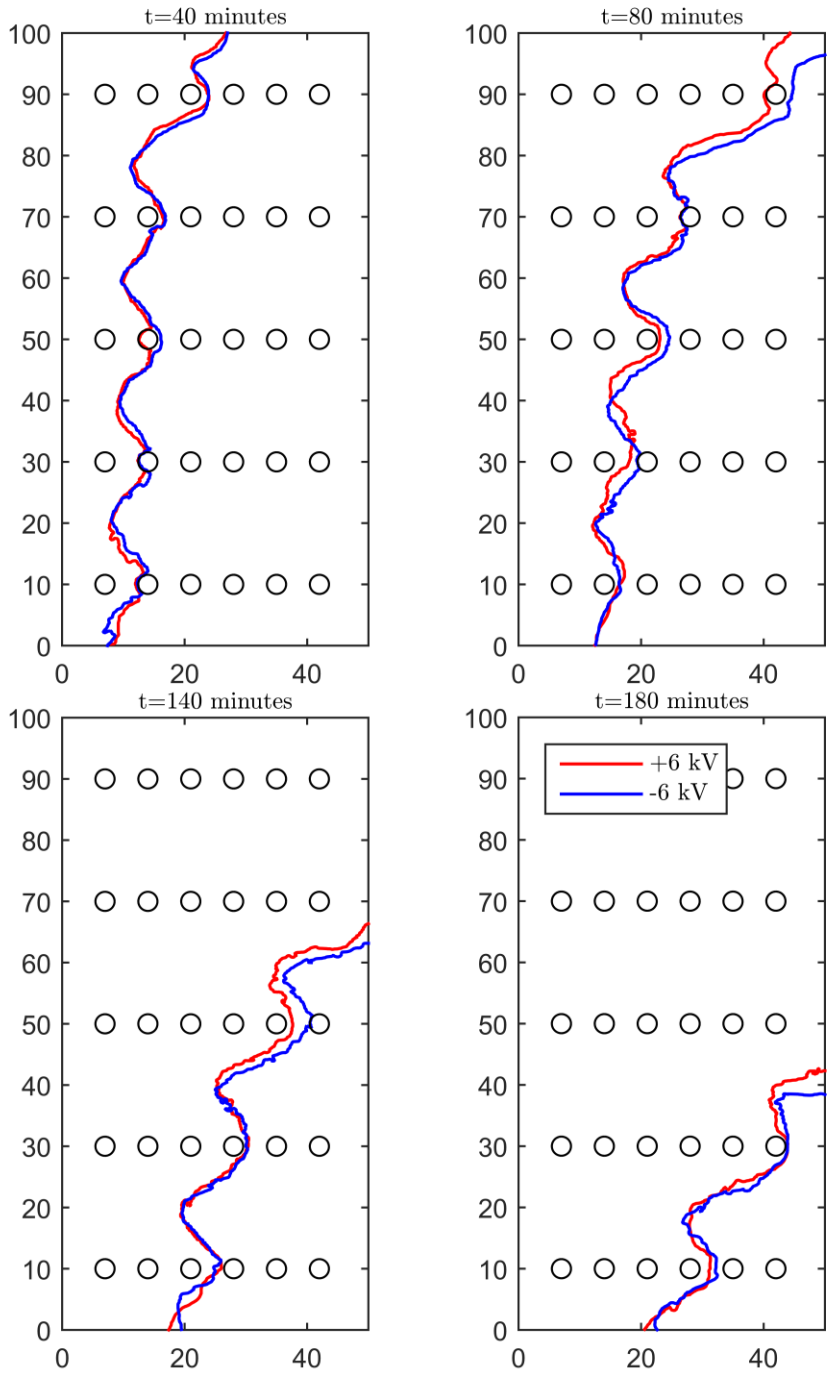

Figure 6.34 Comparison of temporal melt front profiles upon changing the polarity of the applied voltage [+6 vs -6 kV] for Ra=1.8E8 and Ste=0.089

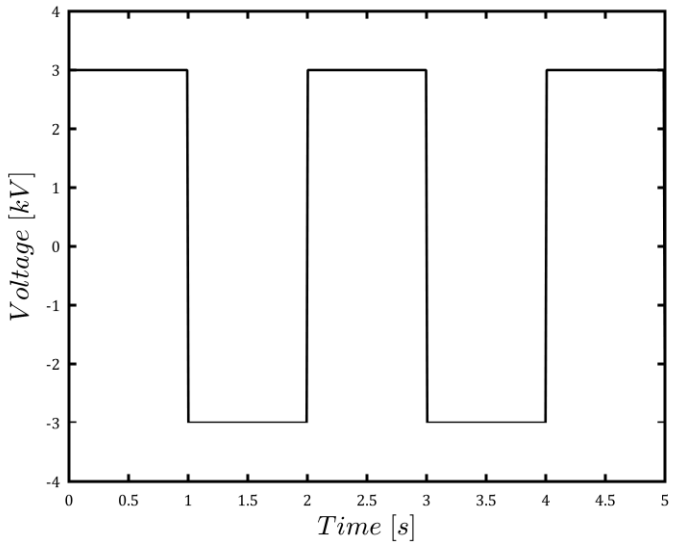

Figure 6.35 Square waveform of 3 kV amplitude and 0.5 Hz frequency

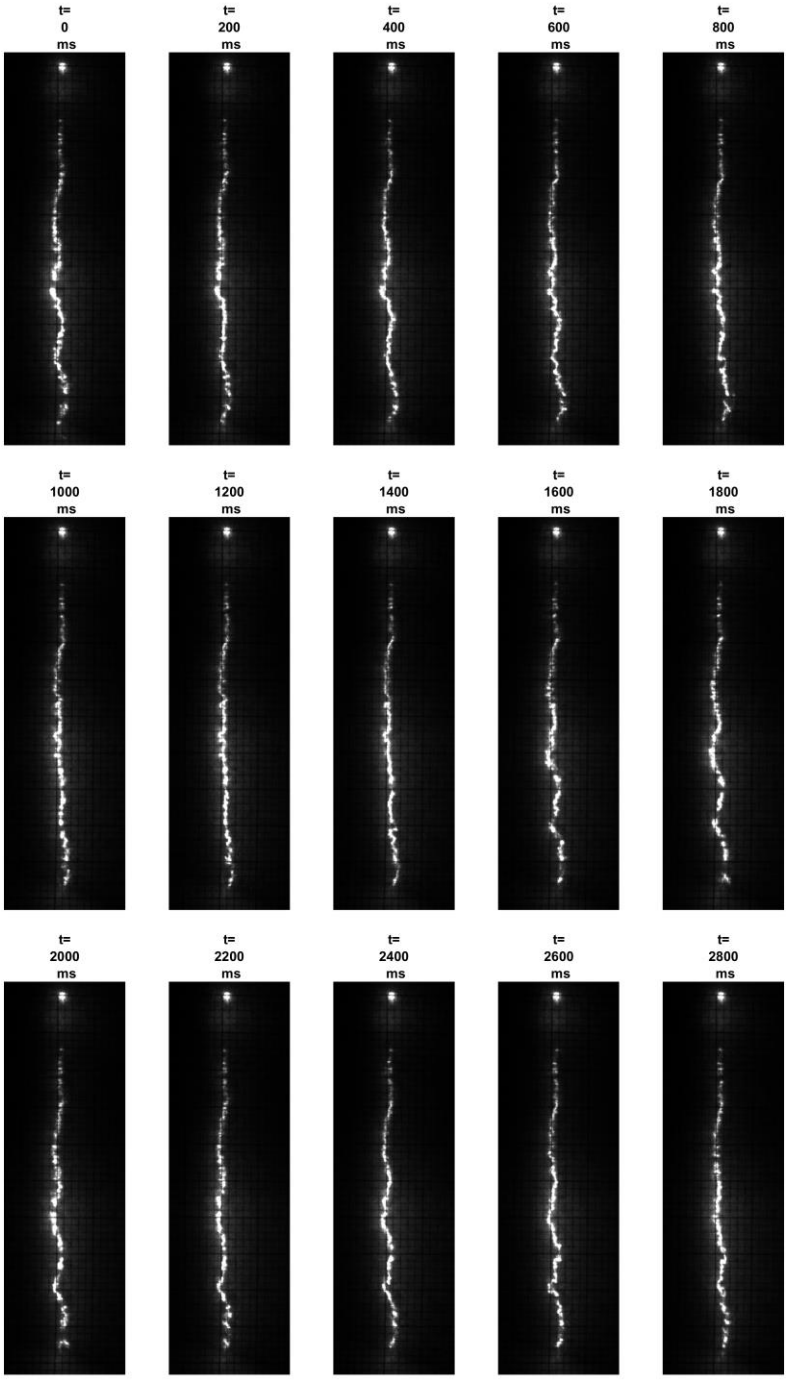

Figure 6.36 shadowgraph measurement transient response for an applied 3 kV square wave with frequency of 0.5 Hz

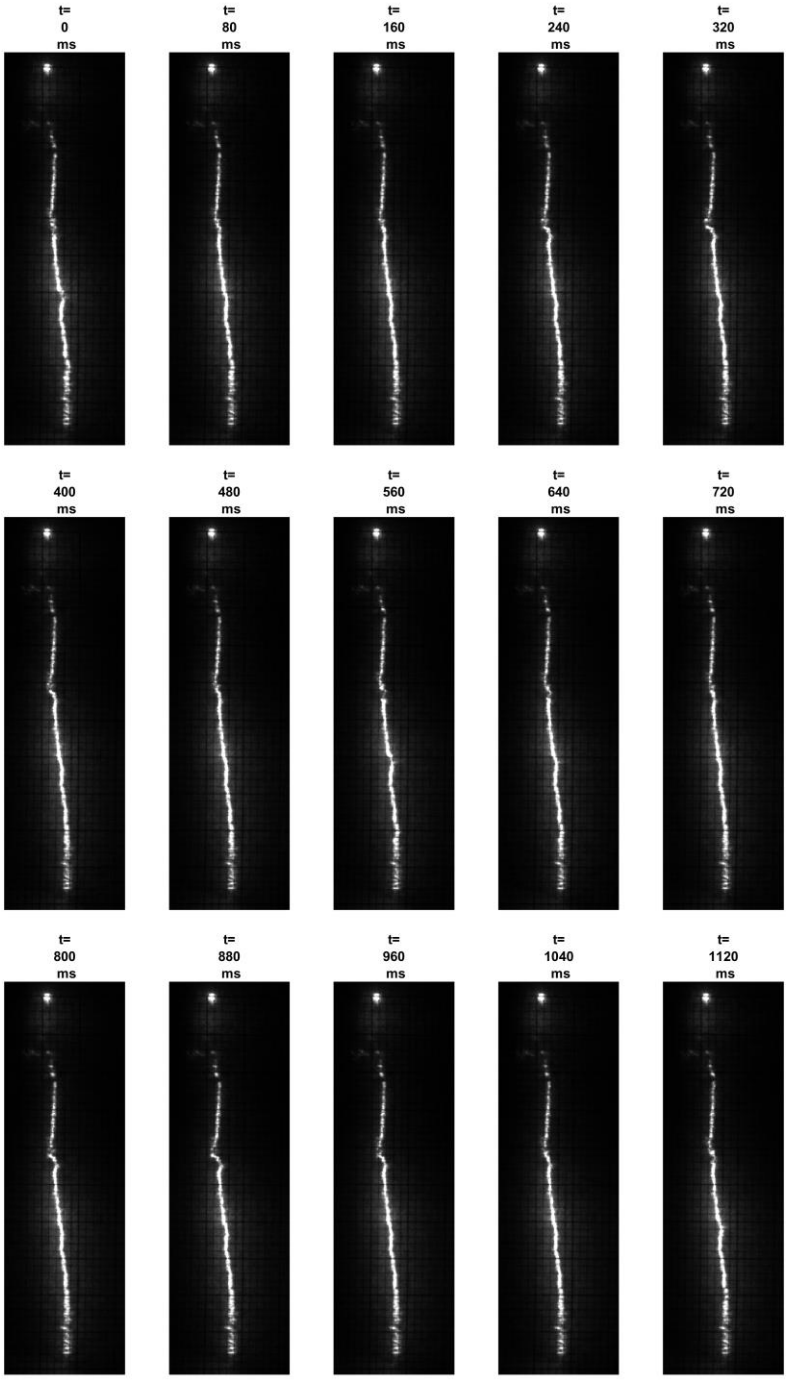

Figure 6.37 Shadowgraph measurement transient response for an applied 3 kV square wave with frequency of 1.75 Hz

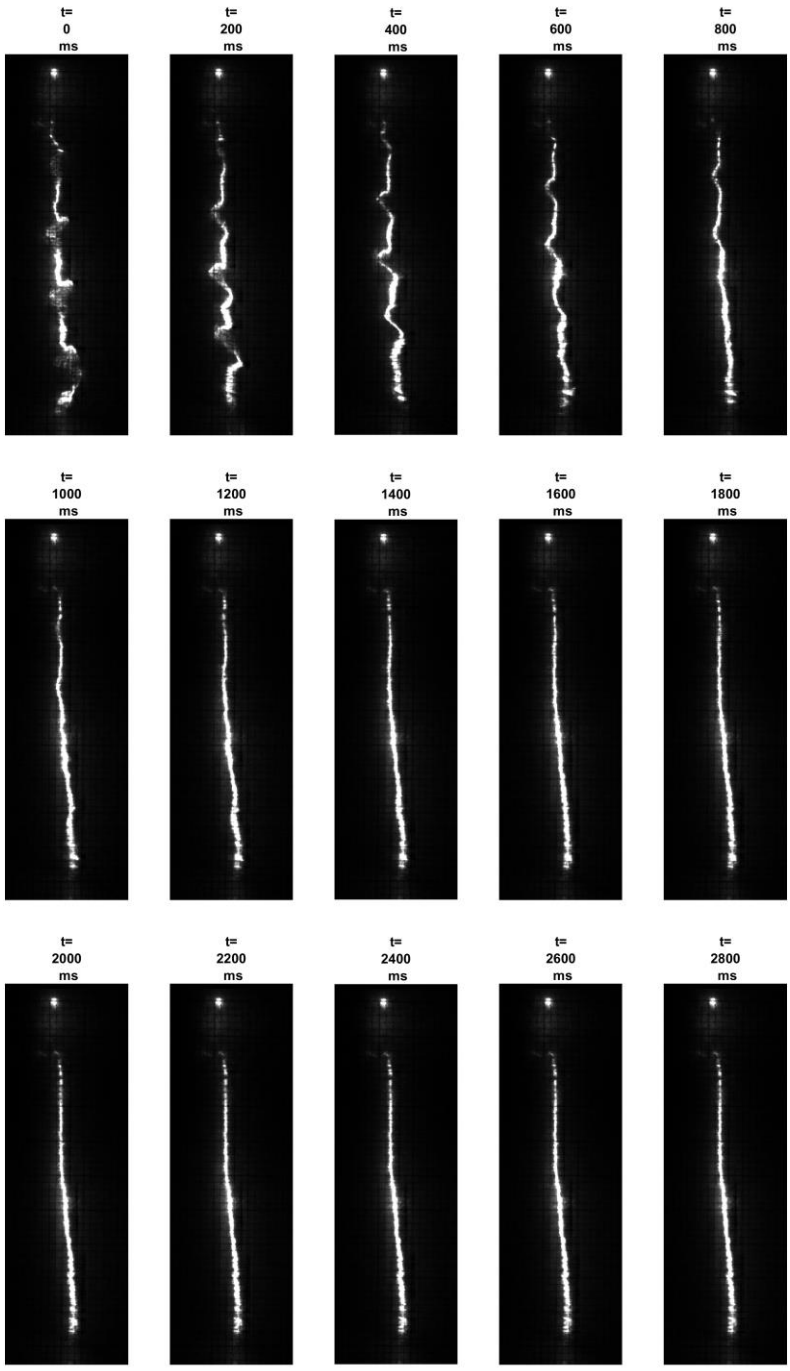

Figure 6.38 Shadowgraph measurement transient response for an applied 3 kV square wave with frequency of 20 Hz. [t=0 corresponds to -3 kV DC]

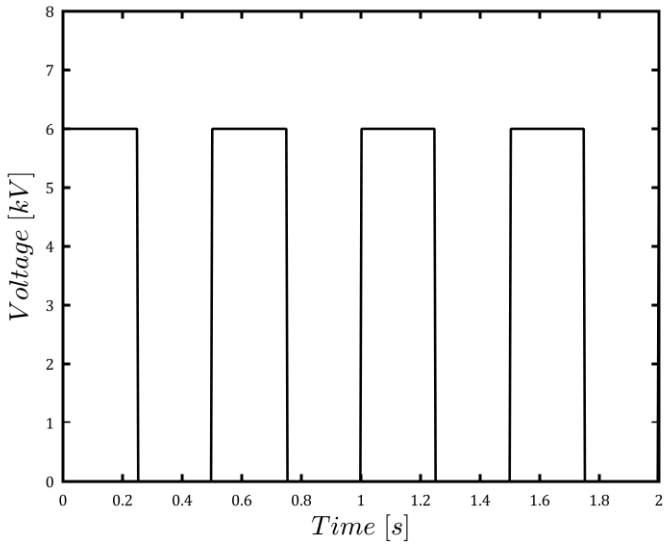

Figure 6.39 Pulse wave form of +6 kV amplitude and 2 Hz frequency

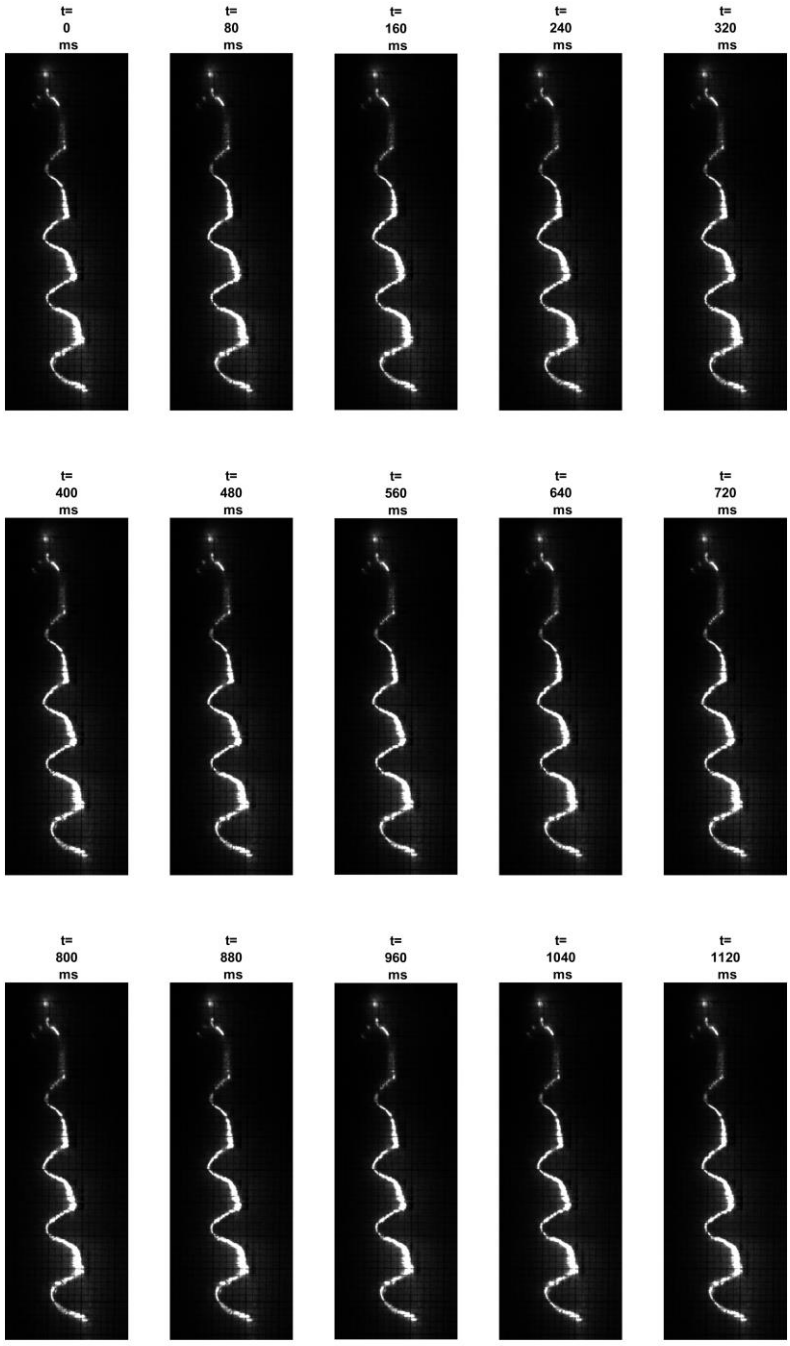

Figure 6.40 Shadowgraph measurement transient response for an applied 6 kV Pulse wave with frequency of 2 Hz and Duty cycle of 50%

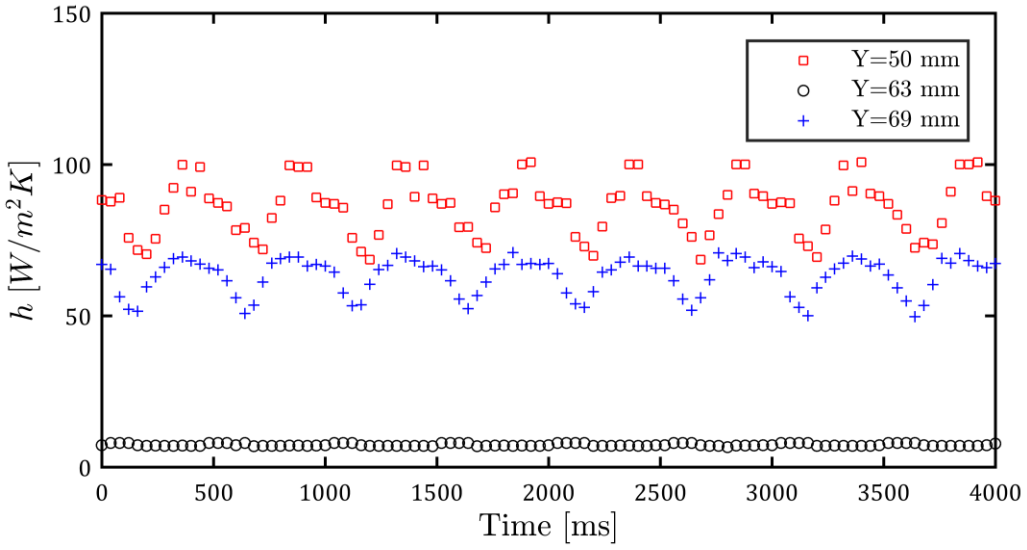

Figure 6.41 local heat transfer coefficient transient response for an applied pulse waveform of +6 kV amplitude and 2 Hz frequency for three positions along the heat exchanger wall

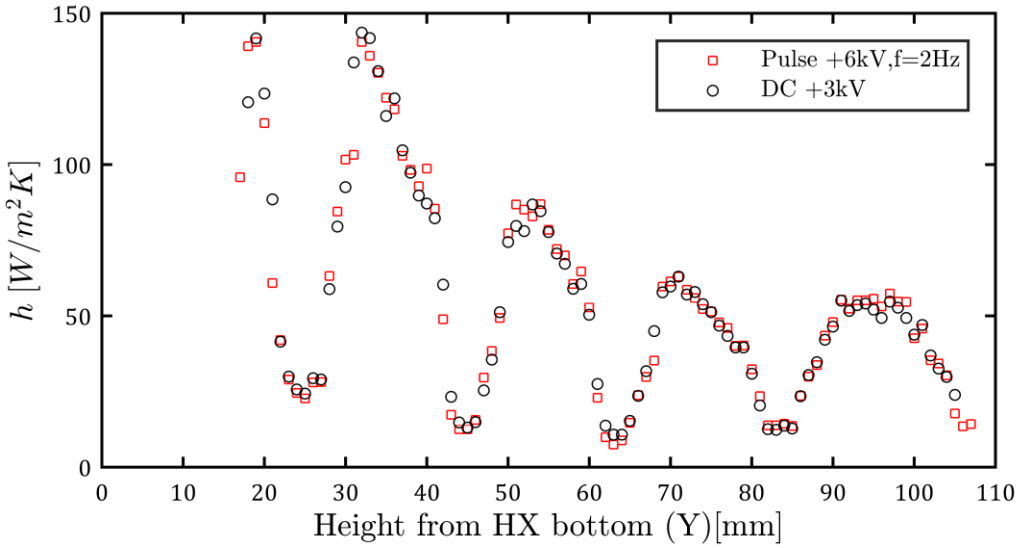

Figure 6.42 Local heat transfer coefficient distribution comparison between +6kV Pulse wave form and +3 kV DC

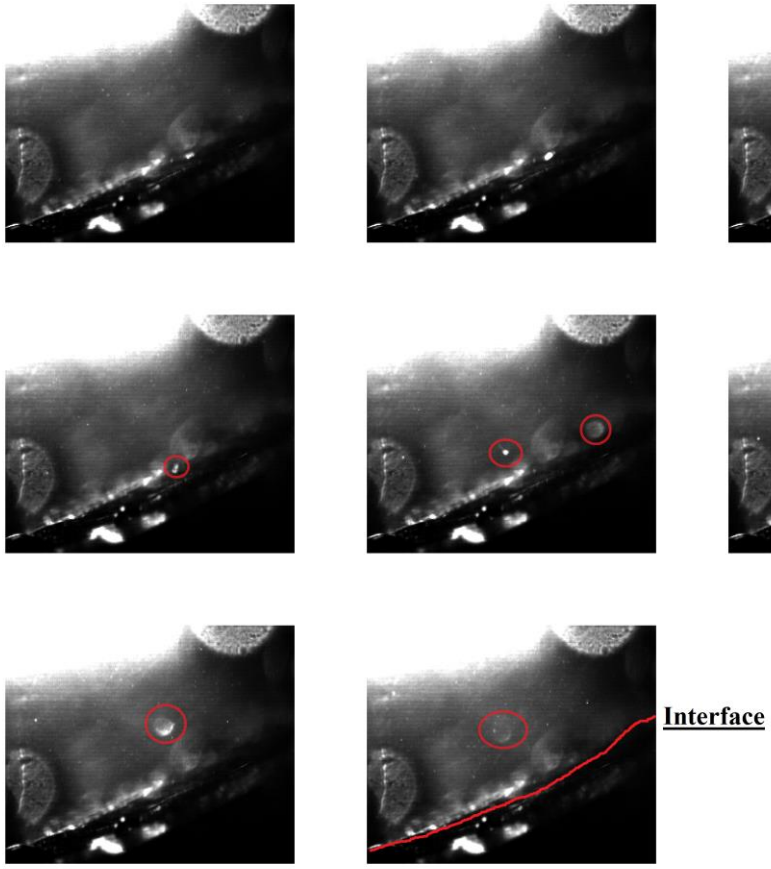

Figure 6.43 Interface high speed imaging for -6 kV DC applied voltage at Ra=1.8E8, Ste=0.089[dt= 240 ms]

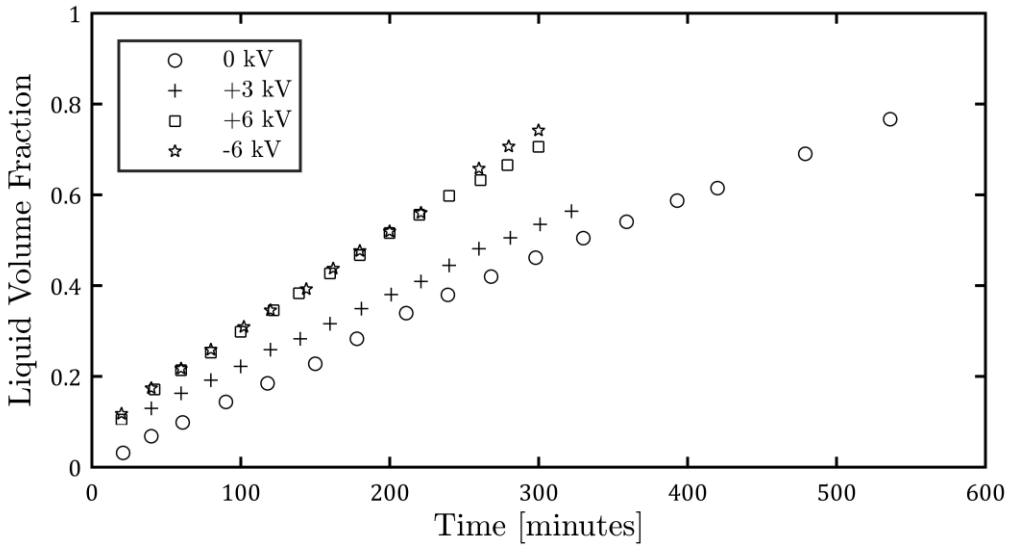

Figure 6.44 The liquid volume fraction temporal progress summary for the different applied voltages for Ra=9E7, Ste=0.0445

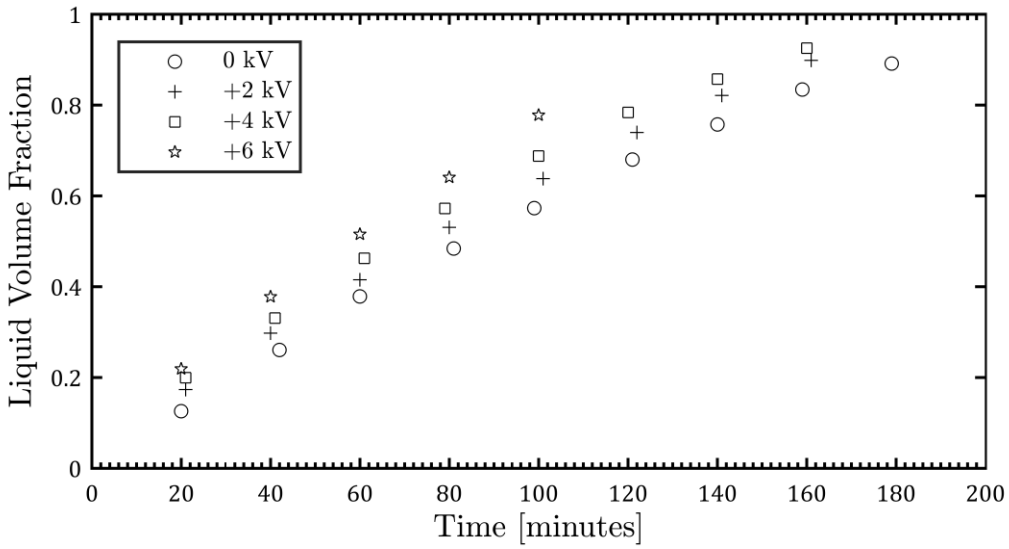

Figure 6.45 The liquid volume fraction temporal progress summary for the different applied voltages for Ra=1.8E8, Ste=0.13

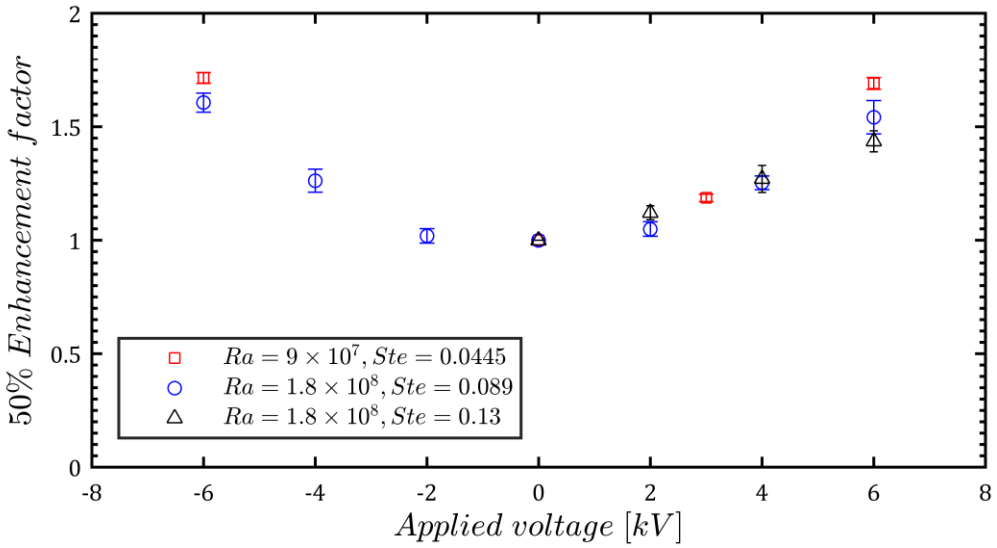

Figure 6.46 EHD enhancement factor vs applied voltage for the different Rayleigh cases

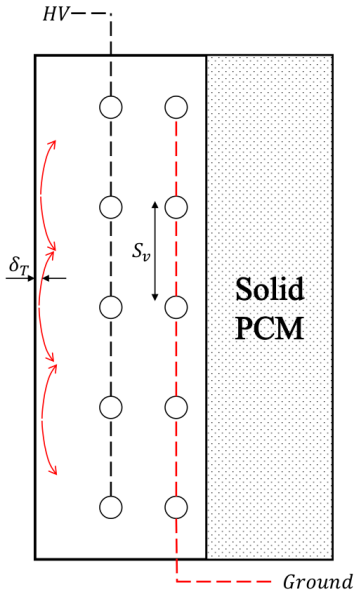

Figure 6.47 Schematic of the test cell and the important parameters used in scaling analysis

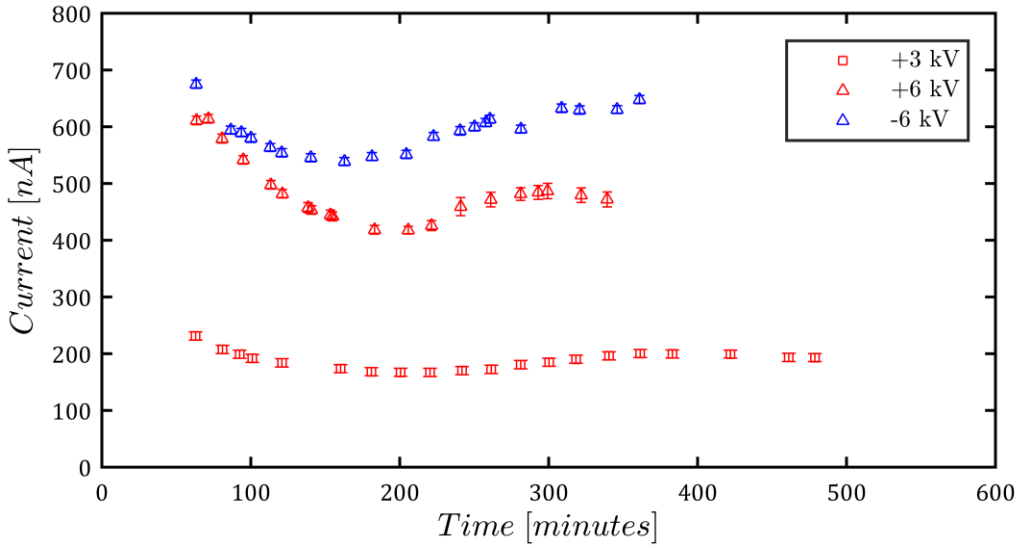

Figure 6.48 Temporal current measurement at different applied voltages for Ra=9E7, Ste=0.0445

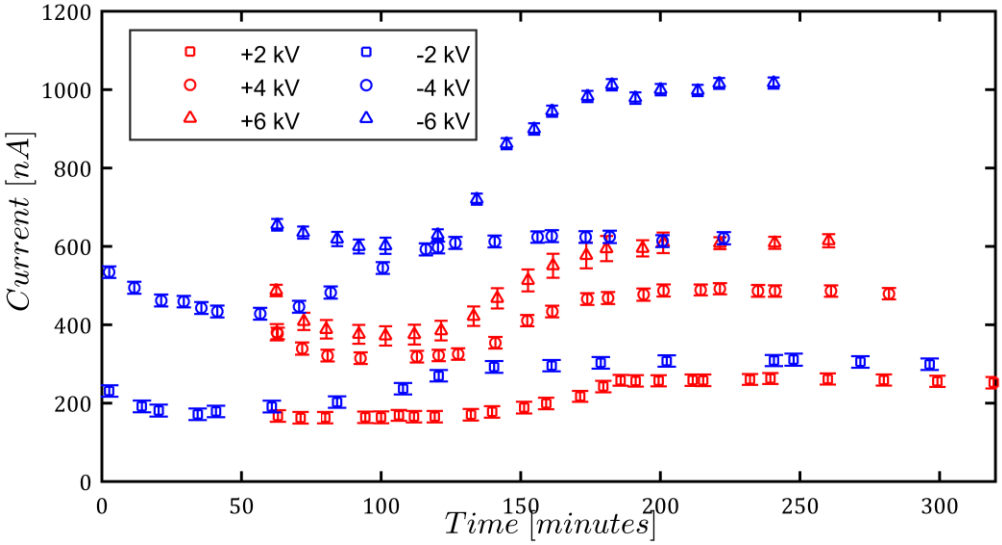

Figure 6.49 Temporal current measurement at different applied voltages for Ra=1.8E8, Ste=0.089

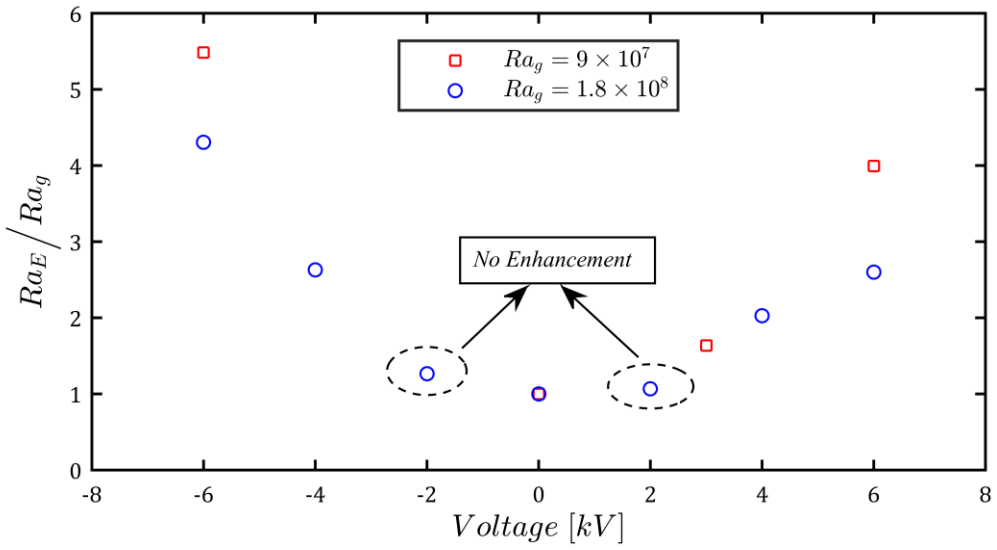

Figure 6.50 Ratio of conductive electrical Rayleigh number to gravitational Rayleigh number at the different applied voltages

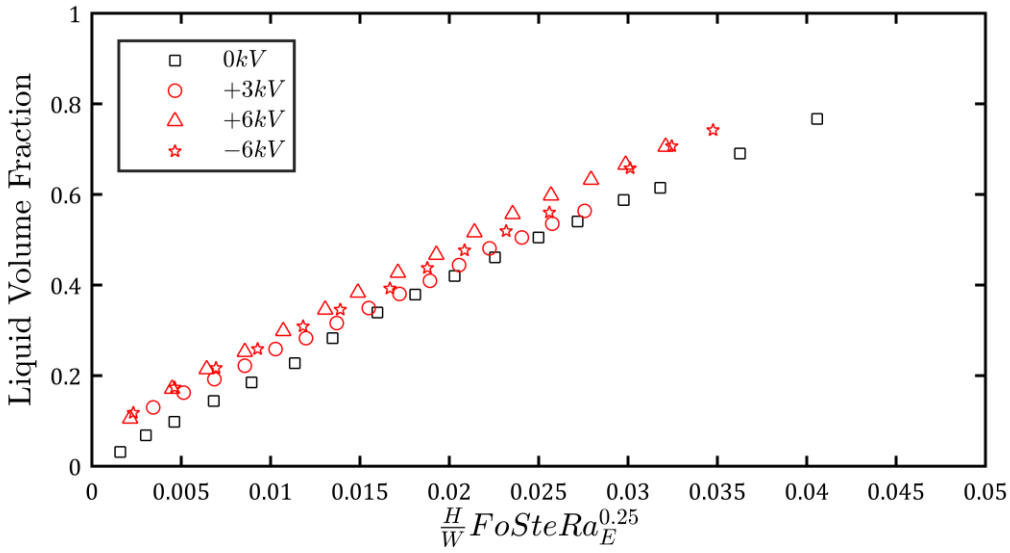

Figure 6.51 Melt volume fraction vs the dimensionless parameter for Rag=9E7

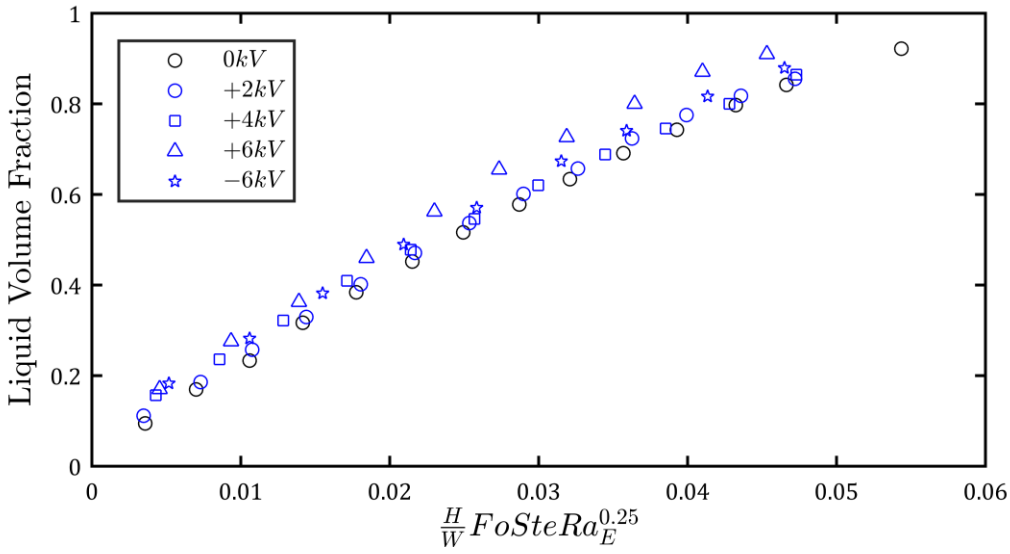

Figure 6.52 Melt volume fraction vs the dimensionless parameter for Rag=1.8E8

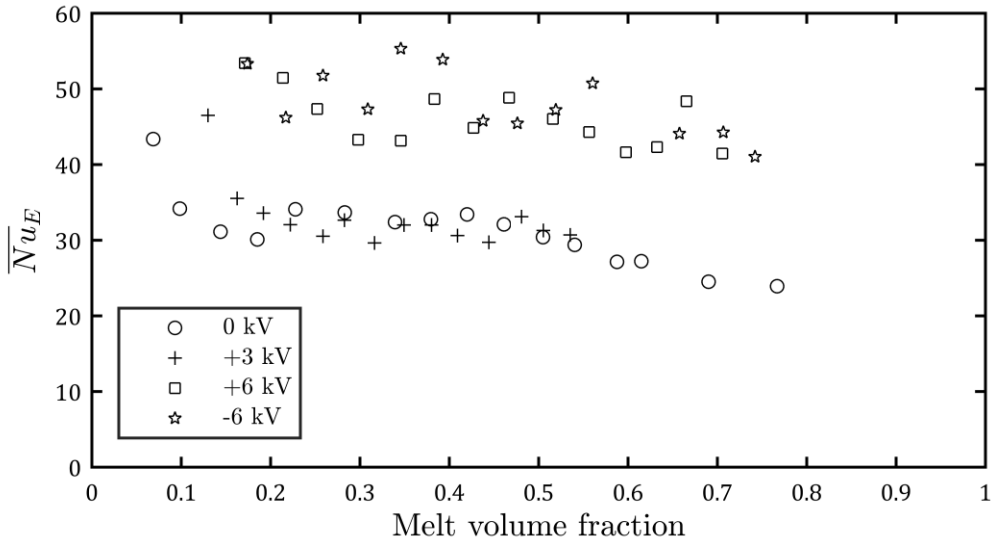

Figure 6.53 Average electrical Nusselt number at the wall vs the melt volume fraction for Ra=9E7

Chapter 7 Numerical Modelling

The numerical work presented in this chapter contributes to the literature in exploring the capability of using EHD body forces in enhancing the heat transfer process in moving boundary problems. Per the best of our knowledge, very limited work has been conducted in this field and most of the existing studies cover the effect of EHD in a defined aspect ratio enclosure but not for a variable one. The moving boundary problem adds complexity to the system and a smart dynamic EHD system must be designed to adapt for such complexity.

In the course of the experimental work conducted in this research, it was found that the electrophoretic forces were the main mechanism of enhancement under the tested voltages and that the dielectrophoretic forces effect is minimal. In this chapter, the effect of the dielectrophoretic force in the liquid PCM on the heat transfer enhancement will be examined numerically and verified with a scaling analysis. The results of the numerical and the theoretical work will be used to better understand the experimental results and will provide a guidance of the applicability of the dielectrophoretic forces as a tool for enhancement and the suggested region of operation.

An EHD assisted melting system working on the effect of the dielectrophoretic forces solely might be more reliable and experience a longer life span compared to another system relying solely on electrophoretic forces. The reason for that is well known in literature

owing to the fact that strong ion injection causes a degradation in the dielectric fluid upon long term use[111] and it may alter the surface geometry of the electrodes[112] and therefore change the thermal performance of the system.

The effect of the electrophoretic forces was not examined numerically in the course of this work and will require further investigation on the ion injection behavior from the high voltage electrodes. This in fact needs further experiments to be deduced and is a recommendation for future work in this field.

In this chapter, first the basics of the numerical model for the dielectrophoretic forces will be presented followed by the validation of the model, design, scaling analysis and lastly the numerical results.

7.1 Dielectrophoretic Numerical Model

The electrical body forces that arise in the PCM due to the application of high voltages are given by

$$\overrightarrow{f_e} = \rho_q \vec{E} - \frac{1}{2} E^2 \nabla \varepsilon + \frac{1}{2} \nabla \left(\rho E^2 \left(\frac{\partial \varepsilon}{\partial \rho} \right)_T \right) \tag{7.1}$$

As mentioned before, the third component in the right-hand side of the equation which is the electrostrictive force can be neglected for incompressible fluid as $\left(\frac{\partial \varepsilon}{\partial \rho}\right)_T = 0$ [113].

The first section of this chapter deals with the second component which is the dielectrophoretic forces. Dielectrophoretic forces vector of action is in line with the spatial gradient vector of the electrical permittivity of the dielectric material. For non-polar

dielectrics like Octadecane, the electric permittivity is dependent on density and thus temperature. The electric permittivity within small temperature ranges can be approximated as

$$\varepsilon = \varepsilon_0 \varepsilon_r (1 - e\theta) \tag{7.2}$$

Where $(\theta = T - T_0)$, In this case, the dielectrophoretic forces can be simplified to

$$-\frac{1}{2} E^2 \nabla \varepsilon = \frac{1}{2} \varepsilon_0 \varepsilon_r e E^2 \nabla \theta \tag{7.3}$$

The magnitude of the dielectrophoretic body forces in this case solely depends on the magnitude of the electric field and the temperature gradients and the direction of the forces is acting from the cold to the hot dielectric fluid regions.

The numerical model was solved by using the commercial software package ANSYS FLUENT. The electrical model and the electrical body forces were coded with C++ language into the software using user defined functions.

The electrical governing equation for the dielectrophoretic model are: Gauss's law

$$\nabla . [D] = \rho_q \tag{7.4}$$

For high frequency AC signals with time scales less than the ionic transient time for non-polar dielectrics, the electric free charges density (ρ_q)in the bulk of the dielectric fluid can be assumed to be equal zero. In such case the free charges cannot respond to the fast-

varying electric field and any free charges are either neutralized or dissipated [114]. Gauss's law then reduces to

$$\nabla.[\varepsilon(T)\mathrm{E}] = 0 \tag{7.5}$$

$$\mathrm{E} = -\nabla V \tag{7.6}$$

$$-\nabla.[\varepsilon(\theta)\nabla V] = 0 \tag{7.7}$$

The mass, momentum and energy conservation equations can then be formulated assuming laminar, incompressible flow and using Boussinesq approximation.

Mass Conservation

$$\nabla.(\vec{u}) = 0 \tag{7.8}$$

Momentum Conservation

$$\rho\frac{\partial}{\partial \mathrm{t}}(\vec{u}) + \rho\vec{u}.\nabla\vec{u} - \mu\nabla^2\vec{u} = -\rho g\beta\theta - \nabla P + \frac{1}{2}\varepsilon_0\varepsilon_r eE^2\nabla\theta \tag{7.9}$$

Energy Conservation

$$\rho C_p\frac{\partial \mathrm{T}}{\partial \mathrm{t}} + \rho C_p\vec{u}.\nabla T - k\nabla^2 T = q_e''' \tag{7.10}$$

Where the (q_e''') term is the heat generation per unit volume due to the presence of the electric field and the accompanied Joule heating effect. This term can often be neglected for non-polar dielectrics as the electric current is very small and the heat generated from

the current is usually orders of magnitude less than that of the external heat sources. In the current study, the electric current was in the nano-ampere scale.

7.1.1 Validation of the numerical model

The dielectrophoretic numerical model was validated against the early work of Roberts (1968) [115] and Stiles (1991) [116] of linear stability analysis. Roberts and Stiles studied the stability of a dielectric fluid confined between two horizontal infinite parallel plates separated by a distance (d). The confined dielectric layer was subjected to a stabilizing temperature gradient (ΔT) (Hot plate on top) and a vertical electric field simultaneously. The results of these studies were presented in non-dimensional parameters, the electrical Rayleigh number, Prandtl number and gravitational Rayleigh number. Robert's study identified the critical electric Rayleigh number at which the dielectrophoretic forces destabilizes the dielectric layer under micro-gravity conditions and low values of gravitational Rayleigh number (-1000). Stiles expanded the study to investigate the stability under high gravitational Rayleigh numbers up to (-10^9).

The electrical Rayleigh number was identified in these studies in a similar manner to that of the gravitational one, in which the gravity term is replaced with an electrical gravity component. The dielectrophoretic force in the analysis can be decomposed as

$$-\frac{1}{2}E^2\nabla\varepsilon = \nabla\left(e\theta\varepsilon_{ref}\frac{E^2}{2}\right) - \theta e\nabla\left(\frac{\varepsilon_{ref}E^2}{2}\right) \tag{7.11}$$

The first component is a gradient of a scalar term and can be lumped in the pressure term, the second term is analogous to the buoyance force and an electric gravity term can be derived as

$$-\frac{1}{2}E^2\nabla\varepsilon = \nabla\left(e\theta\varepsilon_{ref}\frac{E^2}{2}\right) - \theta e\nabla\left(\frac{\varepsilon_{ref}E^2}{2}\right) \tag{7.12}$$

$$\theta e\nabla\left(\frac{\varepsilon_{ref}E^2}{2}\right) = \rho\, g_e\, \alpha\theta \tag{7.13}$$

$$g_e = \frac{e}{\rho\beta}\nabla\left(\frac{\varepsilon_{ref}E^2}{2}\right) \tag{7.14}$$

The electric gravity term can then be used to establish the electric Rayleigh number (Ra_E) which is defined as a non-dimensional parameter for the ratio between the dielectrophoretic forces to the viscous forces.

$$Ra_E = \frac{g_e\beta\Delta T d^3}{\nu\alpha} = \frac{e\nabla\left(\frac{\varepsilon_{ref}E^2}{2}\right)\Delta T d^3}{\mu\alpha} \tag{7.15}$$

$$Ra_E = \frac{e^2\varepsilon_{ref}V^2\Delta T^2}{\mu\alpha} \tag{7.16}$$

Roberts estimated the critical electric Rayleigh number (Ra_{E-c}) under zero-gravity to be 2128. Stiles expanded the instability study to cover a number of different negative Rayleigh numbers (thermally stratified) and developed the following correlation between the critical electric Rayleigh number and the gravitational Rayleigh number

$$Ra_{E-c} = -1.246Ra + 2129 \tag{7.17}$$

The developed numerical model was validated against the instability criterion for two cases. The first is instability under microgravity conditions (Ra=0) and the second under stabilizing temperature gradient (Ra=-1000). The numerical model was used to estimate the critical electric Rayleigh number for both cases and comparing them against those estimated in the instability analysis.

The distance between the two parallel plates in the model were kept at 1 mm and the width of the domain to 57 mm. The high aspect ratio was required to supress the effect of the lateral walls on the instability criterion and the amplitude of the velocity. Hexahedral mesh was used in solving this problem, the mesh size was 20 divisions by 1140 divisions in the height and width respectively.

The following procedures were taken for validating the numerical model.

1. A steady state simulation was conducted first without considering the dielectrophoretic momentum source terms. This was conducted to establish the non-perturbed thermal and electrical field in the domain, the steady state solution was then taken to initialize both the thermal and electric fields for the subsequent transient simulations.
2. The dielectrophoretic momentum source terms in the x and y direction were then added and a transient simulation is conducted. The transient simulations were important in order to get the exponential growth rate of the instability. During the transient simulation, both the heat flux from one of the walls and the

maximum velocity in the domain were monitored until the final steady state was achieved.

3. The above procedures were repeated for several electric potentials for the upper plate to replicate different magnitudes of electric Rayleigh number.

As mentioned earlier the dielectrophoretic forces destabilization is analogous to the buoyancy forces and similarly a bifurcation into convection roll cells is produced similar to Benard convection cells. The amplitude of the convection roll velocity is related to the degree of super-criticality of the system. The degree of super-criticality (δ) is defined as

$$\delta = {Ra_E}/{Ra_{E-c}} - 1 \tag{7.18}$$

Near the instability threshold, in the weak non-linear regime the relation between the square of the amplitude of the non-dimensional velocity (v/d) and the magnitude of the electric Rayleigh number holds a linear correlation. The theory behind this is explained in detail in the work of Yoshikawa et al. (2013) [117].

Figure 7.1 shows the results for the numerical simulation for the two cases conducted for validation. The graphs show the relation between the electrical Rayleigh number vs the square of the amplitude of the non-dimensional velocity.

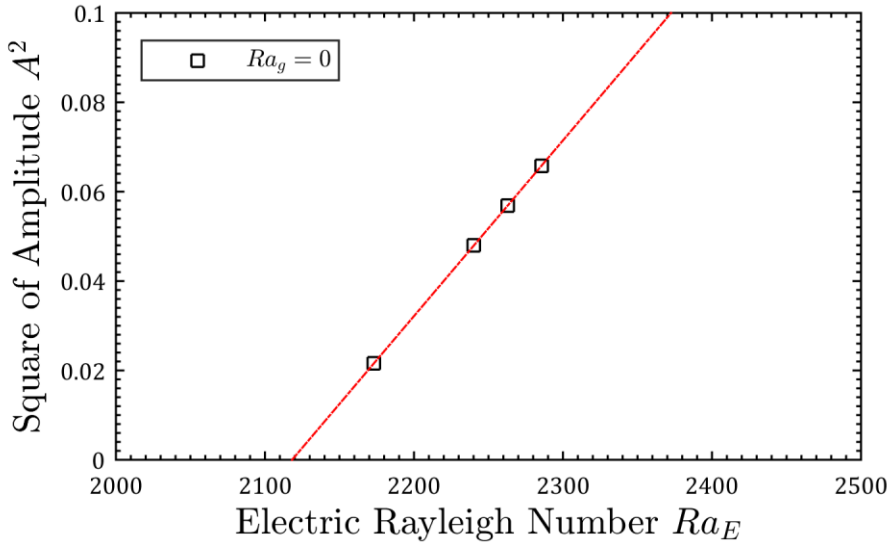

(a)

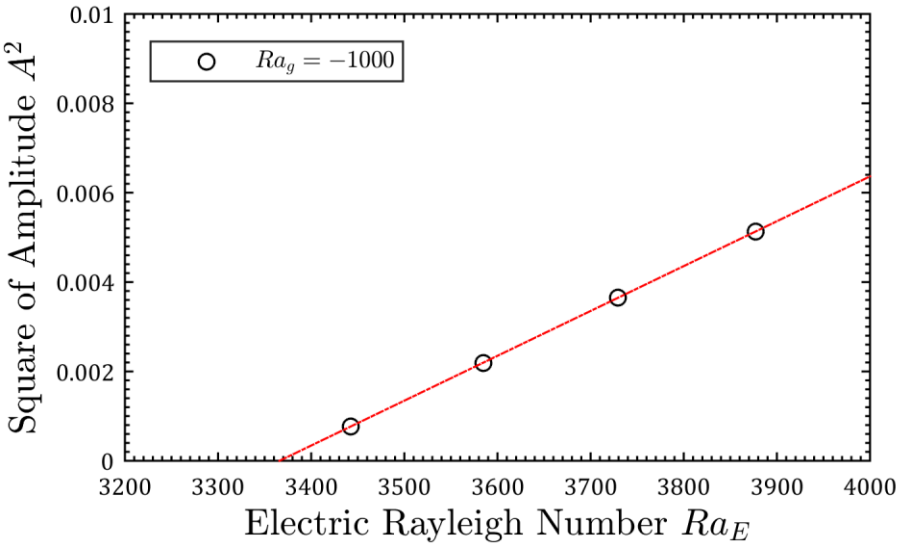

(b)

Figure 7.1 Electric Rayleigh number vs. square of the non-dimensional velocity amplitude. (a) Ra=0, (B) Ra=-1000

Table 7.1 Numerical vs Theoretical estimations of critical electric Rayleigh number

Rayleigh Number (Ra_g)	Ra_{E-c} **Theoretical**	Ra_{E-c} **Numerical**
0	2128.7	2118.2
-1000	3370	3365.9

The results of the numerical simulation were fitted with a polynomial fit of 1st degree. The intercept of the linear fit with the x-axis determines the critical electrical Rayleigh number.

The estimated critical electric Rayleigh numbers from the numerical simulations were compared against the theoretical ones from stability analysis [115] [*Table 7.1*] and the results showed a good agreement within a maximum of 0.4 % deviation between the theoretical and numerical values. Figure 7.2 shows the velocity and the temperature contours for the first case at an electrical Rayleigh number of 2285. The produced contours are very similar to that of Benard convection cells as predicted. The magnitude of the velocity was chosen at the mid line of the numerical domain for the upward or downward maximum vertical velocity.

The numerical model was then used to understand the effect of the dielectrophoretic forces during the melting process of Octadecane. The model facilitated the design of a rectangular PCM module that uses EHD as an active enhancement technique.

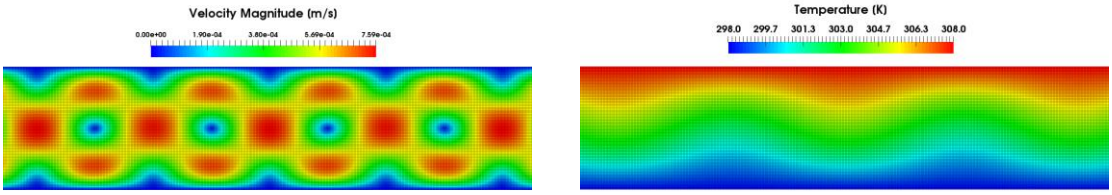

Figure 7.2 Velocity Magnitude (left) and Temperature contours (right) for Ra_g=0 and Ra_E = 2285

7.1.2 The Dielectrophoretic Theory in enhancing heat transfer in vertically oriented PCMs

In vertically oriented enclosures, the dielectrophoretic forces mode of action is different than the one described in the validation case. With natural convection in effect due to the vertical orientation, the highest thermal gradients and thus the highest dielectrophoretic forces are more pronounced at the thermal boundary layer.

There are two known methods to enhance the natural convection heat transfer process in vertically oriented enclosures. These two methods are either thinning the thermal boundary layer by increasing the circulation mass flow rate, or by successive breaking of the thermal boundary layer by forming multiple convection cells instead of one big convection cell.

The first method was investigated theoretically and numerically before by Turnbull [118]. Turnbull used non-uniform alternating electric fields- with frequencies higher than the charge relaxation time of the dielectric fluid- to either thin or thicken the thermal

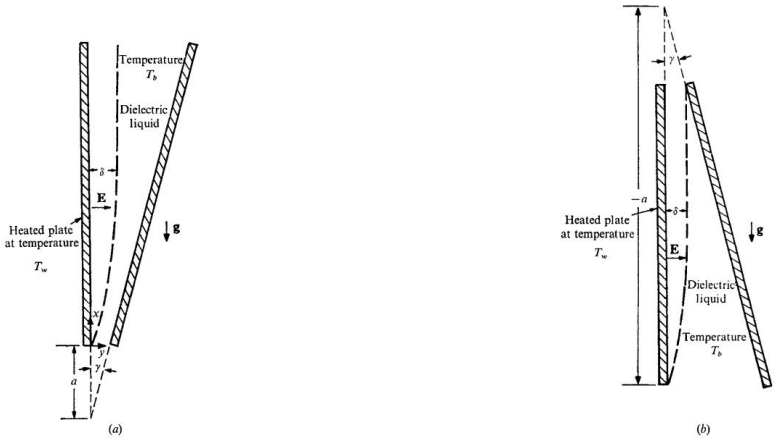

Figure 7.3 Non-Uniform electric fields used to thin or thicken the thermal boundary layer [118]

boundary layer thus enhancing or retarding the heat transfer process. Figure 7.3 shows the type of electrode configuration needed to produce non-uniform electric field needed for this method, the left side of the figure shows the case of heat transfer enhancement when the highest electric field is at the bottom. In such case, the high electric field pulls the cold fluid at the bottom towards the hot plate, leading to the enhancement of heat transfer. The right side of the figure represents the opposite case when the electric field is highest at the top.

The second method for enhancing the natural convection process (The bifurcation technique) is known in the field of study of melting with natural convection. It is well known that containing the PCM in multiple short enclosures is better than using one tall enclosure. The time required for melting the multiple short cells is shorter than the one long cell, despite of the higher Rayleigh number for the taller one. This fact was studied experimentally and theoretically by several authors Benard et al and Bareiss et al [21], [94]. Although, it might seem simple to use short cells and stack them vertically as a

solution for enhancing natural convection, yet it imposes several logistic and engineering difficulties.

The bifurcation method needs a different type of non-uniform electric field than the first method. The degree of electric field's non-uniformity must be higher, yet symmetric to produce the bifurcation of the cells. In this method, the non-uniform and symmetric electric field is often achieved by using cylindrical electrodes connected to high voltage. Previous studies showed the feasibility of this method but for constant aspect ratio enclosure (non-moving boundary) [119],[120]. However, in these cases the Coulomb force was main driving force for enhancement not the dielectrophoretic one.

Recently the attention was drawn to the dielectrophoretic forces and their effect on the enhancement of heat transfer enhancement in natural convection [73],[109]. The dielectrophoretic forces offer an advantage over the Coulomb force in terms of being non-sensitive to the direction of the electrical field, and in terms of not affecting the material electrical properties on the long run. As it is known that dielectric fluids subjected to strong ion injection often face a deterioration in their electrical and thermal properties.

7.1.2.1 Hypothesis

Figure 7.4 shows the mechanism of action when using cylindrical electrodes and alternating electric field to enhance the heat transfer between two plates held at different temperatures. The cylindrical electrodes are kept at high voltage, while both plates are grounded. In this case, the electrodes act as a source of jet impingement, where the cold stream of fluid is pulled from the cold side and impinged on the hot side. Schematic (a) in

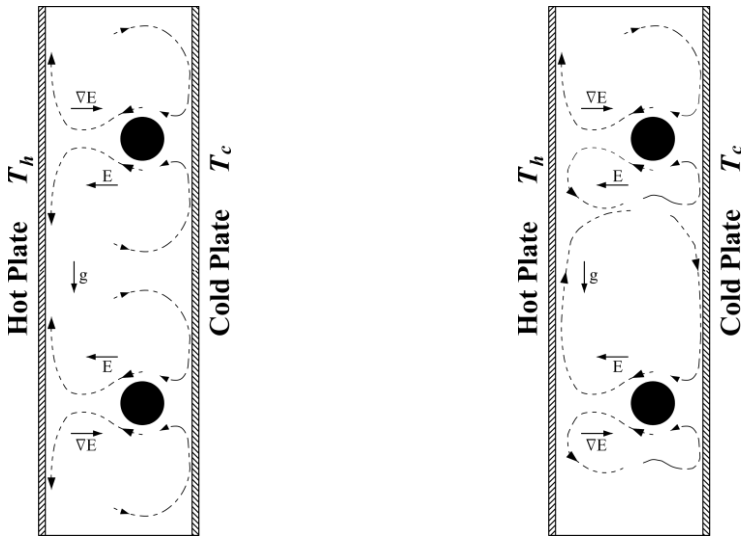

(a) (b)

Figure 7.4 Dielectrophoretic forces mechanism of action with gravitational forces (a) Dielectrophoretic forces are dominant (b) Dielectrophoretic and gravitational forces same order of magnitude

Figure 7.4 presents a case where the dielectrophoretic forces are order of magnitude higher than the gravitational forces. As a result, two opposing electro-convection cells will be formed between each pair of electrodes. The counter-clockwise convection cell acts in the direction opposite to the natural buoyant flow (gravity), while the clockwise convection cell is working along the natural buoyant flow direction. The two electro-convection cells can significantly enhance the heat transfer process in this case, due to the breaking of the original thermal boundary layer into multiple thinner ones.

In Schematic (b), the dielectrophoretic and gravitational forces are within the same order of magnitude. In such case, the dielectrophoretic forces promote the growth of the clockwise electro-convection cells, while the opposing cell starts to shrink in size. A

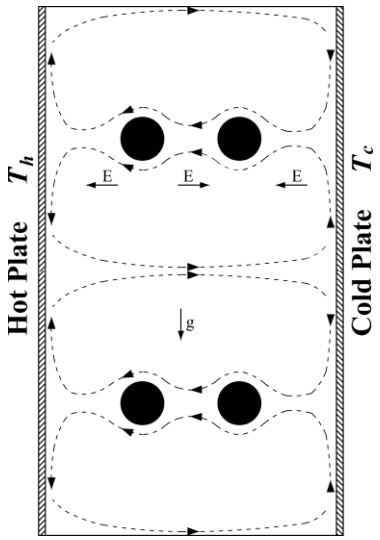

Figure 7.5 Novel design promoting the jet impingement mechanism in moving boundary problems

theoretical limit could be formulated in this case where only one convection cell between the electrodes is formed in the clockwise direction.

The interaction between the natural buoyant flow, dielectrophoretic forces and the similar jet impingement behavior inspired the current design to be used in a moving boundary configuration or to promote modular designs that can be used to reduce the magnitude of the high voltage significantly. The principle of the current novel design is presented in Figure 7.5.

The use of successive columns of electrodes treated each electrode in a row as a source of jet or aided in pumping the jet. This can sustain the formation of the convection cells in a manner that cannot be achieved by using Coulomb forces due to its dependence on the magnitude and the direction of the electric field, while the dielectrophoretic forces are only dependent on the magnitude of the electric field. The electrical configuration between each

column of electrodes must be set as: one column connected to high voltage and the next one grounded and so on [similar to electrical connection in Figure 4.4]. This electrical configuration will always maintain high electric fields between electrodes columns, keeping the pumping effect between the electrodes strong and persistent.

This design can be used for different aspect ratios as well as PCMs enclosures owing to the modularity of the system which could be advantageous in reducing the high voltage needed to maintain a strong electric field.

In the next section, a scaling analysis for the system will be presented for a single column of electrodes to understand the governing parameters of the system and to determine the transition criterion between an electrically dominated flow to a gravitationally dominated one.

7.1.3 Scaling Analysis

The basic fundamental understanding for the scaling analysis for natural convection was adapted in this study from the principle laid out by Bejan [106] and recently by Kunti et al [109]. In this study, one will examine first an electrically dominated flow and then the coupling between them and what transition criterion can be estimated from the scaling analysis.

In case of an electrically dominated flow [gravitational forces are negligible], the system can be treated similarly to a rectangular enclosure heated from below where the electrical gravity vector is acting in the same direction of the temperature gradient vector. As mentioned before the flow behavior produces a semi-Benard convection cells [Figure 7.4a].

The dielectrophoretic forces will induce a plume like structure originating from the electrodes and impinging on the hot side of the cell. The scaling analysis will be conducted on one convection cell and can be applied in general assuming an infinitely long vertical enclosure. This kind of assumption is always valid for the first step without taking into account the effect of the rigid boundaries for simplicity.

The conservation equations (mass, momentum and energy) will be scaled in x -axis according to (L) which is the width of the convection cell and in y-axis according to (δ_T) which is the thermal boundary layer on the horizontal plates.

From mass balance

$$v.L \sim u.\delta_T \tag{7.19}$$

The rising plume momentum balance in y-direction represents a balance between the viscous forces and the electrical gravitation forces

$$\vartheta \frac{v}{L^2} \sim g_e \frac{d\varepsilon}{dT} \Delta T \tag{7.20}$$

The stagnation pressure from the rising plume is scaled to

$$\Delta P \sim \rho v^2 \tag{7.21}$$

The x- momentum balance on the boundary layer will result in a balance between the pressure drop and the viscous force

$$\frac{\Delta P}{L} \sim \mu \frac{u}{\delta_T^2} \tag{7.22}$$

Finally, at steady state, the energy balance on the boundary layers produces a balance between the convected heat to the conducted heat through the boundary layer

$$\frac{u\Delta T}{L} \sim \frac{\alpha \Delta T}{\delta_T^2} \tag{7.23}$$

From equation (7.20), the upward plume velocity can be described by the non-dimensional Grashof number using (H) [the cell height] as the characteristic length

$$v \sim \frac{g_e \, {d\varepsilon}/{dT} \, \Delta T H^3}{\vartheta^2} \frac{\vartheta L^2}{H^3} \sim Gr_E \frac{\vartheta L^2}{H^3} \tag{7.24}$$

Solving equations (7.19) and (7.23) leads to

$$v \sim \frac{\alpha}{\delta_T} \tag{7.25}$$

Combining equations (7.21) and (7.22)

$$v^2 \sim \vartheta \frac{uL}{\delta_T^2} \tag{7.26}$$

Solving equation (7.25) and (7.24)

$$L^2 \delta_T \sim {H^3}/{Ra_E} \tag{7.27}$$

By substituting equations (7.23), (7.25) in (7.26)

$$L^2 \sim {\delta_T^2}/{Pr} \tag{7.28}$$

Solving for the last two equations

$$\delta_T \sim H\ Pr^{1/3} Ra_E^{-1/3} \tag{7.29}$$

As the convection cell width (L) is

$$L \sim H\ Pr^{-1/6} Ra_E^{-1/3} \tag{7.30}$$

The average Nusselt number can then be estimated as

$$Nu_E \sim \frac{{k\,\Delta T}/{\delta_T}}{{k\,\Delta T}/{H}} \sim Pr^{-1/3} Ra_E^{1/3} \tag{7.31}$$

The scaling analysis for this kind of configurations where the electric gravity vector is working parallel to the temperature gradient vector leads to a dependency on Electric Rayleigh number raised to the power (1/3) as shown by Bejan [106]. In case of a uniform gravity field and infinite horizontal plates, the width of the cell shows the same dependency on the electric Rayleigh number, where as the electric Rayleigh number increases the width of the cell decrease and the number of the cells multiplies.

However, in our case the electric gravitational field is not the same across the whole domain due to the use of cylindrical electrodes which produce a divergent electric field. In such case there is an asymmetry in the velocity between the rising (v) and the descending plume (v_2). The width of the rising plume will be scaled with the electrode's diameter (d), while that of the descending plume by $(S_H - d)$, where (S_H) is the horizontal spacing

between two electrodes. In case of $S_H \gg d$, the mass balance between the two plumes leads to

$$vd \sim v_2 S_H \tag{7.32}$$

The same procedures can be repeated with respected to (v_2) except for the rising plume equation. In this case equation (7.24) will be rewritten as

$$v_2 \frac{S_H}{d} \sim \frac{g_e \, {d\varepsilon}/{dT} \, \Delta T H^3}{\vartheta^2} \frac{\vartheta L^2}{H^3} \sim Gr_E \frac{\vartheta L^2}{H^3} \tag{7.33}$$

Thus equation (7.27) will be reformulated to

$$L^2 \delta_T \sim {S_H H^3}/{d \, Ra_E} \tag{7.34}$$

The thermal boundary layer can then be scaled to

$$\delta_T \sim H \left(\frac{S_H}{d}\right)^{-1/3} Pr^{1/3} Ra_E^{-1/3} \tag{7.35}$$

And the average electrical Nusselt number as

$$Nu_E \sim Pr^{-1/3} Ra_E^{1/3} \left(\frac{d}{S_H}\right)^{1/3} \tag{7.36}$$

The last correlation identifies the effect of the electrodes diameter and their horizontal spacing upon the average electric Nusselt number. It points out that as the diameter to spacing ratio increases, the Nusselt number increases. This is mainly due to the effect of asymmetry and the subsequent rise in the descending plume velocity.

Validity of the scaling analysis

The above analysis is valid only under the following list of assumptions:

a) No electrophoretic forces are present in the bulk if the dielectric fluid. This can be only fulfilled by the application of high frequency AC signals which surpass the ionic transit times scales of the dielectric fluid.
b) No Solid Extraction at the interface. This assumption might be true for pure paraffins as explained in the previous chapter
c) The above analysis assumed a semi-infinite horizontal plate and that the convection cell width was left to be freely varying depending upon the electrical Rayleigh number. However, the cell width will be bounded to the horizontal spacing between the two electrodes and subsequently the number of convection cells are not allowed to change in real case. This will have an affect on altering the dependency on the Rayleigh number, as one may see higher Nusselt values at lower Rayleigh number compared to the correlation, owing to the fact that the cell width cannot be higher than the horizontal spacing between the electrodes and the opposite is true.

7.2 Dielectrophoretic Numerical Results

7.2.1 Electrically dominated convection regime

In this section, the hypothesis stated under section (7.1.2), will be proved by the aid of numerical simulations. Although, the main scope of this work is to focus on the potential heat transfer enhancement during melting of Organic PCMs, that the numerical simulations

presented here first will be conducted under a quasi-steady approximation. The numerical simulations will be conducted first for non-moving boundary walls. The temperature boundary conditions will be set constant for the period of the simulation and the conservation equations will be solved numerically for the fluid domain only.

This assumption is valid as long as the viscous time scales in the fluid domain are significantly less than the melting time scales. In case of Octadecane and most of the organic PCMs, the ratio between the viscous time scale ($t_v \sim {s^2}/{\vartheta}$) to the melting time scale ($t_m \sim {s^2}/{\alpha Ste}$) is given by the

$$\frac{t_v}{t_m} \sim {Ste}/{Pr} \sim 10^{-2} \tag{7.37}$$

For moderate degrees of superheating, the Stefan number (Ste) is below 0.2 and the Prandtl number for most of the Organic PCMs is around (~ 50). This shows that the viscous time scale is the governing scale in this kind of problems and the assumption can be used within acceptable validity.

The dielectrophoretic enhancement theory was examined by testing different melt thickness in a rectangular enclosure of 50 mm in width and 100 mm in height. The geometry of the rectangular enclosure and the electrical configuration for the embedded electrodes are the same as those described in the experimental facility and what was used in the experimental section. The vertical spacing between the electrodes (S_V) was 20 mm and the horizontal spacing (S_H) between them was 7 mm.

The three independent variables in these numerical simulations were the thickness of the liquid region, the voltage and thus the electrical gravitational force and the gravitational field acceleration (g). In the first part of the analysis, the gravitational field (g) was turned off and only the electric gravity term was considered to understand the behavior for electrically dominated flow first.

Four different melt thicknesses were solved numerically and thus four different aspect ratios were examined. These melt thicknesses and their corresponding aspect ratios are 7.5, 12.5, 22.5 and 32.5 mm for thicknesses and 13.33, 8, 4.44 and 3.07 respectively for aspect ratios. The voltages examined in these simulations ranged from 1 to 19 kV which correspond to electrical Rayleigh numbers from $\sim 10^3 \rightarrow 10^8$. Although, this range of voltages were not achieved during experimental testing, it is theoretically achievable in the liquid side of Octadecane. The electrical breakdown of liquid hydrocarbons is in the range of 25 to 100 MV/m [121], [122] which corresponds to a minimum breakdown voltage of 65 kV in the current configuration.

7.2.1.1 Solver and Results

The commercial ANSYS FLUENT finite volume solver was used in the numerical simulations in this work. FLUENT solver is very efficient in dealing with fluid dynamics and heat transfer coupled problems and provides a large-scale parallelization which is important in dealing with these types of problems. A C++ code was written to solve for the electrical field and the dielectrophoretic forces in the fluid domain and was then compiled through FLUENT user defined functions (UDFs) platform. The source code can be found

in appendix D. A mesh independence study was conducted to estimate the sensitivity of the solution to the mesh size and the results were compared against the bench-mark solution for laminar natural convection in rectangular enclosures. It was found that a structured mesh of a maximum element size of 0.25 mm can be used without sacrificing the accuracy of the solution. The mesh was created using ICEM mesher, ICEM is known for its high quality in producing hexahedral meshes with good range of controllability to produce a high quality with minimum skewness structured meshes.

The numerical simulation for each case was first started by solving for the continuity, momentum, energy and electrical field equations to get a steady state solution without adding the dielectrophoretic forces as momentum source terms. This initial steady state solution was used to establish the temperature and electrical fields inside the liquid domain. The steady state solution was then used to initialize transient simulations where the dielectrophoretic forces were added as momentum sources in the liquid domain. During the transient simulations, the average heat flux at the hot wall was monitored along with the maximum velocity in the liquid domain.

The objective of running transient simulations was to capture any form of periodic instability and to examine the magnitude of time scale in the problem. The transient simulations' duration was decided upon reaching a steady state or a quasi-steady periodic state and the transient monitoring of the average heat flux and velocity were used as the judgement criterion.

The dielectric fluid used in these simulations was octadecane and the main electrical and thermos-physical properties can be found in *Table 7.2*. The dielectric constant and its

Table 7.2 Octadecane electrical and thermal properties

Property	**Value**
Density	775 $[kg/m^3]$
Viscosity	0.0039 $[kg/m.s]$
Thermal conductivity	0.152 $[W/m.K]$
Specific heat capacity	2180 $[J/kg.K]$
Thermal expansion coefficient	0.00085 $[1/K]$
Dielectric constant[Liquid]	2.1
Dielectric constant[Solid]	2.24
$d\varepsilon/dT$	-0.00167 $[1/k]$

dependence on temperature were estimated from experiments conducted in the lab as outlined in Appendix A. The dielectric constant can be evaluated theoretically from the electromagnetic theory in correlation to the refractive index and the temperature dependence from the Clausius Mosotti equation, and it was found that the maximum deviation between the experimental and theoretical values for the dielectric constant was less than 2% and that for the temperature dependence was less than 20 %.

The first part of the analysis will show the effectivity of using alternating electric configuration in sustaining multiple convection cells at different aspect ratios. The second part of the analysis studies the heat transfer characteristics of the electrically dominated flow and analysing the results in non-dimensional form and the third part further expanded the study to study the impact of different geometrical parameters on the level of enhancement and validate the scaling analysis.

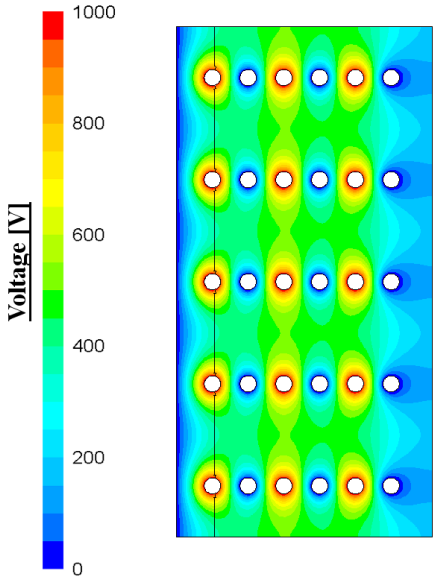

Figure 7.6 Typical voltage distribution under 1kV applied voltage highlighting the alternating electrical configuration between the columns of electrodes

Figure 7.6 shows the undisturbed voltage distribution (i.e. without electrical or gravitational forces) used in all numerical simulations. The contour plot represents the distribution for a unit kV applied through the electrodes.

The alternating electrical connection between one column of electrodes to other *[HV-G-HV-G-HV-G]* created strong electric field around all the electrodes and a weaker field between each two successive rows of electrodes [Refer to Figure 7.7]. The electric field distribution is showed for the different aspect ratios tested in the numerical simulations, showing small deviations between the different aspect ratios for the undisturbed field. This was expected due to the small variations in permittivity within the liquid Octadecane and between the solid and the liquid phase as well.

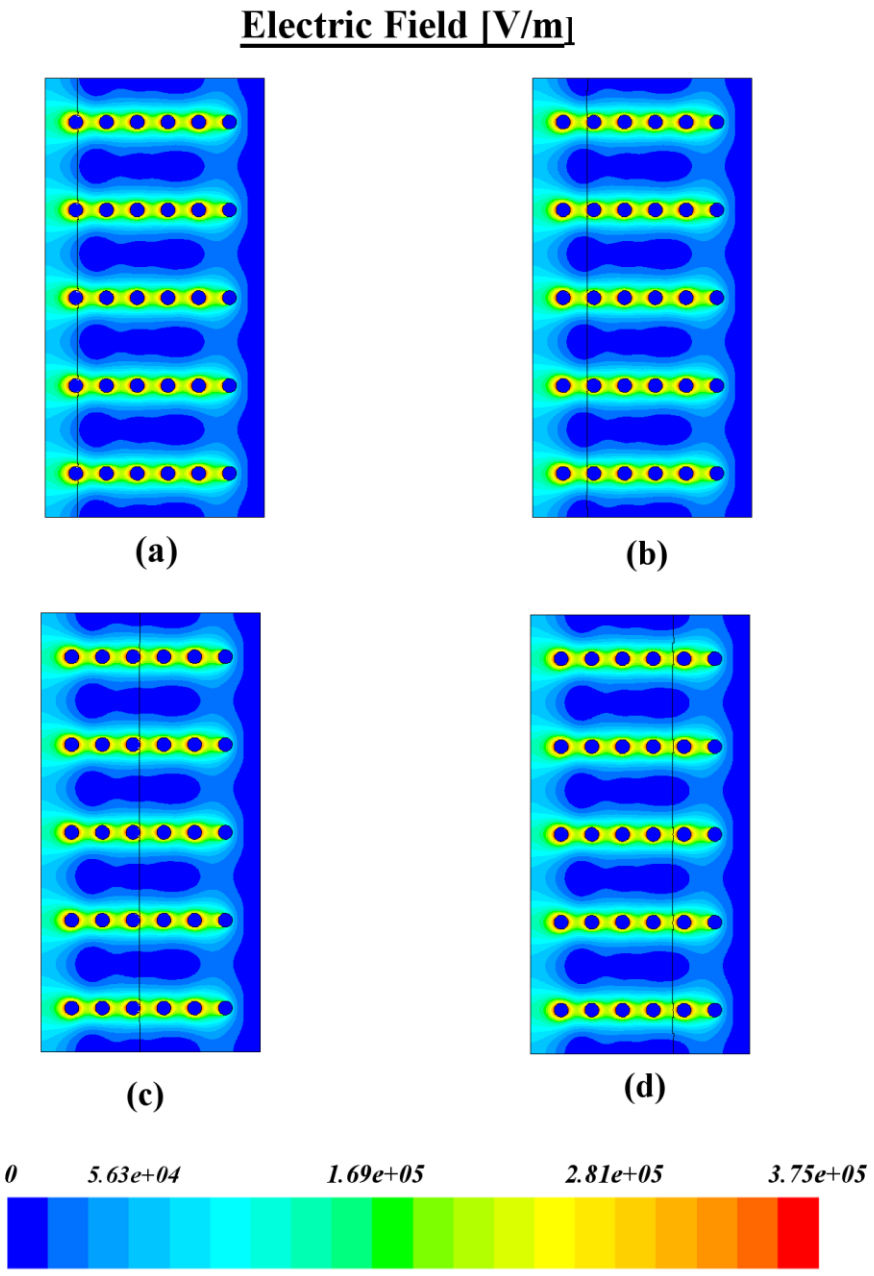

Figure 7.7 The electrical field distribution under 1kV applied voltage for the different aspect ratios. (a)S=7.5 mm (b)S=12.5 mm (c)S=22.5 mm (d)S=32.5 mm

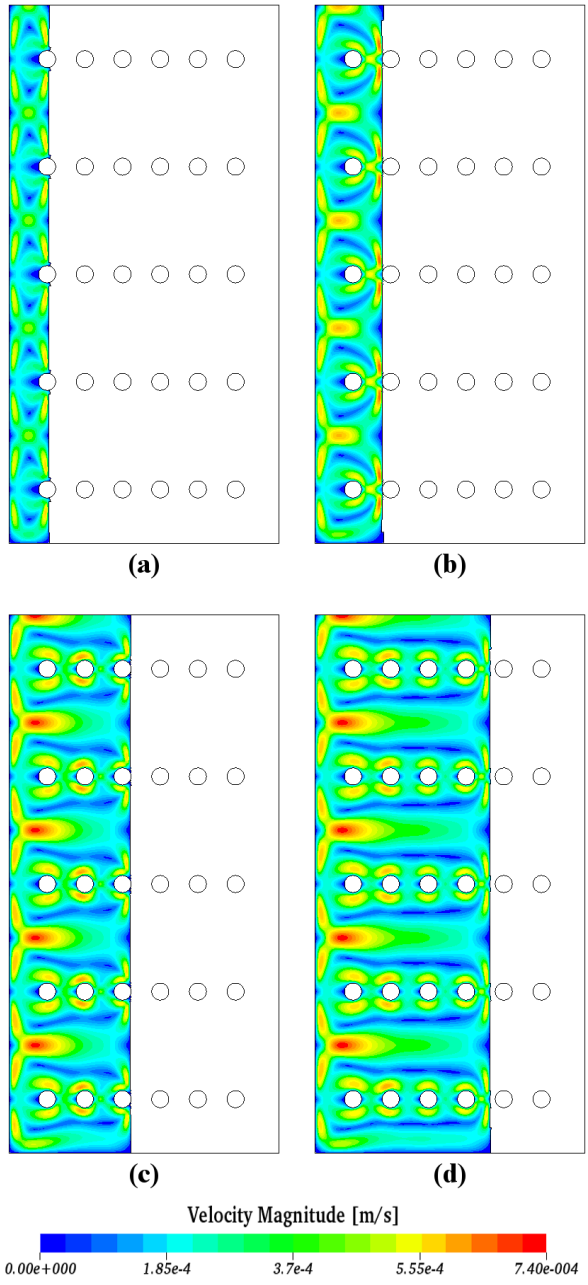

Figure 7.8 Velocity contour plots for 11 kV applied voltage (a) S=7.5 mm, (b) S=12.5 mm, (c)S=22.5 mm, (d) S=32.5 mm

Figure 7.8 shows the velocity contour plots for 11 kV applied voltage case. The figure shows the effectiveness of the design at different aspect ratios under the same applied voltage. The dielectrophoretic forces in this design were able to sustain two convection cells between each successive rows of electrodes regardless of the melt thickness. Each electrode in a row is acting as a pump that can overcome the viscous and pressure drag around the electrodes to sustain a jet structure impinging on the hot heat exchanger surface.

The impinging jets carry the cold streams from the liquid/solid interface (cold boundary layer) and convect the energy stream towards the hot heat exchanger surface [Figure 7.9]. The higher heat transfer coefficients will always be opposite to the electrodes at the hot heat exchanger side and between each two rows of electrodes at the solid/liquid interface side. The highest heat transfer coefficients locations will always coincide with the positions of jet stagnation. At the jet stagnation zone, the thermal boundary layer is the thinnest and away from it, is when the thermal boundary layer starts to grow.

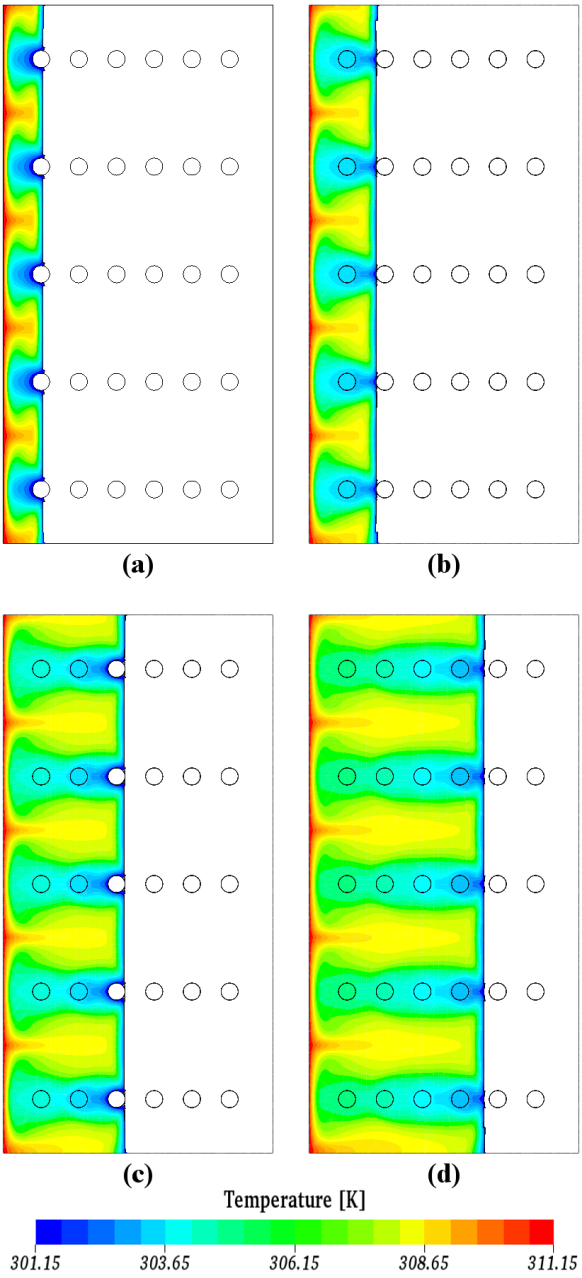

Figure 7.9 Temperature contour plots for 11 kV applied voltage (a) S=7.5 mm, (b) S=12.5 mm, (c)S=22.5 mm, (d) S=32.5 mm

The theory was tested for the four different aspect ratios with 10 different applied voltages with a total of 40 cases and it was found to hold true and the bifurcation of the multiple convection cells was found in these cases.

The results from these simulations was then grouped and examined under non - dimensional form. The scaling analysis presented in section (7.1.3) showed that the average Nusselt number is correlated to the electrical Rayleigh number raised to the third power [equation 8.36]. In order to verify the scaling analysis, the results have to be presented in Nusselt number formulation and the correct electrical Rayleigh number has to be defined. The electrical Rayleigh number is only different than the normal gravitational one in terms of the characteristic length and the electrical gravity term. The correct characteristic length in these simulations is the average thickness of the liquid domain for each case, while the electrical gravity term is defined in equation (7.14) and can be re-derived as

$$g_e = \varepsilon_0 \frac{\nabla E^2}{2\rho} \tag{7.38}$$

Thus, the electrical Rayleigh number as

$$Ra_E = \frac{\rho g_e \, {d\varepsilon}/{dT} \, \Delta T S^3}{\mu \alpha} \tag{7.39}$$

The electrical gravity term has to be computed as an average value for the studied cases due to the highly converging fields of the design. Using Gauss' equations and integrating from the one cylindrical electrode to the centre distance between two successive electrodes

in one row, one can estimate the electric field around cylindrical electrodes as a function of the radial distance from the centre as

$$\vec{E} \cong \frac{V}{2rln\left({}^{d_0}/_{S_H}\right)}\,\hat{r} = \frac{V}{2r\Omega}\,\hat{r} \tag{7.40}$$

Where (r) is the radial distance from the centre of the nearest electrode, (d_0) is the electrodes' diameter, (S_H) is the horizontal spacing between the electrodes and (Ω) is a geometrical parameter that defines the ratio between the electrode diameter and the horizontal spacing between the electrodes. From the electric field, one can calculate the average electrical gravity term between two successive electrodes as

$$\overline{g_e} \cong \frac{\varepsilon_0}{2\rho}\frac{1}{\left(0.5(S_H - d_0)\right)}\frac{V^2}{4\Omega^2}\left[\frac{1}{(0.5S_H)^2} - \frac{1}{(0.5d_0)^2}\right] \tag{7.41}$$

This scaling formulation for the electrical Rayleigh numbers was applied on the results of all the numerical simulations conducted for the electrically dominated flow) neglecting gravity).

The electrical Nusselt number was defined as the ratio between the average heat flux with dielectrophoretic forces to the average heat flux without EHD. The average heat flux with the dielectrophoretic forces was calculated from the numerical simulations as

$$\bar{Q}_{EHD} = \frac{1}{H}\int_0^H -k\frac{\partial T}{\partial x}dy \tag{7.42}$$

Figure 7.10 shows the local heat flux with and without the dielectrophoretic EHD forces for one of the simulated cases of 11 kV applied voltage and an aspect ratio of 3. The local

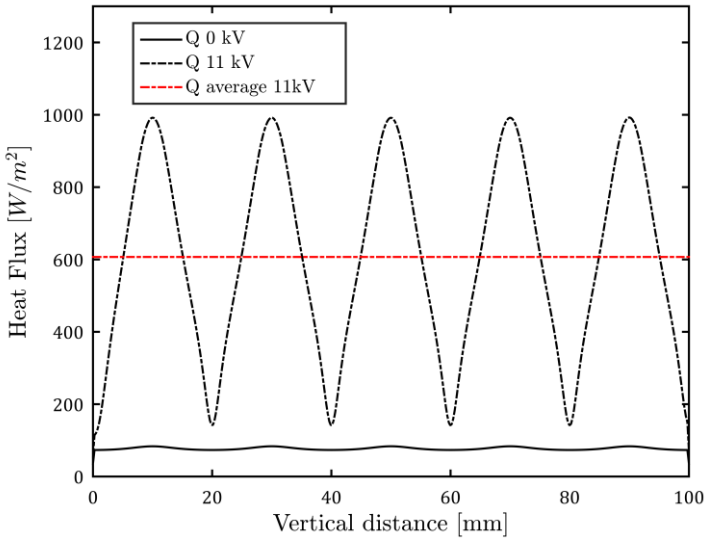

Figure 7.10 Local heat flux with and without dielectrophoretic forces at 11 kV

heat flux is highest opposite to the electrodes corresponding to the locations of the jet stagnation, while for case of 0 kV the heat flux is almost uniform across the length of the hot wall with slight enhancement opposite to the electrodes as well due to the higher thermal conductivity of Brass compared to the liquid Octadecane. The figure shows a maximum local heat transfer enhancement opposite to the electrodes with an order of 15-fold for this case and an average enhancement of 8.5-fold.

The average heat flux was then calculated for all the numerically solved cases of different applied voltages and various aspect ratios and the results are presented in Figure 7.11. The average heat flux was constantly higher for higher aspect ratios (thus smaller melt thicknesses), owing to the initially higher flux at 0 kV for smaller melt thicknesses.

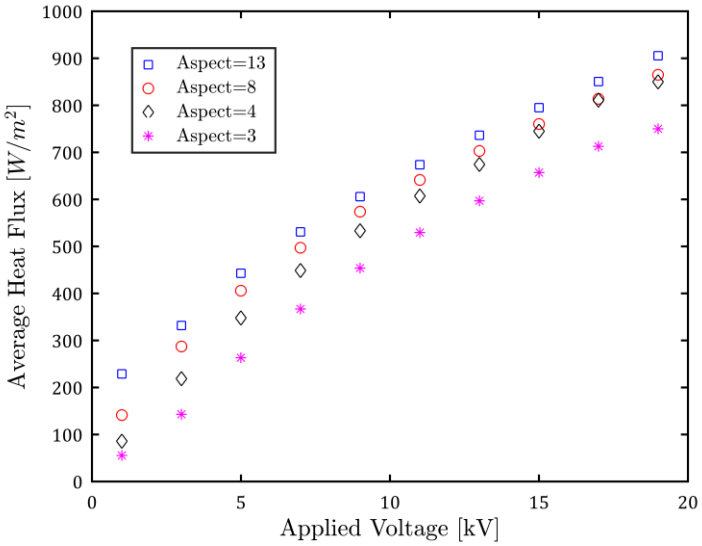

Figure 7.11 Average heat flux vs applied voltage for electrically dominated flow

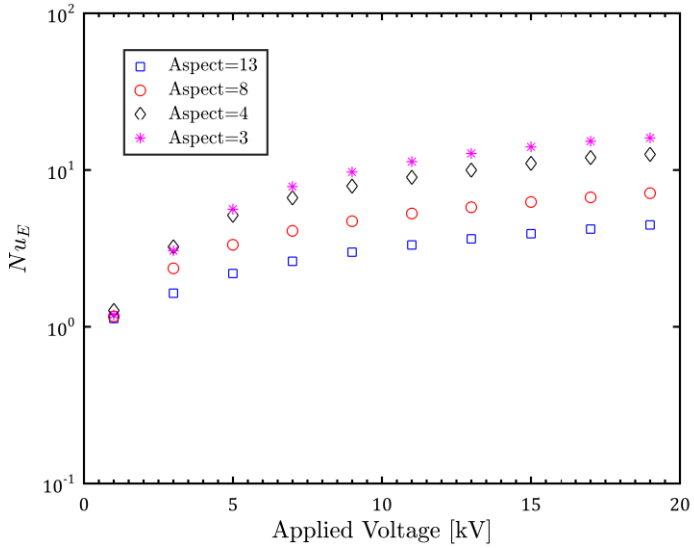

Figure 7.12 Average Electrical Nusselt number vs applied voltage for electrically dominated flow

However, if the results are presented in terms of the dimensionless number and comparing the flux of each case compared to its initial flux at 0 kV, the higher enhancements will be observed for the lower aspect ratios not the higher ones. Figure 7.12 shows the average electrical Nusselt variations with the different cases. The enhancement achieved was up to 16-fold for the smallest aspect ratios under 19 kV applied voltage and up to 4.5-fold for the largest aspect ratio tested.

The results were then correlated to the electrical Rayleigh number formulated in equation (7.39) and using the average gravitational electric field correlation [equation 8.41] instead of using the applied voltage as the independent factor. The electric Rayleigh number is dependent upon the melt thickness and thus the aspect ratio in this case for a fixed height configuration and the square of the applied voltage.

Figure 7.13 shows the average electric Nusselt number vs the Electric Rayleigh number for the different cases on a logarithmic scale. The graph clearly shows that by correctly scaling the problem parameters with the electric Rayleigh number, the results of the different aspect ratios collapse on one single line for $Ra_E > 5 \times 10^5$. Below this value, the magnitude of the electrical Nusselt number is close to 1 indicating a negligible impact of dielectrophoretic force on causing any instability to the thermally stratified flow. The study covered a wide range of electric Rayleigh number from 10^3 to 10^8, with the simulations of the lower aspect ratio characteristics represented the higher electric Rayleigh number range.

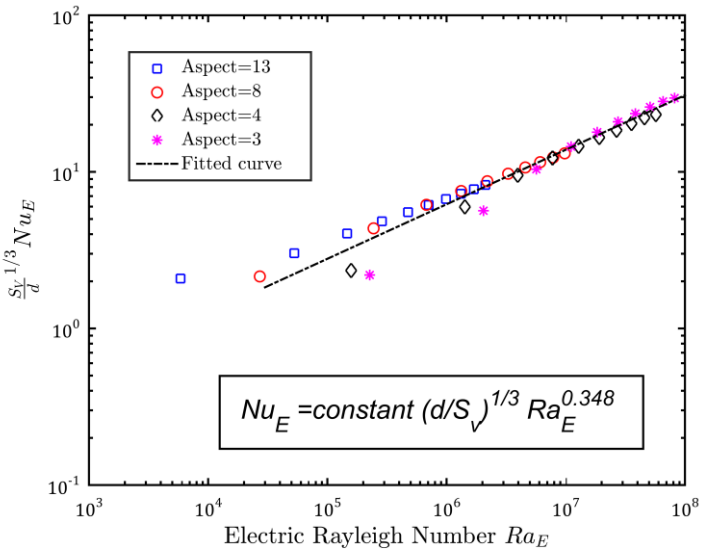

Figure 7.13 Average Electric Nusselt number vs Electric Rayleigh number for electrically dominated flows

The results of the Nusselt number was then fitted with an exponential fit with respect to the electric Rayleigh number using the least squares method and a final correlation was obtained for all the simulations. The best fit equation is

$$\overline{Nu}_E = constant \times \left(\frac{d}{S_V}\right)^{1/3} Ra_E^{0.348} \tag{7.43}$$

The best fit equation showed that the Electric Nusselt number depend on the electric Rayleigh number raised to the power (0.348) which is close to the scaling analysis prediction of (0.333) power dependency. The goodness of fit was judged with the adjusted R^2 of a value of 0.98. The first point in all the four different aspect ratio cases showed the maximum deviation from the fit and thus they were excluded from the fit. These four points corresponds to an applied voltage of 1 kV and the electric Nusselt number corresponds to

1 in these cases, which means that the EHD forces has almost no effect at these values. Aside from these points, the agreement between the Nusselt number correlation and the data points is very good with a maximum deviation of 25 % for only one point.

The third part of the analysis was made for further validating the scaling analysis conclusions and check the validity of the geometrical parametrization. For this part of the analysis, two main important geometrical factors where examined. These two factors are the electrode diameter and the vertical spacing between the electrodes. A summary of the combination of these factors are presented in Table 7.3.

The heat flux at different applied voltages was monitored for the five different cases and the electric Nusselt number vs the applied voltage is shown in Figure 7.14. The effect of the electrode diameter is propagated in the Nusselt number correlation through the electric gravity term and the size of the impinging jet. The bigger the electrode diameter, the lower the electric field magnitude around the electrode as long as the separating distance between the edge of the electrode and the horizontal spacings between the electrodes is kept constant $(S_H - d = constant)$. While using a bigger electrode in diameter results in a wider jet and a higher average electric body force. These two factors work against each other if the above conditions were satisfied, however if the separating distance between the electrodes was kept constant $(S_H = constant)$ the edges between the two electrodes come closer to each other as the diameter of the electrode increase and thus increase the electric gravitational force as well. This is noticed in Figure 7.14 as the bigger electrodes showed a better electric enhancement compared to smaller electrodes at the same applied voltage due to the fixation of the horizontal spacing between the electrodes.

Table 7.3 Geometrical examined parameters for electrically dominated flow

Property / Case	1	2	3	4	5
Electrodes' Diameter [mm]	3.175	1.5875	2.3812	3.175	3.9688
Vertical spacing (S_V) [mm]	15	20	20	20	20
Melt thickness (S) [mm]	22.5	22.5	22.5	22.5	22.5

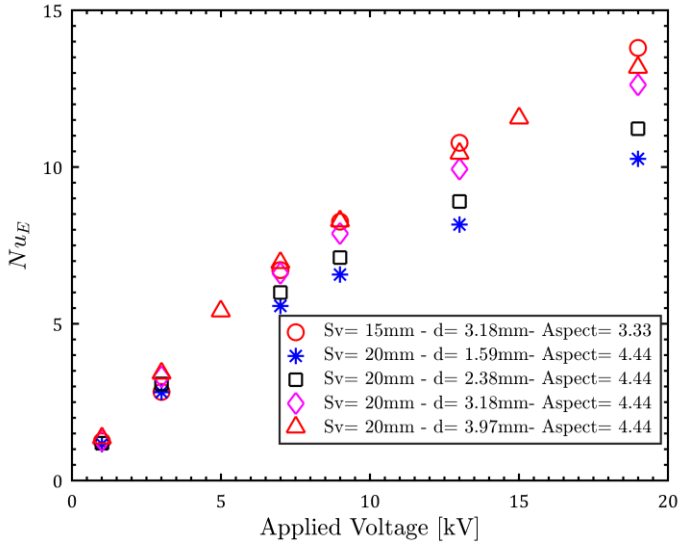

Figure 7.14 Electric Nusselt number vs applied for the different geometrical parameters

The Nusselt number correlation predicted as well that the smaller the vertical spacing between the electrodes results in a higher Nusselt number as observed in Figure 7.14. The first case with the smallest vertical spacing between the electrodes, showed a slightly higher electric Nusselt number than the other cases. The physical reasoning behind this effect is

that as the vertical spacing between the electrodes decreases, the less the thermal boundary layer grows and the higher the temperature gradient. However, this enhancement effect has limitations, as shrinking the distance between the rising and the descending plume, increases the heat conductance between and some heat finds its path between the two plumes without successfully convecting it to the other side. This limitation is known for the natural convection in rectangular enclosures and is defined as shallow enclosure limit [106]. However, further study may be needed here to investigate such limitation with the presence of dielectrophoretic forces.

Figure 7.15 shows the results of the simulations performed for the different geometrical parameters in non-dimensional form. The electric Nusselt number is shown vs the electric Rayleigh number and the results were shown to collapse under one single line. The data points agree with the calculated Nusselt number correlation from the previous simulations except for the first set of data points for each case as mentioned before due to the limited enhancement at these conditions.

The results of these numerical simulations and scaling analysis showed that carefully designing the electrical arrangement of the electrodes can cause a substantial enhancement in the heat transfer that is well maintained for different aspect ratios configurations and thus for a moving boundary problem. The scaling analysis presented in this study successfully correlated the important electrical and geometrical parameters in non-dimensional form with respect to the electric Rayleigh number.

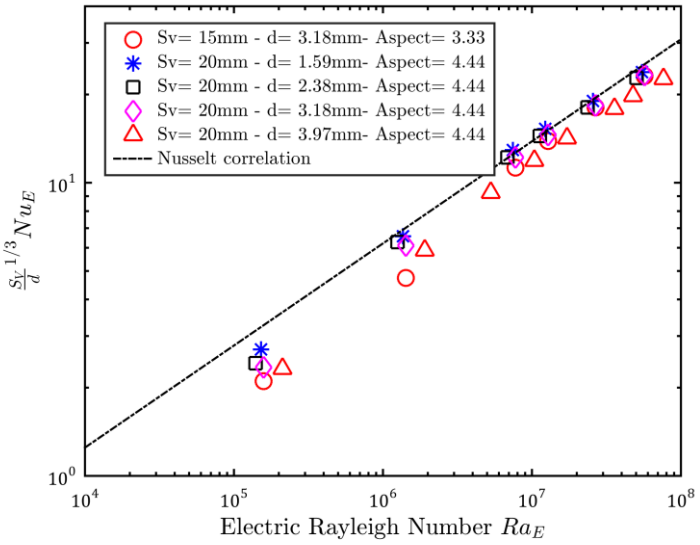

Figure 7.15 Electric Nusselt number vs. Electric Rayleigh number for different geometrical parameters

7.2.2 Mixed Electrical and Gravitational convection regime

The second part of the dielectrophoretic numerical model, deals with studying the regimes where there is a combined effect from electrical and gravitational forces and a mixed regime is developed. This part of the study will look at the behavior of the mixed regimes and identify the contribution of the different body forces in forming convection cell structures, and it will further examine the criterion of switching from gravitational dominated regime to electrically dominated flow regime.

In this study, the case of melt thickness equals to 22.5 mm (which corresponds to an aspect ratio of 4.44) was taken as the base case for the comparison with the 3.2 mm (1/8'') electrode diameter and 20 mm vertical spacing between the electrodes. In the current analysis the gravitational acceleration was fixed at $(9.81\ m/s^2)$, which leads to a

gravitational Rayleigh number of (1.8×10^8) under the same boundary conditions as the previous numerical simulations and equal to that of the experimental work. The applied voltage through the electrodes was varied from 4 kV up to 42 kV to cover a wide range of electric Rayleigh number. The average heat flux was monitored along the hot wall and transient simulations were conducted from an initial steady state of natural convection in the rectangular enclosure. The procedures for conducting the transient simulations are the same as the ones described in the previous section and the time of the simulations was confined upon reaching a steady state or a semi-periodic steady state.

Figure 7.16 shows the stream function contours in (kg/s) for the cases solved numerically. At 4 and 5 kV, only one big convection cell is prominent and representing a gravitationally dominated flow with the regular patterns of natural convection. The flow is laminar for these two cases around the electrodes close to the solid/liquid interface [i.e. cold boundary layer]. As the voltage increases to 7 and 9 kV, the flow at the cold boundary layer starts to be repelled away from the electrodes, indicating a high electric body forces at these electrodes. The main reason for this is that both the temperature gradient and electric field strength are highest in at the cold boundary layer side, promoting a higher dielectrophoretic forces than that at the hot boundary layer. From 11 to 15 kV, the electrical forces are becoming stronger and the initial natural convection cell starts to bifurcate into multiple convection cells with an initial bifurcation of one cell between each two successive rows of electrodes. These results explain the reason of not observing a dielectrophoretic forces effect in the experiments where the highest voltage that was tested was equal to 6 Kv.

As the applied voltage increases above 15 kV up to 42 kV, the electrical forces become more dominant over the gravitational forces and this is pronounced in continual bifurcation of cells. The convection cell that started to appear between two successive rows of electrode, further bifurcate into two convection cells opposing each other. The size of the two cells are different at the beginning, at 19 kV the upper cell (counter clock wise) is smaller in size compared to the lower one (clockwise cell) as the upper cells are working against gravity, while the lower ones are working along the gravitational forces. The difference in size between the two cells, diminishes as the applied voltage increases, indicating a fully dominant electrical flow condition.

Figure 7.17 shows a sample of the cases studied with the local heat flux along the hot wall is plotted against the vertical distance along the wall, where 0 represents the bottom of the enclosure and 0.1 m is the top. Starting from 4 kV, the heat flux is highest at the bottom and then decreases with height as one would expect in a gravitational dominated flow where the thermal boundary starts from the bottom and grows as the flow moves upwards. The heat flux distribution at 11 kV is not far from the 4 kV distribution, however a successive thinning of the thermal boundary layer opposite to the electrodes is obvious which increase the local heat flux at these positions. At 15 kV, the electrical forces are starting to become more prominent and the bifurcation of the natural convection cell is reflected on the heat flux, however the overall gravitational effect is still pronounced in higher heat fluxes at the lower cell locations compared to the upper ones.

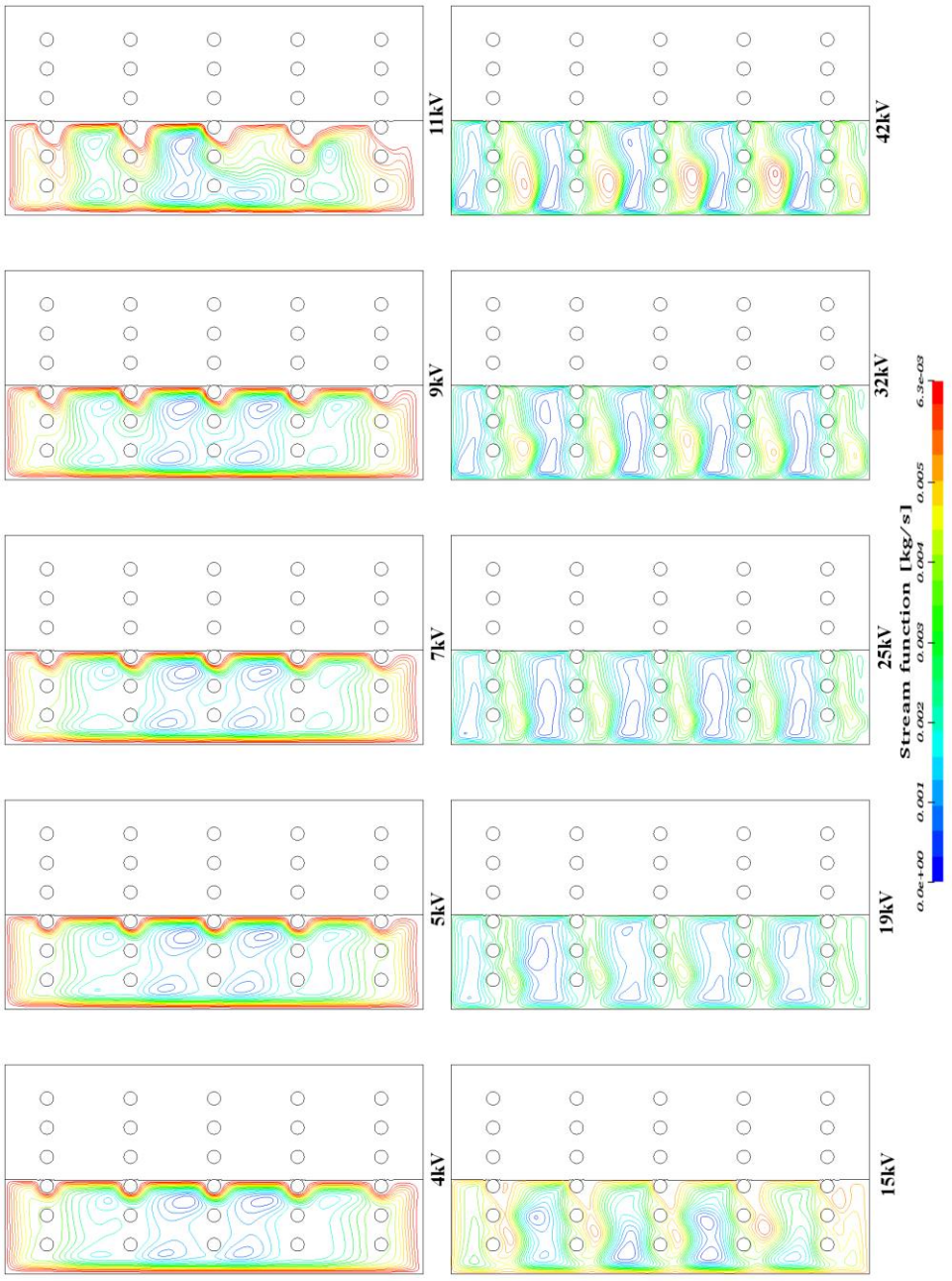

Figure 7.16 Stream functions contours for the different cases of mixed electrical and gravitational forces

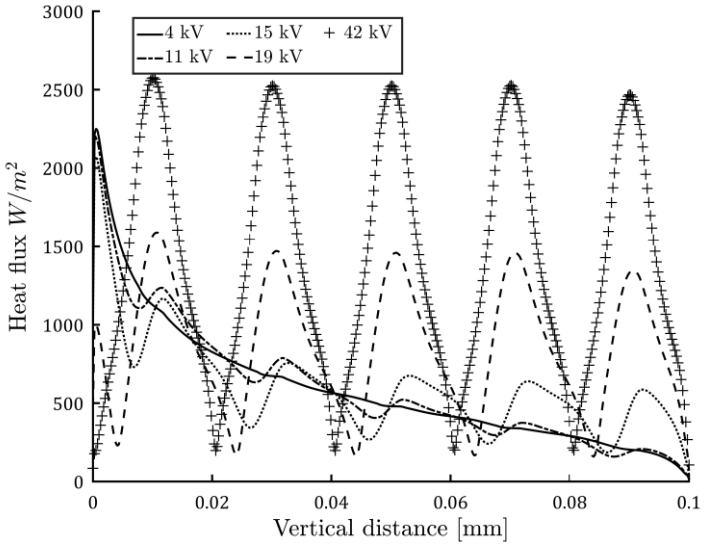

Figure 7.17 local heat flux along the hot wall for mixed gravitational and electrical regimes

As the voltage increases and reaches a value of 19 kV, the further bifurcation of the cell between the electrodes takes place as the wall heat flux shows significant periodic enhancement. In this case the heat flux distribution between the two peaks is not yet symmetric, indicating the difference in size between the convection cells. The heat flux distribution becomes more symmetric as the voltage increases to 42 kV, indicating that electrically dominated flow regime has been established.

The local heat flux values from the different cases were then used to calculate the average Nusselt number for the applied voltages and the results are shown in Figure 7.18. The values of the average Nusselt number from mixed electrical and gravitational forces are plotted and compared to the Nusselt number corresponding to gravitational forces alone. The graph shows that the switch from gravitational dominated flow to a mixed regime starts

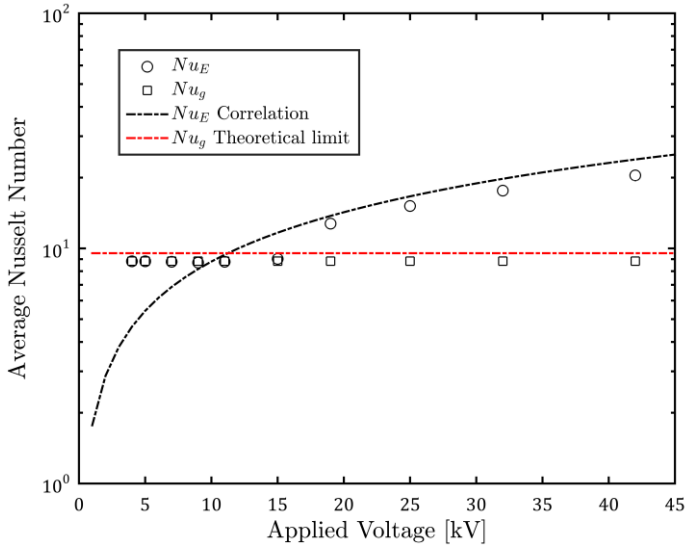

Figure 7.18 Average Nusselt number vs applied voltage for mixed gravitational and electrical regimes

at around 15 kV and the Nusselt number then increases as the voltage increase, approaching an electrically dominated flow depicted by the electrical Nusselt correlation deduced from the previous section.

In order to better understand, what conditions promotes the appearance of the mixed gravitational and electrical regime, the values of the electrical gravitational acceleration were computed according to equation (7.41) and compared to the natural gravitational acceleration. Figure 7.19 shows the ratio between the electrical gravitational acceleration to the natural one vs the applied voltage for the different tested cases. The simulations covered a wide range of the ratios ranging between 0.6 to 68. It was found that from the stream function contours and the Nusselt number correlations that the mixed electrical and

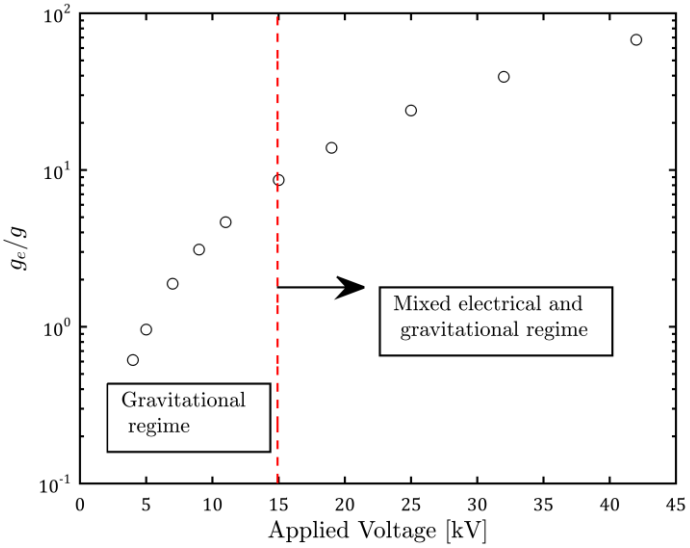

Figure 7.19 Electrical to natural gravitational acceleration ratio vs the applied voltage

convection regime starts from a ratio of $\left({}^{g_e}/_{g} \cong 10\right)$ and continues until the ratio is almost two orders of magnitude.

These findings were confirmed with performing multiple simulations with different gravitational Rayleigh number other than the ones tested above and varying the applied voltage. The simulations were performed for the same geometry discussed in this section, and the gravitational Rayleigh number was changed by varying the gravitational acceleration. A total of 10 simulations were conducted for each aspect ratios studied before and the points were chosen to form a Latin hypercube distribution between gravitational Rayleigh number and the applied voltage [Refer to Figure 7.20]. The ratio between the electrical acceleration to the gravitational acceleration are presented in Figure 7.21. The shape of the convection cells and their size was used to determine the nature of the

dominating regime. It was determined that the electrical acceleration to the gravitational acceleration ratio could be in fact used as the criterion of the switching between the different regimes regardless of the values of the gravitational Rayleigh or Electrical Rayleigh numbers.

$$\frac{g_e}{g} = \begin{cases} < 10 & \rightarrow Gravitational\ Regime \\ 10 < {}^{g_e}/_{g} < 100 & \rightarrow Mixed\ Regime \\ > 100 & \rightarrow Electrical\ Regime \end{cases}$$

The numerical results identify the importance of the dielectrophoretic forces at voltages higher than 15 kV when the gravitational Rayleigh number corresponds to 1.8E8 and St=0.089. These numerical findings support the experimental observations in the convection facility in which the dielectrophoretic forces effect was not observed up to 6 kV. Although the 15 kV range is below the breakdown voltage for liquid Octadecane, it could not be reached in the current experimental facility due to technical difficulties in which the breakdown was occurring between the electrical terminals in the air side before it happens in the liquid Octadecane or either because of earlier breakdown in the solid Octadecane[123].

The predictions of the numerical model can be further verified in future experiments by either addressing the challenges arising from reaching high voltages, or by conducting the experiments under micro-gravity conditions in which the voltages required will be orders of magnitude lower. One also has to point, that the numerical findings were not limited to Octadecane as the PCM but were presented in non-dimensional parameters, this may point the interested researcher to another PCM with more favorable properties.

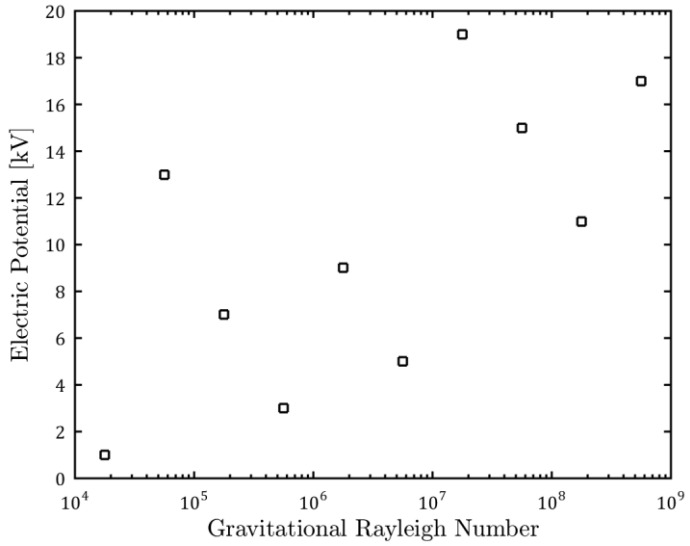

Figure 7.20 Latin hypercube sampling of simulations

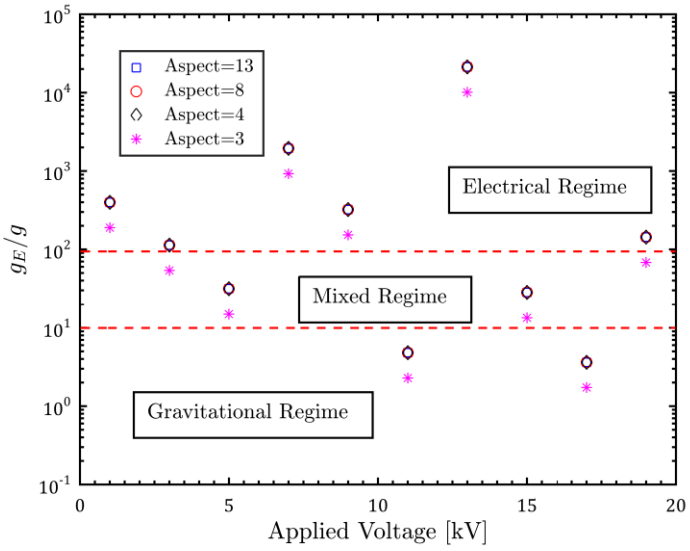

Figure 7.21 Regime switching criterion

Chapter 8 Conclusions and Recommendations

8.1 Summary and Conclusions

The effect of high voltage DC and AC on the heat transfer process during the melting of Octadecane was studied under horizontal and vertical configurations. The melting was studied for rectangular enclosures under two cases: (a) initially conduction dominated melting (b) initially convection dominated melting. The horizontal configuration resembles the conduction dominated melting and the vertical one resembles the convection dominated melting. The study was conducted through three main streams:

1) Experimental study of the effect of DC and AC applied voltages on the melting of a PCM in horizontally oriented rectangular enclosure
2) Experimental study of the effect of DC applied voltage, polarity, AC wave forms, gravitational Rayleigh number and the aspect ratio of the enclosure on the melting of a PCM in vertically oriented rectangular enclosure
3) Numerical study and a scaling analysis on the effect of the dielectrophoretic forces on natural convection enhancement in moving boundary problems

EHD in Horizontal Enclosures

In this study, the PCM was encapsulated between two heat exchangers, the top heat exchanger carried the hot fluid and the bottom carried the cold fluid. The mass flow rate of the working fluid was maintained high enough to ensure minimal temperature drop across the heat exchanger and thus a constant temperature boundary condition was achieved. By adjusting the temperatures of the two heat exchanger, one can control the location of the solid/liquid interface between the two heat exchanger. The heat flux was calculated at steady state through energy balance on the solid phase. Upon applying the high voltage, the solid/liquid interface steady state location change depicting a decrease in the thermal resistance and therefore the augmented heat flux because of EHD forces was calculated. The experimental facility accuracy was first verified against the analytical solution without EHD forces and the results were in good agreement with the analytical model.

The experiments on the conduction facility showed that the EHD forces can significantly enhance the heat transfer process during melting of Octadecane. A maximum heat transfer augmentation in the Nusselt number of 8.6 folds was recorded at a negative 10 kV DC applied voltage. The EHD level of heat transfer enhancement increased by the increase of the DC applied voltage.

The contribution of the dielectrophoretic forces towards the overall heat transfer enhancement was evaluated by applying high frequency AC symmetric square signal to suppress the effect of the Coulomb forces in the bulk of the PCM. It was found that by applying the AC signal that the EHD body forces did not cause any enhancement in the system. It was concluded that the contribution of the dielectrophoretic forces towards the

overall enhancement is minimal at the maximum voltage levels tested and that Coulomb forces are the main mechanism of enhancement in horizontal configurations.

The mechanism of the charge generation was estimated by conducting the same experiments but at higher temperature gradients. It was found that the EHD enhancement is independent of the temperature gradients and that charge injection is the more likely mechanism and not conduction. The effect of the opposing gravitational Rayleigh number was evaluated by conducting the experiments under different initial melt thicknesses. It was found that the level of enhancement decreases by increasing the opposing gravitational Rayleigh numbers, as the EHD body forces have to work against a stronger stabilizing temperature gradient.

EHD in Vertical Enclosures

In this part of the study the melting of the PCM was investigated in a vertical enclosure, therefore the gravitational forces were aiding the melting process and the melting can be considered to be convection dominate. A different experimental facility was built for this system, in which only one heat exchanger that resembled a constant temperature vertical wall and the opposite side of the enclosure was insulated and considered as adiabatic.

A novel shadowgraph optical setup was designed, instrumented and verified for this facility to measure the local heat transfer coefficients along the heat exchanger wall. The shadowgraph system used a 2^{nd} degree polynomial temperature approximation within the vicinity of the thermal boundary layer. The maximum deflection of the projected laser sheet away from the heat exchanger along with the magnitude of sheet dispersion were used to

quantify the local temperature gradient at the wall and therefore the local heat transfer coefficient.

Three initial cases were conducted on this experimental facility without EHD forces to serve as the base cases for performance assessment of EHD. These cases were a combination of two different gravitational Rayleigh numbers and two different aspect ratios of the enclosure. The non-EHD cases were first compared against the experimental bench mark experiment of Ho & Viskanta [20] in melting of Octadecane under natural convection. The current experiment was found to be in good agreement with the bench marked study and they were conducted to cover longer duration of melting than that of Ho's to capture the four different distinct melting regimes. The shadowgraph optical setup was able to accurately capture the four distinct regimes: (1) pure conduction, (2) mixed conduction and convection, (3) fully convection (4) knee regime and the results were verified against an analytical Nusselt correlation. The results for the three experiments were correlated to the non-dimensional parameter ($\frac{H}{W} Fo.Ste.Ra_g^{0.25}$).

The EHD experiments were conducted for different DC voltages for the three different cases. It was found that the EHD forces enhanced the melting process even for an initially convection dominated melting process. The mechanism of enhancement was found to be a bifurcation of the initial convection cell into multiple electro-convective cells between the rows of the electrodes. The shadowgraph system identified the interaction between the electrical and the gravitational forces through visualization of these cells and their symmetry. At lower applied voltages, the bifurcated cells between the electrodes were unsymmetrical representing a balance between the electrical and the gravitational forces.

As the voltage increases, the generated cells started to become more symmetrical indicating the transformation towards an electrically dominated regime.

The EHD heat transfer enhancement factor was found to increase by the increase of the applied voltage, reaching a 1.7 folds enhancement at the lower gravitational Rayleigh number tested and 1.45 folds for the highest gravitational Rayleigh and Stefan number. The effect of the polarity of the applied voltage was tested for the different cases and it was found that there was no significant difference between the positive and the negative polarities when the magnitude of the applied voltage was below 4 kV. At higher voltages- 6kV- the negative polarities showed better level of enhancement when compared to the positive applied voltage. The shadowgraph visualizations showed that the shape of the electro-convective cells did not differ between the two polarities, however the localized peaks in the heat transfer coefficient were higher for the negative case, thus indicating higher impinging velocities. The difference between the two polarities was further investigated through the current measurements and it was found that the current was almost 1.5 times higher for the negative polarity compared to the positive voltages tested.

The effect of the waveform was investigated to evaluate the contribution of the dielectrophoretic forces towards the overall enhancement. Although that the effect of the dielectrophoretic forces was tested in the conduction dominated facility and was found to be minimal, it was further tested in the convection facility as well. The reason for that is in the convection facility, the temperature gradients are expected to be higher at the thermal boundary layer and therefore the possibility of higher dielectrophoretic forces $\left(-\frac{1}{2}E^2\nabla\varepsilon = -\frac{1}{2}E^2\frac{\mathrm{d}\varepsilon}{\mathrm{dT}}\nabla\mathrm{T}\right)$. Symmetric square wave signals were applied with different

range of frequencies 0.5, 1.75 and 20 Hz. The highest frequency signal was high enough to ensure shorter wave period when compared to the viscous time scales and the ionic transit time scales to suppress the effect of Coulomb forces. A high speed shadowgraph was used to understand the effect of the AC signals and it was found that at the low frequency range, the flow responded to the applied signals but still showed an overall EHD effect. At the highest frequency the flow did not respond to the signal but rather transformed to a one of natural convection flow. It was concluded that effect of the dielectrophoretic forces is still minimal for the range of the applied voltages in this work. The solid extraction phenomenon was investigated by using macroscopic high speed imaging, for the experimental range considered, solid extraction was not observed for Octadecane. It was concluded that the Coulomb force is the main mechanism of enhancement for melting of Octadecane and that the source of charge generation is due to charge injection from the high voltage electrodes. The charge injection created a plume originating from the high voltage electrode and impinging to the grounded heat exchanger and this was confirmed by the shadowgraph images.

A scaling analysis was conducted based on the previous conclusions and the dominant mechanism of enhancement to describe the problem in non-dimensional form. An electrical Rayleigh number was introduced and its magnitude was correlated to the magnitude of the injected current. The melt volume fraction was then represented against the non-dimensional parameter $(n+1)\frac{H}{W}\,Fo.Ste.Ra_{E/c}^{0.25}$ and the melt fraction temporal profiles for the different voltages collapsed well against this parameter.

Numerical Modelling

The last chapter in the dissertation presented a numerical analysis on the role of the dielectrophoretic forces during the melting of Octadecane and when they would become of significant importance. The dielectrophoretic forces in general are more favorable to use and rely on when compared to Coulomb forces, because Coulomb forces are usually dependent on the electrode material and its surface roughness and it could cause material degradation in case of strong injection.

The dielectrophoretic model was written as user defined function (UDFs) in C++ and was compiled into Fluent. The model was then validated against Stiles [116] work of instability analysis and the model accurately predicted the threshold of instability for a dielectric fluid confined between two infinite horizontal layers and subjected to an electric field.

The numerical model was used to understand the interaction between the gravitational and the dielectrophoretic forces at different ranges of both gravitational Rayleigh number and electrical Rayleigh number. The model was complemented with scaling analysis to determine the governing scales of the problem and the dielectrophoretic Rayleigh number was deduced from the study.

The numerical results were in agreement with the scaling analysis and showed that the electrical Nusselt number was proportional to the dielectrophoretic Rayleigh number raised to the third power and the correlation was $\overline{Nu}_E = 0.05053 \left(\frac{d}{S_V}\right)^{1/3} Ra_E^{0.348}$ for electrically dominated flow. The model showed that the proposed electrode arrangement can sustain

the formation of multiple convection cells between the multiple rows of electrodes at the different melt thickness.

The model predicted that the transition from gravitational to mixed electrical and gravitational regime occurs when the ration between the electrical gravity to natural gravity becomes higher than 10 and that the flow turns to be fully electrically dominated when the ratio exceeds 100.

The numerical findings were used to better explain the experimental findings and the role of the dielectrophoretic forces towards the overall enhancement.

8.2 Research Contributions

The key research contributions can be summarized in the following points:

a) Experimentally investigated the effect of high voltage DC and AC on the melting enhancement of Octadecane PCM in an initially conduction dominated regime.

   "Measurement of heat transfer enhancement in melting of n-Octadecane under gravitational and electrohydrodynamics (EHD) forces," *Journal of Electrostatics,* vol. 92, pp. 31–37, Apr. 2018"

b) Experimentally investigated the effect of high voltage DC, AC and Rayleigh number on the melting enhancement of Octadecane PCM in an initially convection dominated regime.

c) Evaluated the mechanisms of EHD heat transfer enhancement due to the application of EHD using shadowgraph method and identified the different flow regimes.

d) Examined the transient time response due to the application of high voltage pulse wave forms.

e) Elucidated the problem in non-dimensional parameters through the results of the experimental study and the scaling analysis

f) Developed numerical model to quantify and understand the contribution of the dielectrophoretic body forces and the interaction with the gravitational forces

8.3 Recommendations for future work

The current study outlined the EHD heat transfer enhancement mechanisms in melting of organic PCMs. The study showed great potential for using EHD enhancement by changing the applied voltage and the waveform.

The recommendations for future work are as follows:

- Expand the experimental work to conduct a detailed parametric study on the effect of pulse waveforms on the heat transfer enhancement.
- Experimentally investigate the effect of EHD on tall PCM configurations. This study will evaluate the effect of EHD for very high Rayleigh numbers.
- Use the developed numerical tools to optimize the electrode geometry and to find the best electrical configuration. The electrical configurations can vary from

fixed potentials to smart electrode switching systems that can follow the interface location to maximize the heat transfer during the entire melting process.

- Investigate the solid extraction phenomenon by experimenting with different organic materials and electrical configurations.
- More research is required to understand the nature of the charge injection mechanism in the organic PCM and to develop a unified model for injection under different electric fields.
- Since Coulomb forces were proved to be the main contributor in this study, more experimental work will be needed on the materials to assess its electrical and thermo-physical properties degradation with time.
- Experimentally and numerically investigate the effect of adding other passive techniques such as fins along with EHD and their combined effect on melting and solidification of organic PCMs.

Appendix A. Thermo-physical and electrical properties

This Appendix lists the thermos-physical and electrical properties of Octadecane used in the dissertation [23][19].

Property	Value	Unit
Density	775	$[kg/m^3]$
Liquid thermal conductivity	0.152	$[W/m.K]$
Solid thermal conductivity	0.358	$[W/m.K]$
Specific heat capacity	2180	$[J/kg.K]$
Kinematic viscosity	5.03×10^{-6}	$[m^2/s]$
Latent heat of fusion	243.5	$[kJ/kg]$
Melting temperature	28	[℃]
Dielectric constant	2.1	
Volumetric expansion coefficient	0.00085	$[1/K]$
Refractive index	1.435	
$\frac{dn}{dT}$	-0.0003	$[1/K]$
$\frac{d\varepsilon}{dT}$	-0.00167	$[1/K]$

Appendix B. Shadowgraphy

This Appendix addresses the basics and fundamentals of a shadowgraph system and discuss in detail the modified correlation and shadowgraph system that is used in this dissertation.

The Shadowgraph method along with Schlieren and interferometry are all optical methods in which the spatial variation of the index of refraction caused by density variations are used to infer the temperature field[124]. These optical methods are best suited for 2D temperature measurement, i.e. there is minimal temperature variation along the path of the beam of light. The refractive index of the material and its density can be correlated by the Lorentz-Lorenz formula [125]:

$$\frac{n^2-1}{\rho(n^2+2)} = constant \tag{B.1}$$

In case of small temperature variations, the density of the medium could be related to the temperature linearly by $\rho = \rho_0(1-\beta(T-T_0))$ and the density could be replaced by the temperature in the Lorentz-Lorenz formula. In this case the medium's refractive index dependence on the temperature could be assumed to vary linearly with temperature as well.

The refractive index of a fluid is the ratio of the speed of light in vacuum to the speed of light in this fluid. As the refractive index of the material decreases, the speed of light in this fluid increases. Therefore, for a fluid that is experiencing temperature gradients, a beam of

light projected on it will face a deflection away from it. The equation of the beam of light trajectory is given by

$$\frac{d^2y}{d^2x} = \frac{1}{n}\frac{\partial n}{\partial T}\frac{\partial T}{\partial y} \tag{B.2}$$

In which $\frac{d^2y}{d^2x}$ is the change in the beam of light's slope and $\frac{\partial T}{\partial y}$ is the temperature gradient along the beam's path.

Assume a beam of light that is being projected parallel but touching the surface of a heat exchanger that is heating a stagnant transparent fluid. The heated fluid will develop a thermal boundary layer at the surface of the heat exchanger and a natural convection flow will start to develop. Now, the projected beam of light on the heat exchanger will start to experience spatial gradients in the index of refraction within the vicinity of the thermal boundary layer. The part of the beam closest to the heat exchanger will face the highest gradients and therefore will be deflected away from the surface of the heat exchanger the most [Refer to Figure B.1]. If this beam of light was allowed to project on a screen that is placed far enough from the test section, the ray of light with the maximum bend will have the maximum deflection too and a bright contour will appear on the screen where its position can be measured as an indicative to the temperature gradient at the heat transfer surface.

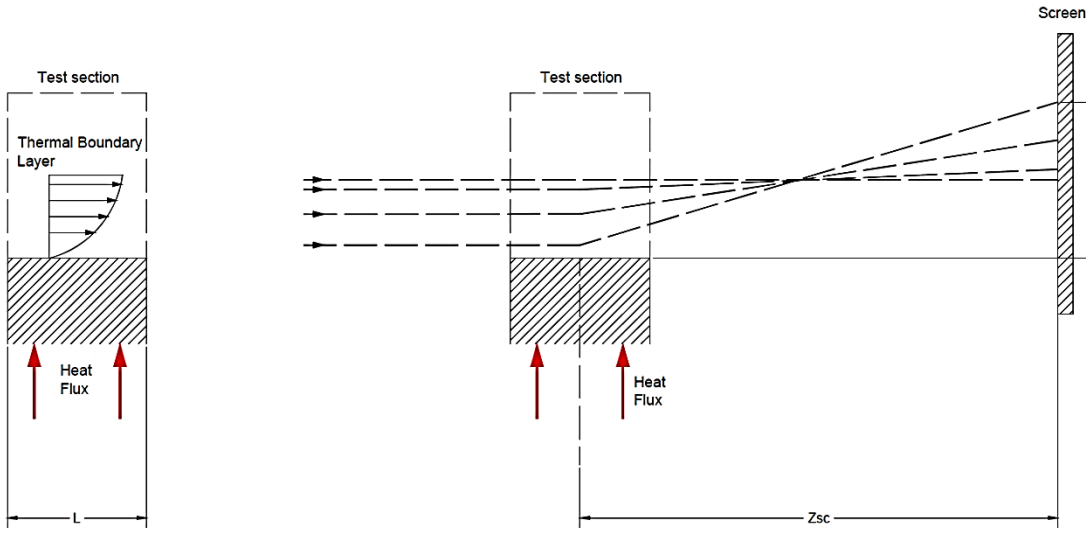

Figure B.1 Light refraction across a thermal boundary layer

The local Nusselt number at each point along the span of the heat exchanger can be evaluated by using this formula

$$Nu = -\frac{Y_{sc,max}}{T_w - T_\infty}\frac{H}{Z_{sc}L(dn/dT)_w} \tag{B.3}$$

In which $Y_{sc,max}$ is the maximum deflection of the beam projected on the screen, Z_{sc} is the distance between the exit of the test section and the projection screen and L is the depth of the heat exchanger in the direction of the path of light.

This method was used before in the analysis of melting driven by natural convection and further details about this method can be found in the experimental work done by Viskanta [98], [99], [126].

The shadowgraph method is an integral method, meaning that it is sensitive to the light path length. The above correlation that is commonly used in literature to estimate the local

heat transfer coefficient, is formulated by assuming a constant temperature gradient along the path of the beam of light [Linear temperature profile in the vicinity of the heat transfer surface]. In this case, equation B.3 is acquired by integrating equation B.2 along the depth of the test section (L) and assuming an initial entrance for the beam of light at 0°. The exit angle of the beam can then be evaluated as

$$\frac{dy}{dx} = \int_0^L \frac{1}{n}\frac{\partial n}{\partial T}\frac{\partial T}{\partial y}\, dx \tag{B.4}$$

In case of linear temperature approximation, the right hand side of equation B.4 is constant along the integration path and the temperature gradient at the wall can then be evaluated as

$$\frac{\partial T}{\partial y_w} = \frac{Y_{sc,max}\, n}{Z_{sc} L (dn/dT)_w} \tag{B.5}$$

The temperature gradient at the wall can then be used to estimate the local heat transfer coefficient and therefore the Nusselt number as described in equation B.3. This assumption is valid only for relatively short cross sections in which the beam deflection is minimal inside the test section [127].

The above assumption fails as the depth of the test section increases and the temperature gradients becomes stronger. In this case, the right hand side of equation B.4. can no further be considered as constant along the path length.

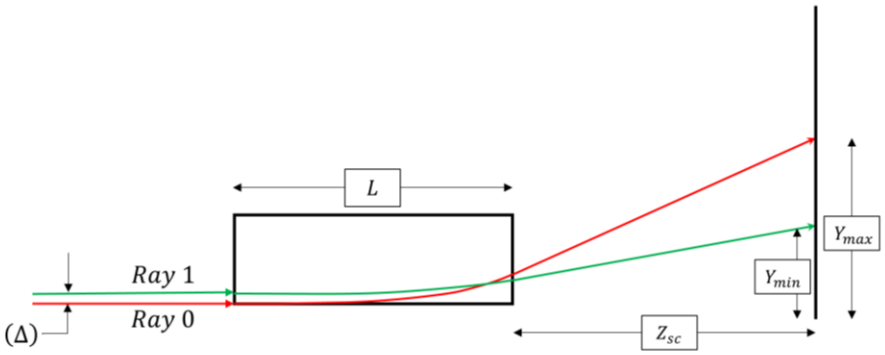

Figure B.2 Schematic of rays' deflection from the heat exchanger

Now let's assume that a parallel beam of light with defined thickness (Δ) is projected parallel to the surface of the heat exchanger. The beam will experience different temperature gradients and therefore it will no longer exit the test section with the same thickness of entrance but it will rather get stretched [Refer to Figure B.2].

In this dissertation a modified shadowgraph correlation was developed that will lead for better accuracy in measuring the local heat transfer coefficients for relatively longer test sections and higher temperature gradients which are experienced with the used of EHD.

The modified correlation assumed a second order temperature profile within the vicinity of the thermal boundary layer instead of the previous mentioned first order temperature approximation. The temperature profile will be assumed to be equal to

$$T = a_0 y^2 + by + T_w \tag{B.6}$$

Where T_w is the heat exchanger surface temperature, b is the temperature gradient at the wall $(\frac{\partial T}{\partial y_w})$ and the first power coefficient and a_0 is the second power coefficient. In this case the path of light equation becomes

$$\frac{d^2y}{d^2x} = \frac{1}{n}\frac{\partial n}{\partial T}\frac{\partial T}{\partial y} = \frac{\alpha}{n}(2a_0y + b) \tag{B.7}$$

The above equation is a second order differential equation that has an analytical solution. The projected beam of light will be analyzed as 2 rays that are distanced apart by the distance (Δ). The ray touching the heat exchanger will be called (Ray 0) and the other one is (Ray 1). Ray 0 will experience the largest deflection away from the heat exchanger surface and the solution of the maximum deflection is

$$Y_{max} = -\frac{0.5b}{a_0}Ln\sqrt{\frac{-2\alpha a_0}{n}}sin\left(\sqrt{\frac{-2\alpha a_0}{n}}Z\right) - \frac{0.5b}{a_0}\left(1-\cos\left(\sqrt{\frac{-2\alpha a_0}{n}}Z\right)\right) \tag{B.8}$$

While Ray 1 will experience the minimum deflection from the heat exchanger surface and the solution of the minimum deflection is

$$Y_{min} = -\left(\Delta+\frac{0.5b}{a_0}\right)Ln\sqrt{\frac{-2\alpha a_0}{n}}sin\left(\sqrt{\frac{-2\alpha a_0}{n}}Z\right) - \left(\Delta+\frac{0.5b}{a_0}\right)\left(1-\cos\left(\sqrt{\frac{-2\alpha a_0}{n}}Z\right)\right)+\Delta \tag{B.9}$$

From the above two equations, both deflections are dependent on the first and the second order coefficients of the temperature equation. By subtracting equation B.9 from equation B.8, one can get the magnitude of beam distortion or stretching (δ) as

$$Y_{max} - Y_{min} = \delta = \Delta\left[dn_0\sqrt{\frac{-2\alpha a_0}{n}}\,sin\left(\sqrt{\frac{-2\alpha a_0}{n}}Z\right) - cos\left(\sqrt{\frac{-2\alpha a_0}{n}}Z\right)\right] \quad \text{(B.10)}$$

From the dispersion correlation, it was found that the magnitude of dispersion is only dependent on the coefficient of the second order term (a_0) and is not dependent on the temperature gradient at the wall (b). However, the maximum beam deflection- which happens to be at the heat transfer wall- will depend upon both the distortion magnitude and the temperature gradient at the wall as

$$Y_{max} = \frac{-0.5b}{a_0}\left[\frac{\delta}{\Delta} + 1\right] \quad \text{(B.11)}$$

By first estimating a_0 from the dispersion equation, one can then estimate the temperature gradient at the wall from the maximum beam deflection and the dispersion of the initial sheet of light.

In order to assess the accompanied uncertainty with both the linear and the second-degree temperature profiles approximation used in the correlation, an optical ray tracing numerical simulation was conducted with COMSOLv5.1. The simulation solved the

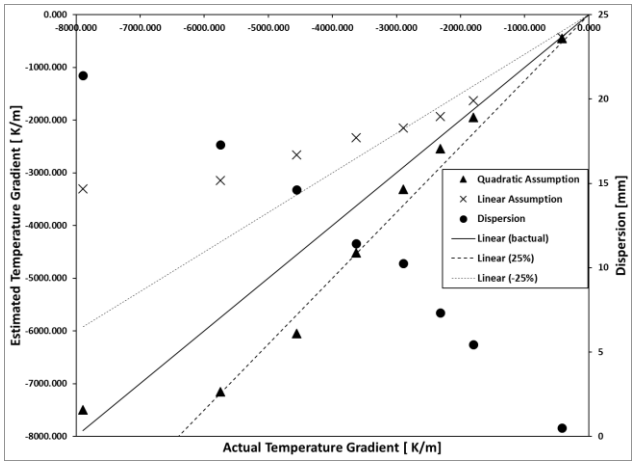

Figure B.3 Linear vs Quadratic correlation uncertainties

trajectory of the light sheet numerically and the exact maximum and minimum deflection from the heat exchanger can be accurately quantified. The temperature contours from CFD numerical simulations for melting of Octadecane were used as an input into the optical simulations. The temperature contours were chosen to cover the range of expected temperature gradients in the test facility and different heat transfer regimes from conduction, mixed conduction and convection and natural convection with stratified core. The maximum and the minimum deflection results from the optical model were then used as an input into the shadowgraph correlations to estimate the temperature gradient at the wall by the original and the modified correlation. The estimated temperature gradient from shadowgraph correlation is then compared against the temperature gradient from the input temperature contours to evaluate the uncertainty in using the current shadowgraph correlation. The linear and the modified quadratic correlation are compared against the input temperature gradient at the wall and the results are presented in Figure B.3.

Three different cases were chosen to represent three different heat transfer regimes, these regimes are conduction heat transfer, mixed conduction and convection and convection with stratified core. The results in this report are presented for the mixed conduction and convection heat transfer regime where the deviation from the quadratic assumption is expected to be maximum.

It was found that the modified (quadratic assumption) correlation can estimate the actual temperature gradient within + 25 %, however the linear temperature correlation is only suitable for small temperature gradients and the error can reach up to 50 % at high temperature gradients. The error in the average temperature gradient at the wall was calculated for this case and compared to the average gradient and was found that the overall average error is less than 19 %. It should be noted that the outcome of this uncertainty analysis is valid for the corresponding test facility only and cannot be generalized for any other system.

The shadowgraph system was used to provide a semi-quantitative tool for assessing the locations of highest temperature gradients and the size of the convection cells. This helped in understanding the flow regimes and the heat transfer coefficient augmentation by EHD compared to 0 kV cases.

Appendix C. Experimental Uncertainty

The experimental uncertainty in any of the measured or the calculated parameters were calculated following the guidelines of Kline and McClintock [128]. The overall uncertainty (δT) associated with the measurement of a parameter (T) is evaluated as

$$\delta T = \sqrt{\sum_{i=1}^{n} (\delta_i)^2} \tag{C.1}$$

Where δ_i is the different uncertainties associated with the measurement(T).

Uncertainty in temperature measurements using thermocouples

A. Uncertainty associated with the RTD

The thermocouples used in this work were of the T-type and they were calibrated against a reference platinum resistance thermometer (DP251 precision). The reported instrument accuracy of this RTD by the manufacturer is ± 0.01 ℃ and ± 0.025 ℃ system accuracy.

$$\delta_1 = \pm\sqrt{(0.01)^2 + (0.025)^2} = \pm 0.027\ ℃ \tag{C.2}$$

B. Uncertainty associated with the DAQ

The thermocouples were connected to a data acquisition card (NI-DAQ 9213). The embedded cold junction compensation of the DAQ was excluded and an ice bath cold junction was used instead for better accuracy. The maximum gain error reported by the

manufacturer is equal to 0.16 %, which corresponds to a maximum temperature uncertainty of ± 0.07℃.

$$\delta_2 = \pm 0.07\ ℃ \tag{C.3}$$

C. Uncertainty associated with the ice bath

The uncertainty in the ice bath temperature was evaluated using the RTD sensor. The maximum deviation from the 0℃ observed was 0.05℃.

$$\delta_3 = \pm 0.05\ ℃ \tag{C.4}$$

D. Uncertainty associated with ITS-90 calibration curve

The ITS-90 standard calibration curve for the thermocouples were used to convert the voltage readings into temperatures. The six coefficients polynomial equation was used for the conversion and the reported accuracy of the equation is ± 0.03℃ when operating between 0 to 400 ℃.

$$\delta_5 = \pm 0.03\ ℃ \tag{C.5}$$

Therefore, the total uncertainty in the temperature measurement can be given by

$$\delta T = \sqrt{(0.027)^2 + (0.07)^2 + (0.05)^2 + (0.03)^2} = \pm 0.1℃ \tag{C.6}$$

Uncertainty in Shadowgraph measurements

The associated uncertainty from the experimental measurements were quantified in all the experiments with a Monte-Carlo simulation. The uncertainty in the experimental measurements of the maximum and the minimum deflection and subsequently the beam distortion were estimated by randomly propagating the error with the maximums statistical error of ± 0.15 mm. The second order coefficient was calculated based on the propagated error and the temperature gradient as well. The uncertainty was estimated based on 95 % confidence interval of $(\mu \pm 2\sigma)$ which is two time the standard deviation.

The average Nusselt coefficient along the wall of the heat exchanger was then evaluated from the propagated error matrix and the associated error is calculated with the same manner.

Appendix D. C++ Source code

```
Author: David Nakhla
Date: Nov 27,2014
Not to be used without permission
e-mail:mech.davidashraf@gmail.com
Cell:+12892372963
**********/

#include "udf.h"
#include "mem.h"
#include "sg.h"
#include "math.h"

/**********
This is a UDF to calculate the electric field intensity and define the dielectrophoretic forces
**********/

DEFINE_ADJUST(Emagnitude,domain)
{
#if !RP_HOST
    cell_t c;
    Thread *tc;
    /* Fill UDS with the variable. */
    thread_loop_c(tc,domain)
```

```
        {
                begin_c_loop(c, tc)
                {
                        if (NNULLP(T_STORAGE_R_NV(tc, SV_UDSI_G(0))))
                        {
                                C_UDMI(c, tc, 0) = NV_MAG(C_UDSI_G(c, tc, 0));/*Electric Field Magnitude saved in user defined memory 0 */
                        }
                        else
                        {
                                C_UDMI(c, tc, 0) = 0.0;
                        }
                }
                end_c_loop(c, tc)
        }
    #endif
    }

    DEFINE_ADJUST(Ex, domain)
    {
    #if !RP_HOST
        cell_t c;
        Thread *tc;
        /* Fill UDS with the variable. */
        thread_loop_c(tc, domain)
        {
                begin_c_loop(c, tc)
                {
                        if (NNULLP(T_STORAGE_R_NV(tc, SV_UDSI_G(0))))
                        {
```

```
                        C_UDMI(c, tc, 1) = -C_UDSI_G(c, tc, 0)[0];/*Ex [ electric field magnitude in x direction- user defined memory 1]*/
                    }
                    else
                    {
                        C_UDMI(c, tc, 1) = 0.0;
                    }
                }
                end_c_loop(c, tc)
        }
    #endif
    }

    DEFINE_ADJUST(Ey, domain)
    {
    #if !RP_HOST
        cell_t c;
        Thread *tc;
        /* Fill UDS with the variable. */
        thread_loop_c(tc, domain)
        {
            begin_c_loop(c, tc)
            {
                if (NNULLP(T_STORAGE_R_NV(tc, SV_UDSI_G(0))))
                {
                    C_UDMI(c, tc, 2) = -C_UDSI_G(c, tc, 0)[1];/*Ey[Electric Field Magnitude in y direction-user defined memory 2]*/
                }
                else
                {
                    C_UDMI(c, tc, 2) = 0.0;
```

```
                }
            }
            end_c_loop(c, tc)
        }
    #endif
    }

    DEFINE_ADJUST(Fx, domain)
    {
    #if !RP_HOST
        real epsilon0, dedt,emean;
        real tcold;
        epsilon0 = 8.85418e-12;
        emean = 2.1;
        dedt = -0.00167;
        cell_t c;
        Thread *tc;
        tcold = 301.2;/*the cold temperature*/
        /* Fill UDS with the variable. */
        thread_loop_c(tc, domain)
        {
            begin_c_loop(c, tc)
            {
                if (NNULLP(T_STORAGE_R_NV(tc, SV_UDSI_G(0))) &&
C_T(c,tc)>=tcold)
                {
                    C_UDMI(c, tc, 3) = -0.5*epsilon0*pow(C_UDMI(c, tc, 0),
2)*dedt*C_T_G(c, tc)[0];/*dielectrophoretic body force in x direction*/
                }
                else
                {
```

```
                    C_UDMI(c, tc, 3) = 0.0;
                }
            }
            end_c_loop(c, tc)
        }
    #endif
    }
    DEFINE_ADJUST(Fy, domain)
    {
    #if !RP_HOST
        real epsilon0, dedt,emean;
        real tcold;
        epsilon0 = 8.85418e-12;
        emean = 2.1;
        dedt = -0.00167;
        cell_t c;
        Thread *tc;
        tcold = 301.2;/*the cold temperature*/
        /* Fill UDS with the variable. */
        thread_loop_c(tc, domain)
        {
            begin_c_loop(c, tc)
            {
                if (NNULLP(T_STORAGE_R_NV(tc, SV_UDSI_G(0))) &&
C_T(c,tc)>=tcold)
                {
                    C_UDMI(c, tc, 4) = -0.5*epsilon0*pow(C_UDMI(c, tc, 0),
2)*dedt*C_T_G(c, tc)[1];/*dielectrophoretic body force in y direction*/
                }
                else
                {
```

```
                        C_UDMI(c, tc, 4) = 0.0;
                    }
                }
                end_c_loop(c, tc)
        }
    #endif
    }


    DEFINE_DIFFUSIVITY(permittivity, c, t, i)
    {
    #if !RP_HOST
        real epsilon, er, epsilon0, th, ts,tl, dedt,tav,e,es;
        epsilon0 = 8.85418e-12;
        er = 2.1;/*relative dielectric constant at reference temperature for liquid*/
        es= 2.247;/*relative dielectric constant for the solid phase */
        ts = 301.1;/*solidous temperature*/
        th = 311.15;/*the hot temperature*/
        tl = 301.2;/*liquidus temperature*/
        dedt = -0.00167;/*de/dt the change in ermittivity with temperature*/
        e = dedt / er;/*the relative change*/
        real temp = C_T(c, t);
        tav = 0.5*(th + tl);
        if (C_T(c,t)<ts)
        {
            epsilon=epsilon0*es;/*return the value for the solid phase*/
        }
        else if (C_T(c,t)>tl)
        {
            epsilon = (epsilon0*er)*(1 + (e*(temp - tl)));/* The linear change in
permittivity with temperature*/
```

```
        }
        else
        {
                epsilon = epsilon0*( er + ((tl - temp)*(es - er) / (tl - ts)));

        }
        return epsilon;
    #endif
    }

    DEFINE_SOURCE(dielectrophoreticx, c, t, dS, eqn)
    {
    #if !RP_HOST
        real source,epsilon0,dedt,alpha,emean,tl,gamma;
        epsilon0 = 8.85418e-12;
        emean = 2.1;
        dedt = -0.00167;
        real temp = C_T(c, t);
        tl = 336;/*the cold temperature*/
        /*source = -0.5*epsilon0*pow(C_UDMI(c, t, 0), 2)*dedt*C_T_G(c, t)[0];
        return source;*/
        if (NNULLP(T_STORAGE_R_NV(t, SV_T_G)))
        {
                source = -0.5*epsilon0*pow(C_UDMI(c, t, 0), 2)*dedt*C_T_RG(c,
t)[0];/*The dielectophoretic x force*/
                dS[eqn] = 0.0;
        }
        else
        {
                source = 0.0;
        }
```

```
    return source;
#endif
}

DEFINE_SOURCE(dielectrophoreticy, c, t, dS, eqn)
{
#if !RP_HOST
    real source, epsilon0, dedt, alpha, emean, tl,gamma;
    epsilon0 = 8.85418e-12;
    emean = 2.1;
    dedt = -0.00167;
    real temp = C_T(c, t);
    tl = 336;/*the cold temperature*/
    /*source = -0.5*epsilon0*pow(C_UDMI(c, t, 0), 2)*dedt*C_T_G(c, t)[0];
    return source;*/
    if (NNULLP(T_STORAGE_R_NV(t, SV_T_G)))
    {
        source = -0.5*epsilon0*pow(C_UDMI(c, t, 0), 2)*dedt*C_T_RG(c, t)[1];/*The dielectophoretic y force*/
        dS[eqn] = 0.0;
    }
    else
    {
        source = 0.0;
    }
    return source;
#endif
}

DEFINE_PROPERTY(knew, c, t)
{
```

```
#if !RP_HOST
        real ktc, temp, ts, tl,ks,kl;
        temp = C_T(c, t);
        ts = 326;
        tl = 336;
        ks = 0.339;
        kl = 0.21;
        if (temp < ts)
        {
                ktc = ks;
        }
        else if (temp > tl)
        {
                ktc = kl;
        }
        else
        {
                ktc = kl + ((tl - temp)*(ks - kl) / (tl - ts));
        }
        return ktc;
#endif
}
```

References

[1] P. Arce, M. Medrano, A. Gil, E. Oró, and L. F. Cabeza, "Overview of thermal energy storage (TES) potential energy savings and climate change mitigation in Spain and Europe," *Appl. Energy*, vol. 88, no. 8, pp. 2764–2774, Aug. 2011.

[2] L. Navarro, A. de Gracia, D. Niall, A. Castell, M. Browne, S. J. McCormack, P. Griffiths, and L. F. Cabeza, "Thermal energy storage in building integrated thermal systems: A review. Part 2. Integration as passive system," *Renew. Energy*, vol. 85, pp. 1334–1356, Jan. 2016.

[3] A. De Gracia and L. F. Cabeza, "Phase change materials and thermal energy storage for buildings," *Energy and Buildings*, vol. 103. Elsevier, pp. 414–419, 15-Sep-2015.

[4] A. Sharma, V. V. Tyagi, C. R. Chen, and D. Buddhi, "Review on thermal energy storage with phase change materials and applications," *Renew. Sustain. Energy Rev.*, vol. 13, no. 2, pp. 318–345, Feb. 2009.

[5] B. Zalba, J. M. Marín, L. F. Cabeza, and H. Mehling, *Review on thermal energy storage with phase change: materials, heat transfer analysis and applications*, vol. 23, no. 3. 2003.

[6] A. Abhat, "Low temperature latent heat thermal energy storage: heat storage materials," *Sol. energy*, vol. 10, no. 4, pp. 313–332, 1983.

[7] A. Gil, M. Medrano, I. Martorell, A. Lázaro, P. Dolado, B. Zalba, and L. F. Cabeza, "State of the art on high temperature thermal energy storage for power generation. Part 1-Concepts, materials and modellization," *Renew. Sustain. Energy Rev.*, vol. 14, no. 1,

pp. 31–55, Jan. 2010.

[8] A. Sarı, H. Sarı, and A. Önal, “Thermal properties and thermal reliability of eutectic mixtures of some fatty acids as latent heat storage materials,” *Energy Convers. Manag.*, vol. 45, no. 3, pp. 365–376, Feb. 2004.

[9] M. Mazman, L. F. Cabeza, H. Mehling, H. Ö. Paksoy, and H. Evliya, “Heat transfer enhancement of fatty acids when used as PCMs in thermal energy storage,” *Int. J. energy Res.*, vol. 32, no. May 2007, pp. 135–143, 2008.

[10] P. Di Marco and W. Grassi, “Motivation and results of a long-term research on pool boiling heat transfer in low gravity,” *Int. J. Therm. Sci.*, vol. 41, no. 7, pp. 567–585, Jun. 2002.

[11] P. Di Marco, “The use of electric force as a replacement of buoyancy in two-phase flow,” *Microgravity Sci. Technol.*, vol. 24, no. 3, pp. 215–228, Jun. 2012.

[12] D. Nakhla, H. Sadek, and J. S. Cotton, “Melting performance enhancement in latent heat storage module using solid extraction electrohydrodynamics (EHD),” *Int. J. Heat Mass Transf.*, vol. 81, pp. 695–704, Feb. 2015.

[13] D. Nakhla, “An Enhanced Latent Heat Thermal Storage System Using Electrohydrodynamics (EHD),” McMaster University, 2013.

[14] D. Feldman, M. M. Shapiro, D. Banu, and C. J. Fuks, “Fatty acids and their mixtures as phase-change materials for thermal energy storage,” *Sol. Energy Mater.*, vol. 18, no. 3, pp. 201–216, Mar. 1989.

[15] Byung Chul Shin, Sang Done Kim, and P. Won-Hoon, “Phase separation and

supercooling of a latent heat-storage material," *Energy*, vol. 14, no. 12, pp. 921–930, Dec. 1989.

[16] A. Sharma, V. V. Tyagi, C. R. Chen, and D. Buddhi, "Review on thermal energy storage with phase change materials and applications," *Renew. Sustain. Energy Rev.*, vol. 13, no. 2, pp. 318–345, Feb. 2009.

[17] J. Stefan, "Uber einige probleme der theorie der warmeletung," *Sitzer. Wien. Akad. Math. Naturw.*, vol. 98, pp. 473–484, 1889.

[18] A. Faghri and Y. Zhang, *Transport phenomena in multiphase systems*. Elsevier, 2006.

[19] C. Ho, "Solid-liquid phase change heat transfer in enclosures," Purdue University, 1982.

[20] C. Ho and R. Viskanta, "Heat transfer during melting from an isothermal vertical wall," *J. Heat Transfer*, vol. 106, no. February 1984, pp. 12–19, 1984.

[21] M. Bareiss and H. Beer, "Influence of natural convection on the melting process in a vertical cylindrical enclosure," *Lett. heat mass Transf.*, vol. 7, no. 5, pp. 329–338, 1980.

[22] M. Bareiss and H. Beer, "Experimental investigation of melting heat transfer with regard to different geometric arrangements," *Int. Commun. Heat Mass Transf.*, vol. 11, no. 4, pp. 323–333, 1984.

[23] C. Benard, D. Gobin, and a. Zanoli, "Moving boundary problem: heat conduction in the solid phase of a phase-change material during melting driven by natural convection in the liquid," *Int. J. Heat Mass Transf.*, vol. 29, no. 11, pp. 1669–1681, Nov. 1986.

[24] P. Jany and A. Bejan, "Scaling theory of melting with natural convection in an enclosure," *Int. J. Heat Mass Transf.*, vol. 31, no. 6, pp. 1221–1235, Jun. 1988.

[25] H. M. Teamah, M. F. Lightstone, and J. S. Cotton, "An alternative approach for assessing the benefit of phase change materials in solar domestic hot water systems," *Sol. Energy*, vol. 158, pp. 875–888, Dec. 2017.

[26] M. Y. Abdelsalam, P. Sarafraz, J. S. Cotton, and M. F. Lightstone, "Heat transfer characteristics of a hybrid thermal energy storage tank with Phase Change Materials (PCMs) during indirect charging using isothermal coil heat exchanger," *Sol. Energy*, vol. 157, pp. 462–476, Nov. 2017.

[27] M. Kenisarin and K. Mahkamov, "Solar energy storage using phase change materials," *Renew. Sustain. Energy Rev.*, vol. 11, no. 9, pp. 1913–1965, Dec. 2007.

[28] S. Jegadheeswaran and S. D. Pohekar, "Performance enhancement in latent heat thermal storage system: A review," *Renew. Sustain. Energy Rev.*, vol. 13, no. 9, pp. 2225–2244, Dec. 2009.

[29] F. Agyenim, N. Hewitt, P. Eames, and M. Smyth, "A review of materials, heat transfer and phase change problem formulation for latent heat thermal energy storage systems (LHTESS)," *Renew. Sustain. Energy Rev.*, vol. 14, no. 2, pp. 615–628, Feb. 2010.

[30] N. S. Dhaidan and J. M. Khodadadi, "Improved performance of latent heat energy storage systems utilizing high thermal conductivity fins: A review," *J. Renew. Sustain. Energy*, vol. 9, no. 3, 2017.

[31] M. Lacroix and M. Benmadda, "Numerical Simulation of Natural Convection-Dominated Melting and Solidification From a Finned Vertical Wall," *Numer. Heat Transf. Part A Appl.*, vol. 31, no. January, pp. 71–86, 1997.

[32] U. Stritih, "An experimental study of enhanced heat transfer in rectangular PCM thermal

storage," *Int. J. Heat Mass Transf.*, vol. 47, no. 12–13, pp. 2841–2847, Jun. 2004.

[33] A. A. Rabienataj Darzi, M. Jourabian, and M. Farhadi, "Melting and solidification of PCM enhanced by radial conductive fins and nanoparticles in cylindrical annulus," *Energy Convers. Manag.*, vol. 118, pp. 253–263, Jun. 2016.

[34] B. Kamkari and H. Shokouhmand, "Experimental investigation of phase change material melting in rectangular enclosures with horizontal partial fins," *Int. J. Heat Mass Transf.*, vol. 78, pp. 839–851, Nov. 2014.

[35] Y. H. Wang and Y. T. Yang, "Three-dimensional transient cooling simulations of a portable electronic device using PCM (phase change materials) in multi-fin heat sink," *Energy*, vol. 36, no. 8, pp. 5214–5224, Aug. 2011.

[36] L. W. Fan, Y. Q. Xiao, Y. Zeng, X. Fang, X. Wang, X. Xu, Z. T. Yu, R. H. Hong, Y. C. Hu, and K. F. Cen, "Effects of melting temperature and the presence of internal fins on the performance of a phase change material (PCM)-based heat sink," *Int. J. Therm. Sci.*, vol. 70, pp. 114–126, Aug. 2013.

[37] R. Pakrouh, M. J. Hosseini, and A. A. Ranjbar, "A parametric investigation of a PCM-based pin fin heat sink," *Mech. Sci.*, vol. 6, no. 1, pp. 65–73, 2015.

[38] R. Velraj, R. V. Seeniraj, B. Hafner, C. Faber, and K. Schwarzer, "Heat Transfer Enhancement in a Latent Heat Storage System," *Sol. Energy*, vol. 65, no. 3, pp. 171–180, Feb. 1999.

[39] E.-B. S. Mettawee and G. M. R. Assassa, "Thermal conductivity enhancement in a latent heat storage system," *Sol. Energy*, vol. 81, no. 7, pp. 839–845, Jul. 2007.

[40] A. Sarı and A. Karaipekli, "Thermal conductivity and latent heat thermal energy storage characteristics of paraffin/expanded graphite composite as phase change material," *Appl. Therm. Eng.*, vol. 27, no. 8–9, pp. 1271–1277, Jun. 2007.

[41] N. S. Dhaidan, "Nanostructures assisted melting of phase change materials in various cavities," *Appl. Therm. Eng.*, vol. 111, pp. 193–212, Jan. 2017.

[42] S. Kim and L. T. Drzal, "High latent heat storage and high thermal conductive phase change materials using exfoliated graphite nanoplatelets," *Sol. Energy Mater. Sol. Cells*, vol. 93, no. 1, pp. 136–142, Jan. 2009.

[43] Y. Zeng, L. W. Fan, Y. Q. Xiao, Z. T. Yu, and K. F. Cen, "An experimental investigation of melting of nanoparticle-enhanced phase change materials (NePCMs) in a bottom-heated vertical cylindrical cavity," *Int. J. Heat Mass Transf.*, vol. 66, pp. 111–117, Nov. 2013.

[44] C. J. Ho and J. Y. Gao, "An experimental study on melting heat transfer of paraffin dispersed with Al2O3 nanoparticles in a vertical enclosure," *Int. J. Heat Mass Transf.*, vol. 62, pp. 2–8, Jul. 2013.

[45] L.-W. Fan, Z.-Q. Zhu, Y. Zeng, Q. Ding, and M.-J. Liu, "Unconstrained melting heat transfer in a spherical container revisited in the presence of nano-enhanced phase change materials (NePCM)," *Int. J. Heat Mass Transf.*, vol. 95, pp. 1057–1069, Apr. 2016.

[46] Y. K. Oh, S. H. Park, and Y. I. Cho, "A study of the effect of ultrasonic vibrations on phase-change heat transfer," *Int. J. Heat Mass Transf.*, vol. 45, no. 23, pp. 4631–4641, Nov. 2002.

[47] B.-T. Chu, "Thermodynamics of Electrically Conducting Fluids," *Phys. Fluids*, vol. 2,

no. 5, p. 473, 1959.

[48] J. R. Melcher, *Continuum Electromechanics*. 1981.

[49] J. E. Bryan and J. Seyed-Yagoobi, "Influence of Flow Regime, Heat Flux, and Mass Flux on Electrohydrodynamically Enhanced Convective Boiling," *J. Heat Transfer*, vol. 123, no. 2, p. 355, 2001.

[50] J. R. Melcher, "Traveling-Wave Induced Electroconvection," *Phys. Fluids*, vol. 9, no. 8, p. 1548, 1966.

[51] J. R. Melcher and M. S. Firebaugh, "Traveling-Wave Bulk Electroconvection Induced across a Temperature Gradient," *Phys. Fluids*, vol. 10, no. 6, p. 1178, 1967.

[52] B. J. F. Hoburg and J. R. Melcher, "Internal electrohydrodynamic instability and mixing of fluids with orthogonal field and conductivity gradients," vol. 73, pp. 333–351, 1976.

[53] P. Atten and J. Seyed-Yagoobi, "Electrohydrodynamically induced dielectric liquid flow through pure conductionin point/plane geometry," *IEEE Trans. Dielectr. Electr. Insul.*, vol. 10, no. 1, pp. 27–36, Feb. 2003.

[54] S. Jeong and J. Seyed-Yagoobi, "Experimental study of electrohydrodynamic pumping through conduction phenomenon," *J. Electrostat.*, vol. 56, no. 2, pp. 123–133, Sep. 2002.

[55] Y. Feng and J. Seyed-Yagoobi, "Understanding of electrohydrodynamic conduction pumping phenomenon," *Phys. Fluids*, vol. 16, no. 7, p. 2432, 2004.

[56] M. Pearson and J. Seyed-Yagoobi, "Advances in electrohydrodynamic conduction pumping," *IEEE Trans. Dielectr. Electr. Insul.*, vol. 16, no. 2, pp. 424–434, Apr. 2009.

[57] J. C. Lacroix, P. Atten, and E. J. Hopfinger, "Electro-convection in a dielectric liquid layer subjected to unipolar injection," *J. Fluid Mech.*, vol. 69, no. 3, pp. 539–563, 1975.

[58] A. Watson and J. S. Chang, "Electromagnetic Hydrodynamics," *IEEE Trans. Dielectr. Electr. Insul.*, vol. 1, no. 5, 1994.

[59] R. J. Turnbull and J. R. Melcher, "Electrohydrodynamic Rayleigh-Taylor Bulk Instability," *Phys. Fluids*, vol. 12, no. 6, p. 1160, 1969.

[60] A. Yabe, "Active heat transfer enhancement by applying electric fields," in *Proceedings of the 1991 ASME JSME thermal engineering joint conference*, 1991.

[61] A. Yabe, T. Taketani, H. Maki, K. Takahashi, and Y. Nakadai, "Experimental study of electrohydrodynamically(EHD) enhanced evaporator for nonazeotropic mixtures.," *... , Anaheim, CA, USA, 01/25-29/ ...*, 1992.

[62] C. E. Norris, J. S. Cotton, M. Shoukri, J. S. Chang, and T. Smith-Pollard, "Electrohydrodynamic effects on flow redistribution and convective boiling in horizontal concentric tubes under high inlet quality conditions," *ASHRAE Trans.*, vol. 105, 1999.

[63] J. S. Cotton, M. Shoukri, J. Chang, and T. Smith-Pollard, "Electrohydrodynamic (EHD) Flow and Convective Boiling Augmentation in Single-Component Horizontal Annular Channels," *Am. Soc. Mech. Eng. Heat Transf. Div. HTD*, vol. 366, 2000.

[64] G. McGranaghan and A. J. Robinson, "EHD Augmented Convective Boiling: Flow Regimes and Enhanced Heat Transfer," *Heat Transf. Eng.*, vol. 35, no. 5, pp. 517–527, Nov. 2013.

[65] M. Salehi, M. M. Ohadi, and S. Dessiatoun, "EHD Enhanced Convective Boiling of R-134a in Grooved Channels—Application to Subcompact Heat Exchangers," *J. Heat Transfer*, vol. 119, no. 4, p. 805, Nov. 1997.

[66] M. E. Franke, "Effect of Vortices Induced by Corona Discharge on Free-Convection Heat Transfer From a Vertical Plate," *J. Heat Transfer*, vol. 91, no. 3, pp. 427–432, 1969.

[67] J. L. Fernández and R. Poulter, "Radial mass flow in electrohydrodynamically-enhanced forced heat transfer in tubes," *Int. J. Heat Mass Transf.*, vol. 30, no. 10, pp. 2125–2136, 1987.

[68] T. Fujino, Y. Yokoyama, and Y. H. Mori, "Augmentation of Laminar Forced-Convective Heat Transfer by the Application of a Transverse Electric Field," *J. Heat Transfer*, vol. 111, no. May, pp. 345–351, 1989.

[69] N. Kasayapanand, "Electrode arrangement effect on natural convection," *Energy Convers. Manag.*, vol. 48, no. 4, pp. 1323–1330, 2007.

[70] N. Kasayapanand, "Numerical modeling of natural convection in partially open square cavities under electric field," *Int. Commun. Heat Mass Transf.*, vol. 34, no. 5, pp. 630–643, 2007.

[71] N. Kasayapanand and T. Kiatsiriroat, "Numerical modeling of the electrohydrodynamic effect to natural convection in vertical channels," *Int. Commun. Heat Mass Transf.*, vol. 34, no. 2, pp. 162–175, 2007.

[72] N. Kasayapanand, "A computational fluid dynamics modeling of natural convection in finned enclosure under electric field," *Appl. Therm. Eng.*, vol. 29, no. 1, pp. 131–141,

2009.

[73] B. Futterer, N. Dahley, and C. Egbers, “Thermal electro-hydrodynamic heat transfer augmentation in vertical annuli by the use of dielectrophoretic forces through a.c. electric field,” *Int. J. Heat Mass Transf.*, vol. 93, pp. 144–154, Feb. 2016.

[74] S. Laohalertdecha, P. Naphon, and S. Wongwises, “A review of electrohydrodynamic enhancement of heat transfer,” *Renewable and Sustainable Energy Reviews*, vol. 11, no. 5. Pergamon, pp. 858–876, 01-Jun-2007.

[75] S. Rashidi, H. Bafekr, R. Masoodi, and E. M. Languri, “EHD in thermal energy systems - A review of the applications, modelling, and experiments,” *Journal of Electrostatics*, vol. 90. Elsevier, pp. 1–14, 01-Dec-2017.

[76] A. Singh, M. M. Ohadi, S. Dessiatoun, and W. Chu, “In-tube boiling heat transfer coefficients of R-123 and their enhancement using the EHD technique,” American Society of Heating, Refrigerating and Air-Conditioning Engineers, Inc., Atlanta, GA (United States), 1995.

[77] J. Cotton, A. J. Robinson, M. Shoukri, and J. S. Chang, “A two-phase flow pattern map for annular channels under a DC applied voltage and the application to electrohydrodynamic convective boiling analysis,” *Int. J. Heat Mass Transf.*, vol. 48, no. 25–26, pp. 5536–5579, 2005.

[78] S. Nangle-Smith and J. S. Cotton, “EHD-based load controllers for R134a convective boiling heat exchangers,” *Appl. Energy*, vol. 134, pp. 125–132, 2014.

[79] S. Nangle-Smith, H. Sadek, and J. S. Cotton, “The influence of the electrophoretic and polarization forces on two phase flow redistribution in a horizontal annular tube,” *Int. J.*

Plasma Environ. Sci. Technol., vol. 7, no. 1, pp. 64–70, 2013.

[80] J. Ogata and A. Yabe, "Augmentation of boiling heat transfer by utilizing the EHD effect-EHD behaviour of boiling bubbles and heat transfer characteristics," *Int. J. Heat Mass Transf.*, vol. 36, no. 3, pp. 783–791, Feb. 1993.

[81] H. J. Cho, I. S. Kang, Y. C. Kweon, and M. H. Kim, "Numerical study of the behavior of a bubble attached to a tip in a nonuniform electric field," *Int. J. Multiph. Flow*, vol. 24, no. 3, pp. 479–498, Apr. 1998.

[82] H. R. Velkoff and J. H. Miller, "Condensation of Vapor on a Vertical Plate With a Transverse Electrostatic Field," *J. Heat Transfer*, vol. 87, no. 2, p. 197, May 1965.

[83] A. Yabe, T. Taketani, K. Kikuchi, Y. Mori, and K. Hijikata, "Augmentation of condensation heat transfer around vertical cooled tubes provided with helical wire electrodes by applying nonuniform electric fields," in *Proceedings of the International Symposium on Heat Transfer*, 1987, pp. 812–819.

[84] K. Cheung, M. M. Ohadi, and S. V. Dessiatoun, "EHD-assisted external condensation of R-134a on smooth horizontal and vertical tubes," *Int. J. Heat Mass Transf.*, vol. 42, no. 10, pp. 1747–1755, 1999.

[85] A. Gidwani, M. Molki, and M. Ohadi, "EHD-Enhanced Condensation of Alternative Refrigerants in Smooth and Corrugated Tubes," *HVAC&R Res.*, vol. 8, no. 3, pp. 219–237, Jul. 2002.

[86] H. Sadek, A. J. Robinson, J. S. Cotton, C. Y. Ching, and M. Shoukri, "Electrohydrodynamic enhancement of in-tube convective condensation heat transfer," *Int. J. Heat Mass Transf.*, vol. 49, no. 9–10, pp. 1647–1657, May 2006.

[87] H. Sadek, J. S. Cotton, C. Y. Ching, and M. Shoukri, "Effect of frequency on two-phase flow regimes under high-voltage AC electric fields," *J. Electrostat.*, vol. 66, no. 1–2, pp. 25–31, Jan. 2008.

[88] G. S. Dulikravich, M. J. Colaço, B. H. Dennis, T. J. Martin, I. N. Egorov-Yegorov, and S. Lee, "Optimization of intensities and orientations of magnets controlling melt flow during solidification," *Mater. Manuf. Process.*, vol. 19, no. 4, pp. 695–718, 2004.

[89] B. H. Dennis and G. S. Dulikravich, "Magnetic field suppression of melt flow in crystal growth," *Int. J. Heat Fluid Flow*, vol. 23, no. 3, pp. 269–277, Jun. 2002.

[90] P. R. Dellorusso, "ElectroHydrodynamic heat transfer enhancement for a latent heat storage heat exchanger," Technical University of Nova Scotia, 1997.

[91] E. Thompson, "Electrohydrodynamic solidification of phase change materials," McMaster University, 2017.

[92] P. Michael, C. Alison, G. Cooper, and J. VanTol, "Testing Facility Design for EHD Enhancement of Latent Heat Thermal Storage," 2016.

[93] B. Lacroix, "Study of an Enhanced Latent Heat Thermal Storage System using ElectroHydrodynamics in Steady State," 2016.

[94] C. Bénard, D. Gobin, and F. Martinez, "Melting in Rectangular Enclosures: Experiments and Numerical Simulations," *J. Heat Transfer*, vol. 107, no. 4, p. 794, 1985.

[95] D. M. Taylor and I. E. Noble, "Mobility studies in liquid n-octadecane," in *Conference on Electrical Insulation & Dielectric Phenomena - Annual Report 1976*, 1976, pp. 167–174.

[96] W. Hauf and U. Grigull, "Optical Methods in Heat Transfer," *Adv. Heat Transf.*, vol. 6, pp. 133–366, 1970.

[97] G. S. Settles, *Schlieren and shadowgraph techniques: visualizing phenomena in transparent media*. Springer Science & Business Media, 2012.

[98] C. Ho and R. Viskanta, "Heat transfer during melting from an isothermal vertical wall," *J. Heat Transfer*, vol. 106, no. 1, pp. 12–19, 1984.

[99] A. G. Bathelt, R. Viskanta, and W. Leidenfrost, "Latent Heat-of-Fusion Energy Storage: Experiments on Heat Transfer from Cylinders During Melting," *J. Heat Transfer*, vol. 101, no. 3, p. 453, Aug. 1979.

[100] M. J. Gross and J. E. Porter, "Electrically induced convection in dielectric liquids," *Nature*, vol. 212, pp. 1343–1345, 1966.

[101] D. M. Taylor and I. E. Noble, "Electrical conduction in n-octadecane crystals," *J. Phys. D. Appl. Phys.*, vol. 13, no. 11, pp. 2123–2133, Nov. 1980.

[102] M. Dover and W. Hensley, "Properties of 1-Octadecene, n-Octadecane, and Di-m-tolylethane," *Ind. Eng. Chem.*, vol. 27, no. 3, pp. 1933–1935, Mar. 1935.

[103] M. Daaboul, P. Traore, P. Vazquez, and C. Louste, "Study of the transition from conduction to injection in an electrohydrodynamic flow in blade-plane geometry," *J. Electrostat.*, vol. 88, pp. 71–75, 2017.

[104] S. Jayaram, J. D. Cross, and E. J. Weckman, "Electrokinetic study in non-polar liquids by laser Doppler anemometry," *J. Electrostat.*, vol. 34, no. 1, pp. 1–16, 1995.

[105] Y. Dutil, D. R. Rousse, N. Ben Salah, S. Lassue, and L. Zalewski, "A review on phase-

change materials: Mathematical modeling and simulations," *Renew. Sustain. Energy Rev.*, vol. 15, no. 1, pp. 112–130, Jan. 2011.

[106] A. Bejan, *Convection Heat Transfer*. Hoboken, NJ, USA: John Wiley & Sons, Inc., 2013.

[107] J. M. Crowley, "Dimensionless ratios in electrohydrodynamics," in *Handbook of Electrostatic Processes*, New York Marcel Dekker, Inc, 1995, pp. 99–119.

[108] I. Adamczewskit and J. H. Calderwood, "Viscosity and charge carrier mobility in the saturated hydrocarbons," *J. Phys. D. Appl. Phys.*, vol. 8, no. 0, p. 1211, 1975.

[109] G. Kunti, A. Bhattacharya, and S. Chakraborty, "A scaling analysis for electrohydrodynamic convection with variable thermophysical and electrical properties," *Int. J. Heat Mass Transf.*, vol. 109, 2017.

[110] I. E. Noble and D. M. Taylor, "Electrical conduction in liquid and solid octadecane," *J. Phys. D. Appl. Phys.*, vol. 13, no. 11, pp. 2115–2121, Nov. 1980.

[111] J. Seyed-Yagoobi, "Augmentation of two-phase and single-phase heat transfer and mass transport with electrohydrodynamics in thermal equipment," in *IEEE 13th International Conference on Dielectric Liquids*, 1999, pp. 378–383.

[112] J. Darabi and H. Wang, "Development of an electrohydrodynamic injection micropump and its potential application in pumping fluids in cryogenic cooling systems," *J. Microelectromechanical Syst.*, vol. 14, no. 4, pp. 747–755, Aug. 2005.

[113] T. B. Jones, "Electrohydrodynamically Enhanced Heat Transfer in Liquids—A Review," *Adv. Heat Transf.*, vol. 14, no. C, pp. 107–148, Jan. 1979.

[114] A. Denat, B. Gosse, and J. P. Gosse, “Ion injections in hydrocarbons,” *J. Electrostat.*, vol. 7, no. C, pp. 205–225, 1979.

[115] B. P. H. Roberts, “Electrohydrodynamic Convection,” *Q J Mech. Appl Math*, vol. XXII, no. March, 1968.

[116] P. J. Stiles, “Electro-thermal convection in dielectric liquids,” *Chem. Phys. Lett.*, vol. 179, no. 3, pp. 311–315, 1991.

[117] H. N. Yoshikawa, M. Tadie Fogaing, O. Crumeyrolle, and I. Mutabazi, “Dielectrophoretic Rayleigh-Bénard convection under microgravity conditions.,” *Phys. Rev. E. Stat. Nonlin. Soft Matter Phys.*, vol. 87, no. 4, p. 43003, 2013.

[118] R. J. Turnbull, “Effect of a non-uniform alternating electric field on the thermal boundary layer near a heated vertical plate,” *J. Fluid Mech.*, vol. 49, no. 4, p. 693, Oct. 1971.

[119] N. Kasayapanand, “Numerical modeling of the effect of number of electrodes on natural convection in an EHD fluid,” *J. Electrostat.*, vol. 65, no. 7, pp. 465–474, 2007.

[120] H. S. Shu and F. C. Lai, “Effect of electrical field on buoyancy-induced flows in an enclosure,” *IAS ’95. Conf. Rec. 1995 IEEE Ind. Appl. Conf. Thirtieth IAS Annu. Meet.*, vol. 2, no. 2, pp. 1465–1471, 1995.

[121] T. J. Lewis, “Mechanism of Electrical Breakdown in Saturated Hydrocarbon Liquids,” *J. Appl. Phys.*, vol. 27, no. 6, pp. 645–650, Jun. 1956.

[122] Y. V. Torshin, “Impulse electrical breakdown of liquid hydrocarbons. Dynamics of phenomena with increasing voltage amplitude and decreasing of nonuniformity field.

Prediction of the liquid breakdown voltage," *High Temp.*, vol. 49, no. 1, pp. 12–21, Feb. 2011.

[123] E. O. Forster, "Electrical breakdown in liquid hydrocarbons," *J. Electrostat.*, vol. 12, pp. 1–12, Apr. 1982.

[124] R. Goldstein, "Optical techniques for temperature measurement," *Meas. Heat Transf.*, 1976.

[125] R. Goldstein, *Fluid mechanics measurements*. 1996.

[126] A. Bathelt and R. Viskanta, "Heat transfer and interface motion during melting and solidification around a finned heat source/sink," *J. Heat Transfer*, vol. 103, no. 4, pp. 720–726, 1981.

[127] Z. F. Dong and M. A. Ebadian, "A modified formula for calculating the heat transfer coefficient by the shadowgraph technique," *Int. J. Heat Mass Transf.*, vol. 35, no. 7, pp. 1833–1836, 1992.

[128] S. J. Kline and F. A. McClintock, "Describing uncertainties in single-sample experiments," *Mech. Eng.*, vol. 75, no. 1, pp. 3–8, 1953.